Instructions to Authors

Instructions to authors concerning manuscript organization and format apply to hardcopy submission by mail, and also to electronic online submission via the Journal homepage website (http://jjp.yu.edu.jo).

Manuscript Submission

1- **E-mail to** : jjp@yu.edu.jo

2- **Online**: Follow the instructions at the journal homepage website.

Original *Research Articles*, *Communications* and *Technical Notes* are subject to critical review by minimum of two competent referees. Authors are encouraged to suggest names of competent reviewers. *Feature Articles* in active Physics research fields, in which the author's own contribution and its relationship to other work in the field constitute the main body of the article, appear as a result of an invitation from the Editorial Board, and will be so designated. The author of a *Feature Article* will be asked to provide a clear, concise and critical status report of the field as an introduction to the article. *Review Articles* on active and rapidly changing Physics research fields will also be published. Authors of *Review Articles* are encouraged to submit two-page proposals to the Editor-in-Chief for approval. Manuscripts submitted in *Arabic* should be accompanied by an Abstract and Keywords in English.

Organization of the Manuscript

Manuscripts should be typed double spaced on one side of A4 sheets (21.6 x 27.9 cm) with 3.71 cm margins, using Microsoft Word 2000 or a later version thereof. The author should adhere to the following order of presentation: Article Title, Author(s), Full Address and E-mail, Abstract, PACS and Keywords, Main Text, Acknowledgment. Only the first letters of words in the Title, Headings and Subheadings are capitalized. Headings should be in **bold** while subheadings in *italic* fonts.

Title Page: Includes the title of the article, authors' first names, middle initials and surnames and affiliations. The affiliation should comprise the department, institution (university or company), city, zip code and state and should be typed as a footnote to the author's name. The name and complete mailing address, telephone and fax numbers, and e-mail address of the author responsible for correspondence (designated with an asterisk) should also be included for official use. The title should be carefully, concisely and clearly constructed to highlight the emphasis and content of the manuscript, which is very important for information retrieval.

Abstract: A one paragraph abstract not exceeding 200 words is required, which should be arranged to highlight the purpose, methods used, results and major findings**.**

Keywords: A list of 4-6 keywords, which expresses the precise content of the manuscript for indexing purposes, should follow the abstract.

PACS: Authors should supply one or more relevant PACS-2006 classification codes, (available at http://www.aip.org/pacs/pacs06/pacs06-toc.html)

Introduction: Should present the purpose of the submitted work and its relationship to earlier work in the field, but it should not be an extensive review of the literature (e.g., should not exceed 1 ½ typed pages).

Experimental Methods: Should be sufficiently informative to allow competent reproduction of the experimental procedures presented; yet concise enough not to be repetitive of earlier published procedures.

Results: should present the results clearly and concisely.

Discussion: Should be concise and focus on the interpretation of the results.

Conclusion: Should be a brief account of the major findings of the study not exceeding one typed page.

Acknowledgments: Including those for grant and financial support if any, should be typed in one paragraph directly preceding the References.

References: References should be typed double spaced and numbered sequentially in the order in which they are cited in the text. References should be cited in the text by the appropriate Arabic numerals, enclosed in square brackets. Titles of journals are abbreviated according to list of scientific periodicals. The style and punctuation should conform to the following examples:

1. Journal Article:
   a) Heisenberg, W., Z. Phys. 49 (1928) 619.
   b) Bednorz, J. G. and Müller, K. A., Z. Phys. B64 (1986) 189
   c) Bardeen, J., Cooper, L.N. and Schrieffer, J. R., Phys. Rev. 106 (1957) 162.
   d) Asad, J. H., Hijjawi, R. S., Sakaji, A. and Khalifeh, J. M., Int. J. Theor. Phys. 44(4) (2005), 3977.

2. Books with Authors, but no Editors:
   a) Kittel, C., "Introduction to Solid State Physics", 8th Ed. (John Wiley and Sons, New York, 2005), chapter 16.
   b) Chikazumi, S., C. D. Graham, JR, "Physics of Ferromagnetism", 2nd Ed. (Oxford University Press, Oxford, 1997).

3. Books with Authors and Editors:
   a) Allen, P. B. "Dynamical Properties of Solids", Ed. (1), G. K. Horton and A. A. Maradudin (North-Holland, Amsterdam, 1980), p137.
   b) Chantrell, R. W. and O'Grady, K., "Magnetic Properities of Fine Particles" Eds. J. L. Dormann and D. Fiorani (North-Holland, Amsterdam, 1992), p103.

4. Technical Report:
Purcell, J. "The Superconducting Magnet System for the 12-Foot Bubble Chamber", report ANL/HEP6813, Argonne Natt. Lab., Argonne, III, (1968).

5. Patent:
Bigham, C. B., Schneider, H. R., US patent 3 925 676 (1975).

6. Thesis:
Mahmood, S. H., Ph.D. Thesis, Michigan State University, (1986), USA (Unpublished).

7. Conference or Symposium Proceedings:
Blandin, A. and Lederer, P. Proc. Intern. Conf. on Magnetism, Nottingham (1964), P.71.

8. Internet Source:
Should include authors' names (if any), title, internet website, URL, and date of access.

9. Prepublication online articles (already accepted for publication):
Should include authors' names (if any), title of digital database, database website, URL, and date of access.

For other types of referenced works, provide sufficient information to enable readers to access them.

Tables: Tables should be numbered with Arabic numerals and referred to by number in the Text (e.g., Table 1). Each table should be typed on a separate page with the legend above the table, while explanatory footnotes, which are indicated by superscript lowercase letters, should be typed below the table.

Illustrations: Figures, drawings, diagrams, charts and photographs are to be numbered in a consecutive series of Arabic numerals in the order in which they are cited in the text. Computer-generated illustrations and good-quality digital photographic prints are accepted. They should be black and white originals (not photocopies) provided on separate pages and identified with their corresponding numbers. Actual size graphics should be provided, which need no further manipulation, with lettering (Arial or Helvetica) not smaller than 8 points, lines no thinner than 0.5 point, and each of uniform density. All colors should be removed from graphics except for those graphics to be considered for publication in color. If graphics are to be submitted digitally, they should conform to the following minimum resolution requirements: 1200 dpi for black and white line art, 600 dpi for grayscale art, and 300 dpi for color art. All graphic files must be saved as TIFF images, and all illustrations must be submitted in the actual size at which they should appear in the journal. Note that good quality hardcopy original illustrations are required for both online and mail submissions of manuscripts.

Text Footnotes: The use of text footnotes is to be avoided. When their use is absolutely necessary, they should be typed at the bottom of the page to which they refer, and should be cited in the text by a superscript asterisk or multiples thereof. Place a line above the footnote, so that it is set off from the text.

Supplementary Material: Authors are encouraged to provide all supplementary materials that may facilitate the review process, including any detailed mathematical derivations that may not appear in whole in the manuscript.

Revised Manuscript and Computer Disks

Following the acceptance of a manuscript for publication and the incorporation of all required revisions, authors should submit an original and one more copy of the final disk containing the complete manuscript typed double spaced in Microsoft Word for Windows 2000 or a later version thereof. All graphic files must be saved as PDF, JPG, or TIFF images.

Allen, P.B., "……………", in: Horton, G.K., and Muradudin, A. A., (eds.), "Dynamical…….", (North……..), pp….

Reprints

Twenty (20) reprints free of charge are provided to the corresponding author. For orders of more reprints, a reprint order form and prices will be sent with the article proofs, which should be returned directly to the Editor for processing.

Copyright

Submission is an admission by the authors that the manuscript has neither been previously published nor is being considered for publication elsewhere. A statement transferring copyright from the authors to Yarmouk University is required before the manuscript can be accepted for publication. The necessary form for such transfer is supplied by the Editor-in-Chief. Reproduction of any part of the contents of a published work is forbidden without a written permission by the Editor-in-Chief.

Disclaimer

Opinions expressed in this Journal are those of the authors and neither necessarily reflects the opinions of the Editorial Board or the University, nor the policy of the Higher Scientific Research Committee or the Ministry of Higher Education and Scientific Research. The publisher shoulders no responsibility or liability whatsoever for the use or misuse of the information published by JJP.

Indexing

JJP is currently applying for indexing and abstracting to all related International Services.

Editorial Preface

This special issue of Jordan Journal of Physics (JJP) presents 11 selected papers presented at the international conference that was held under the patronage of Her Royal Highness Princess Sumaya Bint Al-Hassan between 3-5/4/2014 in Amman/ Jordan under the title: "Building International Networks for Enhancement of Research in Jordan". These papers were subjected to standard refereeing of JJP.

Building International Networks for Enhancement of Research in Jordan
Int. Conference / Humboldt Kolleg
April 3 - 5, 2014

Conference Preface

The conference "Building Int. Networks for Enhancement of Research in Jordan" was held in Amman between April 3rd - 5th, 2014 at Princess Sumaya University for Technology (PSUT) and the German Jordanian University (GJU). Generous support by the Alexander von Humboldt Foundation (AvH), Science Research Support Fund (SRSF), King Abdullah II Fund for Development, among others, played an important role in the success of the Conf.

The Conf. was one of the most successful activities the Jordanian Club of Humboldt Fellows (JCHF) ever organized since it was established in 1997. More than 300 people attended the Conf., including 100 Int. participants from 25 countries. Ph.D. students, as well as representatives of Associations; AvH, DAAD, AGYA (Arab German Young Association), Federal Foreign Office, German Embassy in Amman, German Archaeological Protestant Institute in the Holy Land, the AvH - MED (Mediterranean) Network participated in this distinguished event.

Eighty papers and 75 posters were presented. Parallel sessions were organized. Several workshops took place in the fields of: Culture, Physics, Chemistry, Biological and Pharmaceutical Sciences and Archaeology. Humboldtian Prof. Luay Rashan organized the Pharmaceutical Workshop. A price for the best poster was awarded by a Selection Committee chaired by Dr Nelli Wanderka from Berlin.

A 2-day pre-Conference training workshop, organized at the Univ. of Jordan (JU) in Amman, entitled: "Opportunities & Problems of Scientific Research in MENA Region", for Jordanian and MENA graduate students was run by three German top scientists and an active Humboldtian Prof. Bothina Hamad. Those young scientists presented their improved works at the Conf.

A workshop for Junior Scientists was also organized, where Dr. Thomas Hesse made a presentation about the AvH Foundation and its programs. DAAD Director in Amman gave a presentation about DAAD programs.

The AvH- MED (Mediterranean) Network Chairman Prof. Claudio Borri chaired a workshop which discussed major issues of common interest. Strengthening cooperation, joint research and exchange were discussed.

Archaeology German team (2 Professors and 9 Ph.D. students from several German universities) stayed 16 days in Jordan. The Chairman of the team, Prof. Dr. Hans-Peter Kuhnen from Mainz University, chaired a workshop with presentations from the visiting scientists and their Jordanian counterparts in cooperation with the German Archaeological Protestant Institute in Amman.

Participants were able to visit some Jordanian universities. Prof. Mohammad El Khateeb arranged the visit to JUST in Irbid. A meeting with staff members took place. Prof. Ziad Al-Saad and Prof. Hani Hiagneh arranged the visit to Yarmouk Univ. and its Archaeology Museum.

Humboldtians Prof. Bothina Hamad and Prof. Hani Khoury arranged the visit to JU. Humboldtian Prof. Dr. Sultan Abu Orabi, Secretary General of the Association of Arab Universities, participated in the activities aiming at reinforcing cooperation with German Universities.

Visits were facilitated to the Royal Geographic Center, Jerash, Um Qeis, Madaba, Baptism Site, Dead Sea, Petra, Wadi Rum, Aqaba, Iraq El Amir and Roman Theater in Amman.

A busy program with successful outcome with Ambassador/ Foreign Office in Germany Dr. Heinrich Kreft and Deputy Sec. General of the AvH Dr. Thomas Hesse gave distinguished talks.

HRH Princess Sumaya bint el Hassan opened the Conf. and gave an excellent talk praising scientific and cultural cooperation, von Humboldt Foundation, JCHF and its role. Ambassador of Germany to Jordan, HE Mr. Ralph Tarraf expressed appreciation of what JCHF is doing to strengthen the German-Jordanian relations. Chairman of the Conf. HE Prof. Dr. Khaled Toukan gave an excellent talk at the Conf. Evaluation of the Conf. took place, with participation of HE Ralph Tarraf, Dr. Kreft and Dr. Thomas Hesse. Director of DAAD Office in Jordan Mr. Andreas Wutz was very supportive.

Marwan S. Mousa

Director of the Conference/Kolleg
Humboldt Ambassador Scientist
President of the Jordanian Club of Humboldt Fellows
President of the Jordanian Physics Society
Prof. of Materials
Dept. of Physics
Mu'tah University
Al-Karak, Jordan
Tel.: 00962-79-5659761
Fax.: 00 962-3-2375540

Building International Networks for Enhancement of Research in Jordan Int. Conference / Humboldt Kolleg
April 3 - 5, 2014

Conference Organizing Committee:

• Prof. Dr. Khaled Toukan Chairman of JAEC (Chairman of the Conference)

• Prof. Dr. Natheer Abu-Obeid President of GJU (Co-Chairman of the Conference)

• Prof. Dr. Marwan S. Mousa (Physics Dept., Mu'tah Univ) (Director of the Conference)

• Dr. Nelli Wanderka (Helmholtz Zentrum Berlin for Materials and Energy, Berlin, Germany)

Conference Scientific Committee:

HE Prof. Dr. Khaled Toukan	chairman@jaec.gov.jo; Dr.khaled.toukan@jaec.gov.jo
Prof. Dr. Natheer Abu Obeid	natheer.abuobeid@gju.edu.jo
Prof. Dr. Marwan S. Mousa	marwansmousa@yahoo.com, mmousa@mutah.edu.jo
Dr. Ramia Al Bakain	ramia.bakain@yahoo.com, r.bakain@ju.edu.jo
Prof. Dr. Hani Khoury	khouryhn@ju.edu.jo
Prof. Dr. Nizar Abu Jaber	nizar.abujaber@gju.edu.jo
Prof. Dr. Majed Abu Zreig	majed.abuzreig@gju.edu.jo
Prof. Dr. Muwaffaq Alomoush	ma@aabu.edu.jo
Prof. Dr. Talal Abu Rjai	deanphar@ju.edu.jo aburjai@ju.edu.jo
Prof. Dr. Eid Al Tarazi	eid@hu.edu.jo, ealtarazi@yahoo.com
Prof. Dr. Ahmad Malabeh	am@hu.edu.jo; malabite.ahmad@yahoo.com
Prof. Dr. Mohammed Al-Khateeb	kateeb@just.edu.jo
Prof. Dr. Lauy Rashan	luayrashan@yahoo.com
Prof. Dr. Yousef Hiary	hiary@ju.edu.jo
Prof. Dr. Mohammed Al-Omari	alakmoh@just.edu.jo
Prof. Dr. Bothina Hammad	b.hamad@ju.edu.jo
Dr. Awni Khasawneh	kawni@yahoo.com
Dr. Khaldoun Tarawneh	khaldoun@psut.edu.jo
Dr. Galeb Saraireh	g_saraireh@aou.edu.jo
Dr. Khaled Al- Nawayseh	Khalid.na@arabpotash.com
Dr. Hmoud Dmour	hmoud79@mutah.edu.jo
Prof. Dr. Kamil Al-Shiekh	kamilaliamen@yahoo.com
Dr. Abdullah AL-Zaghameem	aoz_q2q@yahoo.com
Dr. Ahmad Telfah	telfah.ahmed@gmail.com
Prof. Dr. Abdelrahim Hunaiti	hunaiti2001@yahoo.com
Prof. Dr. Nihad Yusuf	nihadyusuf@yu.edu.jo
Prof. Dr. Ibrahim Abu Al-Jarayseh	ijaraysh@yu.edu.jo
Prof. Dr. Saed Dababneh	dababneh@bau.edu.jo
Prof. Dr. Eqab Rabei	eqabrabei@gmail.com
Prof. Dr. Mousa Abu Orabi	mousa@just.edu.jo
Prof. Dr. Mohammed Khasawneh	mkha@just.edu.jo
Prof. Dr. Ziad Al Saad	alsaad@gmail.com
Prof. Dr. Hani Hayajneh	hani@yu.edu.jo

Prof. Dr. Ahmad Mousa	mousa@rocketmail.com
Prof. Dr. Riad Kasasbeh	rjordanjo@yahoo.co.uk
Prof. Dr. Osama Mohawesh	osama.mohawesh@gmail.com
Prof. Dr. Ahmad Al Ajlouni	aajlouni@just.edu.jo
Prof. Dr. Yaseen Al Soud	alsoud@aabu.edu.jo
Dr. Samer Kahook	samer.kahook@jaec.gov.jo
Dr. Yazan Al Tell	yazztal@yahoo.com
Dr. Jamal Alali	drj_alali@yahoo.com, jamal.alali@aljanoub.com.jo
Dr. Fawaz Al- Shawawreh	fawaz_shawawreh@yahoo.com
Dr. Khaled H. A. Abu-Elteen	salma@hu.edu.jo
Dr. Sherin Saraireh	sh2002jo@yahoo.com
Prof. Malik Juweid	Mjuweid@yahoo.com
Prof. Omar Al omari	alomari.omar@yahoo.com
Prof. Dr. Tayel El Hassan	tayel.elhasan@gmail.com

Conference Int. Scientific Committee:

1. Dr. Nelli Wanderka (Helmholtz Zentrum Berlin for Materials and Energy, Berlin, Germany)
2. Dr. Andreas Fischer (Chemnitz Univ., Chemnitz, Germany)
3. Prof. Dr. Peter Langer (Rostock University, Rostock Germany)
4. Prof. Dr. Florin Ionescu (Konstanz Univ., Konstanz, Germany)
5. Prof. Dr. Guido Schmitz (Stuttgart Univ., Stuttgart, Germany)
6. Prof. Dr. Hans-Peter Kuhnen (Johannes-Gutenberg Univ., Mainz, Ger.)
7. Dr. Ahmad Telfah (Leinnitz-Institut fuer Analytische Wissenschaften, Dortmund, Germany)
8. Dr. Richard Forbes (Faculty of Eng and Sciences, Surrey Univ., UK)
9. Prof. Dr. Thomas Kelly (Cameca, Madison WI, USA)
10. Prof. Dr. Simon Ringer (Univ. of Sydney, Australia)
11. Prof. Dr. Gregory Thomson (Univ. of Alabama, USA)
12. Prof. Dr. Bernard Deconihout (Univ of Rouen, France)
13. Prof. Dr. Majda Sekkal-Rahal (Univ. Sidi Bel Abbas, Algeria)
14. Prof. Dr. Mohamed Ellouze (Sfax Univ., Tunisia)
15. Prof. Dr. Abdelhadi Soudi (Rabat Univ., Morocco)
16. Prof. Dr. Hadef Redjem (Univ. Oum El Bouaghi, Algeria)
17. Prof. Dr. Boguslaw Buszewski (Nicolaus Copernicus Univ., Torun, Pola)
18. Prof. Dr. Ashraf Abadi (Pharmacy Faculty Dean, German Univ. Cairo)
19. Prof. Dr. Fathy Abdelrazek (Chemistry Dept., Cairo Univ., Egypt)
20. Prof. Dr. Claudio Borri (Univ. di Firenze, Italy)
21. Prof. Dr. Mohammed Shabat (VP, Islamic Univ, Gaza)
22. Andreas Wutz, Director of DAAD Information Center in Amman, Jordan.

Jordan Journal of

P H Y S I C S

An International Peer-Reviewed Research Journal

Table of Contents:

Volume 8, No. 2

Jordan Journal of Physics

ARTICLE

Structural and Magnetic Properties of $Pr_{0.7}Bi_{0.3}Mn_{1-x}Fe_xO_3$ $(0 \leq x \leq 0.2)$ Manganites Oxides Prepared by Sol-gel Method

Kh. Sbissi[a], D. Fatnassi[a], M. Ellouze[b], E. K. Hlil[c] and F. Elhalouani[a]

[a] *University of Sfax, National Engineering School of Sfax, B. P. W-3038, Tunisia.*
[b] *University of Sfax, Faculty of Sciences of Sfax, B. P. 1171, 3000, Tunisia.*
[c] *Institut Néel, B. P. 166, B. P. W-38042 Grenoble Cedex 9, France.*

Abstract: The morphology, structural and magnetic properties of $Pr_{0.7}Bi_{0.3}Mn_{1-x}Fe_xO_3$ manganites oxides, prepared by sol-gel method, have been investigated to study the effect of the substitution of Mn by Fe. X-ray powder diffraction, Scanning Electron Microscopy (SEM), Fourier transforms infrared spectroscopy (FT-IR) and magnetic measurements for the systems have been investigated. Rietveld analysis of the X-ray powder diffraction show that the samples crystallize in the orthorhombic perovskite system with Pnma space group. The average particle size of about 60 nm was obtained from X-ray diffraction. We have found that with increasing x doping concentration of Fe, the unit cell volume decreases. Magnetic measurements *versus* temperature with an applied magnetic field of 0.05T show that all samples exhibit antiferromagnetic to paramagnetic transition with increasing temperature, at Neel temperature.
Keywords: Sol-gel; Manganites; Perovskite; Magnetic properties; Rietveld analysis.

Introduction

Perovskite oxide is generally described by stoichiometric formula ABO_3, where A and B represent a lanthanide (or alkaline earth ion) and a transition metal ion, respectively. The structural tolerance factor (t) for these oxides ranges from 0.75 to 1, which helps in multiple cation substitutions for cations with small difference in their ionic sizes [1, 2]. Perovskite manganites with the general formula $R_{1-x}A_xMnO_3$ (where R is a rare earth element and A is a divalent alkaline earth metal) have received much attention in the recent years due to the discovery of the colossal magnetoresistance (CMR) and its potential applications [3–8].

The functional properties of perovskite oxides are generally influenced by the synthesis methods, calcination conditions (temperature, time and atmosphere) and A and / or B site substitution [9–12]. The transport properties of perovskite can be altered by the partial substitution of A-site cation by other proper cations, e.g. lanthanum by strontium [13, 14] or cerium [15, 16]. However, the catalytic activity of perovskites is mainly controlled by the type of cation type occupying B site and the partial substitution of the site [1, 2, 17–19]. Substitutions in the A and/or B sites create defects and hence modify the catalytic and other functional properties [15, 20]. Many techniques have been employed to elaborate perovskites-based rare-earth manganites; *i.e.,* as conventional solid-state reaction [21], combustion thermal spray [22] and sol-gel [23]. The sol-gel method is an important ceramic oxide technique generally used to prepare nanopowders. It involves several advantages like short reaction time, low reaction temperature, besides producing homogeneous products with high purity.

Corresponding Author: M. Ellouze   **Email**: mohamed.ellouze@fss.rnu.tn

In the present paper, we report the structural, morphological and magnetic properties of $Pr_{0.7}Bi_{0.3}Mn_{1-x}Fe_xO_3$ with x = 0, 0.1 and 0.2 samples elaborated by sol-gel method.

Experimental

The $Pr_{0.7}Bi_{0.3}Mn_{1-x}Fe_xO_3$ samples were prepared by a modified sol –gel method [24-26] by mixing Pr_6O_{11}, MnO_2, Bi_2O_3 and Fe_2O_3 up to 99.9 % purity in stoichiometric proportions used in the desired proportion, according to the following reaction:

0.116 Pr_6O_{11} + 0.15 Bi_2O_2 + (1-x) MnO_2+ x/2 Fe_2O_3 → $Pr_{0.7}Bi_{0.3}Mn_{1-x}Fe_xO_3$.
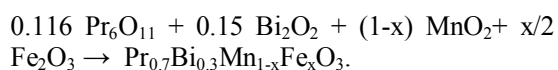
The starting materials Pr_6O_{11}, MnO_2, Bi_2O_3 and Fe_2O_3 were dissolved in dilute nitric acid at 90°C and then suitable amounts of citric acid and ethylene glycol as coordinate agents were added. The resulting gel was decomposed at 300°C and the acquired precursor powder was heated in air at 1000°C for 3 hours to improve the structure and homogeneity.

Phase purity, homogeneity and crystal properties were determined by powder X-ray diffraction at room temperature using a

SIEMENS D500 diffractometer with CuK_α radiation source in the range from 20° to 80° by the Rietveld analysis. The average particle size of the samples was estimated from X-ray peak width by using the Scherrer formula, and also from the SEM micrograph. Furthermore, the structural analysis of the compound has been carried out using Fourier transform infrared spectroscopy (FTIR) spectroscopic technique. The magnetization measurements were carried out using a vibrating sample magnetometer in the temperature range 2–150 K under an applied field up to 0.05 T.

Results and Discussion

Energy Dispersive Analysis of X-ray (EDAX)

In order to check the existence of all elements in our powders, an example of the energy dispersive analysis of X-ray analysis (EDAX) of $Pr_{0.7}Bi_{0.3}Mn_{1-x}Fe_xO_3$ (x = 0.1 and x = 0.2) was performed in Figs. 1(a) and (b). The EDAX spectra revealed the presence of oxygen (O), bismuth (Bi), praseodymium (Pr) and manganese (Mn) in appropriate concentrations, confirming that there is no loss of any integrated element during the sintering.
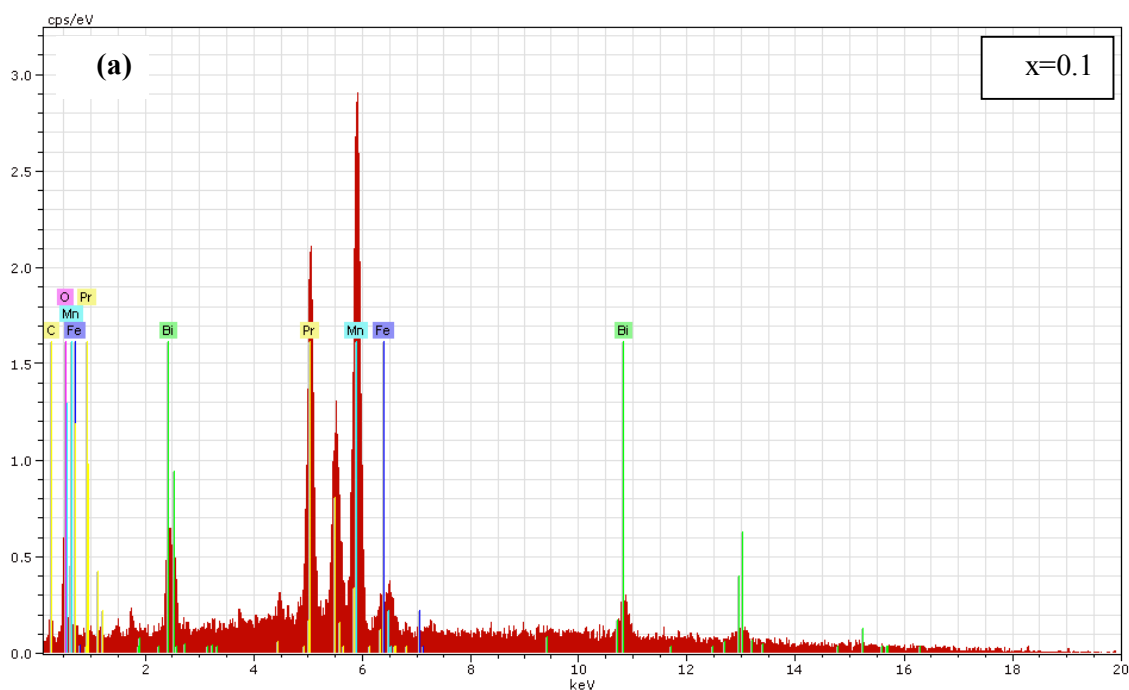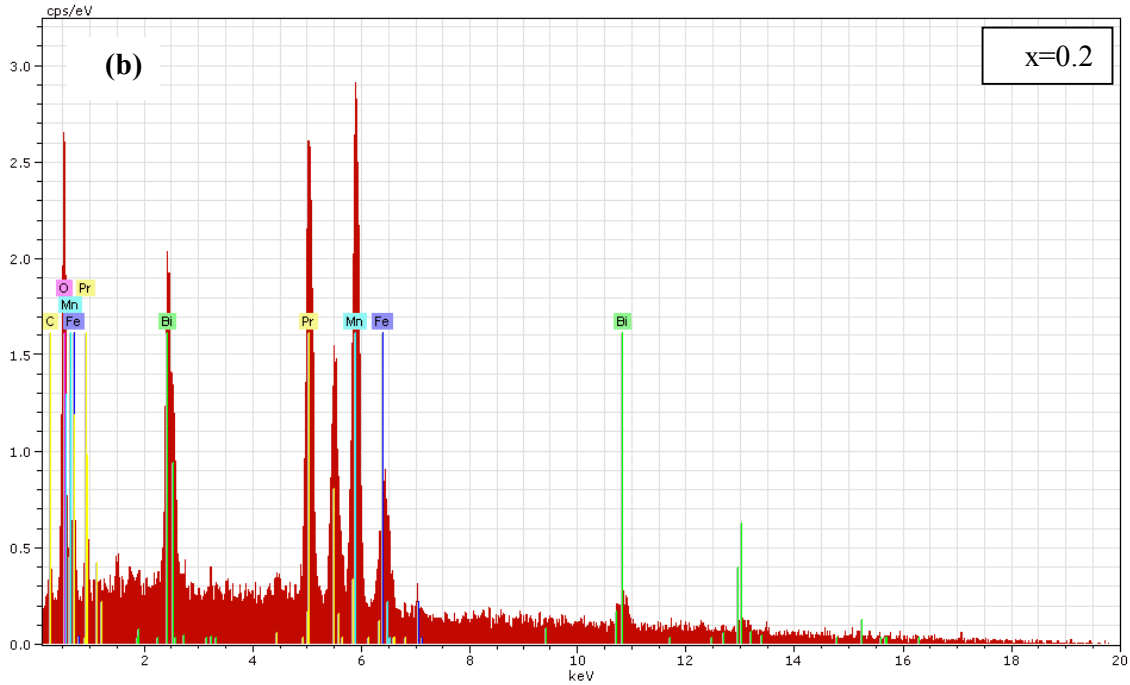
FIG. 1. EDAX analysis of $Pr_{0.7}Bi_{0.3}Fe_xMn_{1-x}O_3$ (a: x=0.1 and b: x= 0.2) compounds.

Scanning Electron Microscopy

Scanning Electron Microscopy was used to check the morphology and particle size as seen in Figs. 2(a) - (c). The nature, shape and distribution of grains suggest that all compounds have polycrystalline characteristics. Some agglomerations are shown on each pellet surface. The major morphology of these samples was huge gray grains with grain sizes in the range of a few micrometers. In addition, we can clearly observe that the grain size is different in all the samples.
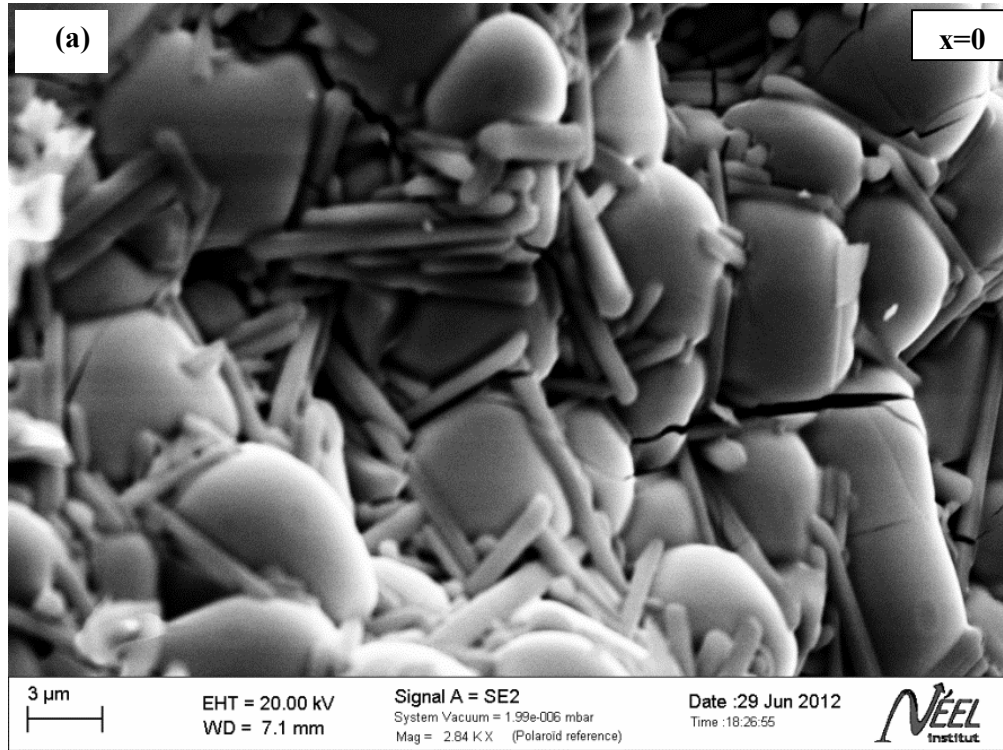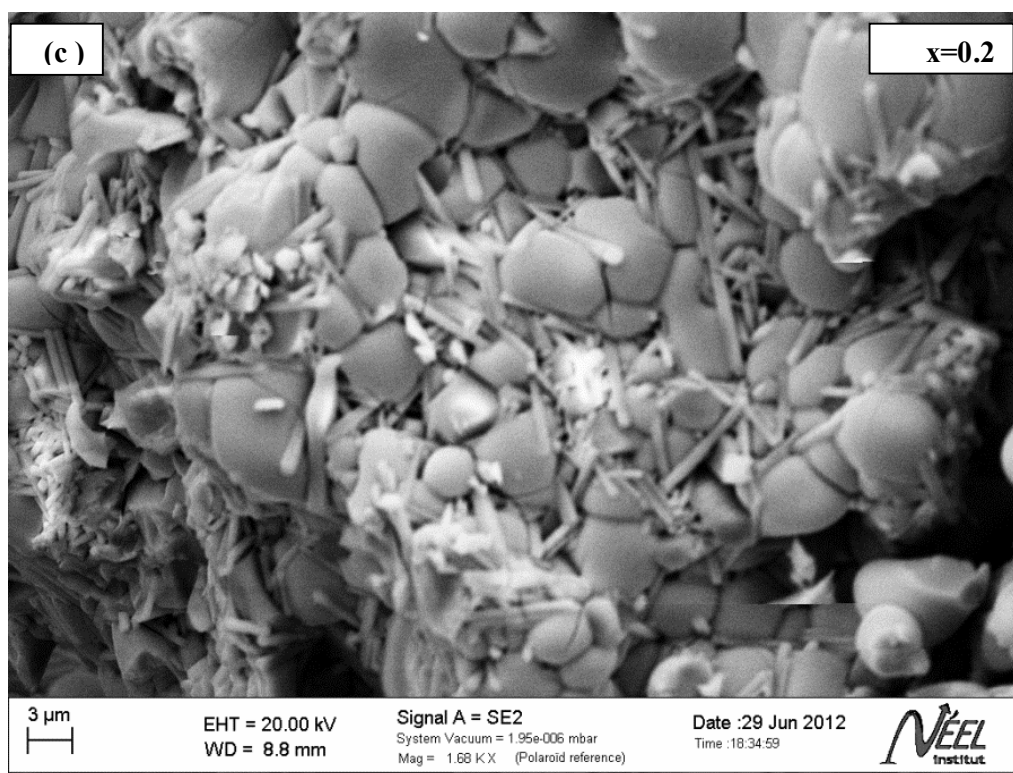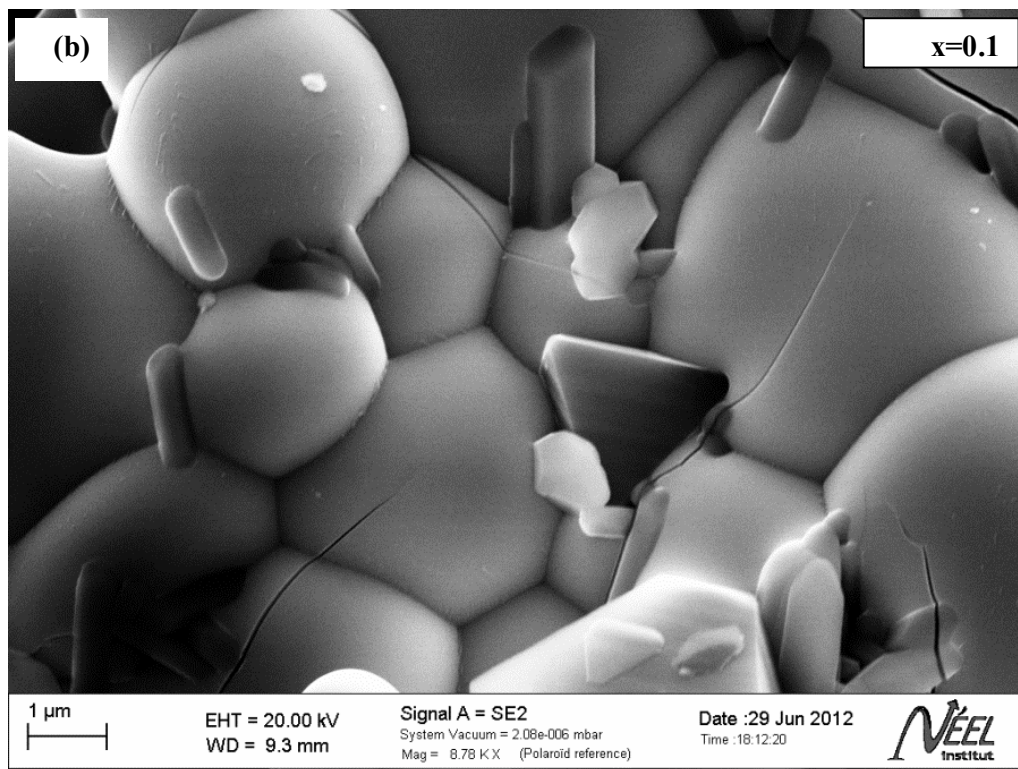
FIG. 2. SEM micrographs of $Pr_{0.7}Bi_{0.3}Fe_xMn_{1-x}O_3$ (a: x = 0, b: x=0.1 and c: 0.2) compounds.

Structural Properties

The powder X-ray diffraction (XRD) was used to verify the crystal structure of the samples. The XRD pattern and the Rietveld analysis using the FULLPROF program [27, 28] are shown in Figs. 3 (a) - (c). For all samples, the X-ray data are fitted to three different phases; the first one corresponding to $Pr_{0.7}Bi_{0.3}Mn_{1-x}Fe_xO_3$ fitted in the orthorhombic structure with the Pnma *s*pace group, the second phase corresponding to unreacted to Mn_3O_4, space group **I 41/amd** and the third one corresponding to $PrMn_2O_5$ in the orthorhombic structure with the **Pbam** *s*pace group. The red continuous line indicates the experimental data, and the calculated data is the continuous black line overlapping them. The lowest curve shows the difference between experimental and calculated patterns. The vertical bars indicate the expected reflection positions. The unit cell volume and the lattice parameters obtained by whole pattern refinements are given in Table 1. The quality of the refinement is evaluated through several parameters such as the pattern R factor (R_f) and the goodness-of- fit indicator (χ^2). We note that Pr/Bi atoms have been located at 4c (x, 0.25, z) position, Mn/Fe atoms at 4b (0, 0, 0.5) and oxygen atoms occupy two different sites; namely O_1 at 4c (x, 0.25, z) and O_2 at 8d (x, y, z) positions. The structural refinement data are reported in Table 2.
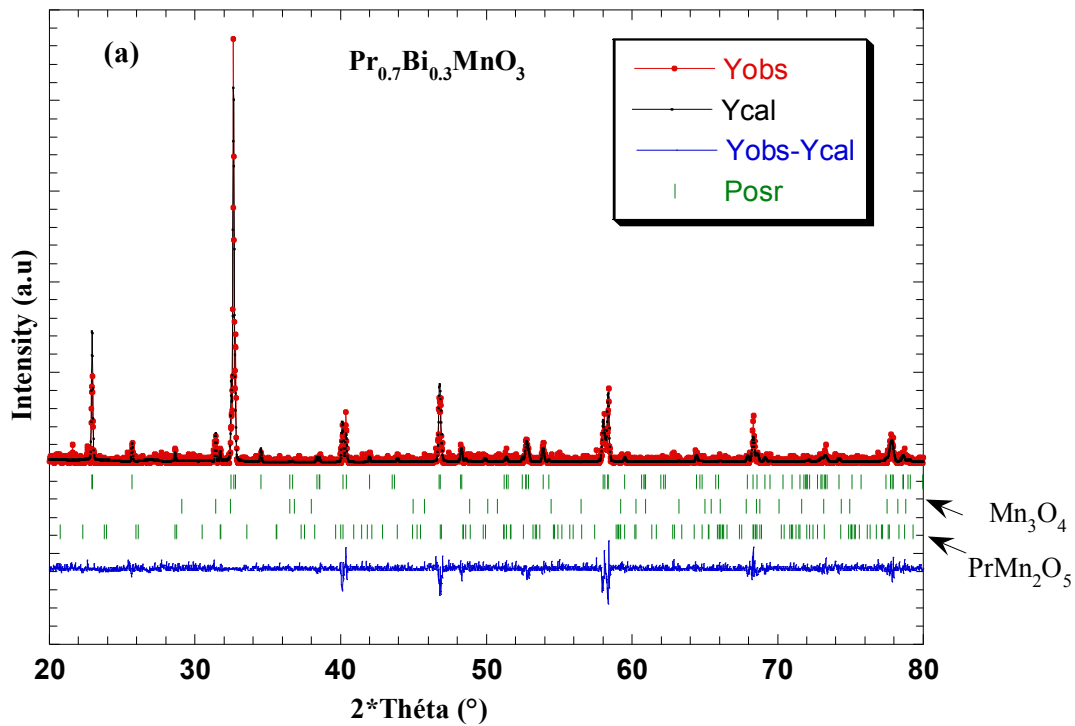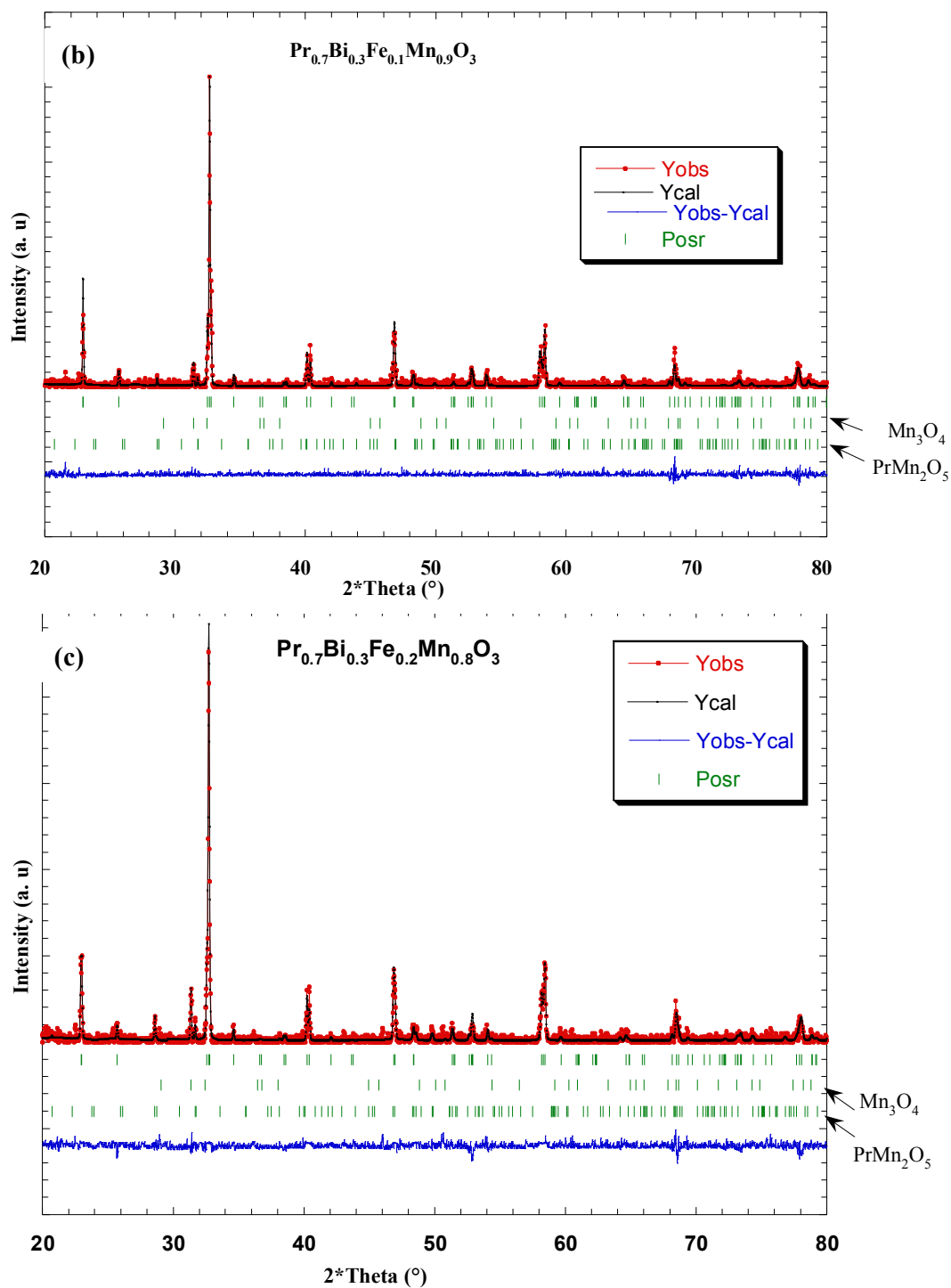
FIG. 3. Powder X-ray diffraction pattern and refinement of $Pr_{0.7}Bi_{0.3}Fe_xMn_{1-x}O_3$ (a: x = 0, b: x=0.1 and c: x= 0.2) compounds.

TABLE 1. Unit cell parameters and volume of $Pr_{0.7}Bi_{0.3}Fe_xMn_{1-x}O_3$ (x = 0, 0.1 and 0.2).

Samples	a (Å)	b (Å)	c (Å)	V (Å³)
x = 0	5.513₅	7.7581₆	5.4718₂	234.05
x =0.1	5.504₉	7.739₄	5. 4695₂	233.05
x = 0.2	5.492₁	7.733₁	5.4626₆	232.01

TABLE 2. Refined structural parameter $Pr_{0.7}Bi_{0.3}Fe_xMn_{1-x}O_3$ (x = 0, 0.1 and 0.2) samples. Numbers in subscript represent the error bars.

Samples	x = 0	x = 0.1	x = 0.2
Pr/Bi			
x	0.0326_6	0.0289_5	0.0201_6
y	0.25	0.25	0.25
z	0.0115_9	0.0115_9	0.0116
x	0.0326_6	0.0289_5	0.0201_6
Mn/Fe			
x	0	0	0
y	0	0	0
z	0.5	0.5	0.5
O1			
x	0.4927_4	0.4926_5	0.4927_5
y	0.25	0.25	0.25
z	0.2208_1	0.2206_1	0.2206_9
O2			
x	0.2842_8	0.2785_4	0.2936_1
y	0.0040	0.0070_8	0.0242
z	0.7527_8	0.6883_3	0.6995_2
χ^2	1.06	1.04	1.16
R_f	15.7	19.3	34.3

Our crystallographic parameters were found to be similar to those obtained by Rudskaya et al. [29] for $Pr_{0.7}Bi_{0.3}MnO_3$ sample elaborated by solid state reaction. They are also similar to those obtained by Chand et al. [30] for $Pr_{0.7}Sr_{0.3}MnO_3$ powder synthesized by Sol–gel method, and to those obtained by Cherif et al. [31] for $Pr_{0.67}Sr_{0.33}MnO_3$ manganite oxide prepared by ball milling method.

The Mn atom is coordinated by six oxygen atoms forming octahedral, almost regular. Fig. 4 shows the crystal structure of $Pr_{0.7}Bi_{0.3}MnO_3$ and the coordination polyhedron on Mn, and the distances between Mn and the first neighbor oxygen are so that there are three different Mn–O distances. The interatomic distances for the $Pr_{0.7}Bi_{0.3}Mn_{1-x}Fe_xO_3$ (with x = 0, 0.1 and 0.2) samples are listed in Table 3.
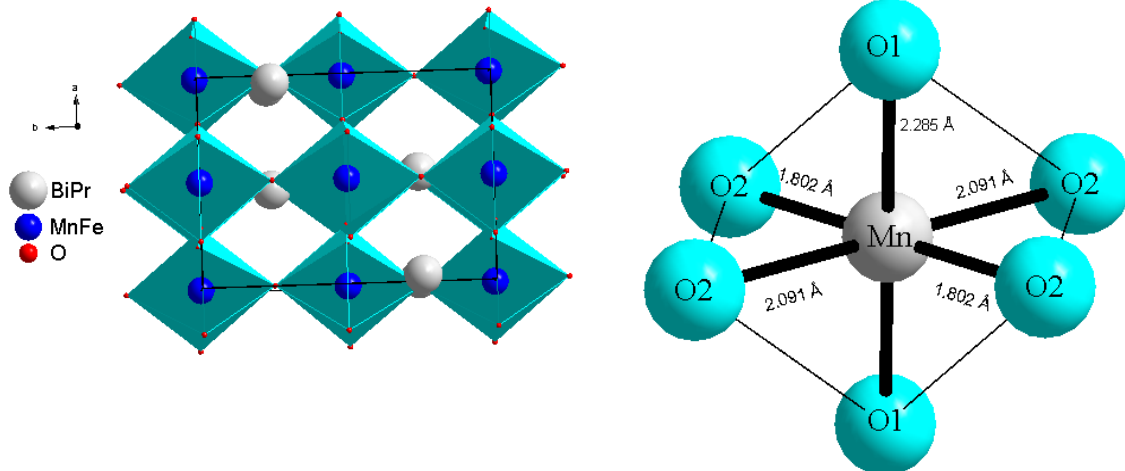
FIG. 4. Crystal structure of $Pr_{0.7}Bi_{0.3}MnO_3$ and the coordination polyhedron on Mn.

TABLE 3. The interatomic distances for the $Pr_{0.7}Bi_{0.3}Fe_xMn_{1-x}O_3$ (x = 0, x=0.1 and 0.2) samples.

Samples	x=0	x=0.1	x=0.2
Distances (Å)			
Mn–O(1)	2.09	2.28	2.27
Mn–O(2)	2.22	2.24	2.00
Mn–O(2)	2.45	2.09	1.95
Angles (°)			
Mn–O(2)–Mn	175.98	175.98	156.11
Mn–O(1)–Mn	112.63	112.63	116.08
O(1)–Mn–O(1)	180	180	180
O(1)–Mn–O(2)	135.20	145.01	144.66
O(2)–Mn–O(2)	180	180	180

The change of average ionic radius $<r_A>$ influences the unit cell volume. The influence can be explained by its ability to modify the Mn–O distances and Mn–O–Mn angles, and consequently the distortion of the ideal perovskite structure in which the Mn–O–Mn angle is equal to 180°. To confirm this, we calculated the Mn–O distances and Mn–O–Mn angles for $Pr_{0.7}Bi_{0.3}MnO_3$ nanopowders.

To corroborate experimental observation, the result has been compared to the Goldsmidt [32] tolerance factor (t):

$$t = \frac{r_A + r_O}{\sqrt{2}(r_B + r_O)}$$

with r_O = r (O^{2-}) = 1.32 Å,   r(Mn^{3+}) = 0.645Å, r(Mn^{4+}) = 0.53Å,   r(Bi^{3+}) = 1.52Å and r(Pr^{3+}) = 1.179Å.

The r_A, r_B and r_O are the ionic radii of A, B and O site atoms in ABO_3 structure, respectively [33, 34]. In the perovskite type compounds, the tolerance factor is between $0.78 < t < 1.05$ [35]. It should be noticed that the value equals unity for ideal structure. For our nanopowders, the tolerance factor (t) is about 0.80, pointing out that our nanopowders have an orthorhombic perovskite structure. This result is in agreement with the results found by Tomioka and Tokura [36]. The average particle diameter D for different specimens was obtained from the main peaks of the X-ray powder diffraction using Scherer's formula [37] for the peak width broadening as a function of the size of the particles.

$$D = \frac{K\lambda}{\beta \cos(\theta)} \qquad (1)$$

where λ ($Cu_{K\alpha}$ = 1.5418 Å), is the X-ray wavelength, k is the machine constant (0.916), θ and β are the diffraction angle and the full width for the most intense peak with.

$$\beta = \beta_m^2 - \beta_i^2 \qquad (2)$$

β_m is the experimental full width at half maximum (FWHM), β_i is the FWHM of a standard silicon sample and θ is the peak position. The obtained D values are about 60 nm regardless of the compounds. The D values are found to be 50, 55 and 62 nm for $x = 0$, x=0.1 and x = 0.2 samples, respectively.

FTIR Spectroscopy

Among numerous applications of vibrational spectroscopy to solid-state problems, those dealing with structural evolution of samples obtained by sol–gel process appear particularly interesting. IR spectroscopy gives qualitative information about the way in which the adsorbed molecules are bounded to the surface as well as structural information of solids. The spectra of $Pr_{0.7}Bi_{0.3}Mn_{1-x}Fe_xO_3$ nanopowders are given in Fig. 5. The observed band at 571 cm^{-1} corresponds to $\nu(MnO_2)$ stretching mode that involves the internal motion of change in the Mn–O–Mn bond length [38]. The peak observed at 970 cm^{-1} is attributed to the deformation and O–H stretching mode of absorbed water molecules [39].
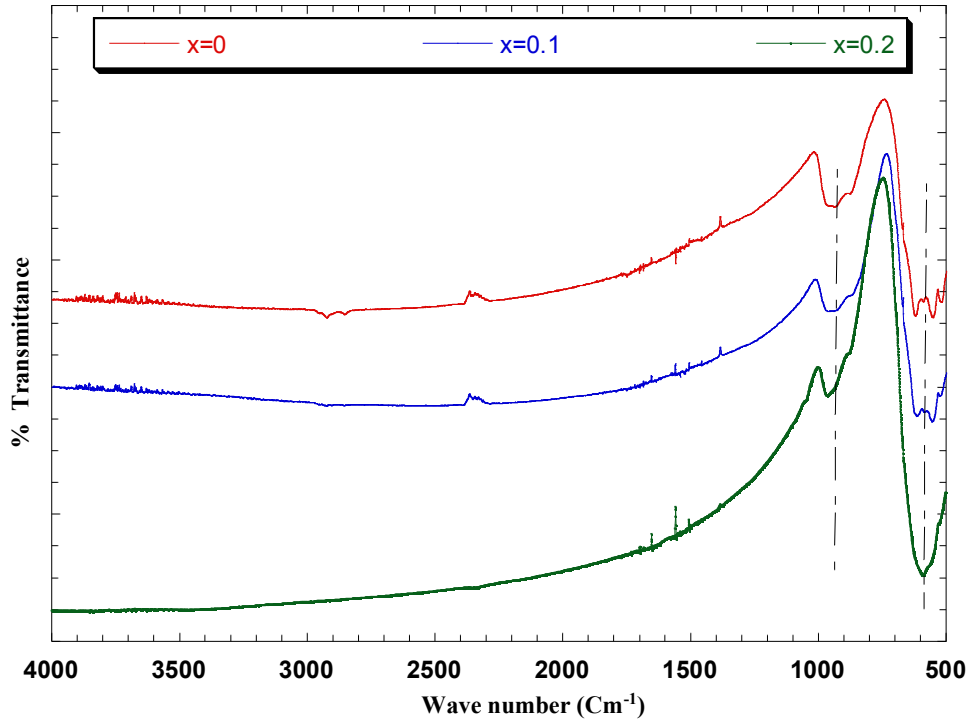
FIG. 5. Fourier transform infrared (FTIR) transmission spectrum of $Pr_{0.7}Bi_{0.3}Fe_xMn_{1-x}O_3$ (x = 0, 0.1 and 0.2) compounds at room temperature.

Magnetic Properties

The temperature dependence of the magnetization M (T) under an applied magnetic field of 0.05 T for the $Pr_{0.7}Bi_{0.3}Mn_{1-x}Fe_xO_3$ ($0 \leq x \leq 0.2$) samples is shown in Fig. 6. The magnetization decreases with increasing Fe content. All samples show an anti-ferromagnetic paramagnetic AFM–PM transition, at Neel temperature T_N. The T_N temperature values were determined from dM/dT curves. The Neel temperature is found to increase from 42 K for x = 0 to 45 K for x = 0.2 for the $Pr_{0.7}Bi_{0.3}Mn_{1-x}Fe_xO_3$ samples. The magnitude of the magnetization at low temperature decreases with increasing Fe content. The iron doping induces a weakening of the ferromagnetism at low temperatures. This weakening can be explained by the competition between the (Mn^{3+}–O–Mn^{4+}) double exchange and the (Fe^{3+}–O–Mn^{4+}) superexchange.

In order to investigate the magnetic behavior of the system at low temperature, we have carried out magnetization measurements *versus* the magnetic applied field up to 6 T at 5 K, Fig. 7. From this figure, we see that the magnetization decreases with increasing Fe content. In fact, the magnetization is not saturated, this is associated with the relaxations in the nanoparticles of the samples and also due to the presence of the AFM interactions caused by the important content of iron in the structure.

The values of the saturation magnetization were calculated using the total spins of Mn^{3+}, Mn^{4+}, Fe^{3+} and Pr^{3+} ions (μ_{Mn}^{3+} = 4 μ_B, μ_{Mn}^{4+} = 3 μ_B, μ_{Fe}^{3+} = 5 μ_B, and μ_{Pr}^{3+} = 2 μ_B). The saturation magnetization of the $Pr_{0.7}^{3+}Bi_{0.3}^{2+}((Mn_{1-x}-Fe_x)_{0.7})^{3+}Mn_{0.3}^{4+}O_2^{3-}$ compounds is expressed as:

$$M_{sat} = [4 \times 0.7 \times (1 - x)] - 5 \times (0.7 \times x) + 3 \times 0.3 + 2 \times 0.7]\mu_B = [5.1 - 6.3 \times x]\mu_B$$

where x is the iron content and μ_B is the Bohr magneton. The calculated values of saturation magnetization for full spin alignment of all the magnetic moments for (x= 0, 0.1 and 0.2) are found to be 5.1 μ_B, 4.47 μ_B and 3.84 μ_B, respectively. The measured values of saturation magnetization at T = 5 K for (x= 0, 0.1 and 0.2) are found to be 3.17 μ_B, 2.01 μ_B and 1.81 μ_B, respectively. The saturation magnetization decreases with increasing Fe content which confirms that the magnetic moments of the Fe are coupled antiparallel with the Mn one. The difference between measured and calculated values especially should be explained by spin canted state at low temperature as well as the presence of Mn_3O_4 as a secondary phase.
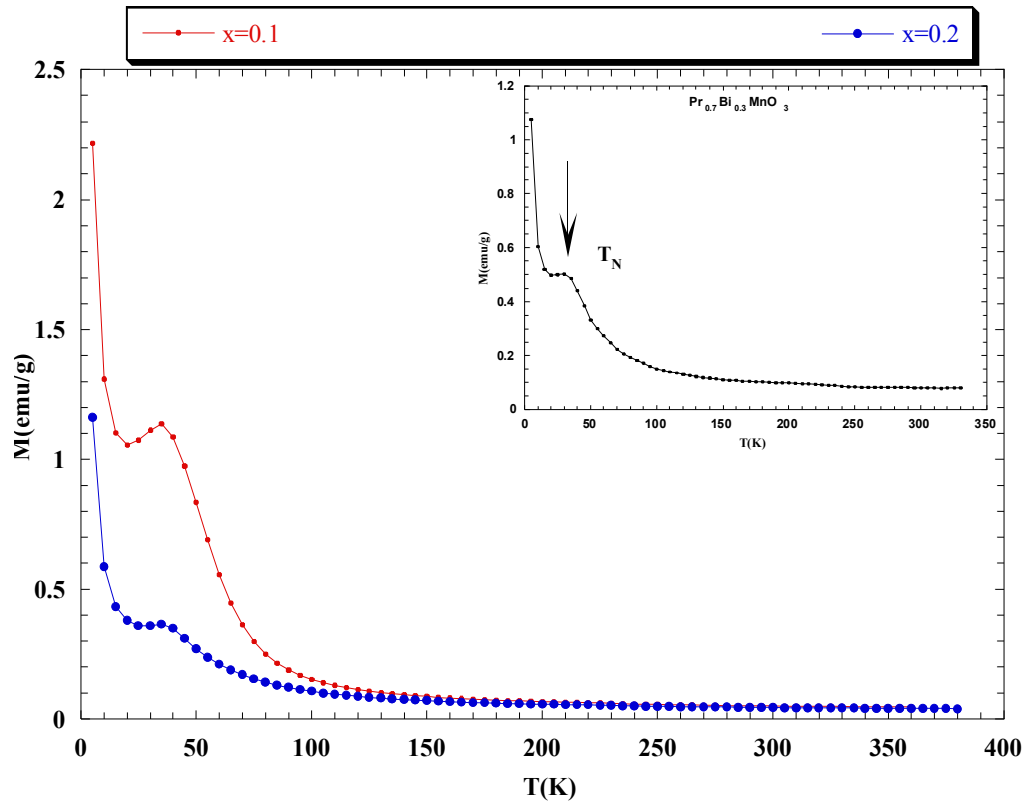
FIG. 6. Temperature dependence of the magnetization of $Pr_{0.7}Bi_{0.3}Fe_xMn_{1-x}O_3$ (x = 0, 0.1 and 0.2) at H = 0.05 T.
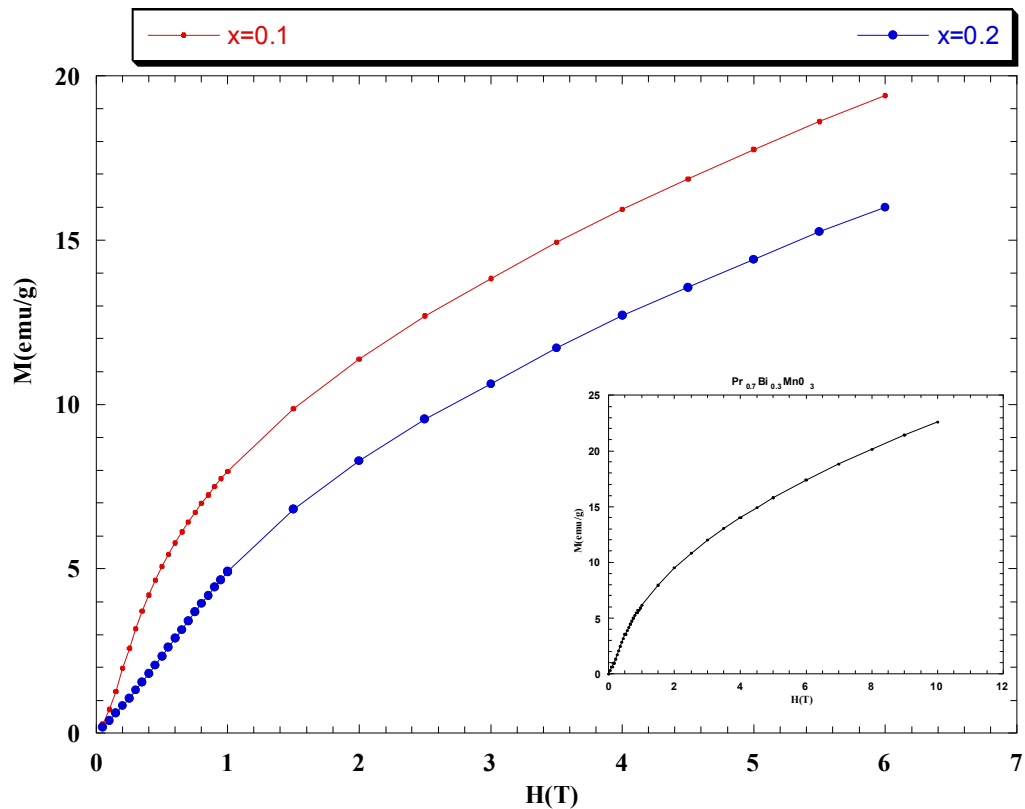
FIG. 7. Variation of magnetization as a function of applied magnetic field measured at 5 K for $Pr_{0.7}Bi_{0.3}Fe_xMn_{1-x}O_3$ (x = 0, 0.1 and 0.2).

Conclusion

$Pr_{0.7}Bi_{0.3}Mn_{1-x}Fe_xO_3$ powder samples have been synthesized using the sol-gel method for the composition range $0 \leq x \leq 0.2$. We have investigated their structural, morphological and magnetic properties. Our synthesized samples crystallize in the orthorombic structure with Pnma space group. Using Scherer's formula, all our samples have a grain size less than 65 nm. The FTIR spectra revealed the presence of the stretching and bending modes for all samples. Our synthesis samples exhibit an antiferromagnetic-paramagnetic transition when temperature increases. The magnetic transition temperature T_N increases slightly with the presence of iron in the structure, which confirms that the magnetic moments of iron are coupled antiparallel with the Mn one.

Acknowledgements

References

[1] Tanaka, H. and Misono, M., Curr. Opin. Solid State Mater. Sci., 5 (2001) 381.

[2] Yamazoe, N. and Teraoka, Y., Catal. Today, 8 (1990) 175.

[3] Rao, C.N.R. and Raveau, B., "World Scientific", (Singapore, 1998).

[4] Dhahri, A., Dhahri, J., Zemni, S., Oumezzine, M., Said, M. and Vincent, H., J. Alloys Compd., 450 (2008) 12.

[5] Dagotto, E., New J. Phys., 7 (2005) 67.

[6] Pattabiramana, M., Adepub, R., Singh, N.P., Venkatesh, R., Angappane, Ramaa, S.N. and Rangarajan, G., J. Alloys Compd., 452 (2008) 230.

[7] Hua, X.K., Xub, M.H., Wang, Z.S., Wua, Z.S.Y. and Si, Q.P.Z., Solid State Commun., 149 (2009) 243.

[8] Dhahri, N., Dhahri, A., Cherif, K., Dhahri, J., Belmabrouk, H. and Dhahri, E., J. Alloys Compd., 507 (2010) 405.

[9] Campagnoli, E., Tavares, A.L., Fabbrini, Rossetti, I., Dubitsky, Y.A., Zaopo, A. and Forni, L., Appl. Catal. B. Env., 55 (2005) 133.

[10] Liu, S., Tan, X., Li, K. and Hughes, R., Ceram. Int., 28 (2002) 327.

[11] Leontiou, A., Ladavos, A.K. and Pomonis, P.J., Appl. Catal. A: Gen., 241 (2003) 133.

[12] Kleveland, K., Einarsrud. M.A. and Grande, T., J. Eur. Ceram. Soc., 20 (2000) 185.

[13] Klvana, D., Vaillancourt, J., Kirchnerova. J. and Chaouki, J., Appl. Catal. A. Gen., 109 (1994) 181.

[14] Gunasekaran, N., Saddawi, S. and Carberry, J.J., J. Catal., 159 (1996) 107.

[15] Alifanti, M., Auer, R., Kirchnerova, J., Thyrion, F., Grange, P. and Delmona, B., Appl. Catal. B: Env., 41 (2003) 71.

[16] Nitadori, T. and Misono, M., J. Catal., 93 (1985) 459.

[17] Azada, K., Eriksson, S.G., Ivanov, S.A., Mathieu, R., Svedlindh, P., Eriksen, J. and Rundlof, H., J. Alloys. Compd., 364 (2004) 77.

[18] Buciuman, F.C., Patcas, F., Menezo, J.C., Barbier, J., Hahn, T. and Lintz, H.G., Appl. Catal. B: Env., 35 (2002) 175.

[19] Spinicci, R., Tofanari, A., Faticanti, M., Pettiti, I. and Porta, P., J. Mol. Catal. A: Chem., 176 (2001) 247.

[20] Saracco, G., Geobaldo, F. and Baldi, G., Appl. Catal. B: Env., 20 (1999) 277.

[21] Cherif, K., Zemnia, S., Dhahri, Ja., Dhahri, Je., Oumezzine, M. and Ghedira, H., J. Alloys Compd., 396 (2005) 29.

[22] Yu, M.H., Devi, S.P., Lewis, L.H., Sampath, S., Parise, J.B. and Gambino, R.J., Mater. Sci. Eng. B., 97 (2003) 245.

[23] Lin, G.C., Yu, X.L., Wei, Q. and Zhang, J.X., Mater. Lett., 59 (2005) 2149.

[24] Zayat, H.C. and Levy, M., D. J. Sol-Gel Sci. Technol., 35 (2005) 175.

[25] Gash, A.E., Tillotson, T.M., Satcher, J.H., Poco, J.F., Urubesh, L.W. and Simpson, R.L., Chem. Mater., 33 (2001) 999.

[26] Pechini, M.P., U.S. Patent, 3 (1967) 330.

[27]   Rodriguez-Carvajal, J., Physica B. Condensed Matter, 192 (1993) 55.

[28] Rietveld, H.M., J. Appl. Cryst., 2 (1969) 65.

[29]   Rudskaya, A.G., Pustovaya, L.E., Kofanova, N.B. and Kupriyanov, M.F., Journal of Structural Chemistry, 47(2006) 711.

[30] Chand, U., Yadav, K., Gaur, A. and Varma, G.D., J. of Rare Earths, 28 (2010) 760.

[31] Chérif, W., Ellouze, M., Lehlooh, A.-F., Elhalouani, F. and Mahmood, S.H., J. Magn. Magn. Mater., 324 (2012) 2030.

[32] Goldschmidt, V., "Geochemistry", (Oxford University Press, 1958).

[33] Shannon, R.D., Gen. Crystallogr., 32 (1976) 751.

[34] Shannon, R.D. and Prewitt, Ch.T., Sect. B. Cryst. Chem., 25 (1969) 925.

[35] Randall, C.A., Bhalla, A.S., Shrout, T.R. and Cross, L.E., J. Mater. Res., 5 (1990) 829.

[36] Tokura, Y. and Tomioka, Y., J. Magn. Magn. Mater., 200 (1964) 1.

[37] Guinier, A., X. Dunod (Ed.). (1964) 482.

[38] Roy, S. and Bandyopadhyay, S., J. Mater. Sci. Lett., 15 (1996) 1872.

[39] Quijada, M., Cerne, J., Simpson, J.R., Drew, H.D., Ahn, K.H., Millis, A.J., Shreekala, R., Ramesh, R., Rajeswari, M. and Venkatesan, T., Phys. Rev. B, 58 (1998) 16093.

Jordan Journal of Physics

ARTICLE

Electron Microscopy-Based Performance Evaluation of Various Tungsten Field-Emitter Tips Apex Radii

M. A. Madanat[a], M. S. Mousa[a], A. N. Al-Rabadi[b] and A. Fischer[c]

[a] *Department of Physics, Mu'tah University, Al-Karak 61710, Jordan.*

[b] *Computer Engineering Department, The University of Jordan, Amman, Jordan.*

[c] *Institut für Physik, Technische Universität Chemnitz, Chemnitz, Germany.*

Abstract: Field electron emission measurements have been performed on emitters consisting of electrochemically etched tungsten (W) wires, where the microemitters apex radii have been varied ranging from 90 to 300 nm. A conventional field electron microscope (FEM) with 10 mm tip (cathode) – screen (anode) distance was used to electrically characterize the electron emitters under ultra high vacuum (UHV) conditions. By these means, the field electron emission characteristics; namely the recorded current with respect to the corresponding applied voltage (the current-voltage (I-V) characteristics) and the spatial current distribution have been recorded. Both, a scanning electron microscope (SEM) and a transmission electron microscope (TEM) were used to investigate the tips' profiles at high magnifications. Within this work, we compared and analyzed the data extracted from tungsten tips having different radii; and thus determined the deviations between the results of the two applied extraction methods. Mainly, we derived the apex radii of different tungsten tips by both electron microscopy methods and analyzed the I-V characteristics which are presented as the Fowler-Nordheim (FN) plots. The obtained results show a good agreement between the two methods (SEM and the FEM) that are used to extract the tip apex radii.

Keywords: Field electron emission; Field Electron Microscope (FEM); Fowler-Nordheim (FN) plots; Scanning Electron Microscope (SEM); Transmission Electron Microscope (TEM); Tungsten tips.

Introduction

Tungsten [1, 2] is still one of the materials which are most frequently used for field electron emitter tips manufacturing [3-5]. As a cathode material, it brings several benefits due to its favorable properties, such as: high melting point of 3422 ˚C (highest of all metals and second only to carbon among the elements), high level of hardness (strength), low vapor pressure, simplicity of emitter preparation by electrochemical etching and durability as an emitter [1].

Within this work, various tungsten microemitters with different apex radii ranging from 90 – 300 nm were prepared. By using electron microscopes ((SEM) and (TEM)) to extract the tip profile (i.e., apex radii) and by comparing the resulting radii with the radii extracted from the FN plots, one can calculate the deviation between both extraction methods.

The current-voltage (I-V) measurements were carried out (using FEM) under high vacuum conditions with a base pressure of about 10^{-9} mbar.

The remainder of this paper describes the emitter's preparation and the performed experimental work, followed by presenting the results obtained within this work and discussing

---

Corresponding Author: M. S. Mousa   **Email**: marwansmousa@yahoo.com

them, while conclusions and future work are presented in the last section.

Experimental Setup

The cathodes incorporated here were electrolytically etched from 0.1 mm high purity (99.95%) tungsten wire (produced by Goodfellow Metals Company) using a two-molar solution of sodium hydroxide. The etching process is controlled by choosing a suitable initial etching current of ~ 15 mA, where a voltage of 10-12V produced the required current for our experiments. After the etching process was accomplished, the etched sample was cleaned from any remains of the NaOH solution on the surface of the tip by being immersed in distilled water and subjected to an ultrasonic bath for some minutes. The prepared tip is then mounted in an ultra high vacuum (UHV) system, which is baked for 12 hours at a temperature of 180°C. The corresponding analyses were carried out using a standard, home-built field electron microscope (FEM) [6].

Before and after each of the previous steps, the sample was mounted on an optical microscope to obtain a first glance of the sample profile within small magnification (~1000X). Finally, the samples were mounted in TEM and SEM to obtain images at high resolution and magnification (up to ~30000X - 40000X).

Results and Discussion

The tungsten microemitters that were prepared have various apex radii ranging from 90 to 300 nm. The presented results include SEM [7-9] and TEM [10, 11] images of the emitters' apex as well as the I-V characteristics and FN-type plots of the field emission characteristics. The area efficiency α has been calculated as the ratio between the actual emission area required to generate the electron emission current (I) according to the FN theory and the area of the hemispheric emitter model given by $A = 2\pi r^2$.

The TEM and SEM images in Figs. (1-3) show smooth needle-like emitters, which possess approximately hemispherical tips. Fig. 1 presents a TEM image and an SEM image for sample W1 from which an apex radius of $r_{SEM,W1} = 145$ nm has been extracted. A small irregularity of the tip's apex was found. The I-V characteristics and the FN plots obtained for sample W1 during the

voltage decrease show a common emission current behavior and a linear FN plot of the clean tungsten microemitters [11].

The TEM and SEM micrographs are presented in Fig. 2 (a-b) for sample W2 from which an apex radius of $r_{SEM,W2} = 93$ nm has been extracted. A regular tip shape was found. The surface of the sample was contaminated most likely by the NaOH remaining on the surface as a result of insufficient sample cleaning. At the same time, it is shown that the apex of the tip was actually clean. The I-V characteristics and the FN plots obtained for the sample W2 during the corresponding current-voltage cycle show a common emission current behavior and a linear FN plot as this is a characteristic for clean tungsten microemitters.

The emission characteristics obtained from a non-sharp tip with extracted apex radius of $r_{SEM,W3} = 215$ nm (cf. Fig. 3), with a uniform apex shape, show an interesting behavior. As the applied voltage is slowly increased through the virgin emitter, the emission current increases respectively while the voltage increases, at the low voltage region. At a higher voltage region, the emission current starts to behave in an unstable behavior (cf. Fig. 3 (c)). This clearly indicates that the emission at high voltage starts to emit from different spots (sub-emission centers) on the tip apex.

Fig. 4 (a-b) presents TEM and SEM micrographs of an exploded tip with an extracted apex radius of $r_{SEM,W3} = 100$ nm. The corresponding I-V characteristics were recorded before and after the apex explosion. As presented in Fig. 4 (c), before the apex explosion, the I-V characteristics behave as a sharp clean microemitter, where the emission current started at a voltage of ~ 500 V and increased respectively while the voltage increased. This shows a stable emission current, where the FN plot for the same sample (cf. Fig. 4 (d)) shows a general behavior as a linear plot.

After the apex explosion, the I-V characteristics and the corresponding FN plot (cf. Fig. 5) show a high similarity in the behavior similar to that before the apex explosion, only with a small difference that occurs in the emission-current starting voltage, where - after the apex explosion - the emission started from ~ 1100 V. This change occurs because of the fact that the emitting area became larger.
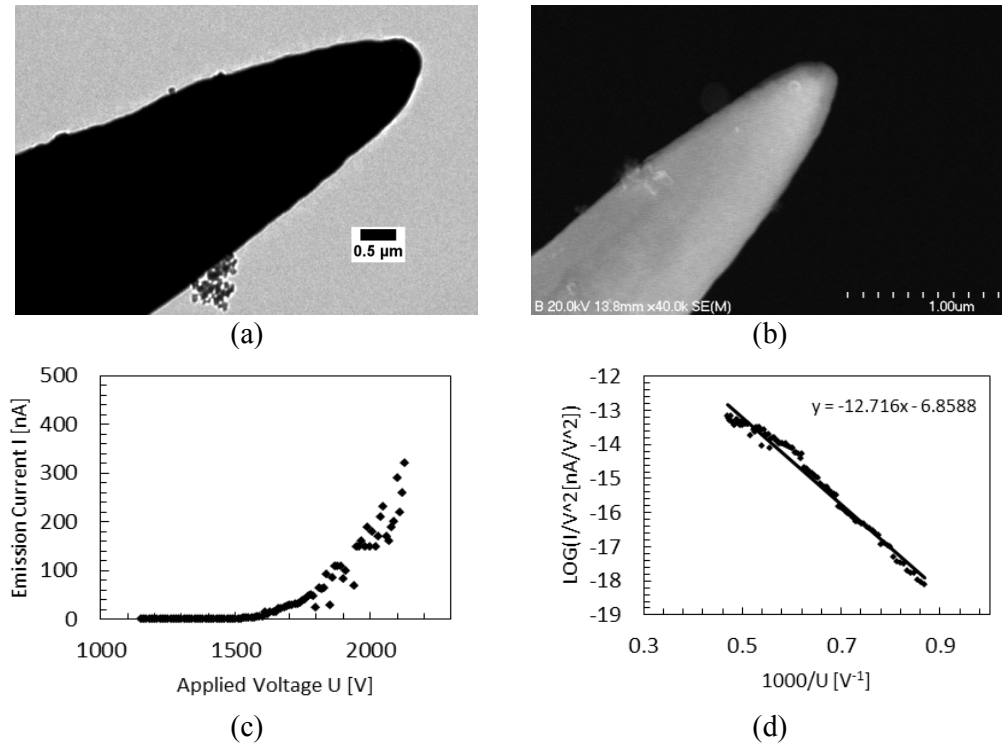
FIG. 1. Sample W1: (a) TEM micrograph and (b) SEM micrograph of a micropoint cathode at 30000X and 40000X magnifications, respectively, showing the tip apex shape and size, (c) plot that presents the corresponding I-V characteristics and (d) plot that presents the corresponding FN plot. Note that the FN plot is in a very good approximation that resembles a straight line which enables the calculation of the slope as $S_{W1} = 12715$.
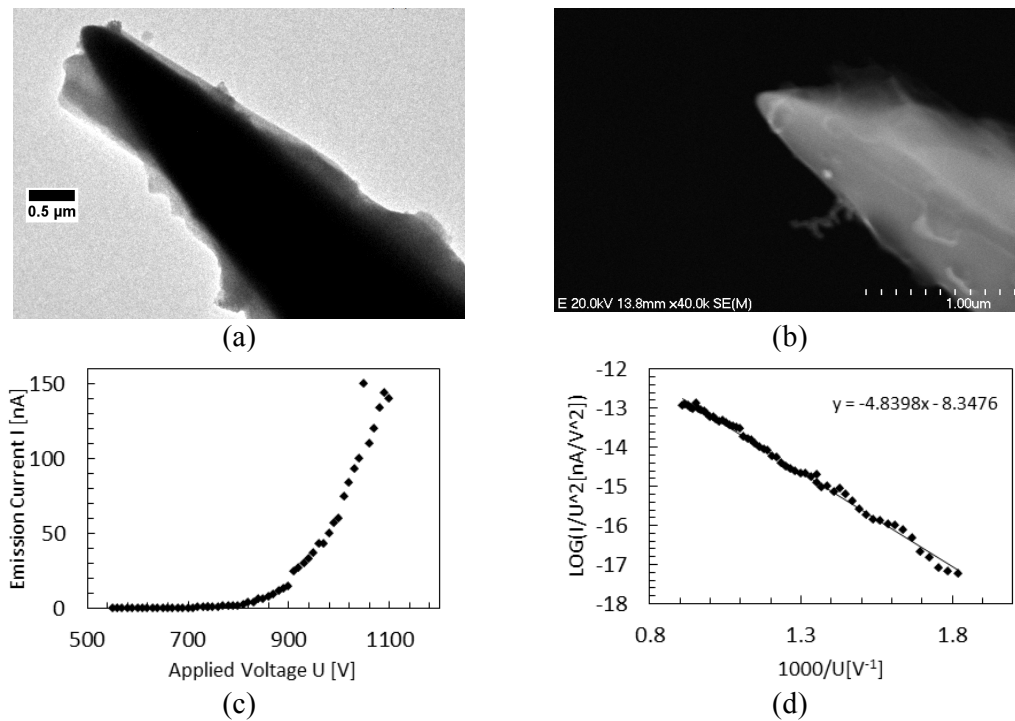
FIG. 2. Sample W2: (a) TEM micrograph and (b) SEM micrograph of a micropoint cathode at 30000X and 40000X magnifications, respectively, showing the tip apex shape and size, (c) plot that presents the corresponding I-V characteristics and (d) plot that presents the corresponding FN plot. Note that the FN plot is in a very good approximation which resembles a straight line that enables the calculation of the slope as $S_{W2} = 4839$.

(a)   (b)

(c)   (d)
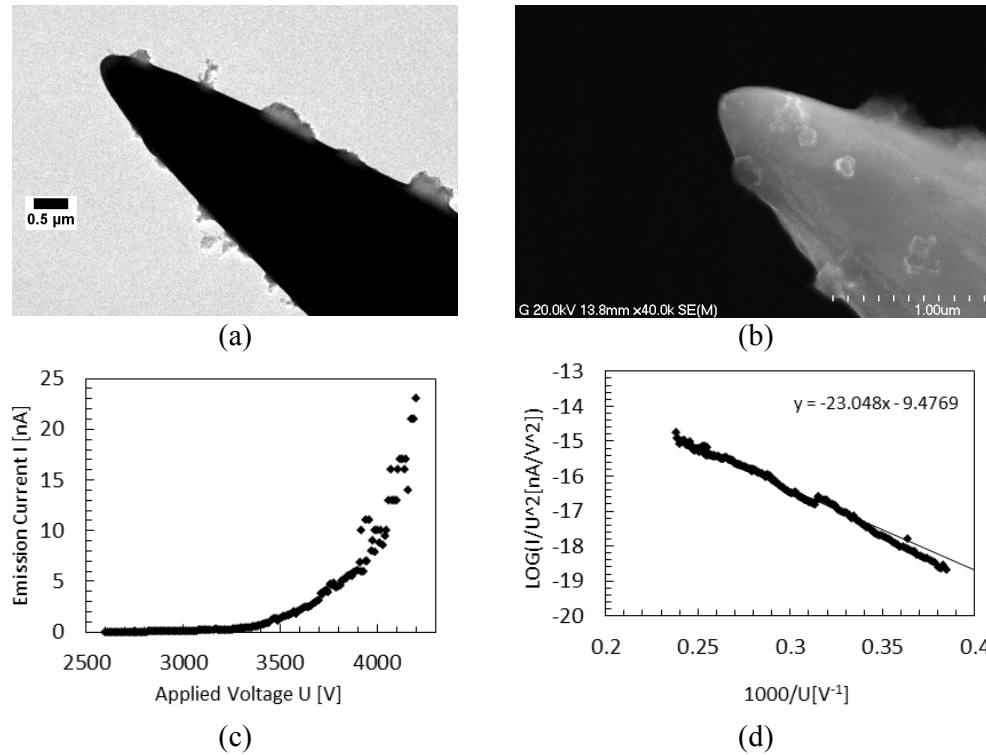
FIG. 3. Non-sharp tip sample W3: (a) TEM micrograph and (b) SEM micrograph of a micropoint cathode at 30000X and 40000X magnifications, respectively, showing the tip apex shape and size, (c) plot that presents the corresponding I-V characteristics and (d) plot that presents the corresponding FN plot. Note that the FN plot is in a very good approximation that resembles a straight line which enables the calculation of the slope as S_{W3} = 23048.

(a)   (b)

(c)   (d)
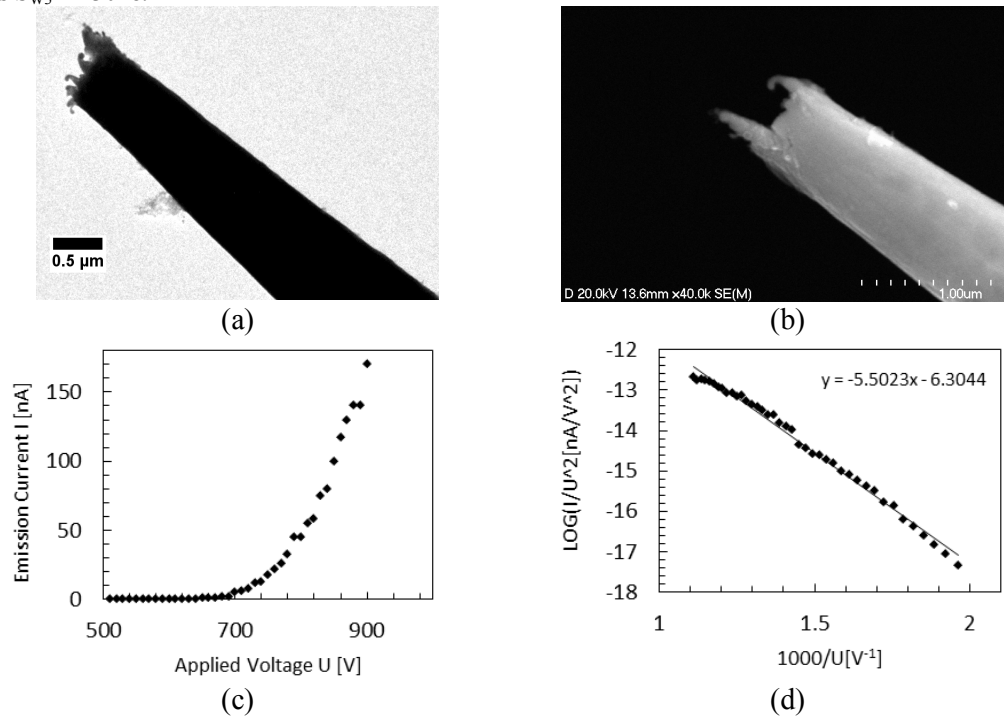
FIG. 4. Exploded tip W4: (a) TEM micrograph and (b) SEM micrograph of a micropoint cathode at 30000X and 40000X magnifications, respectively, showing the tip apex shape and size, (c) plot that presents the corresponding I-V characteristics and (d) plot that presents the corresponding FN plot. Note that the FN plot is in a very good approximation that resembles a straight line which enables the calculation of the slope as S_{W4} = 5502.

(a)

(b)
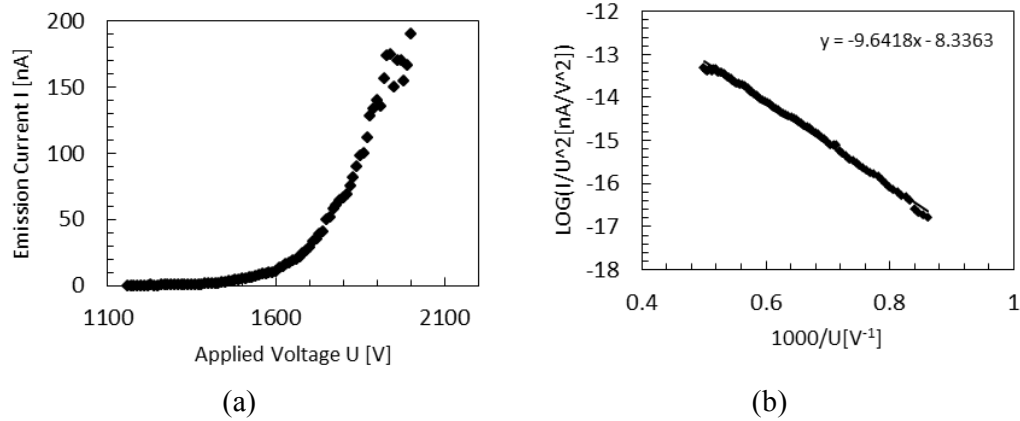
FIG. 5. Sample W4 after the tip apex explosion: (a) plot for the corresponding I-V characteristics and (b) plot presenting the corresponding FN plot. The slope is calculated as S_{W4} = 9641.

Fig. 6 shows the corresponding tested samples, at one magnification (1000X), using the utilized optical microscope.

The apex radius r_{SEM} for each tip has been derived from the corresponding SEM image by graphically fitting a circle to the tip apex. The blurriness of the edges was taken into account due to the irregularity in the apex shape as well as the contamination on the tip surface. The extracted apex radii r_{FEM} were derived from the FN plots and the relative emission area α has been calculated [12] from the extracted data.

Table 1 shows the various obtained values of the apex radii utilizing both methods (SEM and FEM) and the corresponding relative emission area. The presented results do support the relation [13]: r_{FEM} = 1.35 x r_{SEM} − 20 nm, where Fig. 7 shows also the good agreement between the two extracted SEM and FEM tips apex radii.

It is worth noting that the investigated field emission is used to characterize various emitting materials in the continuous efforts to develop new types of electron sources and to understand the physics behind their behavior [14-18].

(a)

(b)

(c)

(d)
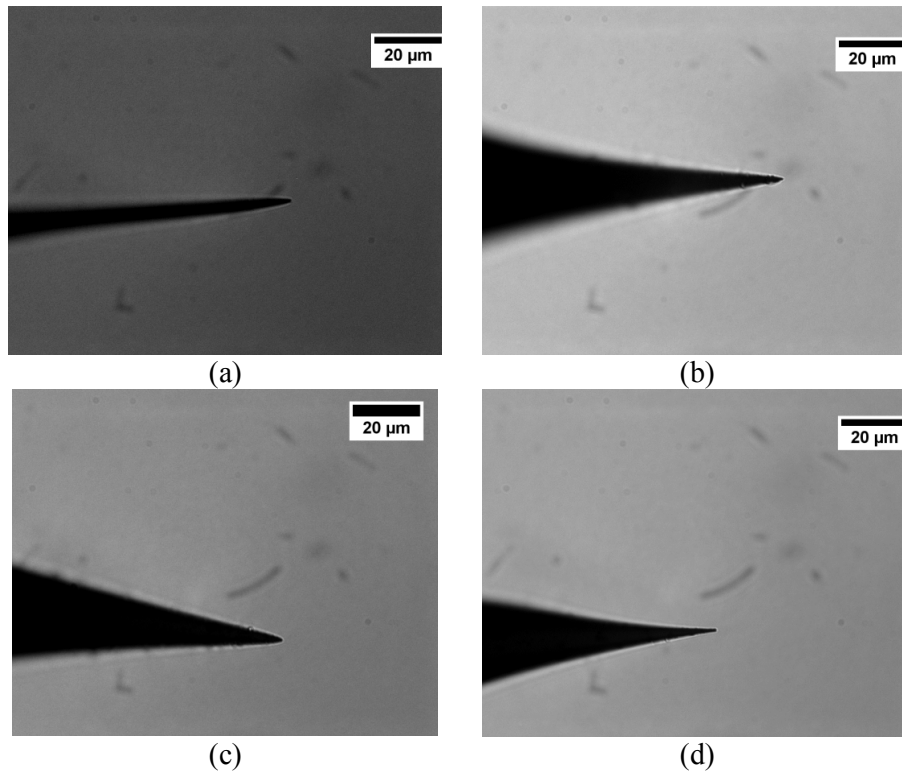
FIG. 6. Optical images at 1000X magnification: (a) W1, (b) W2, (c) W3 and (d) W4.

TABLE 1. Data of tungsten micropoints cathodes. The microemitters with various apex radii ranging from 90 to 300 nm were tested using SEM and FEM. The values of the apex radii were derived by the two methods (SEM and FEM) and showed close values with small deviation. The corresponding relative emission area (α) was also calculated.

Sample no.	Radius (SEM) r_{SEM} [nm]	Radius (extracted) r_{FEM} [nm]	Relative emission area (extracted) α
W1	145	187	6.94×10^{-4}
W2	93	108	1.16×10^{-4}
W3	215	278	2.05×10^{-3}
W4	100	115	1.69×10^{-4}
W5	191	241	1.30×10^{-3}
W6	220	288	2.21×10^{-3}
W7	139	183	5.59×10^{-4}

$r_{FEM} = 1.3899 \, r_{SEM} - 19 \text{ nm}$
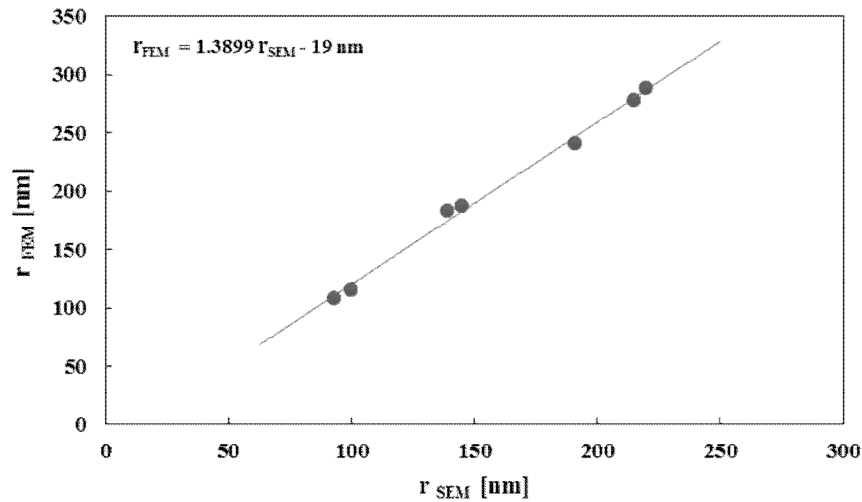
FIG. 7. Comparing the values of r_{FEM} and r_{SEM} produced good agreement between the two extracted tips apex radii.

Conclusions and Future Work

This work introduces the calculations of the tips apex radii using two different experimental methods. The first method is carried out using graphically best-fitting circles on the SEM images (r_{SEM}), while the second one is performed by extracting the radii from the emission characteristics recorded in the FEM (r_{FEM}).

From the obtained results, one notes a good agreement for the values of the apex radii that are extracted by the two methods. Also, by comparing the extracted data with the previously recorded results, a high level of agreement with the introduced results is found. This indicates, as

one important factor, that there was no relevant contamination by NaOH from the etching process on the tips' surface. The correlation within the data obtained through this work supports the corresponding relation between (r_{FEM}) and (r_{SEM}) as $r_{FEM} = 1.35 \times r_{SEM} - 20$ nm.

Future work will include coating the samples with dielectric layers of epoxy resin and re-doing the performed investigations in new experimental setups to study the effects of coating on the resulted emission current behaviors.

References

[1] Young, R.D., Phys. Rev., 113 (1955) 110.

[2] Latham, R.V., High Voltage and Vacuum Insulation: The Physical Basis (London: Academic, 1981).

[3] Eriksson, C., Wiklund, B. and Astrand, B., Physica Scripta, 24(2) (1981) 447.

[4] Marrese, C.M., IEEE Aerospace Conference Proceedings, 4 (2000) 85.

[5] Zhbanov, V., Pogorelov, E. and Chang, Y.C., "Carbon Nanotube Field Emitters", Marulanda, J.M. (Ed.), (Carbon Nanotubes InTech. 2010), pp. 311–340. ISBN: 978-953-307-054-4.

[6] Latham, R.V. and Mousa, M.S., Appl. Phys., 19 (1986) 699.

[7] FEI Company, "Introduction to Electron Microscope", (2010).

[8] Weilie, Z., Apkarian, R., Wang, Z. and Joy, D., "Scanning Microscopy for Nanotechnology". (Springer, New York, 2007), 1-40.

[9] Hitachi S-4700 SEM, "Training and Reference Guide", (2007).

[10] Koninklijke Philips Electronics N.V., "Transmission Electron Microscope (TEM)", (2008).

[11] Williams, D.W. and Carter, C.B., "The Transmission Electron Microscope", 2nd Ed. (Springer-Verlag US. 1996), pp. 3-17.

[12] Mussa, K.O., Mousa, M.S. and Fischer, A., Ultramicroscopy, 132 (2013) 48.

[13] Forbes, R.G., J. Vac. Sci. Technol. B 27(3) (2009) 1200.

[14] Fischer, A., Mousa, M.S. and Forbes, R.G., J. Vac. Sci. Technol. B 31 (2013) 032201.

[15] Forbes, R.G., Fischer, A. and Mousa, M.S., J. Vac. Sci. Technol. B 31 (2013) 02B103.

[16] Zhao, C.X., Li, Y.F., Chen, Jun, Deng, S.Z. and Xu, N.S. Ultramicroscopy, 132 (2013) 36.

[17] Visart de Bocarme, T. and Kruse, N., Ultramicroscopy, 111 (2011) 376.

[18] Forbes, R.G., J. Appl. Phys., 111 (2012) 096102.

Jordan Journal of Physics

ARTICLE

COLTRIMS Imaging of Molecular Fragmentation Dynamics of CO Molecules Induced by Slow He^{2+} Ions

Feras R. Afaneh

Physics Department, The Hashemite University, Zarqa, 13115, Jordan.

Abstract: We study the multiple ionization and fragmentation of CO in collisions with slow He^{2+} ions. Correlated measurements of all fragment ions and the projectile final charge state were performed using our coincidence COLTRIMS imaging technique coupled to projectile charge state separation. Complete fragmentations of CO, following double electron capture, into $C^{m+} + O^{n+}$ with a total charge of 4 were investigated. The kinetic energy release (KER) distributions and their dependence on the molecule-axis orientation and on the projectile ion velocity were studied. A strong dependence of the kinetic energy release on the velocity of the He ions is observed. Furthermore, we find that the KER values are shifted toward higher energies when the molecule is aligned with the beam direction.

Keywords: Ion-molecule collisions; Molecular fragmentation; Kinetic energy release; Recoil-ion spectroscopy; Molecular orientation; Multi-hit COLTRIMS imaging.

PACS: 34.70.+e, 34.80.Gs, 34.50.Gb.

Introduction

The multiple ionization and fragmentation of molecules have recently been an active area of research [1-4]. In a collision with an energetic ion, a target molecule receives a considerable amount of electronic energy, leading to molecular excitation, multiple ionization and fragmentation. Furthermore, the amount of electronic energy deposition into a target is supposed to change considerably depending on the impact parameter between collision partners and on the orientation of the target molecule. Recent and rapid development of multicoincidence and momentum imaging techniques allows to measure important parameters such as molecular orientation before collisions, kinetic energy of fragment ions, initial charge state of molecules prior to dissociation, … and so forth [2,3]. To date, however, collision induced molecular fragmentation using slow ions is not fully understood yet.

In this work, we study the fragmentation processes of CO molecules induced by slow ions. The dependence of kinetic energy release (KER) on the molecular orientation is investigated. Measurements were performed by using a technique of momentum 3D imaging, enabling us to achieve a kinematically complete study of molecular fragmentation. The technique is known as COLTRIMS imaging technique (COLTRIMS stands for cold target recoil ion momentum spectroscopy). It is one of the most powerful imaging techniques. It has a high multi-fragment detection efficiency and an excellent momentum resolution in fragmentation processes. The COLTRIMS technique has been reviewed by Dörner et al. [2].

Experiment

A schematic diagram of our COLTRIMS imaging setup is shown in FIG. 1. Within the COLTRIMS spectrometer, a supersonic gas jet

---

intersects with the ion beam. All charged particles formed during the interaction are projected on time and position sensitive detectors by a well-designed electric field configuration. This way, the measurement covers the full 4π solid angle. The fragment ions produced in a single collision were measured in coincidence with the scattered projectile. The final charge state of the projectile was determined using a two-dimensional position sensitive MCP detector located 1.5 m downstream from the target. The 1.5 m flight length for the projectiles after leaving the target region was made for good separation of charge states on the projectile detector ~ 1.5 cm, which has a resolution of 0.2 mm. By measuring the impact position for each fragment ion on the detector and its time-of-flight, the fragment ion trajectory, and thus the ion momentum gained in the fragmentation, can be determined. To improve the momentum resolution, electrostatic lenses can be incorporated into the spectrometer system. Thus, the influence of the extended target region, from where the fragments originate, can be strongly reduced [3, 4]. In this experiment, particle detectors with fast delay-line position read-out were used to enable us to simultaneously detect two particles impacting on

the detector at the 'same' instant ($\Delta t < 1$ ns) – as long as they are separated in space by at least 10 mm. The data are acquired and stored in list mode event by event. The rate of fragmentation processes that can be processed per second can approach 100 kHz. To ensure good momentum resolution for the ionic fragments, the target must have a well-defined momentum or be at rest in the laboratory frame. Thus, the CO gas jet is made up of a modified Leybold coldhead with a 0.01 mm nozzle mounted to its tip. The gas passes through a copper tube and is precooled in the coldhead before it is allowed to expand through the nozzle. In the resulting directed gas stream, the so-called "zone of silence" is formed. In this region, the internal temperature of the CO gas in the zone of silence is only a few Kelvin. To realize a cold well localized CO target from the expanding gas, the CO jet is clipped out of the zone of silence by a cone-like aperture with a sharp edge (skimmer). For this work, a differential pumping stage with a second skimmer, which is pumped separately, is located between the expansion and the reaction chamber. Thereby, it is guaranteed that the vacuum in the reaction chamber does not become perturbed by the operation of the jet [2,3].
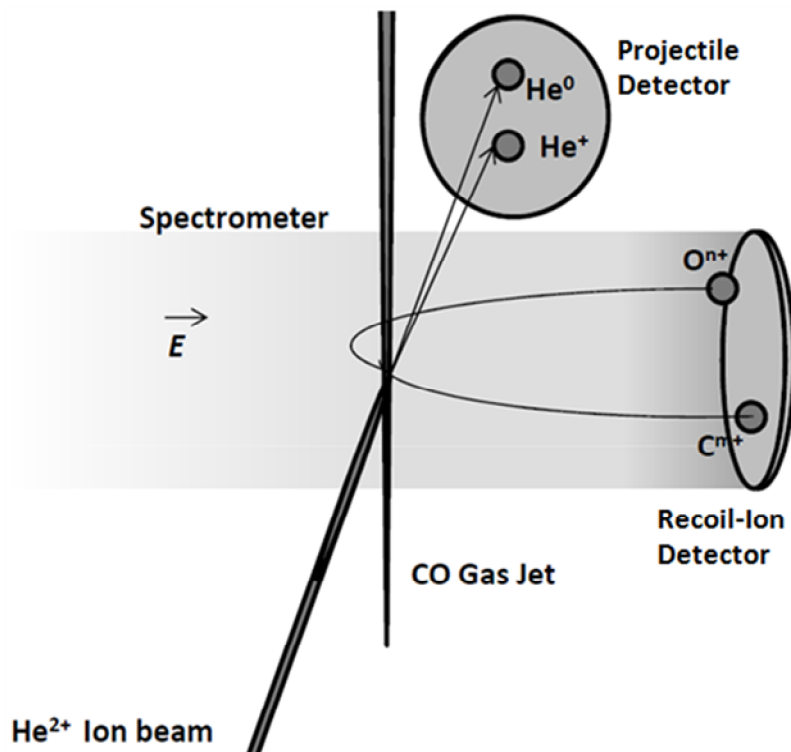
FIG. 1. A schematic diagram of COLTRIMS imaging setup.

Data and Discussion

The fragmentation of CO molecule induced by He^{2+} ion has been investigated at two different impact velocities of 0.7 au and 0.84 au. The fragment ions which resulted from the fragmentation of CO have been measured in coincidence with the scattered projectile. It is well known from the studies of ion–atom collisions at low energy that the capture process dominates the target electron removal and mainly valence target electrons are involved in the capture process [5, 6]. It is thus expected that this process should produce molecular ions in their lowest electronic energy levels. In the current study, we focused on the fragmentation channels which resulted from the capture processes.

It has been suggested that the molecular fragmentation process can be considered a two-step process [7]. In the first step, the neutral CO target is collisionally excited to a dicationic electronic state,

$$He^{2+} + CO \rightarrow He^0 + (CO^{2+})^*$$
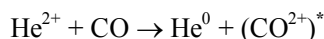
followed by fragmentation,

$$(CO^{2+})^* \rightarrow C^+ + O^+ .$$
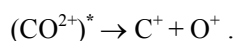
As mentioned above, the other fragmentation channels: $(C^{2+}+O^+)$, (C^++O^{2+}) and $(C^{2+}+O^{2+})$ have been also detected. For each fragmentation channel, the time-of-flights of the two fragments which resulted from the fragmentation were measured in coincidence with the scattered

projectile. FIG. 2 shows the time of flight spectrum (integrated overall impact positions) of the first arriving fragment ion measured relative to the projectile. We observe sharp peaks of CO$^+$ and CO^{2+} ions having thermal energies. These ionic peaks arise from direct ionization of the CO molecule. Additionally, four ion fragments (O$^+$, C$^+$, O^{2+}, and C^{2+}) are also formed which arise from the fragmentation of the multiply charged CO^{q+} (q $\leq$ 4) ions. One can see that peak widths of monoatomic fragment ions of C^{m+} and O^{n+} are substantially broader than intact CO$^+$ ions, indicating that fragment ions are produced with larger kinetic energies gained from Coulomb explosion. To identify the different fragmentation channels, it is convenient to display the data in a Projectile-ion1-Projectile-ion2-Coincidence Spectrum (PIPICO), where the time of flight of the first hit is plotted against the time of flight of the second hit. Correlations in the time of flight of the first and second hit might indicate momentum conservation and thus represent fragmentation channels. In a PIPICO spectrum, these correlations can be recognized as "stripe-like" structures as presented in FIG. 3. From this coincidence map, four fragmentation channels (C$^+$ + O$^+$, C^{2+} + O$^+$, O^{2+} + C$^+$, and C^{2+} + O^{2+}) originating from the complete Coulomb fragmentation of CO^{q+} (q = 2–4) are observed. For all observed four channels shown in FIG. 3, wherein the complete Coulomb fragmentation processes occur, we consider only those counts which obey the law of momentum conservation.
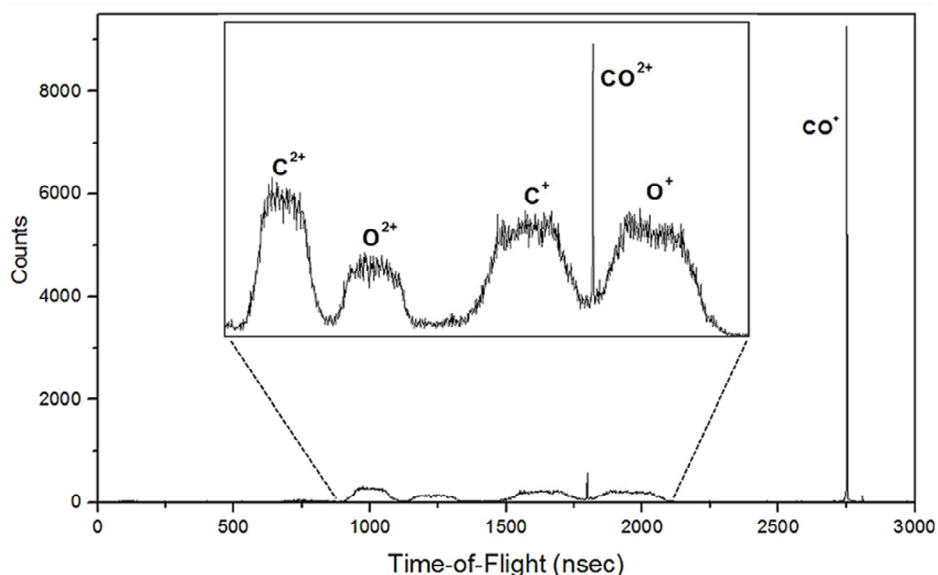
FIG. 2. Time-of-flight (TOF) spectrum of fragment ions from CO fragmentation produced in "double-electron capture" collisions of 0.84 a.u. He^{2+} ions.
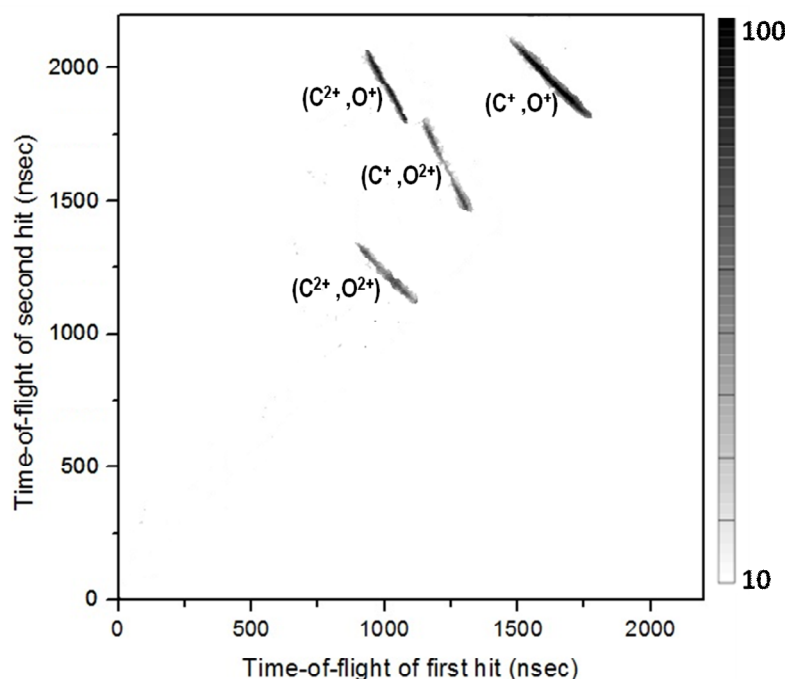
FIG. 3. PIPICO spectrum for CO fragmentation induced by He^{2+} ion impact showing TOF for first fragment *versus* TOF for second fragment. Four fragmentation channels can be observed.

From the experimental results presented in FIG. 3, two main features can be deduced. First, the (C$^+$ + O$^+$) and (C^{2+} + O^{2+}) fragmentation channels are stronger than the (C$^+$ + O^{2+}) and (C^{2+} + O$^+$) channels. This means that when multiple electrons are removed from the target, charge-symmetric dissociation is the favored dissociation pathway. This phenomenon has been observed in other collision systems [8, 9] and is understood to be a consequence of the ability of the electron cloud to rearrange quickly compared to the much slower nuclear motion in the dissociation process. Second, for the charge asymmetric channels (C$^+$ + O^{2+}) and (C^{2+} + O$^+$), the production of multiply ionized carbon ions is generally favored over the production of the corresponding oxygen ions, most likely because oxygen has a larger binding energy. In other words, CO^{3+} fragmentation into the channel (C^{2+}, O$^+$) is significantly larger than the channel (C$^+$, O^{2+}) for all the incident ions. This is attributed, as mentioned above, to the smaller total ionization energy required to produce these states due to the smaller ionization potentials of the C atom compared to the O atom; the ionization potentials required for these ionized states are 49.3 and 59.9 eV for (C^{2+}, O$^+$) and (C$^+$, O^{2+}), respectively.

The dependence of the kinetic energy release (KER) distribution on the projectile ion velocity was investigated for different fragmentation channels. FIG. 4 shows the KER distributions for the C$^+$ – O$^+$ fragmentation channel for two different impact velocities of 0.7 au and 0.84 au. It is observed that with decreasing the impact velocities, the width of the KER distribution increases and high energy components start to show up in the KER distribution. This indicates that new highly excited states are populated. To understand this behavior, we should investigate the sources of the KER. It is known that the kinetic energy of the two fragments in the final state has two sources: the energy transferred from the projectile during the collision and the energy from the Coulomb repulsion between fragment ions. When the impact velocity decreases the collision time; i.e., the interaction time between the projectile and the molecule will be longer. Therefore, the momentum transfer to the molecule increases and consequently, more energy is collisionally transferred to the CO molecule. This gives the possibility that the resulting transient CO^{2+} ions populate higher excited states. This leads to an energy shift of the KER lines toward higher values. The result supports the picture of the dissociation process as a two-step process [10, 11]. It also confirms that the KER distributions are governed by the fragmentation dynamics; i.e., the potential energy curves of the molecular ion, rather than by the scattering itself.
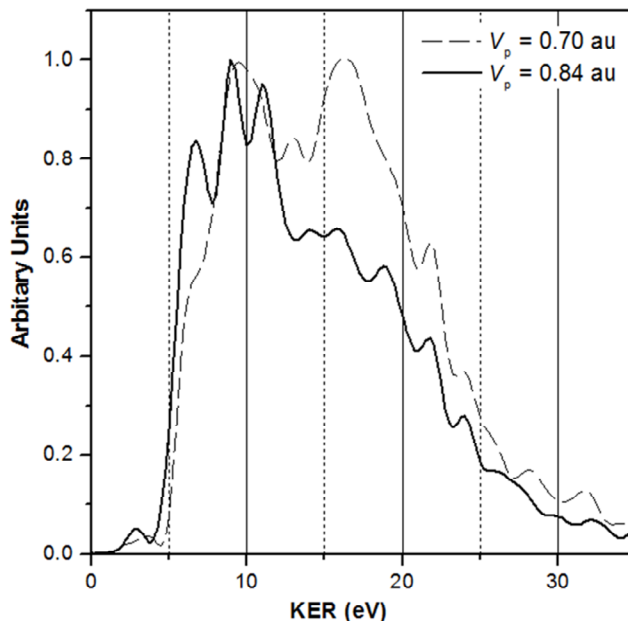
FIG. 4. Kinetic energy release distributions for (C$^+$ - O$^+$) fragmentation channel at two different ion velocities (a) 0.7 a.u. (dashed curve) and (b) 0.84 a.u. (solid curve).

Indeed, it is also possible by COLTRIMS imaging technique used in this study to measure, in coincidence with the KER, the angle between the molecular axis and the beam during the collision. This enables us to investigate the molecular orientation effect on the KER distributions. FIG. 5 shows the KER distributions for the C$^+$ + O$^+$ fragmentation channel at different molecular orientations. We find that the KER values are shifted toward higher energies when the molecule is aligned with the beam direction. This effect was predicted for slow highly charged projectile and light fragments by Classical Trajectory Monte Carlo (CTMC) calculations [12]. They found that fragmentation in the electric field of slow projectiles leads to energy shifts of the KER lines toward higher values when the molecule is aligned with the projectile beam direction.

Conclusions

The multiple ionization and fragmentation of CO induced by collisions with slow He^{2+} ions were studied. Correlated measurements of all fragment ions and the projectile final charge state were performed using our coincidence COLTRIMS imaging technique coupled to projectile charge state separation. Complete fragmentations of CO into C^{m+}+O^{n+} with a total charge of 4 were investigated. The dependence of kinetic energy release (KER) distributions on the molecule-axis orientation and on the projectile ion velocity was studied. A strong dependence of the kinetic energy release on the velocity of the He ions is observed. It is even noted that the KER values are shifted toward higher energies when the molecule is aligned with the beam direction.

Acknowledgments

FIG. 5. Kinetic energy release distributions for different molecular orientations.

References

[1] Schmidt, L., Schössler, S., Afaneh, F., Schöffler, M., Stiebing, K., Schmidt-Böcking, H. and Dörner, R., Physical Review Letters, 101 (2008) 173202.

[2] Dörner, R., Mergel, V., Jagutzki, O., Spielberger, L., Ullrich, J., Moshammer, R. and Schmidt-Böcking, H., Physics Reports, 330 (2000) 95.

[3] Ullrich, J., Moshammer, R., Dorn, A., Dörner, R., Schmidt, L. and Schmidt-Böcking, H., Rep. Prog. Phys., 66 (2003) 1463.

[4] Afaneh, F., Schmidt, L., Schöffler, M., Stiebing, K., Al-Jundi, J., Schmidt-Böcking, H. and Dörner, R., J. Phys. B: At. Mol. Opt. Phys., 40 (2007) 3467.

[5] Schmidt, L., Afaneh, F., Schöffler, M., Titze, J., Jagutzki, O., Weber, T., Stiebing, K., Dörner, R. and Schmidt-Böcking, H., Physica Scripta, T110 (2004) 379.

[6] Afaneh, F., Ph.D. Thesis, J. W. Goethe (Frankfurt/Main) University, (2001), Germany.

[7] Graham, W.G., Latimer, C.J., Browning, R. and Gilbody, H.B., J. Phys. B: At. Mol. Phys., 6 (1973) 2641.

[8] Sampoll, G., Watson, R.L., Heber, O., Horvat, V., Wohrer, K. and Chabot, M., Phys. Rev. A, 45 (1992) 2903.

[9] Remscheid, A., Huber, B.A., Pykavyj, M., Staemmler, V. and Wiesemann, K., J. Phys. B, 29 (1996) 515.

[10] Folkerts, H.O., Hoekstra, R. and Morgenstern, R., Phys. Rev. Lett., 77 (1996) 3339.

[11] DuBois, R.D., Schlathölter, T., Hadjar, O., Hoekstra, R., Morgenstern, R., Doudna, C.M., Feeler, R. and Olson R.E., Europhys. Lett., 49 (2000) 41.

[12] Wood, C.J. and Olson, R.E., Phys. Rev. A, 59 (1999) 1317.

Jordan Journal of Physics

ARTICLE

Investigating the Effects of Sample Conditioning on Nano-Apex Carbon Fiber Tips for Efficient Field Electron Emission

S. Alnawasreh[a], M. S. Mousa[a] and A. N. Al-Rabadi[b]

[a] *Dept. of Physics, Mu'tah University, Al-Karak 61710, Jordan.*
[b] *Dept. of Computer Engineering, The University of Jordan, Amman, Jordan.*

Abstract: Carbon fibers represent a very interesting material for field electron emitters. While the preparation of sharp carbon fiber tips is very similar to the conventional method used for tungsten tips, much smaller apex radii can be obtained. Within the study presented here, such emitters have been prepared and tested using a standard field emission microscope (FEM). Various properties of these emitters were measured including the relationship between emitted electron current and applied voltage to the tip (the current-voltage characteristics) and the corresponding electron emission images. The field emission of carbon fibers has been studied via various methods of sample conditioning treatment; such as thermal relaxation process and cryogenic cooling. The performance of these tips was found to be dependent on the sample conditioning treatment.
Keywords: Electrochemical etching; Field electron emission; Fowler-Nordheim plots; Carbon fiber tips; Vacuum-based analysis.

Introduction

Field electron emission is the emission of electrons from the surface of a cathode under the influence of the applied electric field (of 3×10^9 V/ m) [1], which is strongly dependent upon the work function of the emitting material. The first explanation of what appears to be a field electron emission initiated electric discharge was made by Winkler [2].

One of the most recent studies on analyzing Fowler-Nordheim plots has been conducted by Forbes, Mousa and Fischer, which was concerned with studying the cold field electron emission [3, 4]. One of the important implementations, introduced by Al-Rabadi and Mousa, has been performed within controlled-switching (i.e., multiplexing) applications [5, 6].

The general form of Fowler-Nordheim-type (FN-type) equation is given as follows [7]:

$$ J = \lambda_L a\varphi^{-1} F^2 EXP \left[-\frac{v_F b\varphi^{\frac{3}{2}}}{F} \right]. $$

This equation is used in all cases of field electron emission processes, where J is the local emission current density, a and b are the first and the second Fowler – Nordheim constants, respectively, v_F is the barrier form correction factor and it accounts for the particular shape of the potential barrier model, and λ_L is the local pre-exponential correction factor where it takes into account all of the other factors that influence the emission. ϕ is the work function of the material used. Certainly, v_F and λ_L depend on the applied field F [7].

Electron sources that are based on field emission have a number of applications that include the construction of bright electron sources for high-resolution devices and optoelectronic equipment [8].

Due to the technological importance of carbon fibers, there has been a growing interest in understanding the mechanism of the field

---

electron emission from these fibers under the influence of an applied electrical field [9]. Using carbon fibers as cathodes brings several benefits such as offering the ability to work in a relatively high pressure environment (about 10^{-6} mbar), simplicity of manufacturing the emitter, high current stability and long emitter durability [9]. Such cathodes are made either of carbon fibers or of other carbon-based materials.

The motivation of this work is to examine the influence of the conditioning treatment on the emitter behavior. Preparation techniques were employed to produce conical carbon fiber sharp, medium and blunt tips in order to study the means by which the emission current instability could be overcome [10]. This work aims at developing an electron source that has a long life with high emission current stability and an increased brightness. Another aim of this research is to prepare the ground to study the electron emission physical mechanism from the carbon fiber microemitters and also to be compared with that of other materials such as tungsten. It is worth noting that tungsten is the main material used in the electron emission-based technologies.

Experimental Setup

Carbon fiber emitters can be produced by electrolytic etching technique, where a 0.1 Molar of sodium hydroxide solution (250 ml of distilled water with 2g of NaOH) is used [10]. This etching process could be controlled by choosing a suitable etching current. The etching process starts after dipping the sample to be etched in the solution by about 2 mm and using a power supply to provide the dc voltage until a certain initial current of about 30 μA is reached. The chosen etching current produces sharp tips at the liquid surface. The etched sample immediately afterwards is subjected to ultrasonic cleaning by using an ultrasonic device. The cleaned tip is then mounted in a standard, home-built, field emission microscope (FEM) with a tip-screen distance of 10 mm [10]. The anode is formed as a phosphored tin-oxide coated conductive glass screen in order to allow for the recording of the emission current and the electronic images [9].

The FEM was evacuated to ultra high vacuum (UHV) conditions using a mechanical rotary pump that produces pressures of about 10^{-3} mbar and an oil diffusion pump system, connected to a liquid nitrogen (LN_2) trap which leads to finally

reaching a base pressure of about 10^{-9} mbar [11, 12]. Then, the samples are subjected to sample conditioning treatment which consists of an initial baking of the system for 12 hours at 170 °C, a follow-up baking of the system for 12 hours, thermal relaxation for 12 hours at 170 °C, and finally cooling the sample by liquid nitrogen – while observing the emission behavior. This allowed recording the effects of these conditioning processes on carbon fiber tips.

To record the emission behavior, an additional high tension (EHT) power supply is used to apply the voltage on the tip. This is slowly increased until the emission current rises to about one microampere and is measured on a Kiethley 485 autoranging picoammeter. The applied voltage is then slowly decreased until the emission current vanishes. Within this range, a linear Fowler-Nordheim (FN) plot is expected [13].
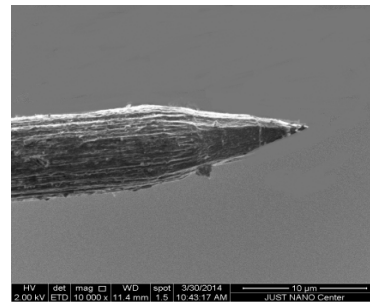
FIG.1. Scanning electron micrograph of a very sharp carbon fiber tip at 10000 × magnification.

Results and Discussion

The emission characteristics derived will be presented as the I-V characteristics and the corresponding Fowler-Nordheim (FN) plots whose equation was given in the introduction. The slope obtained from these plots enables calculating the tip apex radii. These radii of the carbon fiber tips have been measured as the average of the graphically best-fitting circles of the SEM employed in the experiments.

The latter ones are used to interpret the experimental data and extract relevant information such as the apex radii, which is an important data needed for further physical analysis in a future research. During the experiments, electronic emission images have been recorded by a standard digital camera to study the spatial distribution and stability of the emission current. Stability as well as brightness (emitted current/unit emitting area/unit solid angle where the electrons are emitted out of the

surface) are important factors for judging the quality of the electron source for practical applications.

During the sample conditioning treatment, it was discovered that there were statistical variations in the electronic emission of the various tip microemitters under the corresponding UHV conditions [14].

Very Sharp Tips

In this part, one of the very sharp carbon fiber tips (such as the one shown in Fig. 1) has been tested during sample conditioning treatment. The apex radius of this tip was 57 nm.
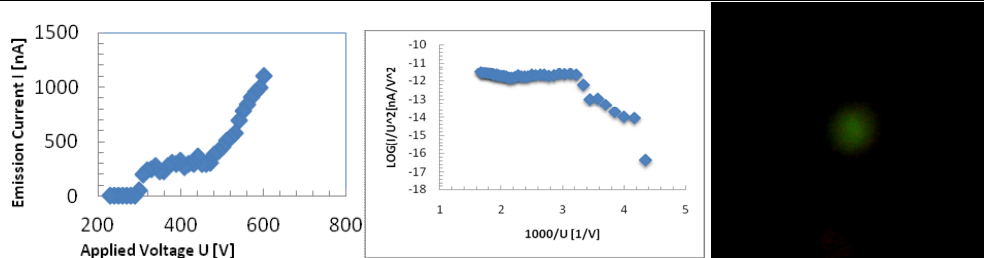
FIG. 2. The I-V characteristics (left) and Fowler-Nordheim plot (center) of a very sharp tip after initial baking for 12 hours at a temperature of 170°C. The emission image (right) is obtained from a carbon fiber very sharp tip after initial baking for 12 hours at 1 μA emission current. The slope of the linear part of the plot is S = 1034.
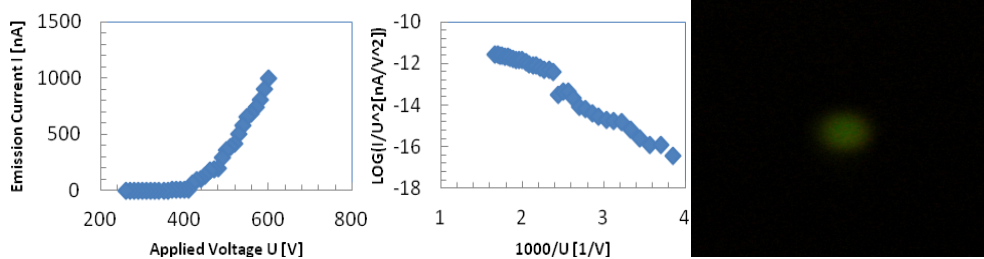
FIG. 3. The I-V characteristics (left) and Fowler-Nordheim plot (center) of a very sharp tip after a follow-up baking for 12 hours at a temperature of 170°C. The emission image (right) is obtained from a carbon fiber very sharp tip after a follow up baking for 12 hours at 1 μA emission current. The slope is S = 2407.
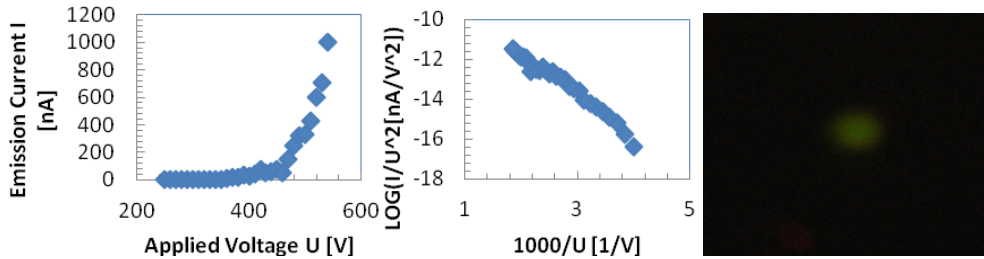
FIG. 4. The I-V characteristics (left) and Fowler-Nordheim plot (center) of a very sharp tip after thermal relaxation process for 12 hours. The emission image (right) is obtained from a carbon fiber very sharp tip after thermal relaxation process overnight at 1 μA. The slope is S = 2027.
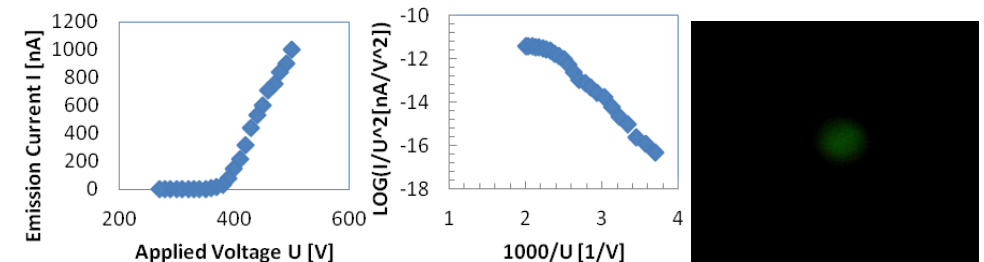
FIG. 5. The I-V characteristics (left) and Fowler-Nordheim plot (center) of a very sharp tip during cooling process. The emission image (right) is obtained from a carbon fiber very sharp tip during cooling process at 1μA emission current. The slope of the FN plot is S = 3069.

After initial baking, as shown in Fig. 2, the F-N plot shows a non-linear behavior, and the emission current was unstable. The follow-up baking, as shown in Fig. 3, shows a disconnected plot because the voltage drops from 66 V to 5.5 V, possibly due to a change in emitter shape. After the sample conditioning, the emission current stability becomes much higher as shown in Fig.s 4 and 5. The emission images as shown in Fig.s 2 - 5 become brighter, more stable and more focused.

Sharp Tips

In the second part, we tested one of the sharp carbon fiber tips which has been tested during sample conditioning treatment. The apex radius of this tip was 70 nm.
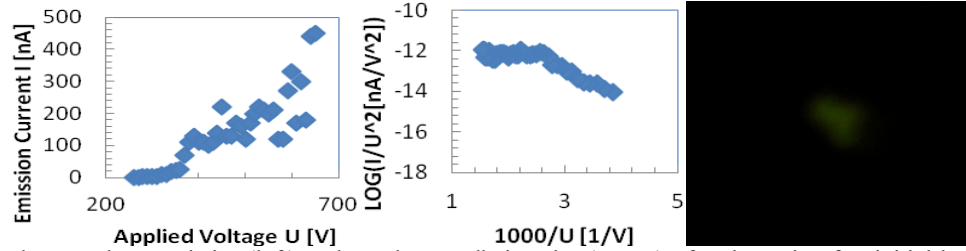
FIG. 6. The I-V characteristics (left) and Fowler-Nordheim plot (center) of a sharp tip after initial baking over night at a temperature of 170°C. The emission image (right) is obtained from a carbon fiber sharp tip after initial baking for 12 hours at 1 μA. The slope is S = 753.
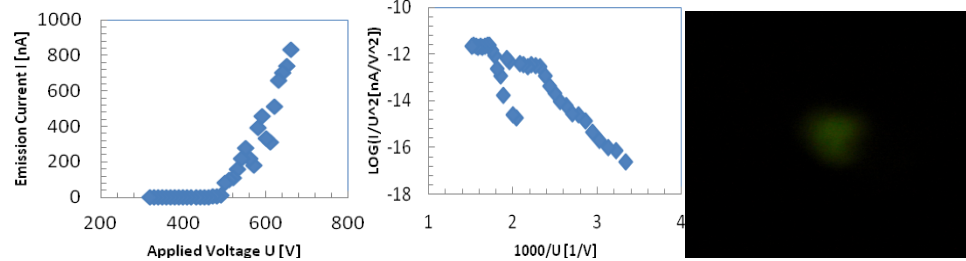
FIG. 7. The I-V characteristics (left) and Fowler-Nordheim plot (center) of a sharp tip after a follow-up baking over night at a temperature of 170°C. The emission image (right) is obtained from a carbon fiber sharp tip after a follow-up baking for 12 hours at 1 μA. The slope is S = 2577.
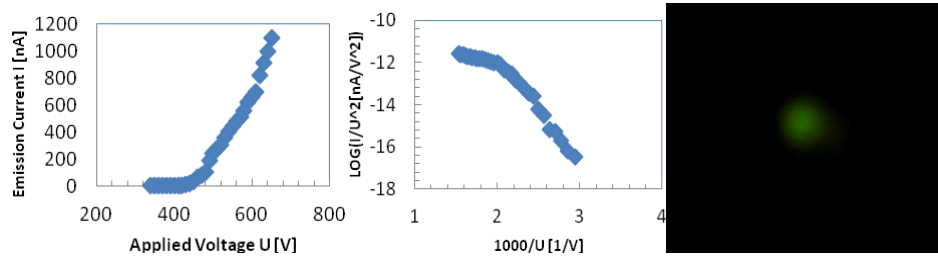
FIG. 8. The I-V characteristics (left) and Fowler-Nordheim plot (center) of a sharp tip after thermal relaxation process over night. The emission image (right) is obtained from a carbon fiber sharp tip after thermal relaxation process treatment for 12 hours at 1 μA. The slope is S = 2472.
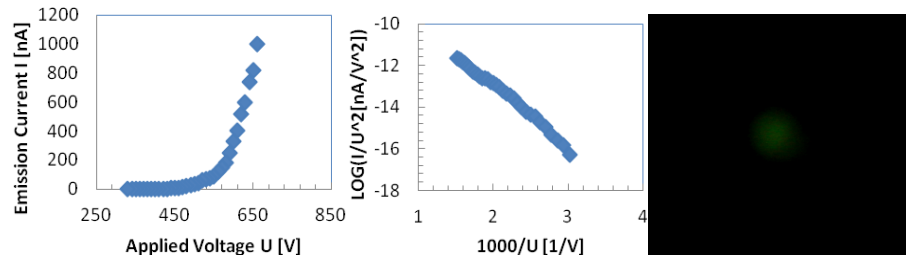
FIG. 9. The I-V characteristics (left) and Fowler-Nordheim plot (center) of a sharp tip during cooling process. The emission image (right) is obtained from a carbon fiber sharp tip during cooling process at 1 μA. The slope is S = 2897.

After the baking treatment, the emission behavior showed little variation on the tip between the initial baking and the follow-up baking as shown in Fig.s 6 and 7. The influence of the thermal relaxation and cooling the sample to the LN_2 temperature on the emission characteristics was studied. There was significant variation in the magnitude of the emission current and its stability as shown in Fig.s 8 and 9. Fig.s 6 - 9 show an improvement in the emission images during these treatments [14].

Medium Sharp Tips

In the third investigation, one of the medium sharp carbon fiber tips has been tested during sample conditioning treatment. The apex radius of this tip was 90 nm.
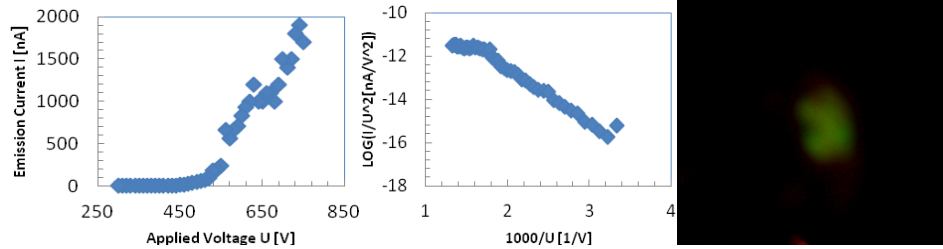
FIG. 10. The I-V characteristics (left) and Fowler-Nordheim plot (center) of a medium sharp tip after initial baking over night at a temperature of 170°C. The emission image (right) is obtained from a carbon fiber medium sharp tip after initial baking for 12 hours at 1 μA. The slope is S = 2274.
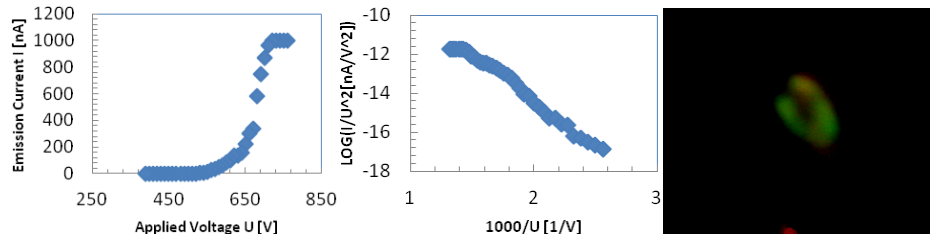
FIG. 11. The I-V characteristics (left) and Fowler-Nordheim plot (center) of a medium sharp tip after second baking over night at a temperature of 170°C.The emission image (right) is obtained from a carbon fiber medium sharp tip after a follow-up baking for 12 hours at 1.2 μA. The slope is S = 4574.
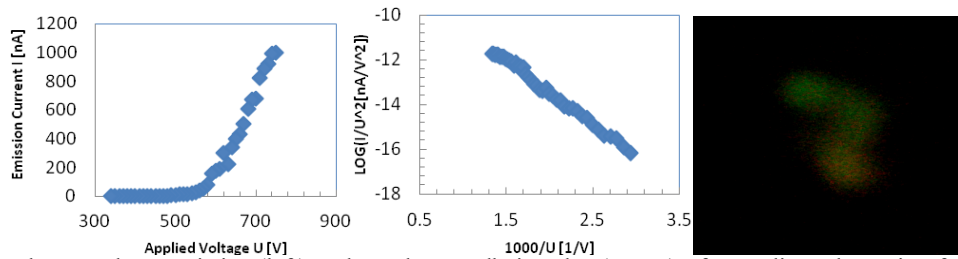
FIG. 12. The I-V characteristics (left) and Fowler-Nordheim plot (center) of a medium sharp tip after thermal relaxation process over night. The emission image (right) is obtained from a carbon fiber medium sharp tip after thermal relaxation process for 12 hours at 1 μA emission current. The slope of the FN plot is S = 2856.
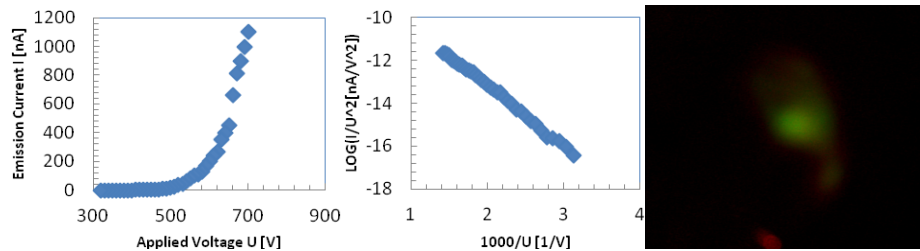
FIG. 13. The I-V characteristics (left) and Fowler-Nordheim plot (center) of a medium sharp tip during cooling process. The emission image (right) is obtained from a carbon fiber medium sharp tip during the cooling process (down to LN_2 temperature) at 1.2 μA. The slope is S = 2824.

The field electron emission characteristics from the follow-up baking did not show much variation from those characteristics of the initial baking as shown in Fig.s 10 and 11. The last two processes, thermal relaxation and cooling process, cause a clear improvement in the emission current stability as shown in Fig.s 12 and 13 [10, 15].

Blunt Tips

In the fourth study, one of the blunt carbon fiber tips has been tested during sample conditioning treatment where the apex radius of this tip was 150 nm.
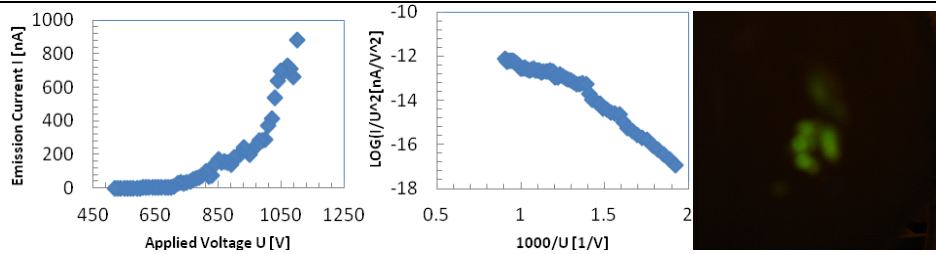
FIG. 14. The I-V characteristics (left) and Fowler-Nordheim plot (center) of a blunt tip after initial baking over night at a temperature of 170°C. The emission image (right) is obtained from a carbon fiber blunt tip after initial baking for 12 hours at 1 μA. The slope is S = 4508.
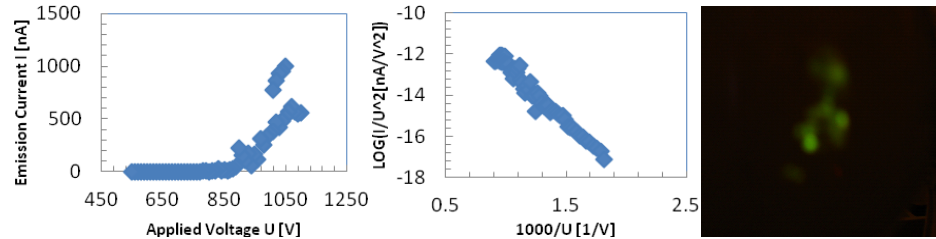
FIG. 15. The I-V characteristics (left) and Fowled-Nordheim plot (center) of a blunt tip after a follow-up baking over night at a temperature of 170°C. The emission image (right) is obtained from a carbon fiber blunt tip after a follow-up baking for 12 hours at 1 μA. The slope is S = 5558.
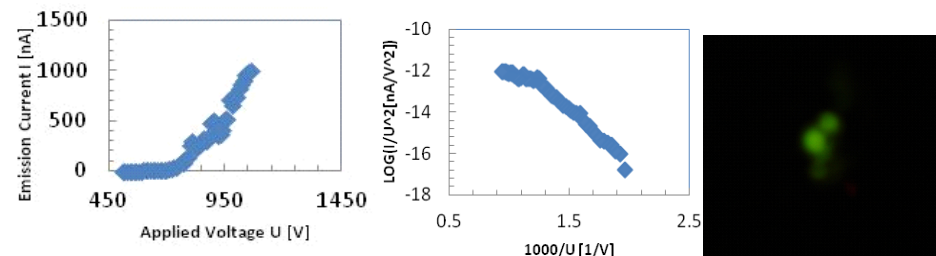
FIG. 16. The I-V characteristics (left) and Fowler-Nordheim plot (center) of a blunt tip after thermal relaxation over night. The emission image (right) is obtained from a carbon fiber blunt tip after thermal relaxation for 12 hours at 1 μA. The slope is S = 4196.
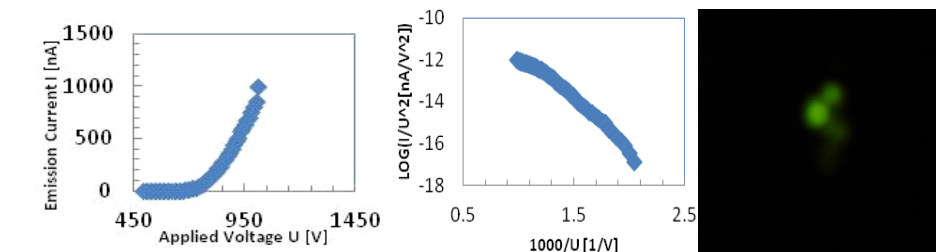
FIG. 17. The I-V characteristics (left) and Fowler-Nordheim plot (center) of a blunt tip during cooling process. The emission image (right) is obtained from a carbon fiber blunt during cooling process at 1 μA. The slope is S = 4361.

Following this sample conditioning, as shown in Fig.s 14 – 17, the typical I - V characteristics exhibited a reduction in the hysteresis effect and the emission current became more stable. Lower field produced the same values of current, and the I-V characteristics produced a linear F-N plot [16]. The electron emission images have shown to possess more stability and higher brightness. Principally, this is comparable with Yahachi Saito and Uemura work while investigating applications to electron sources [17]. Carbon fibers could be further investigated for applications where they were used to fabricate nanometer sized tips at their ends [18-20] and as a tip-based electron source [21]. The results reported here could enrich the theoretical investigations to understand the physical analysis of the reported phenomena. This, in addition to the mechanism assumed to control the emission of electrons from the fibers studied, will be the subject of further investigation

Conclusions and Future Work

Carbon fiber emitters were prepared using an electrolytically etching process. These emitters have been tested within the FEM system. During the conducted experiments, the current values were measured with a change in the voltage values. These experiments were carried out using carbon fibers with different apex radii. The analytical facility used enabled measuring various characteristics of the field electron emission. The sample conditioning procedures that included initial baking, a follow-up baking, thermal relaxation and cooling process down to LN_2 temperatures of about (-196°C), produced an improved stability in the emission current and higher brightness. Thus, the performance of these tips was found to be highly dependant on the utilized sample conditioning treatment. Future work will involve the application of this research findings within controlled-switching.

References

[1] Mousa, M.S., Appl. Surf. Sci., 94/95 (1996) 129.

[2] Winkler, J.H., , „Gedanken von den Eigenschasften, Wirkungen und Ursachen der Electrizität nebst Beschreibung zweier electrischer Maschinen". (Verlag B. Ch. Breitkopf, Leipzig, 1744).

[3] Fischer, A., Mousa, M.S. and Forbes, R. G., J. Vac. Sci. Technol. B 12 (2012) 879.

[4] Forbes, R.G., Fischer, A. and Mousa, M.S., J. Vac. Sci. Technol. B 31 (2013) 1.

[5] Al-Rabadi, A.N. and Mousa, M.S., Facta Universities, Series: Electronics and Energetics, 25 (2012a) 1.
DOI: 10.2298/FUEE1201001A.

[6] Al-Rabadi, A.N. and Mousa, M.S., Facta Universities, Series: Electronics and Energetics, 25 (2012b) 15.
DOI: 10.2298/FUEE1201015A.

[7] Forbes, R.G., IOP Publishing, Nanotechnology, 23(9) (2012).

[8] Latham, R.V. and Wilson, D.A., J. Phys. E. (Sci. Instr.), 15 (1982) 181.

[9] Latham, R.V. and Salim, M.A., J. Phys. E. (Sci. Instr.), 20 (1987) 1083.

[10] Moran Meza, J.A., Lubin, C., Thoyer, F., Villegas Rosales, K.A., Gutarra Espinoza, A.A., Martin, F. and Cousty, J., Carbon, 86 (2015) 363.

[11] Mousa, M.S., Fischer, A. and Mussa, K.O., Jordan J. Phys., 5 (2012) 21.

[12] Mussa, K.O., Mousa, M.S. and Fischer, A., Ultramicroscopy, 132 (2013) 48.

[13] Mousa, M.S. and Al-Share, M., Ultramicroscopy, 79 (1999) 195.

[14] Mousa, M.S., Surf. Sci., 231 (1990) 149.

[15] Alnawasreh, S., M.Sc. Thesis, Mu'tah University, Jordan (2014).

[16] Mousa, M.S., Vacuum, 38 (1998) 835.

[17] Saito, Y. and Uemura, S., Carbon, 38 (2000) 169.

[18] Kim, J., Huang, J. and de Lozanne, A., Mesoscale Nanoscale Phys., (2013) 1.

[19] Dappe, Y.J., Gonzalez, C. and Cuevas, J.C., Nanoscale, 6 (2014) 6953.

[20] Sripirom, J., Noor, S., Koeler, U. and Schulte, A., Carbon N. Y., 49 (2011) 2402.

[21] Albert, C., Guenter, K., Haidar, Z., Robert, B. and Miller, D.R.J., J. Vac. Sci. Technol. B 33 (2015) 03C101.

Jordan Journal of Physics

ARTICLE

The Effect of Z907 Dye on the Performance of Solar Cells Based on the Nc-TiO$_2$ Semiconducting Polymer Heterojunction

H. Al-Dmour

Department of Physics, Faculty of Science, Mu'tah University, Mu'tah, 61710, Jordan.

Abstract: This work studies the effect of cis-bis(isothiocyanato)(2,2'-bipyridyl-4,4'-dicarboxylato)(4,4'-di-nonyl-2'-bipyridyl) ruthenium(II) (Z907 dye) on the performance of nanocrystalline titanium dioxide (nc-TiO$_2$)/Poly3-hexylthiophene (P3HT) heterojunction solar cells. Specifically, the P3HT/Z907dye/nc-TiO$_2$ solar cells increase the short circuit current, J$_{sc}$, from 0.17 mA/cm^2 to 0.3 mA/cm^2, the open circuit voltage, V$_{oc}$, from 0.45 V to 0.7 V and the power conversion efficiency, η, from 0.03% to 0.08% compared with the P3HT/nc-TiO$_2$ solar cells. These changes are attributed to improvements in the absorption of the light falling on the device and the generation of electron–hole pairs in the presence of the dye layer. Additionally, the dye solar cells enhance the charge transport through the interface between the nc-TiO$_2$ and the P3HT. These results have been confirmed by studying the optical properties and the capacitance characteristics of the solar cells.
Keywords: Solar cells; Capacitance; Short circuit current; Rectification; Power conversion efficiency.

Introduction

Over the past two decades, dye-sensitized solar cells (DSSCs) have attracted tremendous interest due to their high power conversion efficiency of up to 10 % and their low-cost photovoltaic cell [1]. A typical DSSC or Graetzel cell is composed of a charge-transporting electrolyte and nanocrystalline titanium dioxide (nc-TiO$_2$) coated by ruthenium-based sensitizers. After the light is absorbed by the sensitizer layer, an electron-hole pair (exciton) is generated at the interface and moves out of the cell to produce the photocurrent. The liquid electrolyte transports holes to the top electrode, while the nc-TiO$_2$ layer injects electrons into the bottom electrode. However, there has been considerable interest in using solid-state hole transport material instead of a liquid electrolyte, which causes several problems in a Graetzel cell, such as evaporation and leakage of the liquid electrolyte when sealing the cell [2-4]. For example, Wei-Zhang reported a

3.85% power conversion efficiency using organic indoline dye D131 as the sensitizer and poly(3-hexylthiophene) (P3HT) as the hole transport[5]. Our previous report demonstrated the effect of nanocrystalline TiO$_2$ morphology on the performance polymer of heterojunction solar cells. The results confirm that the properties of the semiconductor sensitized the solar cell interfaces such that the size and shape of the nc-TiO$_2$ particles affect its power conversion efficiency[6]. Such effects were also studied [7] by Serap Günes, who found that the compact TiO$_2$ layer between the bottom electrode and the nonporous TiO$_2$ layer improved the photovoltaic performance of dye-sensitized solar cells. Our recent report [8] shows the effects of molecular-level insulation on the performance of a dye-sensitized solar cell. The molecular-level insulation has led to a small enhancement in the energy-conversion performance of the fabricated DSSC, with the best result being an increase in the open circuit voltage (V$_{oc}$) from 0.7 to 0.8 V.

Corresponding Author: H. Al-Dmour   **Email**: hmoud203@gmail.com

Therefore, the interface properties play an important role in improving the performance of organic/inorganic solar cells. However, the efficiency of solid-state solar cells based on nc-TiO$_2$ semiconducting polymer heterojunctions like our devices is very low compared with a Graetzel cell [1] and Weishu's work [9] because of the differences in the hole transport layers and interfacial area.

The present paper focuses on the fabrication and characterization of a semiconductor solar cell sensitized using cis-bis(isothiocyanato)(2,2'-bipyridyl-4,4'-dicarboxylato)(4,4'-di-nonyl-2'-bipyridyl) ruthenium(II) (Z907 dye) between nc-TiO$_2$ and P3HT layers. Similar studies have used Z907 dye as a sensitizer with different hole transport layers [9, 10, 11. 12, 13]. However, they have not used P3HT as the hole transport layer or studied the negative capacitance characteristics of their devices. Therefore, the effect of Z907 dye on the performance of P3HT/nc-TiO$_2$ was investigated using capacitance measurements, current voltage measurements and optical properties.

Experimental

The solar cells were composed of five layers (see Fig. 1). The first layer was coated with fluorine-doped tin oxide (SnO$_2$:F) electrodes, which were pre-coated with a thin, dense layer of TiO$_2$ (Solaronix, Switzerland). Using the doctor blade technique [14], a nc-TiO$_2$ paste was then spread over the cured substrates to form the anatase phase according to the procedures described in our previous publication [6]. The cured nc-TiO$_2$ layer was immersed in a solution composed of 50 ml of pure ethanol and 10 mg of Z907 dye for 48 hours. Subsequently, the cell was removed from the solution, cleaned using ethanol and dried under a hot air stream. A drop of the p-type organic semiconductor P3HT in a chloroform solution (15 mgmL^{-1}) was placed onto the surface of the nc-TiO$_2$ for several seconds prior to spinning at 1000 rpm. It was difficult to measure the thickness of the P3HT, because the surface of the nc-TiO$_2$ thin film was very rough. According to the literature [15], the thickness of the P3HT film on a flat surface was approximately 100 nm for a coating using a P3HT solution with a spin coating speed of 1000 rpm. Finally, circular gold electrodes of an area of 3 mm^2 were evaporated on top of the P3HT film. Current–voltage (I–V) characteristics were obtained using a Keithley model 307 source measurement unit. A xenon lamp was used to illuminate the devices through the transparent electrode with the light (incident power 100 mW/cm^{-2}) constrained by an aperture to fall on an area coinciding with one of the gold top electrodes. For capacitance measurements, an Agilent E4980A precision LCR meter in air was used over the frequency range from 20Hz to 1 MHz with a signal amplitude of 100 mV. The X-ray diffraction (XRD) patterns were obtained using a Seifert 3003 TT diffractometer operating at 40 kV and 40 mA. The microstructure of the nc-TiO$_2$ thin film was observed by scanning electron microscopy (SEM) using a Cambridge stereoscan-360 operating at 20 kV.
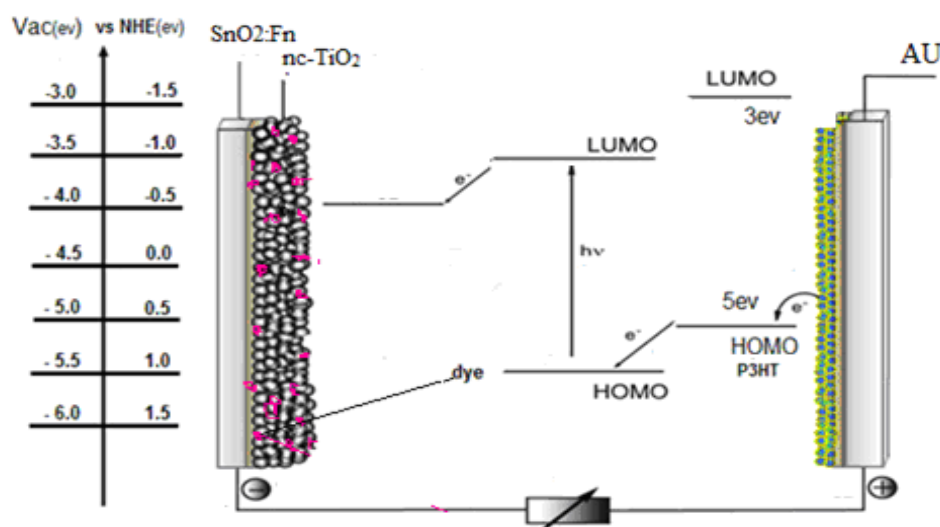
FIG. 1. Energy level diagram of the materials in the solar cells.

Results

Figures 2 and 3 show scanning electronic microscopy images of the nc-TiO$_2$/compact TiO$_2$/SnO$_2$:Fn layer used in our solar cells. These figures show that the thickness of the nc-TiO$_2$/compact TiO$_2$/SnO$_2$:Fn layer used in our solar cells was approximately 1.5 µm. The thickness of compact TiO$_2$/SnO$_2$:Fn is very small (less than 200 nm) and it is very difficult to distinguish the TiO$_2$/SnO$_2$:Fn layer from the nc-TiO$_2$ layer. From the top view image (see Fig. 3), it appears that the particle shape is almost uniform, with a small number of pin holes on the surface and particle size around 25 to 21nm. That may affect the amount of hole transport materials and dye that can penetrate the nc-TiO$_2$ thin film.
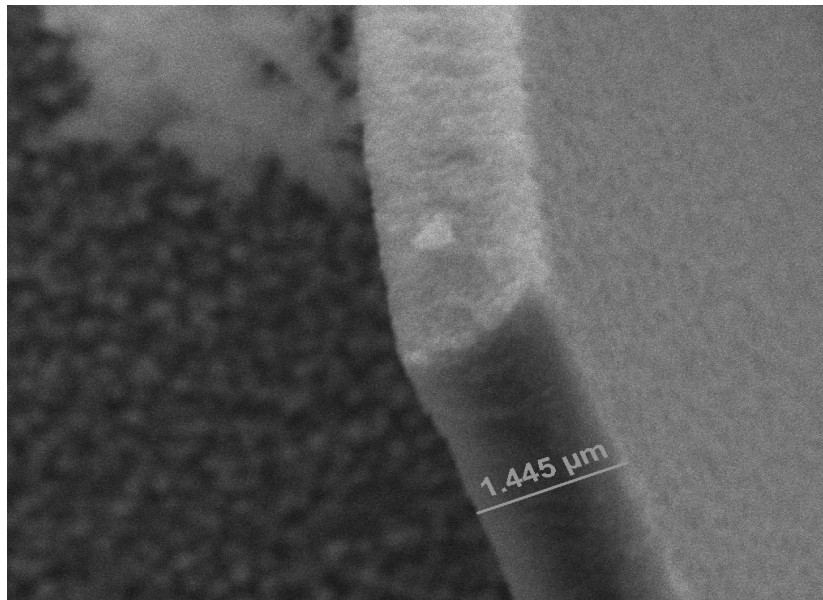
FIG. 2. Cross-section of the nc-TiO$_2$ /compact TiO$_2$ /SnO$_2$:Fn layer.
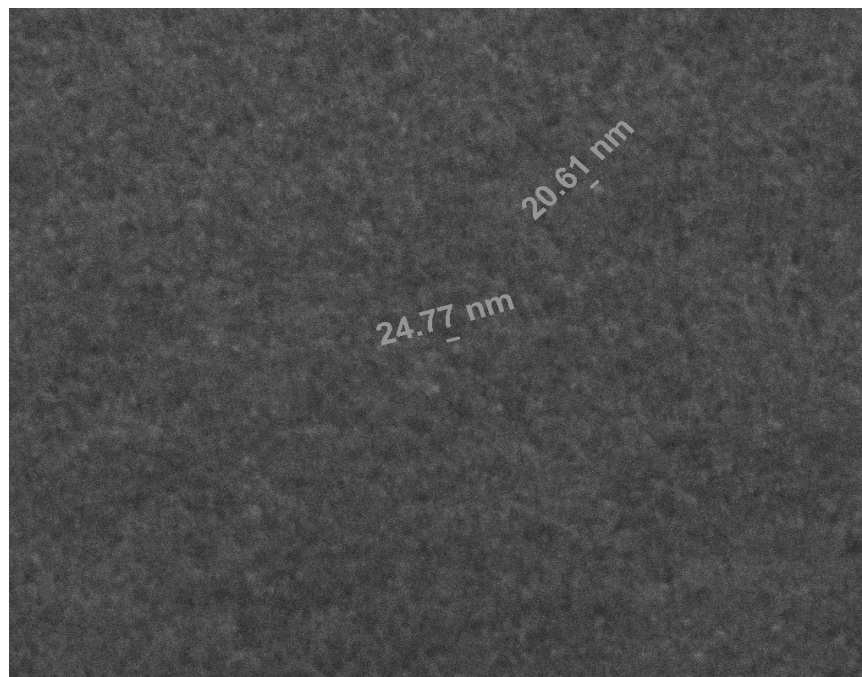
FIG. 3. Top view of the nc-TiO$_2$/compact TiO$_2$/SnO$_2$:Fn layer.

According to Park's paper [16], anatase-based solar cells produce short circuit currents at a rate greater than that of rutile-based solar cells. To determine the mineral form of the nc-TiO$_2$ thin films used in solar cells, X-ray diffraction measurements were conducted on the cells at room temperature. Figure 4 shows the XRD patterns of the nc-TiO$_2$ layer. This figure shows that the 2θ values at 25° were the strongest in the curve whereas smaller peaks were observed near 48° and 54°, and these three peaks are indexed to the (101), (200) and (105) lattice planes of the nc-TiO$_2$, respectively. These lattice planes occur in a tetragonal system and correspond to the anatase phase of TiO$_2$. The grain size of the

particle is determined by applying the Scherrer formula [17-18] to the largest diffraction peak:

$$G_S = \frac{K\lambda}{\beta\cos\theta} \; ; \qquad (1)$$

where λ=0.154 nm is the X-ray wavelength, G$_S$ is the grain size and β is the full width at half maximum of the diffraction peak. As seen in Fig. 4, the largest peak occurs at 2θ = 25.56° for the reflection from the 101 lattice plane. By substituting the values β = 0.0102 radians, cos(12.78) = 0.975 and K = 0.96 into equation (1), the grain size is estimated to be 15 nm.
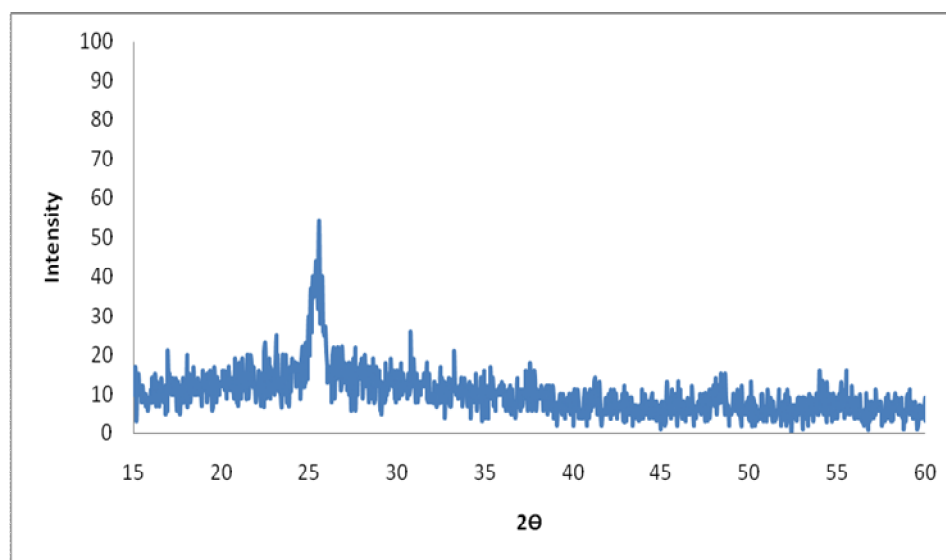
FIG. 4. XRD patterns of the nc-TiO$_2$ layer.

The influence of the Z907 dye on the performance of the P3HT/nc-TiO$_2$ solar cells was studied. Figure 5 shows a semilog plot of the current density *versus* voltage (J-V) characteristics of a nc-TiO$_2$/P3HT solar cell without using the Z907 dye. In the dark, the device behaves like a good diode with a rectification ratio estimated to be 10^3 at ±1 V. Additionally, the turn-on voltage of the nc-TiO$_2$/P3HT solar cell was found to be approximately 0.4 V. These values depend on the energy level alignment between the P3HT and the nc-TiO$_2$ and/or the work function of the bottom and the top electrodes. Under a positive bias voltage (forward bias condition), the electrons are injected from a low work function electrode made of gold, whereas the holes are injected from a low work function electrode made of SnO$_2$:Fn. The holes move toward the junction where the depletion region almost

vanishes when subject to a forward bias condition. Conversely, the negative region of voltage applied on the device produced a low current because of the increase of depletion region and the change in the energy level alignment of the electrodes' work function with respect to the P3HT and the nc-TiO$_2$ device.

Figure 6 shows the log J-V characteristics of the nc-TiO$_2$/P3HT solar cells with a Z907 dye layer. In the dark, the rectification ratio was estimated to be approximately 10^4 at ±1V, which is greater than the rectification ratio of the solar cells without dyes. Additionally, the turn-on voltage of the nc-TiO$_2$/Z907 dye/P3HT was found to be approximately 0.25 V, whereas the turn-on voltage was approximately 0.4 V for the solar cells without the dye. The differences between the two devices in a dark current are attributed to the removal of the depletion region, an interface and the decrease in the shunt

resistance in the dye-containing solar cells. Under a reverse bias condition, the current was very low, because the energy level alignment of the materials was arranged in a way to prevent charge carrier transport through the junction. Under illumination, the two devices were affected by the light falling on them. The zero voltage current was enhanced more than 10^3 times compared with the dark current. At the same time, the rectification ratio was very small in the two devices because of the decrease in the series resistance of the device in the light.
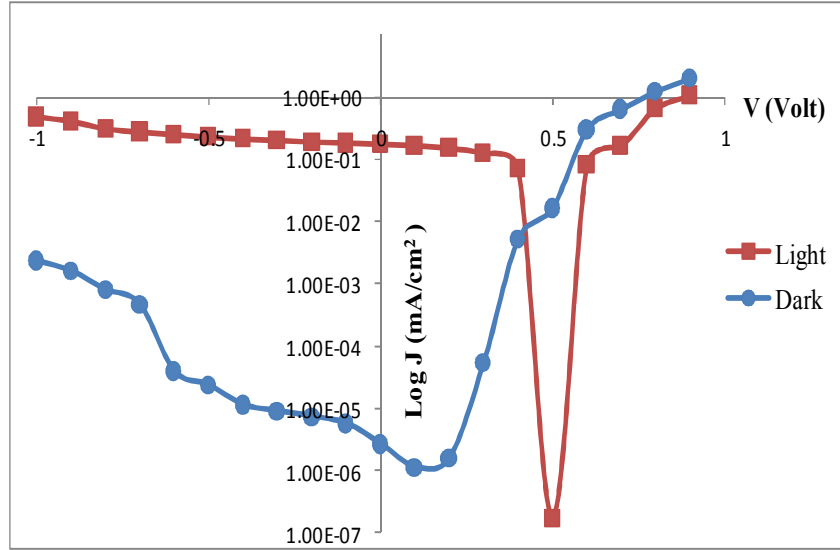
FIG. 5. Log J-V characteristics of the nc-TiO$_2$/P3HT solar cells.
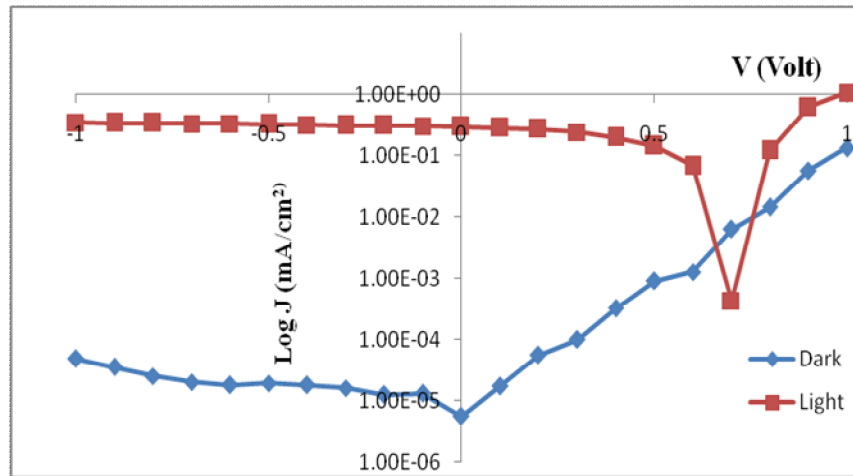
FIG. 6. Log J-V characteristics of the nc-TiO$_2$/Z907 dye /P3HT device.

Figure 7 shows the J-V characteristics of the P3HT/Z907 dye/nc-TiO$_2$ solar cells on a linear scale. This device produced an open circuit voltage (V_{oc}) of 0.7 V, a short circuit current (J_{sc}) of 0.28 mA/cm^2 and a maximum power output (P_{max}) of 0.08 mW/cm^2. The values for the fill factor, FF, and the power conversion efficiency, η, were determined using equations 2 and 3:

$$FF = \frac{P_{max}}{V_{oc} J_{Sc}} \; ; \qquad (2)$$

$$\eta = \frac{P_{max}}{P_L} \; ; \qquad (3)$$

where P_L is the power of the incident light (100 mW/cm^2). The performance of the P3HT/Z907 dye/nc-TiO$_2$ solar cells was observed on 10 devices. For the best device, the power conversion efficiency, η_e, was recorded to be approximately 0.08%, and the fill factor, FF, was 39%. Conversely, the response of the P3HT/nc-TiO$_2$ solar cells without dye to light

was less compared with the solar cells with the dye. Figure 8 shows the J-V characteristics of such a device, which produced a V_{oc} of 0,45 V, a J_{sc} of 0.17 mA/cm^2 and a maximum power output (P_{max}) of 0.035 mW/cm^2. Using equations (2) and (3), the power conversion efficiency was 0.035%, and the fill factor was 45 %.
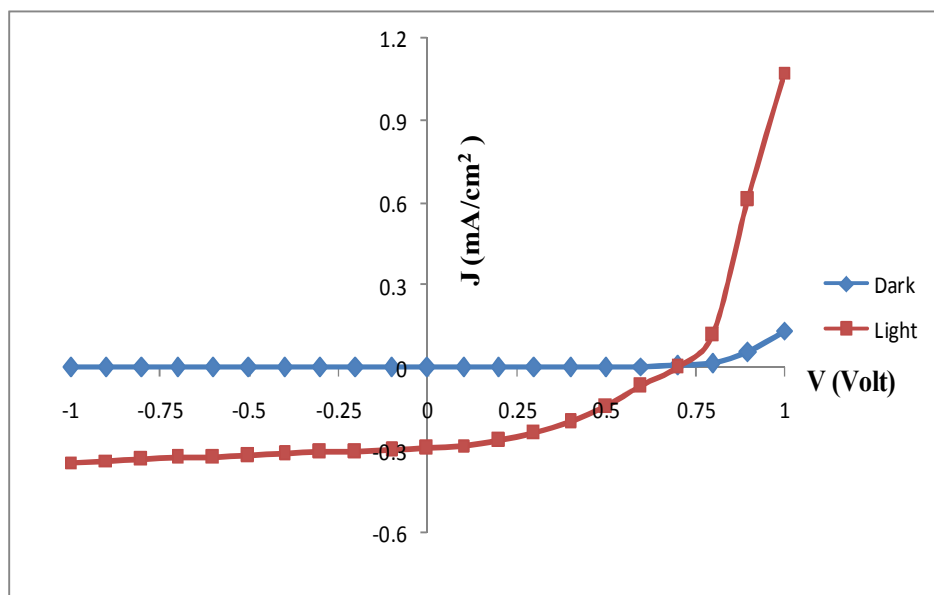
FIG.7. J - V characteristics of nc-TiO$_2$/ Z907 dye/ P3HT solar cells.
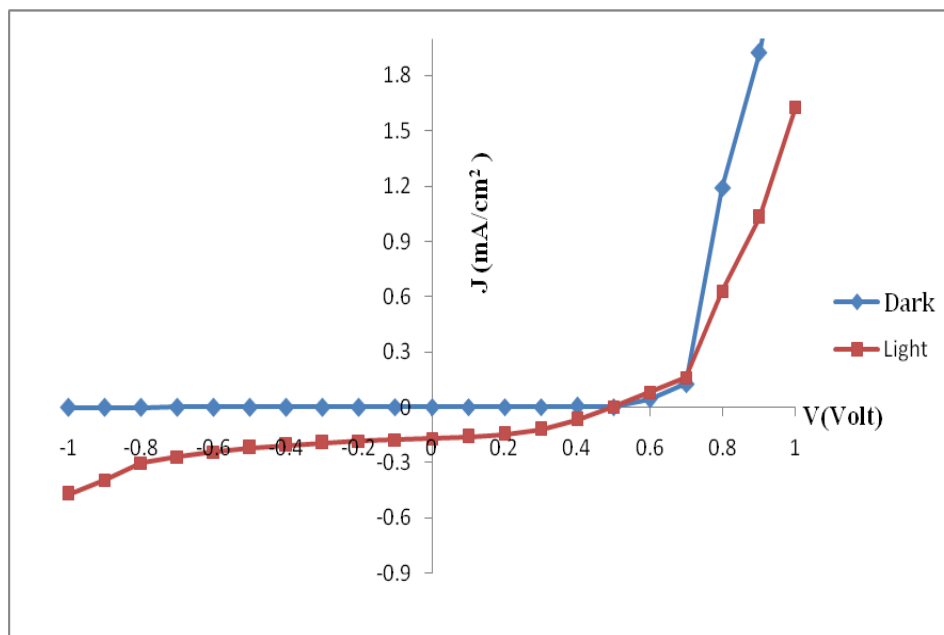
FIG.8. J - V characteristics of nc-TiO$_2$ / P3HT solar cells.

The UV-vis absorption spectra of the SnO$_2$:Fn/nc-TiO$_2$/Z907dye/P3HT, SnO$_2$:Fn/nc-TiO$_2$/P3HT, SnO$_2$:Fn/nc-TiO$_2$ and nc-TiO$_2$/Z907dye are shown in Fig. 9. It can be seen that, compared with the SnO$_2$:Fn/nc-TiO$_2$/P3HT with Z907 dye, the absorbance of the spectra of the SnO$_2$:Fn/nc-TiO$_2$/P3HT decreases in the 380 to 600 nm wavelength region. This result indicates that the Z907 dye improves the absorption of light falling on the device and explains the increase in the power conversion efficiency observed in the SnO$_2$:Fn/nc-TiO$_2$/Z907 dye/P3HT solar cells. This result is similar to those published in [19-20].
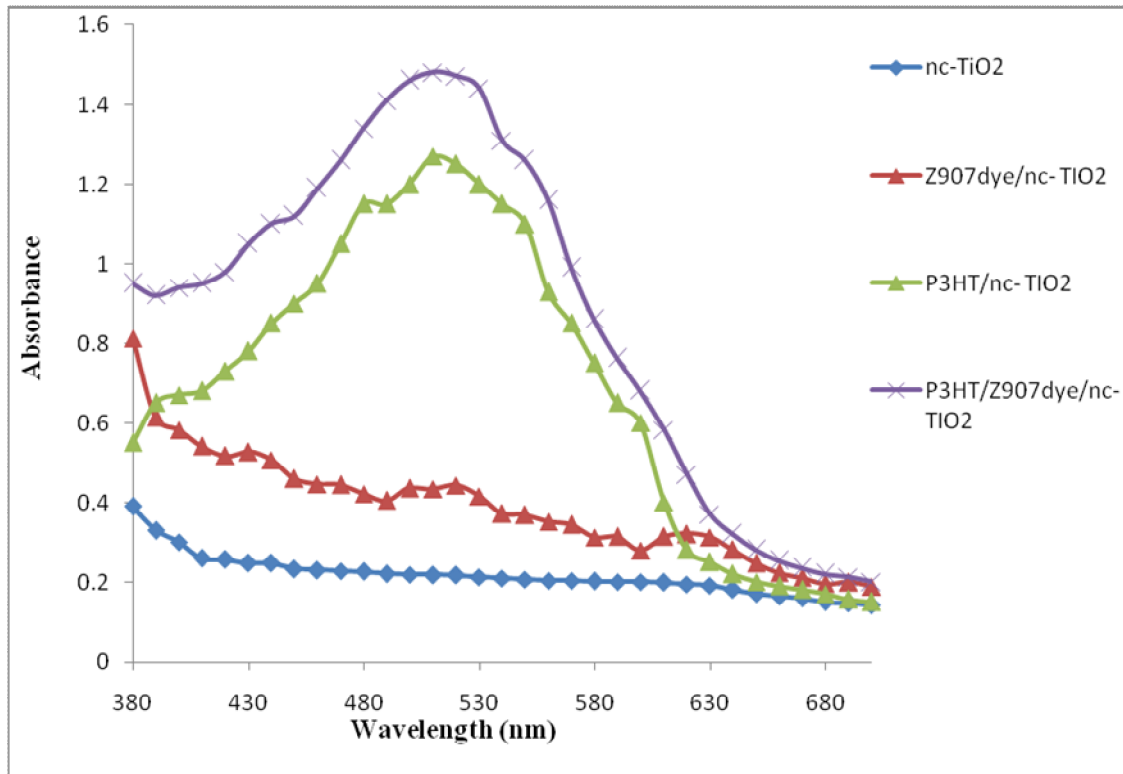
FIG. 9. UV-Vis absorption spectra of the nc-TiO$_2$/Z907 dye /P3HT, nc-TiO$_2$/P3HT, nc-TiO$_2$/Z907 and nc-TiO$_2$ films

Fig. 10 shows the capacitance *versus* loss (conductance/frequency, G/w) curves over a wide range of frequencies for the P3HT/nc-TiO$_2$ solar cells at -1.5 V applied to the SnO$_2$:Fn electrode. At low frequencies (100 Hz to 10 kHz), the measured capacitance decreases because the frequency is less than the relaxation time of the charge carriers. In this case, the junction capacitance starts contributing to the overall capacitance. In the same range of frequency, the decrease of loss is also ascribed to charge carriers, which lag behind the AC field variation at the junction. With a decrease in the frequency, the loss remains almost constant from 100 Hz to 20 Hz. This result is due to a junction capacitance that is dominated by the depletion region capacitance and a reduction of the charge carriers that have accumulated at the junction. At high frequencies (f > 10 kHz), the capacitance represents the geometric capacitance of the device, where the charge carriers hardly follow the AC signal, which is coupled with a decrease in the loss.

In P3HT/dye/nc-TiO$_2$ solar cells, the capacitance *versus* loss curves over a wide range of frequencies are shown in Fig. 11. The low-frequency capacitance is dominated by the junction capacitance, where the diffusion capacitance appears in the absence of the depletion region at the junction. The diffusion capacitance is generated by the accumulation of charge carriers at the interface due to the following: the dye layer easily accumulates at the injection of the charge carriers and the presence of the dipole at the junction [21]. These conditions lead to a decrease in the capacitance to the negative region and increase the loss in a manner that is more than three times than the loss in solar cells without the dye.

The difference in the capacitance measurements of the two devices emphasizes that the Z907 dye modified the interfacial layer between the nc-TiO$_2$ and the P3HT. Additionally, the formation of dipoles by the dye improves the power conversion efficiency by increasing the open circuit voltage from approximately 0.45 to 0.7 V, which agrees with Shyam's work [22]. This increase is accompanied by the appearance of a negative capacitance in the dye solar cells, which indicates a change in the position of the TiO$_2$ conduction band, the accumulation of charge carriers and a reduction in the resistance at the interface.
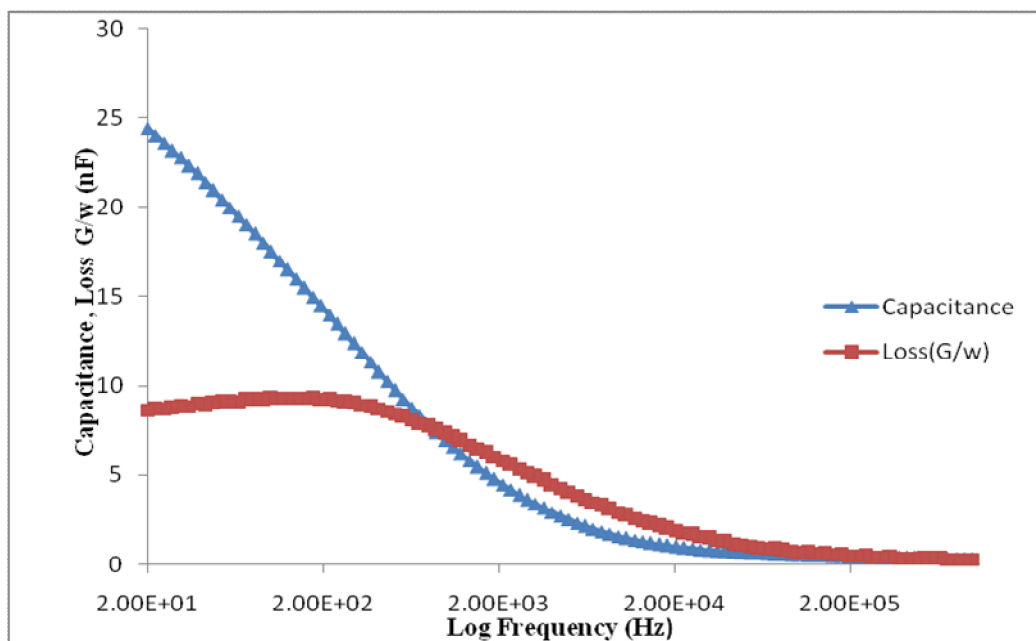
FIG. 10. Capacitance and loss *versus* frequency of SnO$_2$:Fn/nc-TiO$_2$/P3HT/Au solar cells.
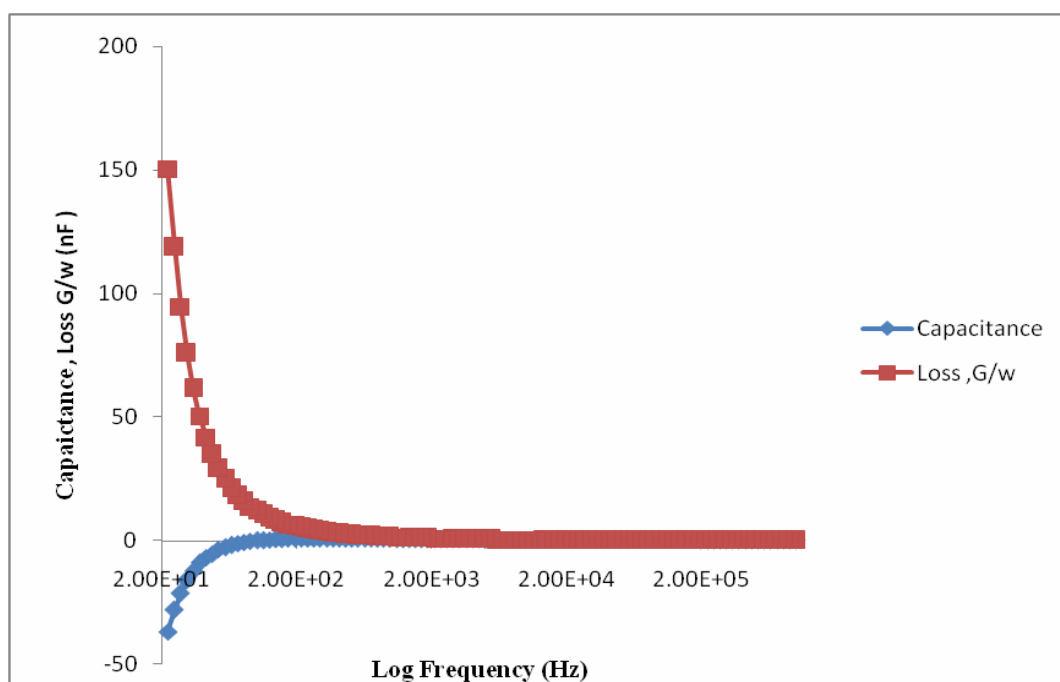
FIG. 11. Capacitance and loss *versus* frequency of SnO$_2$:Fn/ nc-TiO$_2$/Z907 dye /P3HT solar cells

Conclusion

Solar cells with dyes were found to exhibit a combination of a high concentration of charge carriers at the junction, an increase in the short circuit current density and an increase in the power conversion efficiency. These results were ascribed to the modification that occurred by adding the dye layer between the P3HT and the nc-TiO$_2$ layers.

Acknowledgements

References

[1] Oregan, B. and Graetzel, M., Nature, 353 (1993) 737.

[2] Bach, U., Lupo, D., Cornte, P., Moser, J., Weissortel, F., Salbeck, J., Spreitzer and Graetzel, M., Nature, 395 (1998) 583.

[3] Gebeyehu, D., Brabec, C.J., Padinger, F., Fromherz, T., Spiekermann, S., Vlachopoulos, N., Kienberger, F., Schindler, H. and Sariciftci, N., Synth. Met., 121 (2001) 1549.

[4] Beek, W., Weink, N. and Janseen, R., Adv. Mater., 16 (2004) 1009.

[5] Zhang, W., Zhu, R., Li, F., Wang, Q. and Liu, B., J. Phys. Chem. C., 115 (2011) 7038.

[6] Al Dmour, H., Taylor, D. and Cambridge, J., J. Phys. D: Appl. Phys., 40 (2007) 5034.

[7] Gunes, S., Neugebauer, H. and Sariciftci, N., The Electrochemical Society, 12 (2007) 145.

[8] Saleh, N., Al-Tarawneh, S., Al Dmour, H., Al-Taweel, S. and Greaham, J., J. Fluoresc., 6 (2014).

[9] Weishu, J., Lan, Z., Yi Chan, C., Ping, W. and Dia, E., J. Mater. Chem. A., 2 (2014) 8749.

[10] Rahman, M., Umat, A. and Salleh, M., Russian Journal of Electrochemistry, 50 (2014) 1072.

[11] Wang, P., Zakeeruddin, S., Comte, P., Charvet, P., Baker and Graetzel, M., J. Phys. Chem. B., 107 (2003) 14336.

[12] Sung, Y., Xia, J., Cantu, M., Masaki, N. and Yanagida, S., Journal of Photochemistry and Photobiology A: Chemistry, 193 (2008) 77.

[13] Oh Young, J., Chang, D. and Lee, H., Bull. Korean Chem. Soc., 34 (2013) 3183.

[14] Chou, Y., Ko, M. and Yan, M., J. Am. Ceram. Soc., 10 (1987) 70.

[15] Heri, H., Baek, W., Lee, H., Kang, C. and Kim, Y., Journal of Physics: Conference Series, 100 (2008) 082020.

[16] Park, N., Legemaat, J. and Frank, A., J. Phys. Chem. B., 104 (2000) 8994.

[17] Zou, Y., Wang, Z., Lan, X. and Huang, N., Journal of the Korean Physical Society, 55 (2009) 2650.

[18] Cullity, B., "Elements of X-ray Diffraction", (Wesley Publishing Company, Inc., London, 1978).

[19] Yanagida, S., Senadeera, G., Nakamura, K., Kitamura, T. and Wada, Y., J. Photo. Chem. Photo A., 166 (2004) 75.

[20] Wang, C., Li, J., Cai, S., Ning, Z., Zhao, Zhang, Q. and Su, J., Dye and Pigments, 94 (2012) 40.

[21] Westermark, K., Henningsson, A., Rensmo, H., Soodergren, S., Siegbah, H. and Hagfeldt., Chemical Physics, 285 (2002) 157.

[22] Pandey, S., Lee, K., Hayat, A., Ogomi, Y. and Hayase, S., Japanese Journal of Applied Physics, 50 (2011) 06GF08.

Jordan Journal of Physics

ARTICLE

Effect of Dust and Ambient Temperature on PV Panels Performance in Egypt

Ahmed Hamza H. Ali[a], Ahmed. M. Serag ElDin[b] and S. M. Abdel-Gaied[c]

[a]*Department of Mechanical Engineering, Faculty of Engineering, Assiut University, Assiut 71516, Egypt.*
[b]*Energy Resources Engineering Department, Egypt-Japan University of Science and Technology (E-JUST), P.O. Box 179, New Borg El-Arab City, Alexandria 21934, Egypt.*
[c]*Department of Science and Mathematics, Faculty of Science, Assiut University, the New Valley 72111, Egypt.*

Abstract: This study investigated the effects of dust deposition and ambient air temperature on the performance of a thin film photovoltaic module under real outdoor conditions in the humid harsh climate of Egypt. The experimental study investigated the effect of dust deposition and the effect of ambient air dry bulb temperature on the performance of the PV module. Theoretical study predicted the temperature of the PV panels at various metrological conditions in different locations inside Egypt. The study experimental results show that dust deposition has a significant effect on I_{sc} current, while is has less effect on V_{oc} voltage. Dust effect becomes more significant on cloudy days more than on sunny days. The PV modules must be cleaned regularly every 4 days and directly after a dusty storm. The ambient air dry bulb temperature has a significant effect on V_{oc} voltage, while it has less effect on I_{sc} current. The theoretical models results were compared with the experimental results, and good agreement were found. The theoretical results show that the Crystalline PV panels are more affected by the ambient air dry bulb temperature rather than the thin film PV panels.

Keywords: PV panels; performance; Dust; Ambient temperature.

Introduction

Performance of photovoltaic (PV) panels in dry harsh environments is influenced by the ability of the glass cover to transmit solar radiation into the collection surface and the ambient air temperature. The dust particles in the ambient air carried by the wind can deposit on the solar photovoltaic devices external surface and obscure the solar radiation, and, therefore reduce their efficiency. However, only a fraction of the incoming sunlight striking the cell is converted into electrical energy; the remainder of the absorbed energy will be converted into thermal energy in the cell and may cause the junction temperature to rise, which leads to a decrease in efficiency unless the heat is efficiently dissipated to the environment [1].

Moharram et al. [2] investigated experimentally the influence of cleaning PV panels using water and a surfactant using a non-pressurized water system on their performance. They reported that the efficiency of the PV panels decreased by 50% after 45 days of cleaning using non-pressurized water, while the efficiency remained constant when a mixture of anionic and cationic surfactants was used for cleaning. In their study, they did not indicate the relation between the weather conditions like wind speed, relative humidity and ambient air temperature and the cleaning process. Kaldellis and Fragos [3] experimentally investigated the side effect of the atmospheric air pollution on the degradation of photovoltaic (PV) cells'

performance, by using two identical pairs of PV-panels. The first tested cell was clean and the second one was artificially polluted with ash. They carried out a series of systematic measurements of PV panel current intensity, voltage output and incident solar radiation simultaneously for the clean and the polluted PV-panels. They reported that the deterioration of the PV-panels' performance was almost 30% energy reduction per hour or 1.5% efficiency decrease (in absolute terms) for the case when ash deposition on the panels' surface reached up to 0.4 mg/cm^2. In their study, they did not mention the coverage area, particle diameter, dust composition and the relation between weather conditions and dust deposition characterization. Jiang et al. [4] experimentally studied the dust deposition onto different types of solar PV panels and the corresponding efficiency degradation under various conditions. Their experiment was designed and conducted inside the laboratory with a sun simulator and a test chamber. They reported that dust pollution on PV panel surface has a significant impact on PV panel output. However, as dust deposition density increased from 0 to 22 g/m^2, the corresponding reduction of PV panel output efficiency grew from 0 to 26%. The reduction in the PV panel efficiency has a linear relationship with the dust deposition density, and the difference caused by cell types was not obvious. In their study, they did not take into account the effect of inclination angle, weather conditions, dust coverage area and dust composition.

Teo et al. [5] designed an experiment to investigate a hybrid photovoltaic/thermal (PV/T) solar system. To actively cool the PV cells, they designed a parallel array of ducts with inlet/outlet manifold for uniform airflow distribution, where it was attached to the back of the PV panel. They performed their experiments with and without active cooling. A linear trend between the efficiency and temperature was found. Without active cooling, the temperature of the panel was high and solar cells could only achieve an efficiency of 8–9%. However, when the panel was operated under active cooling condition, the temperature dropped significantly leading to an increase in the efficiency of solar cells to between 12% and 14%. A heat transfer simulation model was developed to compare to the actual temperature profile of PV panels, and good agreement between the simulation and the experimental results was obtained. Krauter [6]

proposed experimentally numerous ideas to reduce cell surface temperature by utilizing a flowing film of water on the panel front. He used water, with a refractive index of 1.3, as a viable intermediary between glass (n_{glass}=1.5) and air (n_{air}=1.0). In addition to help keeping the surface clean, water reduces reflection by 2–3.6%, decreases cell temperature up to 22 ^{0}C and the electrical yield can return a surplus of 10.3%; a net-gain of 8–9% can be achieved even when accounting for power needed to run the pump. Tonui et al. [7] investigated the performance of two low cost heat extraction improvement modifications in the channel of a PV/T air system to achieve higher thermal output and PV cooling so as to keep the electrical efficiency at an acceptable level. They suggested the use of a thin flat metal sheet suspended at the middle or finned back wall of an air channel in the PV/T air configuration. In addition, they developed a theoretical model and validated it against experimental data. They concluded that a good agreement between the predicted results and measured data was achieved. After that, they used the validated model to study the effect of the channel depth, channel length and mass flow rate on electrical efficiency, thermal efficiency, PV cooling and pressure drop for both improved and typical PV/T air systems, and their results were compared. They observed from both experimental and theoretical results that the suggested modifications improve the performance of the PV/T air system.

The present study aims to clarify the effect of both dust deposition and ambient air temperature on PV panel performance degradation. Furthermore, this study will provide a recommendation for surface cleaning schedule for the PV panels in Borg El-Aarb Area (Support to EJUST solar power generation). In addition, this study will provide a recommendation for PV system designers regarding which type of PV panels is suitable in a given area according to ambient temperature levels in this area. These aims will be achieved by a methodology of two parts; the first is experimental work to study the effect of both dust deposition and ambient air temperature on the performance of PV panels. The second part is a theoretical work to predict the performance of PV panels at different ambient air temperatures.

Thermal Model

Instead of air as the coolant of the panels, water can be used in order to absorb more heat and to cool the panels more effectively. It transforms the sun's radiation to electrical energy and simultaneously absorbs the heat from the panels. By this way, the panels are working at lower temperatures (higher efficiency). Fig. 1 shows the components of the PV/water cooling circuit. The working fluid is water flowing below the aluminum plate.
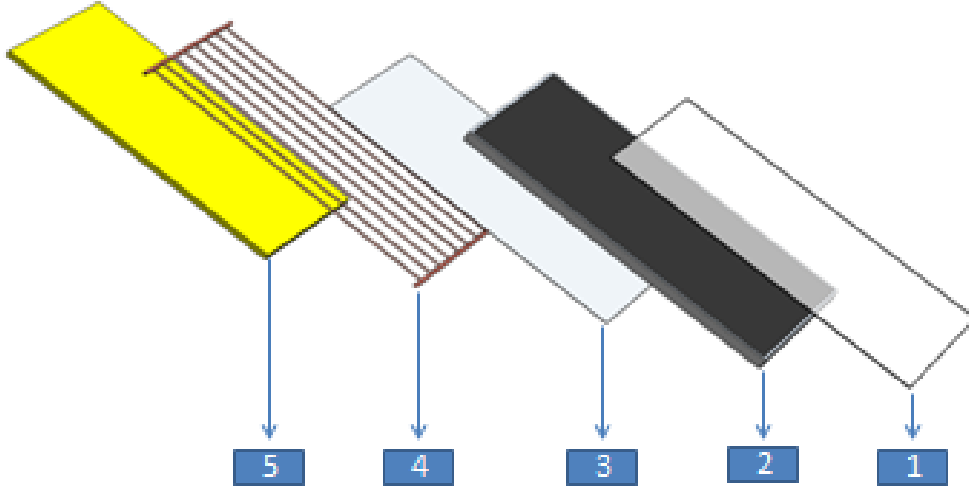
FIG.1. PV/T components (1) Glass cover (2) PV cell with EVA and water proof layer (tedlar) (3) Aluminum absorber plate (4) Copper parallel pipes circuit (5) Wool glass insulation layer.

In order to derive the energy balance equation for each component of the PV/water cooling system, the following assumptions are made:

1. Heat capacity of solar cell materials, tedlar and insulation (wool) is neglected.

2. Heat transfer through aluminum plate is neglected.

3. Transmittivity of ethyl vinyl acetate (EVA) is approximately 100%.

4. Temperature variation along the thickness is negligible.

5. Water flow between the tedlar and insulation material is uniform.

6. The system is in quasi-steady-state condition.

7. Contact surface resistance is neglected.

8. Heat conduction is one-dimensional.

The thermal model will be used to evaluate the parameters such as cell temperature, thermal gain, outlet water temperature and thermal efficiency. Energy balance equations for the components in the integrated PV/T system; namely, PV panels, back surface of the tedlar and water flow below the tedlar, are written as derived by Breu et al. [8]. Applying energy balance equation on PV cell:

$$\left. \begin{array}{l} A\tau_g \left[\alpha_C I \beta_C + (1-\beta_C)\alpha_T I \right] = \\ AU_T(T_C - T_a) + A_T h_T(T_C - T_{bs}) \\ + dA\eta_C \tau_g I \beta_C \alpha_C \end{array} \right\} \quad (1)$$

Applying energy balance equation on back surface of the tedlar:

$$A_T h_T \left(T_C - T_{bs} \right) = A h_W \left(T_{bs} - T_W \right) \quad (2)$$

Applying energy balance equation on flowing water element:

$$\left. \begin{array}{l} h_W \left(T_{bs} - T_W \right) b dx = \\ \dot{m}_W C_W \left(\dfrac{dT_W}{dx} \right) dx + b dx U_b \left(T_W - T_a \right) \end{array} \right\} \quad (3)$$

The software package used to code the model is MATLAB version R2011a. The power simulation (PSIM) software is used to identify and predict the electrical performance of the photovoltaic panels working under different weather conditions.

Experimental Set-up

To study the effect of dust deposition and ambient air temperature on thin film photovoltaic panels performance, the test rig shown in Fig. 2 is used. Two statistically

checked identical pairs of PV-panels (located at the same area) both being south oriented and adjusted at the same inclination 30^0 with the horizontal (latitude of Borg Al-Arab) are used. The experimental measurements are carried out at the roof of the Laboratories of Energy

Resources Engineering Department located at the campus of the Egypt-Japan University of Science and Technology (E-JUST) in New Borg Al-Arab, Alexandria, Egypt (longitude/latitude: E 29° 42' /N 30° 55').
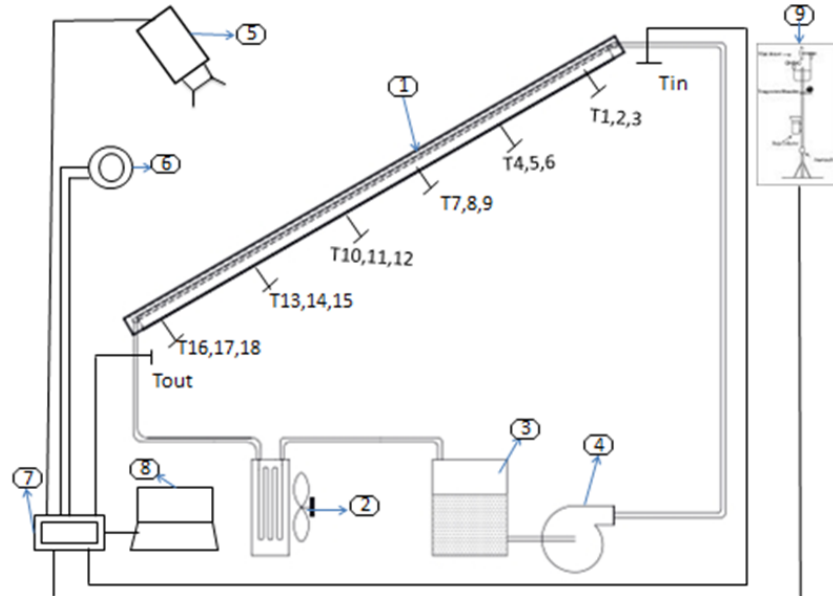
FIG. 2. Schematic diagram of experimental setup consisting of: (1) Two identical thin film PV-panels and 20 thermocouples type (T), (2) Heat exchanger and DC fan, (3) 10 liter tank, (4) Peristaltic pump, with the following measuring instruments, (5) Infrared camera, (6) Pyranometer, (7) Data logger, (8) Laptop (9) Weather station.

1- Photovoltaic Panels

For dust deposition experiment, two CIS (copper, indium and selenium) PV panels are used in the measurements; the first is used to investigate the effect of dust deposition on the output power, while the second is always kept clean by regular daily manual cleaning with surfactant and water mixture, where its output

power is used as a reference. For investigating the effect of ambient air temperature on the panel performance, one PV panel is cooled while the other kept without cooling. The main specifications of the panels are listed in Table (1).

TABLE 1. PV panel specifications used in this study.

Model	SF80-A
Power-generating element	CIS (thin-film)
(P_m) nominal maximum output	80W
Nominal operating voltage maximum output (VP_m)	41.0V
Nominal maximum power current (I_{pm})	1.95A
Nominal open-circuit voltage (V_{oc})	56.5V
Nominal short-circuit current (I_{sc})	2.26A
Gross weight	12.4kg
Overall dimensions, in mm (W × L × D)	641 × 1,235 × 35

2- Dust Deposition Measurement Method

To measure the rate of dust deposition on the solar cell surface as a function of time, 75x22 mm glass slides are fixed side by side with the panels at the same level. Therefore, the

deposition dust on the solar cell PV surface is almost the same as deposited on the glass slide surface, where both have the same environmental conditions.

116

3- Cooling System Set-up

To study the effect of ambient air temperature on the performance of thin film photovoltaic panels, one panel is cooled by an active closed loop water cooling circuit. The circuit consists of an aluminum absorber plate, parallel copper tube heat exchanger, a pump, 10 liter water tank and air cooled heat exchanger with DC fan as shown in Fig. 2. The cooling circuit consists of 8 tubes and 2 headers made of copper with a tube spacing of 5 cm and a diameter of 0.5 inch, while the absorber which is made of red copper (or aluminum plate) has a diameter of 0.25 inch. The parallel copper tubes are fastened on the surface of the aluminum plate by means of ligament sheets. In order to increase the contact surface area and enhance the heat transfer process, thermal conductive silicon past has been used between the copper tubes and the aluminum plate. In addition, two types of thermal insulation have been used; insulation foam and glass wool insulation of 5 cm thickness in order to decrease the heat losses from the copper tubes to the atmosphere.

Results and Discussion

a- Effect of Dust Deposition on PV Panel Performance

(1) Characterization of the Deposited Dust

The main factor affecting dust deposition rate on a surface is the weather data and conditions that are wind speed and direction, relative humidity and dew point. In this study, the dust deposition density is determined by measuring the weight of a glass slide before and after dust deposition. The picked glass slides from the experimental set-up are prepared and scanned by the Scanning Electronic Microscope (SEM) before being coated with golden film to obtain images as shown in Fig. 3. The presented images of the glass slide are picked up every four day intervals except for the period from 3 to 9 of April which was 6 days [the image of Fig. 3(a) is after 4 days, (b) after 8 days from the start of the experiment and so on]. From the experiment… conducted at the period from 14/3/2013 to 22/3/2013 (after 8 days), there was a significant increase in dust coverage area fraction. It reached 20.45% of the total photovoltaic surface area with a dust deposition density of 0.15 mg/cm^2.

This is due to the remarkable activity in the movement of dust-laden wind during this period, as the wind speed reached 8.27 m/s, relative humidity (RH) reached 74%, with an average solar radiation intensity of 604.84 W/m^2. This result is based on the fact that dust promotes dust, and the higher relative humidity (close to the sea conditions) leads to facile the dust coagulation. After that date, the dust coverage area fraction is decreased to reach about 10.27%, while the dust deposition density increased to 0.27 mg/cm^2 (after 12 days) due to lower relative humidity that reached 57.29% and moderate high wind speed that reached 5.38m/s. As the time passed, the dust coverage area fraction and dust deposition density increased again to reach 24.40% and 0.37 mg/cm^2 (after 16 days) as the weather condition of high RH reached 72.15% at a relatively low wind speed of 3.14m/s. With progress of the time, the dust coverage area fraction increased slightly and reached 25.23% (after 20 days), while dust deposition density decreased to 0.33 mg/cm^2.

(a) (after 4 days)	(b) (after 8 days)

(c) (after 12 days)

(d) (after 16 days)

(e) (after 20 days)

(f) (after 26 days)
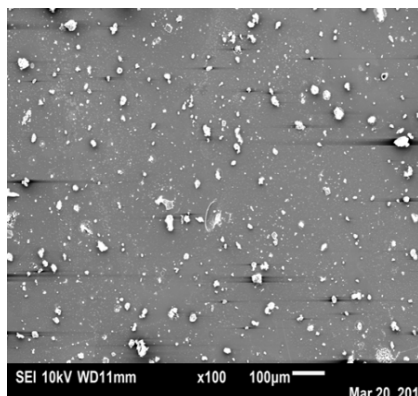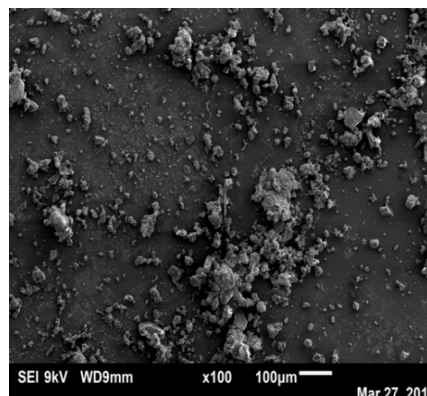
(g) (after 30 days)
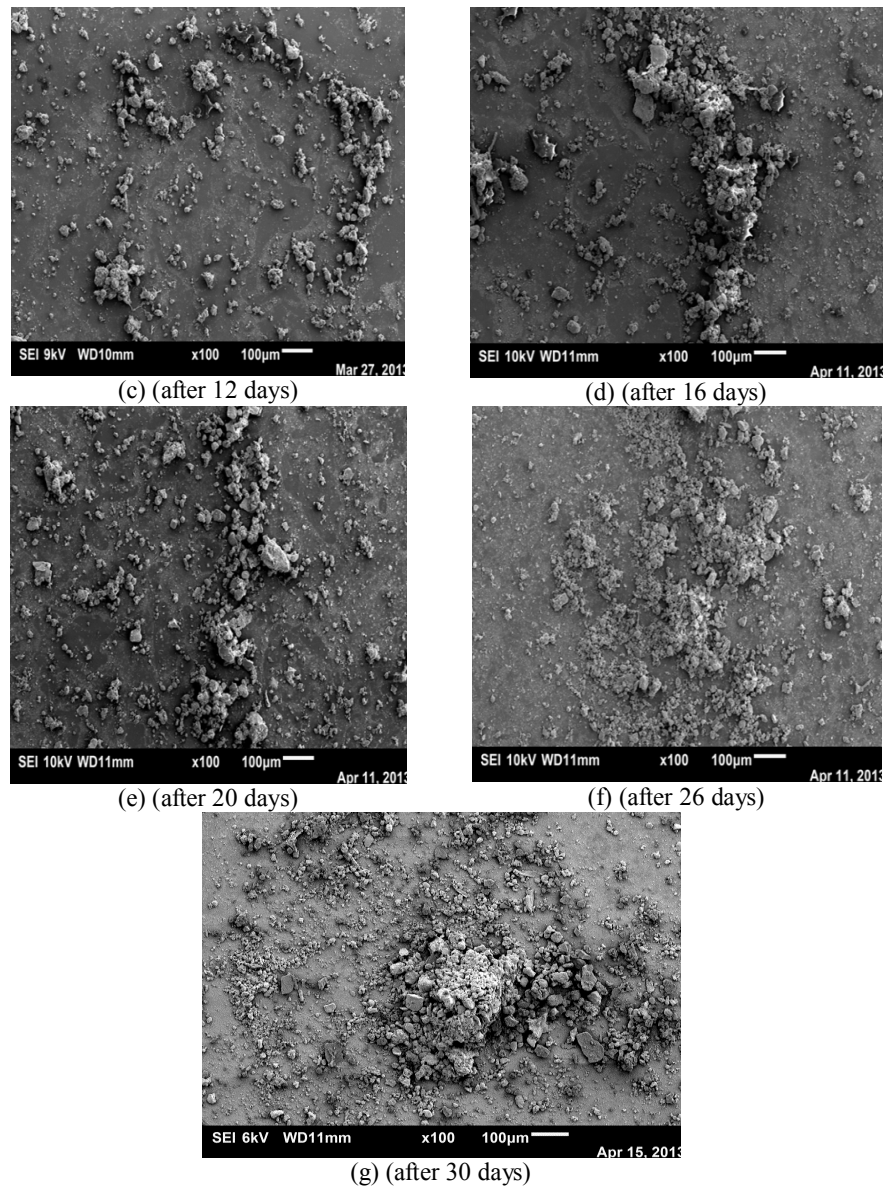
FIG.3. SEM pictures for deposition on PV panel outer surface.

(2) Effect of deposited dust on the PV Panel Performance

Time variations of measured values for panels efficiency, output daily energy, daily solar energy intensity, normalized short circuit current (I_{sc} dusty/I_{sc} clean) and normalized open circuit voltage (V_{oc} dusty/V_{oc} clean) of the two panels are shown in Figs. 4 and 5. The presented data clearly shows that dust has a significant effect on the PV panel short circuit current and the output power. As can be seen from the figure, as the dust deposition density increased from 0 to 0.28 mg/cm^2 after 26 days without cleaning, the value of I_{sc} decreased from 100% to 83.39 % compared with clean panel value, and,

the power degradation (or decrease) reached 12.11 %. This degradation is due to the effect of dust coverage area fraction which reached 26 % during this period. Moreover, the voltage degradation (decrease) due to deposited dust is also clear in the presented results as shown in Fig. 5. However, the reduction in V_{oc} from 100% to 99.7% is slight when compared with that in I_{sc} value. One can conclude that dust deposition has a significant effect on I_{sc} and less effect on V_{oc}. In addition, dust effect is more significant on cloudy days than on sunny days. Finally, PV panels must be cleaned regularly every 4 days and directly after a dusty storm.
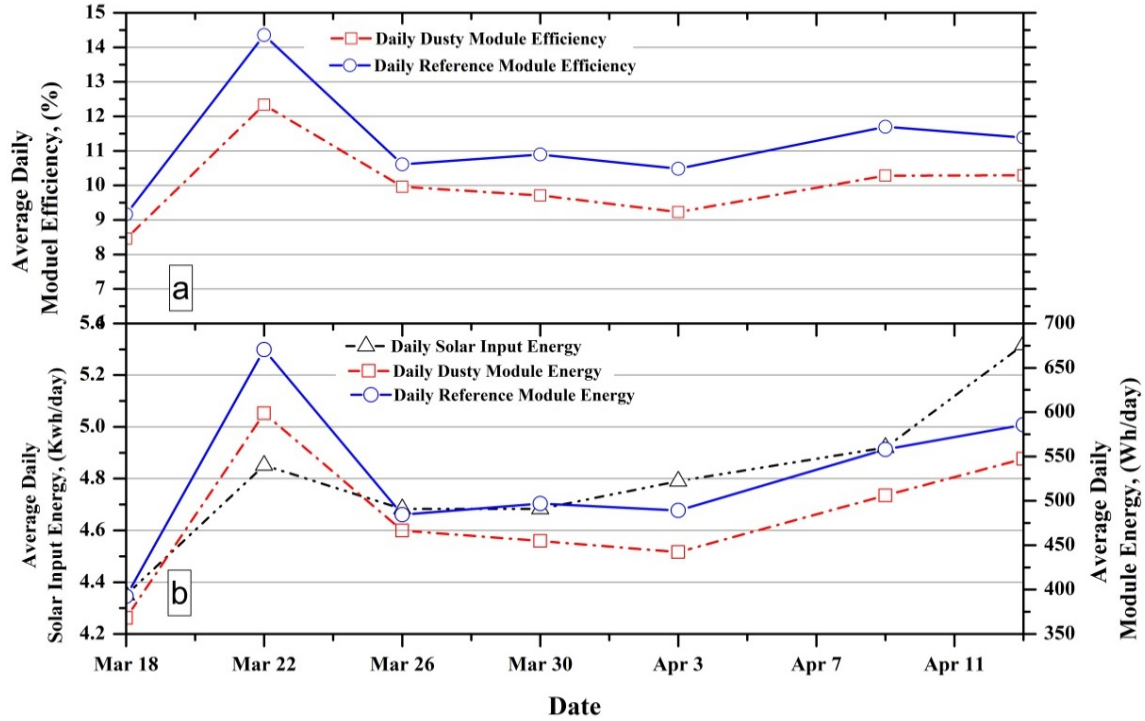
FIG.4. Comparison of panel performance with date variation.
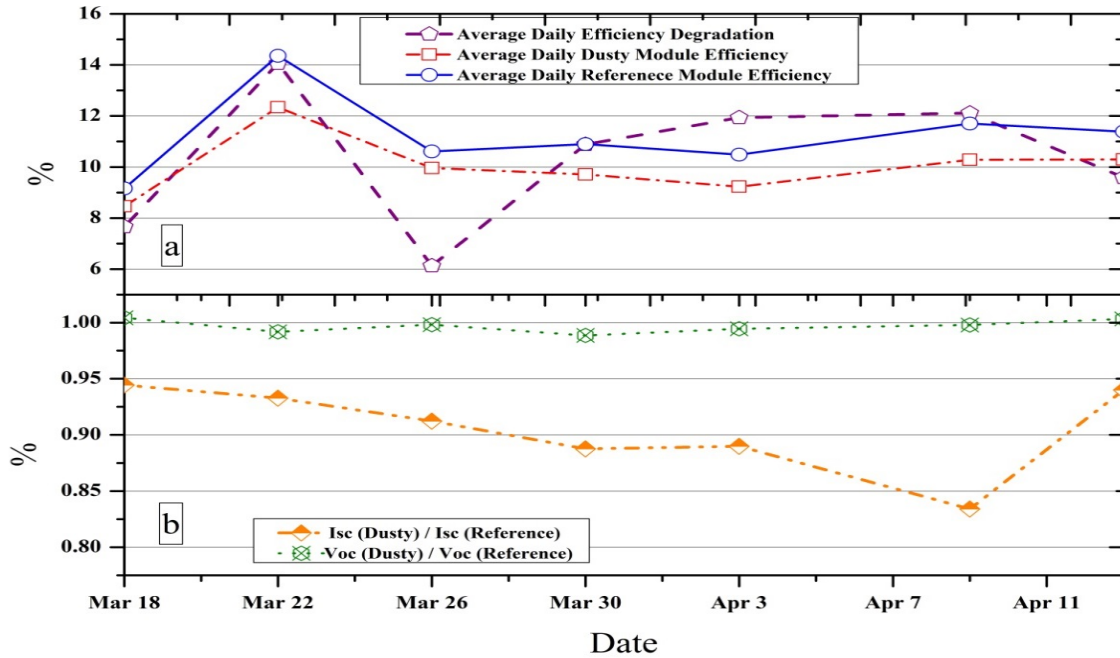
FIG.5. Time variation of experimental values for the panels' efficiency.

b- Effect of PV Panel Temperature on Its Performance Parameters

To investigate the effect of ambient air temperature on the performance of thin film photovoltaic panels, two identical panels were used; one had a cooling system and the other was without cooling. Forced water cooling is more effective than passive or active air cooling; thus, cooling is carried out using a closed loop water cooling circuit with volume flow rate of 0.06 l/sec/m^2. The outputs from the two PV panels are measured simultaneously and compared to illustrate the degradation in power and efficiency. Fig. 6 shows infrared images of PV outer surface temperature. An infrared camera

119

was used to take a thermal image of the two panels simultaneously every one hour between 10:00 AM and 02:00 PM. This was followed by using an infrared analyzer software package to determine temperature distribution of the image of the outer surface of the panels and quantitative values for both panels with cooling and without cooling. From the thermal images quantitative values, the average and local

temperature values are shown in Fig. 6. From this figure, it is clear that the surface temperature decreases with time. From these thermal images, it is clearly seen that there is a poor uniformity of temperature distribution on the surface of the cooled panel; this may be attributed to poor contact (high thermal contact resistance) between the absorber plate and the back of the panel.

(a) 10:00 AM

(b) 11:00 AM

(c) 12:00 PM

(d) 01:00 PM

(e) 02:00 PM
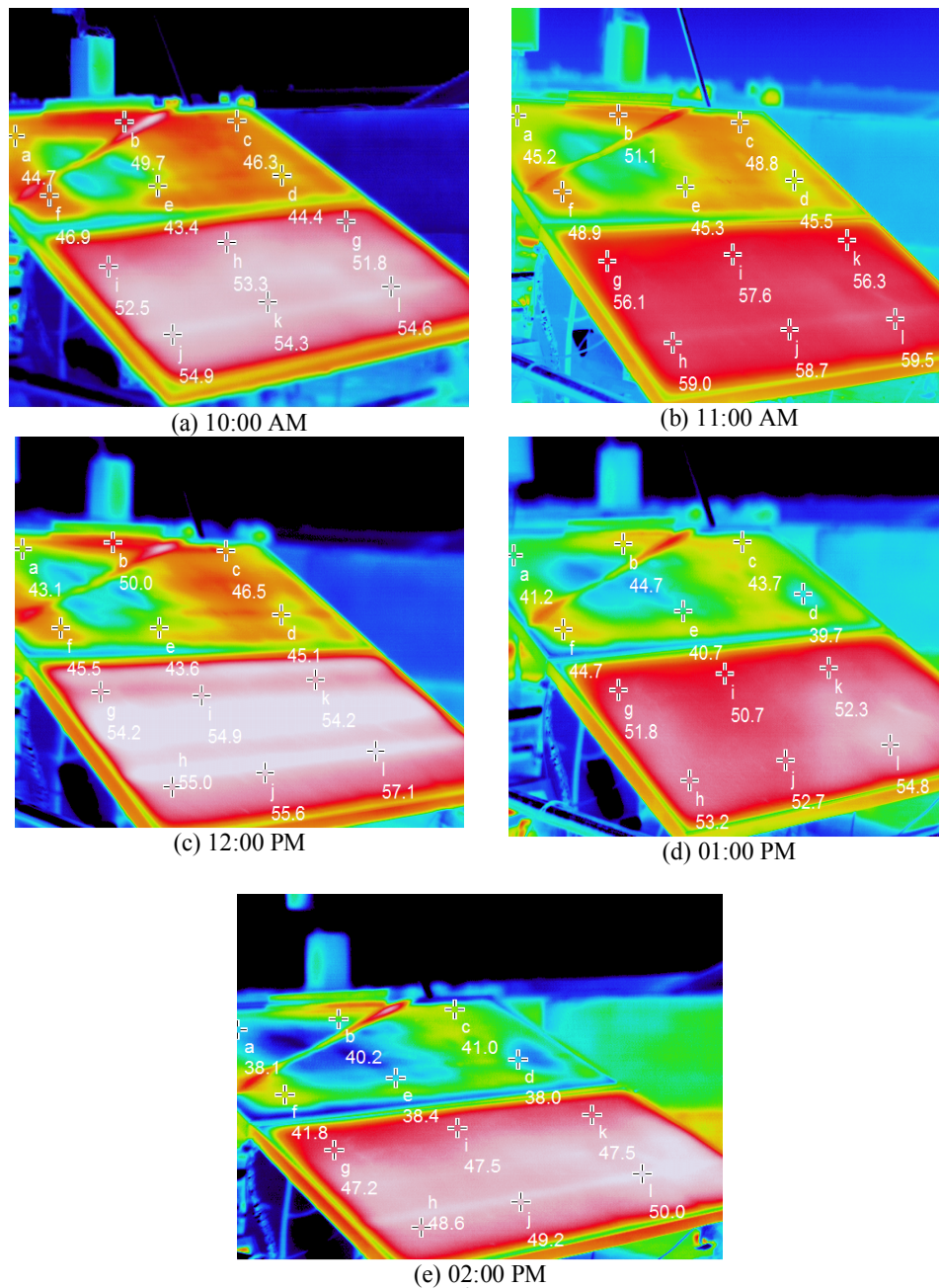
FIG. 6. Infrared camera photos of 0.06 l/sec/m^2 flow rate taken every hour starting at 10:00 AM.

120

To investigate the effect of PV panel cooling on panel voltage, current time variation curves for both panels are shown in Fig. 7 and 8. From presented results, one can see that the PV panel cooling process has a significant effect on V_{oc}, while it has less effect on I_{sc}. In quantitative values, for a water volume flow rate of 0.03 l/sec/m^2, the ratios of (Isc(without cooling)/Isc (with cooling) and (Voc (with out cooling)/Voc (with cooling)) are

100% and 96%, respectively, so there is no degradation in I_{sc}, but there is a 4% increase in V_{oc}. Similar to the previous flow rate, for the other two flow rates (0.04, 0.06 l/sec/m^2), the ratio values of I_{sc} and V_{oc} are (100% and 94.8%) and (100% and 94.7%) with 5.2% and 5.3 % increase in V_{oc}, respectively. As the volume flow rate increases V_{oc} increases. It can be concluded that ambient air temperature has a significant effect on V_{oc} while it has a less effect on I_{sc}.
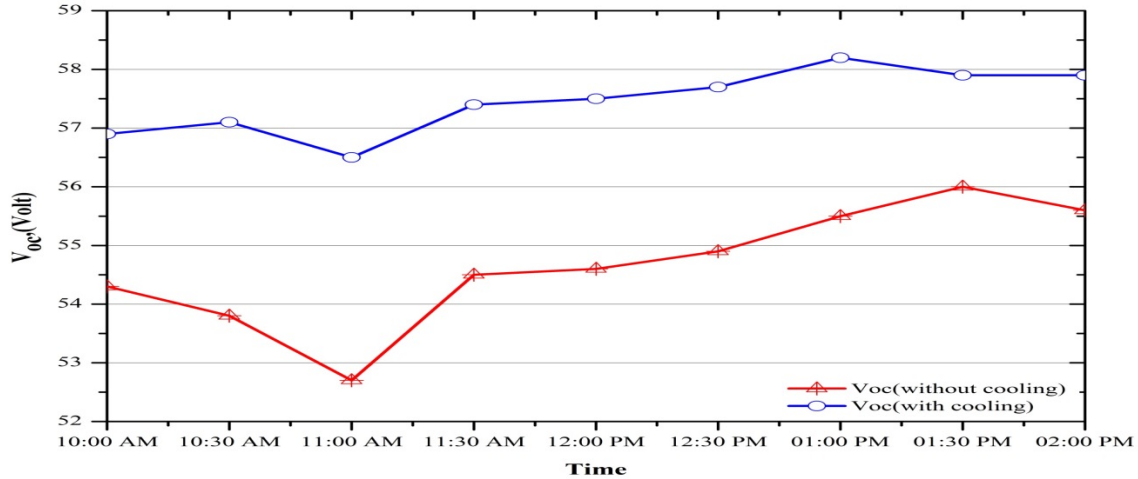
FIG.7. V_{oc} time variation.
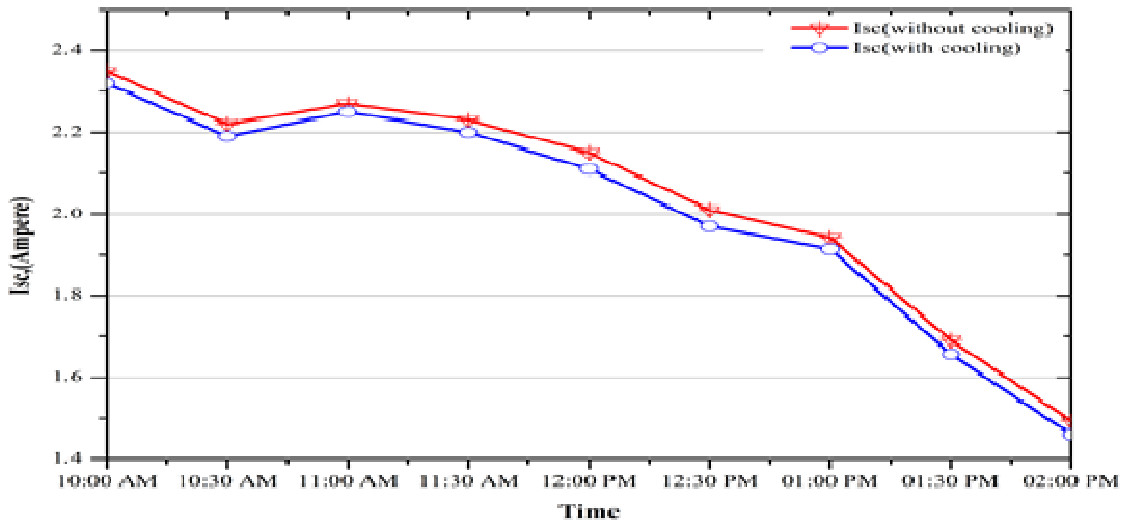
FIG.8. I_{sc} time variation.

Theoretical Results Validation

a)   Electrical Model Verification

Fig. 9 indicates I-V characteristics comparison between model and experimental results for both panels at flow rates of 0.06, 0.04, 0.03 l/sec/m^2, respectively. From this figure, one

can conclude that there is a good agreement between model and experimental data with a maximum error of 11.6 % and a correlation coefficient of 99.5 %.
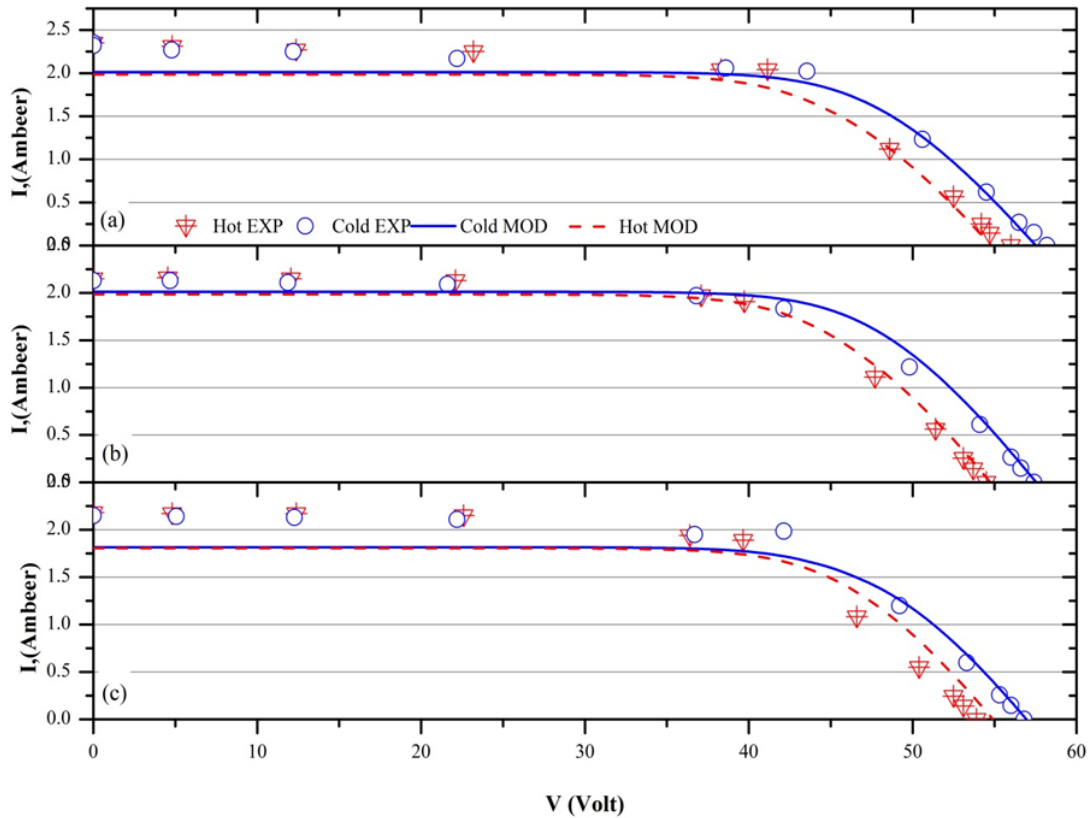
FIG. 9. I-V curve verification for (a) 1 Sept (0.06 l/sec/m^2). (b) 4 Sept(0.04 l/sec/m^2). (c) 11 Sept (0.03 l/sec/m^2).

b) Effect of Ambient Air Temperature on Performance of Different Types of PV Panels

This section investigates the effect of ambient air temperature on performance of three different types of solar cell polycrystalline, monocrystalline and thin film solar cells as predicted by thermal and electrical models. This predicts the characteristic parameters of each panel such as: cell temperature, P$_{max}$ and efficiency for the cases of PV panels with cooling and without cooling. In order to provide a recommendation to the designer and consumers of which type of PV panel is suitable at different locations in Egypt; in Upper Egypt, North of Egypt and Delta, where each region has different meteorological conditions according to efficiency and power output.

TABLE 2. Meteorological data for Alexandria, Cairo and Aswan

	Alexandria	Cairo	Aswan
Solar radiation(w/m^2)	730	770	800
Ambient air temperature	30	34	41
Wind speed(m/sec)	3.7	3.7	4.4

c) Electrical Model Results

Fig. 10 indicates that cooling has a significant effect on monocrystalline and polycrystalline photovoltaic panels maximum power output with a maximum power improvement up to 41.84% for Polycrystalline and 30.54 % for monocrystalline panels. On the other hand, thin film has been affected by a percentage of 7.71% at Aswan. This indicates that thin film panels are less affected by temperature rather than the other two types.
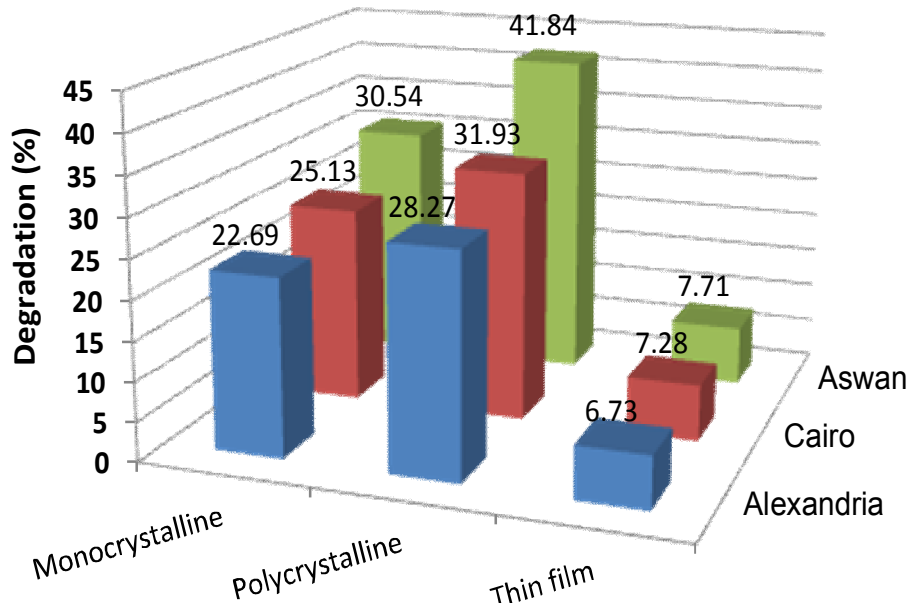
FIG. 10. Maximum power improvement due to cooling effect for three PV panels at different three locations.

Conclusions

This study has investigated experimentally the effects of dust deposition and ambient air temperature on the performance of thin film photovoltaic panels under real outdoor conditions in the humid harsh climate of Borg Al-Arab in Alexandria Egypt. Dust deposition effect has been investigated during a period of remarkable wind activity. The experiments for studying the effect of ambient air temperature on the performance of PV panels have been conducted during the period where there was a remarkable increase in ambient air temperature. Furthermore, two theoretical models were accomplished. The first model is a mathematical one to predict temperature distribution along the photovoltaic panel outer and lower surfaces at various meteorological conditions in different locations in Egypt. The second model is to investigate the PV panel electric characteristics and performance by using PSIM simulation package at different ambient air dry bulb temperatures and incident solar radiation values. Both models output results are verified with experimental results.

The main conclusions from the obtained results in this study are as follow:

- The experimental results show that:

  • Dust deposition has a significant effect on I_{sc} current, with a less effect on V_{oc} voltage.

  • Dust effect becomes more significant on cloudy days than on sunny days.

  • The PV panels must be cleaned regularly every 4 days and directly after a dusty storm in Borg Al-Arab region in the period from 13 of March to 14 of April.

  • The ambient air dry bulb temperature has a significant effect on V_{oc} voltage with a less effect on I_{sc} current.

- The theoretical results have been compared with the experimental results, and good agreement prevailed.

- The theoretical results show that:

  • The crystalline PV panels are more affected by the ambient air dry bulb temperature rather than thin film PV panels.

  • Based on Egypt meteorological conditions as well as the cost performance results, it can be recommended to use crystalline PV panels in Alexandria and Cairo zones, while using thin film PV panels in Aswan area is preferred in case of no cooling for crystalline PV panels. Therefore, in case that of PV panels cooling system is used, the crystalline PV panels become more cost-effective than using thin film PV panels in hot areas.

References

[1] Markvart, T. and Castaner, L., "Practical Handbook of Photovoltaics: Fundamentals and Applications", (2003).

[2] Moharram, K.A., Abd-Elhady, M.S., Kandil, H.A. and El-Sherif, H., Energy Conversion and Management, 68 (2013) 266.

[3] Kaldellis, J.K. and Fragos, P., Journal of Cleaner Production, 19(4) (2011) 311.

[4] Jiang, H., Lu, L. and Sun, K., Atmospheric Environment, 45(25) (2011) 4299.

[5] Chow, T.T., Sol. Energy, 75(2) (2003) 143.

[6] Krauter, S., Solar Energy Materials and Solar Cells, 82(1–2) (2004) 131.

[7] Tonui, J.K. and Tripanagnostopoulos, Y., Sol. Energy, 81(4) (2007) 498.

[8] Breu, F., Guggenbichler, S. and Wollmann, J., "Fundamentals of Photovoltaic Panels and their Applications", (Vasa, 2008).

Jordan Journal of Physics

REVIEW ARTICLE

Fowler-Nordheim Plot Analysis: A Progress Report

Richard G. Forbes[a]**, Jonathan H. B. Deane**[b]**, Andreas Fischer**[c] and
Marwan S. Mousa[d]

[a] *Advanced Technology Institute & Department of Electronic Engineering, Faculty of Engineering and Physical Sciences, University of Surrey, Guildford, Surrey GU2 7XH, UK.*

[b] *Department of Mathematics, Faculty of Engineering and Physical Sciences ,University of Surrey, Guildford, Surrey GU2 7XH, UK.*

[c] *Institut für Physik, Technische Universität Chemnitz, Germany.*

[d] *Department of Physics, Mu'tah University, Al-Karak 61710, Jordan.*

Abstract: The commonest method of characterizing a cold field electron emitter is to measure its current-voltage characteristics, and the commonest method of analyzing these characteristics is by means of a Fowler-Nordheim (FN) plot. This tutorial/review-type paper outlines a more systematic method of setting out the Fowler-Nordheim-type theory of cold field electron emission, and brings together and summarizes the current state of work by the authors on developing the theory and methodology of FN plot analysis. This has turned out to be far more complicated than originally expected. Emphasis is placed in this paper on: (a) the interpretation of FN-plot slopes, which is currently both easier and of more experimental interest than the analysis of FN-plot intercepts; and (b) preliminary explorations into developing methodology for interpreting current-voltage characteristics when there is series resistance in the conduction path from the high-voltage generator to the emitter's emitting regions. This work reinforces our view that FN-plot analysis is best carried out on the raw measured current-voltage data, without pre-conversion into another data format, particularly if series resistance is present in the measuring circuit. Relevant formulae are given for extracting field-enhancement-factor values from such an analysis.
Keywords: Cold field electron emission; Fowler-Nordheim plot analysis.

1. General Introduction

Field electron emission (FE) is the field induced emission of electrons from a solid or liquid emitter. Field electron sources have a number of actual or potential applications, including (in their single-tip form) small bright sources for electron microscopes and similar electron beam instruments, and (in their large-area form) extended sources for electronic devices, microwave generators or spacecraft neutralizers. FE is also a potential primary cause of electrical breakdown in vacuum and needs to be understood so that breakdown can be avoided. There is a technological need for reliable characterization of field emitters.

The commonest method of investigating emitter behaviour is to measure current-voltage (i_m-V_m) characteristics and extract one or more characterization parameters from a Fowler-Nordheim (FN) plot (i.e., a plot of the form $\ln\{i_m/V_m^2\}$ vs $1/V_m$, or equivalent using other variables). In recent

years, the authors of this paper have been developing theory aimed at improving the methodology of FN-plot analysis. In detail, this has turned out to be a very intricate and algebraically complicated problem, far more than originally expected. It has involved repeated improvement and reformulation of theoretical approaches, as details of the overall problem become clearer.

The present paper is, in essence, a tutorial/progress report relating to FN plot analysis. It brings together in a single place and summarizes our previous work on this topic. It aims to set out relevant theory as we currently understand and formulate it, and to provide a brief report on progress made towards more complete understanding. This report focuses more on FN-plot slope values than on intercept values. This is partly because slope data have to be properly understood before reliable interpretations of intercept data can be given, partly because slope data are currently of greater experimental interest. For both reasons, understanding how to analyze slope data is more advanced than understanding intercept data.

The main way in which this account differs from earlier treatments is that more attention is given to series-resistance effects in the measurement circuit. These are a common cause of "saturation" effects in FN plots and are probably the commonest cause of unreliable results.

More generally, this paper should be regarded as updating and (to some extent) replacing earlier discussions of FN-plot theory given by the present authors. Its structure is as follows. Section 2 sets out background theory. Section 3 discusses current-voltage data-analysis using FN plots. Section 4 begins to explore how to analyze current/voltage data gathered from circuits that contain significant series resistance. Section 5 indicates work that remains to be done.

The normal electron emission convention is employed that fields, voltages, currents and current densities are treated as positive, even where they would be regarded as negative in classical electromagnetism.

2. Theoretical Background

2.1 Underlying Assumptions

Basic tunnelling theory is formulated in the ideal theoretical context of the so-called *bulk emitter*, which fills half of space and has a smooth flat planar surface, with an uniform external electrostatic field F_{ext} in vacuum above the emitter. Atomic structure is ignored and a Sommerfeld-type free-electron model [1] is assumed for the emitter, with the electron population taken to obey Fermi-Dirac statistics and to be in thermodynamic equilibrium at thermodynamic temperature T. In the simplest models, T is taken as 0 K. At low to moderate temperatures, emission is only very weakly dependent on temperature; thus, zero-K models are adequately applicable up to well above room temperature.

It is then assumed that, provided the local radius of curvature is not too small (greater than about 10 to 20 nm), and if F_{ext} is replaced by the *local barrier field F_L*, where F_L is the electrostatic field at point "L" in the emitter's electrical surface [2], then bulk-emitter theory is applicable to the electron emission near point L. This field F_L helps specify the local tunnelling barrier for electrons that "escape from point L".

In practice, with real emitters, interest is usually in the *characteristic (local) emission current density (ECD) J_C* at some point "C" in the electrical surface chosen to be characteristic of the emitter. For *single-tip field emitters (STFEs)* and models thereof, it is often convenient to take C at the emitter apex; for *large-area field emitters (LAFEs)*, point C can be thought of as the point where the local ECD is highest for a given voltage, which will often be at the apex of one of the individual emitting sites. Parameters subscripted "$_C$" relate to point C.

2.2 Basic Tunnelling Theory

Fowler-Nordheim (FN) tunnelling is wave-mechanical tunnelling through an exact or rounded triangular barrier. *Deep tunnelling* is tunnelling at a forwards energy level well below the top of the barrier, at a level where the Landau & Lifshitz approximation [3,4] of general tunnelling/transmission theory is adequately valid. *Cold field electron emission (CFE)* is a statistical emission regime where most electrons escape by deep tunnelling from electron states close to the emitter Fermi level.

For electron motion along a coordinate z, in a situation where the single-particle three-dimensional time-independent Schrödinger equation separates in Cartesian coordinates, the equation for the wave-function component $\psi_z(z)$ can be written as:

$$\begin{aligned} \mathrm{d}^2\psi_z/\mathrm{d}z^2 &= -(2m/\hbar^2)[U(z)-E_z]\,\psi_z(z) \\ &\equiv -\kappa^2 M(z)\,\psi_z(z) \end{aligned}, \quad (1)$$

where $\hbar$ is Planck's constant divided by 2π, m is the electron mass in free space, κ $[\equiv(2m)^{1/2}/\hbar]$ is a universal constant defined by FN [5,6], $U(z)$ is the total electron potential energy and E_z is the total-electron-energy component associated with motion in the z-direction. The quantity $M(z)$ is defined as $[U(z)-E_z]$ and is termed the *electron motive energy*.

A one-dimensional *wave-mechanical barrier* is a region of space (along the z-coordinate) where $M(z)$ is continuously positive (where the kinetic energy of a hypothetical classical point particle would be continuously negative). This barrier is characterized by a parameter G defined by:

$$G = 2\kappa\int M^{1/2}(z)\mathrm{d}z \equiv g_e\int M^{1/2}(z)\mathrm{d}z, \quad (2)$$

where the integral is taken "across the barrier" (i.e., across the region where $M(z)\geq0$) and g_e $[\equiv2\kappa=(8m)^{1/2}/\hbar]$ is a universal constant [6]. The parameter G has been called both the "Gamow exponent" and the "JWKB exponent", but the physical name *barrier strength* is now preferred. (Strong barriers are difficult to tunnel through.) Eq. (2) can be called the *barrier-strength integral*.

In the *Landau and Lifschitz approximation* [3, 4], the *tunnelling probability D* that an electron approaching the barrier escapes through it is given by:

$$D \approx P\exp[-G], \quad (3)$$

where P is a *tunnelling pre-factor*. Except in special cases, P is very difficult to calculate accurately, but is thought to typically have values in the range of 0.4 to 1.1 (see Appendix A). In the related *simple-JWKB approximation*, which is the approximation normally used, P is set equal to unity and Eq. (3) becomes:

$$D \approx \exp[-G]. \quad (4)$$

2.3 Barrier Form and Related Topics

Physically, an abstract expression for the motive energy $M(z)$ is:

$$M(z) = H + U^{\mathrm{ES}}(z) + U^{\mathrm{XC}}(z), \quad (5)$$

where H is a constant called the *zero-field barrier height*, and U^{ES} and U^{XC} are terms associated, respectively, with electrostatic (ES) and with exchange-and-correlation (XC) effects. The detailed mathematical form of $M(z)$ defines the *barrier form* (or "shape").

The simplest barrier exhibiting FN tunnelling is the *exactly triangular (ET) barrier* defined by disregarding U^{XC}, taking $U^{\mathrm{ES}}= -eF_Lz$, and writing $M^{\mathrm{ET}}(z)=H-eF_Lz$. Here, e is the elementary positive charge, z is distance measured from the emitter's electrical surface, and F_L is the local barrier field, as defined above. For this barrier, the barrier strength G^{ET} is easily shown to be:

$$G^{\mathrm{ET}} = bH^{3/2}/F_L, \quad (6)$$

where b $[\equiv2g_e/3e=(4/3)(2m)^{1/2}/e\hbar]$ is the *second Fowler-Nordheim constant* [6].

For a "general barrier" (GB) of the same zero-field height H but otherwise of arbitrary but well behaved form, the barrier strength G^{GB} can be evaluated from Eq. (2), by numerical integration if necessary. A

barrier-form correction factor v^{GB} ("nu^{GB}") can then be defined via:

$$G^{GB} = v^{GB} G^{ET}. \tag{7}$$

The simplest barrier including exchange-and-correlation effects is the *Schottky-Nordheim (SN) barrier*, which models these XC effects by *Schottky's planar image potential energy* $U^{XC} = -e^2/16\pi\varepsilon_0 z$ [7], where ε_0 is the electric constant. Adding this term to the ET barrier gives the motive energy for the SN barrier; namely:

$$M^{SN}(z) = H - eF_L z - e^2/16\pi\varepsilon_0 z. \tag{8}$$

The maximum value, M^{SN}(max), of this function defines the *(reduced) barrier height*. It is readily shown that:

$$\left. \begin{aligned} M^{SN}(\text{max}) &= H - (e^3/4\pi\varepsilon_0)^{1/2} F_L^{1/2} \\ &\equiv H - c_S F_L^{1/2} \end{aligned} \right\}, \tag{9}$$

where c_S [$\equiv (e^3/4\pi\varepsilon_0)^{1/2}$] is a universal constant sometimes called the *Schottky constant* [6]. Clearly, for fields larger than the field at which M^{SN}(max) becomes zero, the tunnelling barrier vanishes.

Barriers with H equal to the *local work function* ϕ play a special role in CFE theory. Eq. (9) shows that, for a barrier of zero-field height ϕ, the *reference field* F_R needed to make M^{SN}(max) zero is $F_R = c_S^{-2} \phi^2$. For the SN barrier, a parameter f called the *scaled barrier field* (for an SN barrier of zero-field height ϕ) can then be defined by:

$$\left. \begin{aligned} f &\equiv F_L/F_R = c_S^2 \phi^{-2} F_L = e^3 F_L/4\pi\varepsilon_0 \phi^2 \\ &\approx 1.439964 \ (\text{eV}/\phi)^2 \ (F_L/\text{V nm}^{-1}) \end{aligned} \right\}. \tag{10}$$

Clearly, the barrier height becomes zero when $f=1$. This relatively recently introduced parameter f plays an important role in modern CFE theory, as indicated below.

2.4 Fowler-Nordheim-Type Equations

Fowler-Nordheim-type (FN-type) equations are a large family of approximate equations originally derived to describe CFE from bulk metals. As discussed below, FN-type equations can be formulated using many different sets of independent and dependent variables and using many different detailed approximations. The *core theoretical formulation* gives the local ECD J_L in terms of the local work function ϕ and the local barrier field F_L. This core formulation is obtained by summing ECD contributions from all relevant emitter electron states and writing the result in the form $J_L = Z_F D_F$, where D_F is the tunnelling probability for a barrier of zero-field height ϕ, and Z_F represents the related *effective electron supply* (effective incident current density). Here and elsewhere, the subscript label "$_F$" indicates that a parameter relates to a Fermi-level electron moving "forwards" (i.e., towards and normal to the emitter surface) and/or to the barrier of zero-field height ϕ seen by this electron.

When written out explicitly, this core result is usefully put in the form of the linked equations:

$$J_L = \lambda_L^{GB} J_{kL}^{GB}, \tag{11a}$$

$$J_{kL}^{GB} \equiv a\phi^{-1} F_L^2 \exp[-v_F^{GB} b\phi^{3/2}/F_L], \tag{11b}$$

where a [$\equiv e^3/8\pi h_P$] is the *first FN constant* [6]. h_P is Planck's constant. J_{kL}^{GB} is the *local kernel current density* (for the general tunnelling barrier) and is a mathematical quantity defined by Eq. (11b).

The *local pre-exponential correction factor* λ_L^{GB} is a correction factor that (in principle) takes account of all other relevant physical effects that influence the emission process, including: the tunnelling pre-factor P, exact integration over emitter states, temperature, use of atomic wave-functions and band-structure effects. A (quantitatively unknown) factor that allows for failure to use the correct barrier form, and/or for any other unrecognized mathematical or physical inadequacy in the assumed theory, can also be included as contributing to λ_L^{GB}. In any particular CFE model, the predicted form and value of λ_L^{GB} depend on precisely what theoretical assumptions are made. Exact realistic prediction of λ_L^{GB}-values would be intensively difficult, is in many cases beyond the present capabilities of quantum

mechanics, is of limited economic value and is unlikely to happen in the foreseeable future.

The merit of splitting Eq. (11) as above is that, given particular choices of the barrier form and of the values of ϕ and F_L, the quantity J_{kL}^{GB} can be calculated *exactly*; thus, all theoretical uncertainties are accumulated into the parameter λ_L^{GB}. For metal emitters, assuming tunnelling through an SN barrier, our current best guess (in 2015) is that λ_L^{GB} lies in the range $0.005<\lambda_L^{GB}<11$ (see Appendix A), but this could be an underestimate of the uncertainty range.

As indicated above, these equations apply adequately to metal STFEs, provided that the emitter is "not too small and sharp" (apex radius greater than about 10 to 20 nm). The exact limits of applicability of FN-type equations have never been definitively established.

With the same constraint, FN-type equations can also be used to analyze CFE data from LAFEs consisting of many individual emitters and/or emission sites. FN-type equations are also widely used to analyze experimental data relating to non-metallic materials. In any particular non-metallic case, the validity of doing this is open to question; currently, for non-metals, there are no reliable systematics as to when such an approach is adequate.

2.5 Complexity Levels

In developing FN theory, many different detailed assumptions and approximations can be (and have been) made about the physical origins of and the mathematical forms of the correction factors v_F^{GB} and λ_L^{GB} in Eq. (11). The assumptions made determine the *complexity level* of the resulting FN-type equation. For emitters that are "not too small and sharp", the main complexity levels used historically and recently are shown in Table 1.

The name "*new-standard*" is introduced here, to cover equations that are based on the SN barrier but have a general form for the pre-exponential correction factor. A special case of this is the *orthodox* FN-type equation, where the additional mathematical assumption is made that, apart from the independent variable itself, the only parameter in the equation that varies significantly with the independent variable is the barrier form correction factor.

Note that different choices as to barrier form would lead to different deductions, from experiment, about the value of the pre-exponential correction factor. Hence, this correction factor is formally different for each different choice of barrier form.

TABLE 1. Complexity levels of Fowler-Nordheim-type equations.

Name	Date	Ref.	$\lambda_C^{GB} \rightarrow$	Barrier form	$v_F^{GB} \rightarrow$	Note
Elementary	?	?	1	ET	1	a
Original	1928	[5]	P_{FN}	ET	1	b
Fowler-1936	1936	[9]	4	ET	1	
Extended elementary	2015	here	λ_C^{ET}	ET	1	
Dyke-Dolan	1956	[10]	1	SN	v_F	c
Murphy-Good	1956	[12]	t_F^{-2}	SN	v_F	c
Orthodox	2013	[13]	λ_C^{SN0}	SN	v_F	d
New-standard	2015	here	λ_C^{SN}	SN	v_F	-
"Barrier-effects-only"	2013	[14]	λ_C^{GB0}	GB	v_F^{GB}	d
General	1999	[8]	λ_C^{GB}	GB	v_F^{GB}	

[a]Many earlier imprecise versions exist, but the first clear statement seems to be in 1999 [8].
[b]For details concerning the Fowler-Nordheim tunnelling pre-factor P_{FN}, see [5] and [6].
[c]For modern theory concerning v_F and t_F^{-2}, see [11].
[d]The superscript " [0] " indicates that the factor is to be treated mathematically as constant.

The name of the complexity level applies to the related equation for the characteristic local ECD J_C, as in Table 1, and also applies to the equivalent equations for the emission current i_e, the measured current i_m and macroscopic current density J_M.

2.6 Scaled Form for the Kernel Current Density for the SN Barrier

In the case of the SN barrier, the barrier form correction factor v_F^{SN} is given by the particular value $v(f)$ ["vee(*f*)"] of a special mathematical function $v(l')$ called *the principal SN barrier function*, where l' is a mathematical variable [15]. For mathematical convenience, this particular value $v(f)$ is sometimes denoted by v_F, but the two symbols mean the same thing. Exact and approximate expressions for $v(f)$ are known [11,15]. The simple approximation

$$v_F \equiv v(f) \approx 1 - f + (f/6)\ln f \qquad (12)$$

is valid to better than 0.33% over the whole range $0 \leq f \leq 1$ and is adequate for most technological purposes.

Older approximate formulae for v_F, and related evaluations, exist in the literature (e.g., [16]), but these are often given in terms of the Nordheim parameter y [$=f^{1/2}$], and the approximate formulae are usually less accurate than Eq. (12). There are good physical and mathematical reasons [11] for the modern practice of using f (or l'), rather than y; one good reason is the *linearity* of the relationship between f and F_L, as given by Eq. (10).

One may define work-function-related parameters $\eta(\phi)$ and $\theta(\phi)$ by:

$$\begin{aligned} \eta(\phi) &\equiv b\phi^{3/2}/F_R = bc_S^2\phi^{-1/2} \\ &\cong 9.836238 \,(\text{eV}/\phi)^{1/2} \end{aligned} \right\}, \qquad (13)$$

$$\begin{aligned} \theta(\phi) &= a\phi^{-1}F_R^2 = ac_S^{-4}\phi^3 \\ &\cong (7.433979 \times 10^{11} \,\text{A/m}^2)\,(\phi/\text{eV})^3 \end{aligned} \right\}. \qquad (14)$$

The local kernel current density J_{kL}^{SN} for the SN barrier can then be written exactly *in scaled form* as:

$$J_{kL}^{SN} = \theta f_L^2 \cdot \exp[-v(f_L)\cdot\eta/f_L]. \qquad (15)$$

Values of $\eta(\phi)$ and $\theta(\phi)$ are shown in table 2 in Ref. [13] for a range of work-function values. For illustration, when $\phi = 4.50$ eV, then $\eta \approx 4.637$ and $\theta \approx 6.77 \times 10^{13}$ A/m^2. Merits of form (15) are that: (a) for a given ϕ-value, only a single independent variable (f_L) appears in the right-hand side; and (b) a good simple approximation for $v(f_L)$ is known. Hence, good approximate values for J_{kL}^{SN} are easy to obtain.

2.7 The Universal FN-Type Equation

All FN-type equations can be seen as variants of the *universal FN-type equation:*

$$Y = C_{YX}X^2\exp[-B_X/X], \qquad (16)$$

where X and Y are universal independent and dependent variables, respectively, and represent any of the specific variables shown in Tables 2 and 3. By definition, an *FN-type equation* is an equation with the mathematical form of Eq. (16). The *form* of an FN-type equation (and of the corresponding FN plot) is specified by the particular choices of X and Y. The theory of CFE as described by FN-type equations is sometimes called *Fowler-Nordheim theory*.

C_{YX} and B_X are parameters whose precise forms depend on the equation form and complexity level, and sometimes on other factors. C_{YX} and B_X may be weakly-to-moderately varying functions of X, and this variation will in some cases be significant. If the particular forms used for both B_X and C_{YX} are sufficiently general to encompass all physical effects associated with the particular choices of X and Y used, then the resulting equation is said to be *technically complete.*

Over the past few years, it has become increasingly clear that there is a need to distinguish between (a) *emission variables* (i.e., the *emission current and voltage* {i_e, V_e}, and physical variables derived from them that relate directly to the geometry and electrostatics of the emitting device), and (b) *measured variables* {i.e., the *measured*

current and voltage $\{i_\mathrm{m}, V_\mathrm{m}\}$, and mathematical variables derived algebraically from them). This leads to the three-way classification of variables shown in Table 2. To deal with the resulting complications, it is easiest to first set out the theory for the "theoretical" and "emission" variables.

At the orthodox complexity level, all independent theoretical and emission variables are linearly related to each other, and all dependent theoretical and emission variables are linearly related to each other. In this case, the parameter f can be seen as a scaled form of any of the independent theoretical and emission variables, defined in any particular case by:

$$f = X/X_\mathrm{R}, \tag{17}$$

where X_R is the value of X needed to reduce an SN barrier of zero-field height ϕ to zero.

2.8 Auxiliary Parameters – Independent Variables

For the characteristic point "C", the exponent in Eq. (16) can be expanded in the forms:

$$\left. \begin{aligned} B_X/X &= v_\mathrm{F}^\mathrm{GB} b\phi^{3/2}/F_\mathrm{C} \\ &\equiv v_\mathrm{F}^\mathrm{GB} b\phi^{3/2}/c_X X \equiv v_\mathrm{F}^\mathrm{GB} B_X^\mathrm{el}/X \end{aligned} \right\}, \tag{18}$$

where $B_X^\mathrm{el} \equiv b\phi^{3/2}/c_X$. Parameters that interrelate different independent variables (or different dependent variables) are termed *auxiliary parameters* and are defined via *auxiliary equations*. For the independent variables, Table 2 shows all auxiliary parameters and equations currently thought relevant, even though we would discourage the use of some of them. An important subset consists of those parameters and equations that relate the characteristic barrier field F_C to the chosen independent variable. These have the general form:

$$F_\mathrm{C} = c_X X. \tag{19}$$

Particular instances of c_X are included in Table 2.

A specific issue is how best to write the auxiliary equation linking F_C to the emission voltage V_e, because two different parameters ($\beta_{V,\mathrm{C}}$ and ζ_C) are available, as defined by:

$$F_\mathrm{C} \equiv \beta_{V,\mathrm{C}} V_\mathrm{e} \equiv V_\mathrm{e}/\zeta_\mathrm{C} \equiv V_\mathrm{e}/k_\mathrm{a} r_\mathrm{a}. \tag{20}$$

The characteristic *local conversion length (LCL)* ζ_C is in fact the older of the two, since the parameter "D" used in the 1929 Stern, Gossling and Fowler paper [17] is a form of conversion length. This form is used, for example, in Gomer's well-known formula ([18], p.32), where ζ_C is written as $k_\mathrm{a} r_\mathrm{a}$, where r_a is the emitter apex radius and k_a is a *shape factor* (also called a "field factor"). However, the characteristic *local voltage-to-barrier-field conversion factor (VCF)* $\beta_{V,\mathrm{C}}$ [$=1/\zeta_\mathrm{C}$] (as used, for example, in the 1953 Dyke et al. paper [19]) is probably now the more commonly used. Unfortunately, modern LAFE literature tends to use the symbol β to denote a real or apparent macroscopic field enhancement factor. To avoid confusion between the various uses of the symbol β, it is recommended that, in future work, the form involving the LCL ζ_C should be used to relate F_C to V_e.

Note that a local conversion length is not a physical distance (except in very special cases), but is a parameter that reflects both the sharpness of a single-tip emitter and the overall system geometry (sharp emitters that "turn on" at low applied voltages have relatively small conversion lengths).

With LAFEs, the presence of an emitting nanoprotrusion enhances the field at its emitting apex. If a *macroscopic field F_M* is defined in terms of the emission voltage by:

$$F_\mathrm{M} \equiv V_\mathrm{e}/\zeta_\mathrm{M}, \tag{21}$$

where ζ_M is the *macroscopic conversion length*, then the characteristic value γ_C of the *true (electrostatic) macroscopic field enhancement factor (FEF)* is given by:

$$\gamma_\mathrm{C} \equiv F_\mathrm{C}/F_\mathrm{M} = \zeta_\mathrm{M}/\zeta_\mathrm{C}. \tag{22}$$

TABLE 2. Independent variables and related auxiliary parameters and equations

No.	Independent variable name	symbol	link to	Auxiliary parameter name of parameter	symbol	related formulae
	Theoretical variables					
T1	Characteristic local barrier field	F_C	-	-	-	-
T2	Scaled barrier field	f	F_C	Reference field	F_R	$F_C = f F_R$
	Emission variables					
T3	Emission voltage	V_e	F_C	(True) local voltage-to-barrier-field conversion factor (VCF)[a]	$\beta_{V,C}$	$F_C = \beta_{V,C} V_e$
T4	Emission voltage	V_e	F_C	(True) local conversion length (LCL)	ζ_C	$F_C = V_e/\zeta_C$
T5	True macroscopic field	F_M	V_e	(True) macroscopic conversion length[b]	ζ_M	$F_M = V_e/\zeta_M$
T6	True macroscopic field	F_M	F_C	(True) (electrostatic) macroscopic field enhancement factor (FEF)	γ_C	$F_C = \gamma_C F_M$ $\gamma_C = \zeta_M/\zeta_C$
	Measured variables					
T7	Measured voltage	V_m	V_e	Voltage ratio	Θ	$V_e = \Theta V_m$
T8	Measured voltage	V_m	F_C	Measured-voltage-defined LCL[c]	ζ_C^{mvd} $= \zeta_C/\Theta$	$F_C = V_m/\zeta_C^{mvd}$ $F_C = \zeta_C^{-1}\Theta V_m$
T9	Apparent macroscopic field	F_A	V_m	Macroscopic conversion length	ζ_M	$F_A = V_m/\zeta_M$
T10	Apparent macroscopic field	F_A	V_e	No name – not found useful	$\zeta_M\Theta$	$F_A = V_e/\Theta\zeta_M$
T11	Apparent macroscopic field	F_A	F_M	Voltage ratio	Θ	$F_M = \Theta F_A$
T12	Apparent macroscopic field	F_A	F_C	Apparent-field-defined FEF[d]	γ_C^{afd} $= \gamma_C\Theta$	$F_C = \gamma_C^{afd} F_A$ $F_C = \gamma_C\Theta F_A$ $\gamma_C^{afd} = \zeta_M/\zeta_C^{mvd}$

[a]Future use of the parameter $\beta_{V,C}$ is discouraged. Use ζ_C and related formulae instead.
[b]In planar-parallel-plate geometry, ζ_M is normally taken as equal to the plate separation d_{sep}.
[c]Use of the parameter ζ_C^{mvd} is discouraged. Use the combination (ζ_C/Θ) instead.
[d]Use of the parameter γ_C^{afd} is discouraged. Use the combination $\gamma_C\Theta$ instead.

When measurements take place in planar-parallel-plate geometry, F_M is often taken as the mean field between the plates and ζ_M as the separation d_{sep} of the parallel plates, but formulae (21) and (22) are in fact more general than this. The characteristic FEF γ_C is a useful LAFE characterization parameter, and in an orthodox emission situation (see below), a γ_C-value can be extracted from an $i_m(V_m)$-form FN plot, by applying Eq. (22) to the extracted ζ_C-value.

A well known model case is an isolated nanoprotrusion standing on one of a pair of well separated parallel plates. When the nanoprotrusion takes the form of a hemisphere of radius r_a on a cyclindrical post of total height h (including the hemisphere), γ_C is given approximately by $0.7h/r$ (e.g., [20]), and the related LCL value is given approximately by:

$$\zeta_C \approx (1.4 d_{sep}/h) \cdot r_a. \tag{23}$$

This shows that, in the LAFE case, the shape factor k_a in Gomer's formula $F_a = V/k_a r_a$ is given approximately by $(1.4 d_{sep}/h)$. The approximation $k_a \sim 5$, as given for STFE geometry by Gomer ([18] p. 32, & [21]) is equivalent to $(d_{sep}/h) \sim 3.6$. Values of (d_{sep}/h) used in practical LAFE geometries are usually much larger; this confirms that the approximation $k_a \sim 5$ is not appropriate for LAFEs, as previously pointed out by Edgcombe and Valdrè [22].

2.9 Auxiliary Parameters – Dependent Theoretical and Emission Variables

The dependent theoretical and emission variables normally of interest are shown in Table 3. On letting "L" be "C", J_C and J_{kC} are defined via Eq. (11). The emission current i_e and related parameters are obtained by integrating J_L over the whole surface of the emitter and writing the result in the alternative forms:

$$i_e = \int J_L \, dA \equiv A_n J_C = A_n \lambda_C J_{kC} \equiv A_f J_{kC}, \quad (24)$$

where the *notional emission area* A_n and the *formal emission area* A_f [$\equiv \lambda_C A_n$] are defined via Eq. (24). The reason for introducing both A_n and A_f is the uncertainty in the value of λ_C. A_f is the area-like parameter that would

initially be extracted from an FN plot involving the emission variables, but A_n is the parameter in some existing theory (e.g., [23]) and might correspond more closely to the area seen in a field electron microscope image.

For LAFEs, the *macroscopic current density* J_M is the average ECD taken over the whole *macroscopic area* (or "footprint") A_M of the LAFE, and can be written in the various forms:

$$\left.\begin{array}{l} J_M \equiv i_e/A_M = (A_n/A_M)J_C \equiv \alpha_n J_C \\ = \alpha_n \lambda_C J_{kC} \equiv \alpha_f J_{kC} = (A_f/A_M)J_{kC} \end{array}\right\}, (25)$$

where the *notional area efficiency* α_n [$\equiv A_n/A_M$] and the *formal area efficiency* α_f [$\equiv \lambda_C \alpha_n = A_f/A_M$] are defined via Eq. (25). (In earlier work, α_n was denoted by α_M, and α_f by λ_M, and different names were used.)

For the dependent variables, Table 3 includes all the auxiliary parameters and equations currently thought relevant. An important subset consists of those parameters and equations that relate the chosen dependent variable Y to the characteristic kernel current density J_{kC}

TABLE 3. Dependent variables and related auxiliary parameters

Dependent variable		link to	Auxiliary parameter		
name	symbol		name	symbol	definition
Theoretical variables					
Characteristic kernel current density	J_{kC}	-	-	-	-
Characteristic local emission current density (ECD)	J_C	J_{kC}	Characteristic local pre-exponential correction factor	λ_C	$= J_C/J_{kC}$
Emission variables					
Emission current	i_e	J_{kC}	Formal emission area	A_f	$= i_e/J_{kC}$
Emission current	i_e	J_C	Notional emission area	A_n	$= i_e/J_C$
Macroscopic current density	J_M	i_e	Macroscopic area	A_M	$= i_e/J_M$
Macroscopic current density	J_M	J_{kC}	Formal area efficiency	α_f	$= J_M/J_{kC}$ $= A_f/A_M$
Macroscopic current density	J_M	J_C	Notional area efficiency	α_n	$= J_M/J_C$ $= A_n/A_M$

These have the general form

$$Y = c_Y J_{kC}. \tag{26}$$

For any pair $\{X,Y\}$ of independent and dependent variables, the following relation holds:

$$C_{YX} = c_Y a \phi^{-1} c_X^2. \tag{27}$$

Universal theory relating to the *measured* dependent variables, when these are different in value from the emission variables, is trickier than it might seem and is not yet fully developed.

2.10 The Relationship between Measured and Emission Parameters

Usually, the initial aim of CFE data analysis is to extract (from the measured CFE current-voltage characteristics) values of the parameters equivalent to c_X and (in some cases, where possible) C_{YX} and/or c_Y. This requires appreciation of the role of electrical circuit theory. By far, the simplest way of dealing with these issues is to work with currents and voltages. By applications of Tables 2 and 3, it can be shown that the $i_e(V_e)$ form of the general FN-type equation can be written as:

$$i_e = A_f^{GB} a \phi^{-1} (\zeta_C^{-1} V_e)^2 \exp[-v_F^{GB} b \phi^{3/2} \zeta_C / V_e]. \tag{28}$$

In circuit theory terms, a cold field electron emitter is an electronic device broadly analogous to a pn-junction diode and has an effective electrical resistance (the *emission resistance R_e*) given by:

$$R_e = V_e / i_e = \left. (\phi \zeta_C^2 / A_f^{GB} a V_e) \cdot \exp[v_F^{GB} b \phi^{3/2} \zeta_C / V_e] \right\}. \tag{29}$$

At low emission voltages, R_e is very large, but it becomes much smaller as V_e increases.

Fig. 1 is a schematic circuit diagram for CFE measurements. In principle, there may be resistances both in parallel and in series with the emission resistance. Consequently, in principle, the measured current i_m may not be equal to the emission current i_e, and the measured voltage V_m may not be equal to the emission voltage V_e.
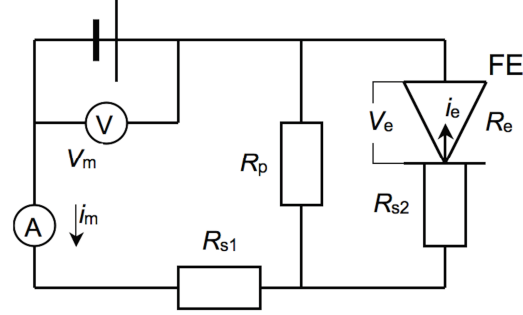
FIG. 1. Schematic electric circuit for measuring the current-voltage characteristics of a field electron emitter.

Resistance in parallel with the emission resistance can usually be made very large by suitable experimental design; hence, it is usual and reasonable to assume that $i_m = i_e$. However, a resistance in series with the emission resistance often cannot be eliminated. Let the total series resistance be denoted by R_s [$=R_{s1}+R_{s2}$]. Elementary circuit analysis gives the relationship between V_e and V_m as:

$$V_e = V_m - i_m R_s. \tag{30}$$

Defining a parameter Θ (the *voltage ratio*) by $V_e = \Theta V_m$ yields:

$$\Theta = V_e / V_m = R_e / (R_e + R_s). \tag{31}$$

Inserting relationship (31) into Eq. (28) and putting $i_m = i_e$ yield the $i_m(V_m)$ form of the general FN-type equation:

$$\left. \begin{array}{l} i_m = \\ A_f^{GB} a \phi^{-1} (\zeta_C^{-1} \Theta V_m)^2 \exp[-v_F^{GB} b \phi^{3/2} \zeta_C / \Theta V_m] \end{array} \right\}. \tag{32}$$

Alternatively, this equation could in principle be written in terms of the *measured-voltage-defined* characteristic local LCL ζ_C^{mvd}, given by:

$$\zeta_C^{mvd} \equiv \zeta_C / \Theta. \tag{33}$$

However, we have concluded that the mathematics is more transparent if the voltage-ratio term Θ is always shown explicitly in equations, notwithstanding the slightly greater algebraic complexity that this involves.

In modern LAFE literature, it is customary to assume (often incorrectly) that the emission situation is orthodox or elementary, and to state (what the authors probably intend to be) a $J_M(F_M)$-form equation. In very many cases, the published equation is ambiguous and/or incorrect, often in more than one respect. To formulate a correct "macroscopic" equation for non-orthodox situations, it is necessary to define a mathematical *apparent macroscopic field* F_A by:

$$F_A \equiv V_m/\zeta_M = V_e/\Theta\zeta_M = F_M/\Theta . \quad (34)$$

Assuming, as before, that $i_m = i_e$, the related correct general FN-type equation for a non-orthodox situation is the $J_M(F_A)$-form equation:

$$\left. \begin{array}{l} J_M = \\ \alpha_f^{GB} a\phi^{-1}(\gamma_C\Theta F_A)^2 \exp[-\nu_F^{GB} b\phi^{3/2}/\gamma_C\Theta F_A] \end{array} \right\}. \quad (35)$$

Note that the formal area efficiency α_f^{GB} and the voltage ratio Θ appear in this equation.

In our view, the relationship between F_A and the true macroscopic field F_M is intellectually more awkward to deal with than the corresponding relationship between V_m and V_e, especially for students. Hence, because theory involving V_m and V_e is more straightforward, our firm view is that FN-plot analysis is best carried out on $i_m(V_m)$-form FN plots based on the raw experimental data (or, failing this, on $J_M(V_m)$-form FN plots). Discussion below deals with $i_m(V_m)$-form FN plots.

3. Current-Voltage Data Analysis Using Fowler-Nordheim Plots

3.1 Introduction

Given Eqs. (16) and (18), a quantity $L(X^{-1})$ can be defined by:

$$\left. \begin{array}{ll} L(X^{-1}) & \equiv \ln\{Y/X^2\} \\ & = \ln\{C_{YX}\} - B_X/X \\ & = \ln\{C_{YX}\} - \nu_F b\phi^{3/2}/(c_X X) \end{array} \right\}. \quad (36)$$

An FN-type equation written in this way is said to be *"written in FN coordinates"*.

A *Fowler-Nordheim plot (FN plot)* is a plot of $L(X^{-1})$ versus X^{-1}. General features of FN-plot theory are common to all *forms* of FN plot (i.e., such general features do not depend on the particular independent and dependent variables used), and are best discussed using the universal FN-type equation above. This has been done elsewhere [14]. A summary of the most relevant part of this treatment is presented here. For notational simplicity, the superscript "GB" is now dropped, but relevant quantities still apply to a general barrier unless indicated otherwise.

Except in the case of the ET barrier, ν_F (and hence B_X) are functions of X^{-1}. The parameters c_X, c_Y and C_{YX}, too, will often be functions of X^{-1}. Hence, theoretical FN plots are expected to be curved (though for metal emitters, this curvature is so slight as to be barely noticeable). At any given value of the horizontal-axis value X^{-1}, the slope $S_{YX}(X^{-1})$ of a theoretical FN plot is given by:

$$\left. \begin{array}{l} S_{YX}(X^{-1}) = dL/d(X^{-1}) \\ = \left[d\ln C_{YX}/d(X^{-1}) - X^{-1}\nu_F d(b\phi^{3/2}c_X^{-1})/d(X^{-1}) \right] \\ \quad - \left[(b\phi^{3/2}c_X^{-1})\{\nu_F + X^{-1}d\nu_F/d(X^{-1})\} \right] \end{array} \right\}. \quad (37)$$

By introducing the *slope correction function* $\sigma_{YX}(X^{-1})$ defined by:

$$\sigma_{YX}(X^{-1}) \equiv [dL/d(X^{-1})]/(b\phi^{3/2}c_X^{-1}), \quad (38)$$

the slope $S_{YX}(X^{-1})$ can be written in the much simpler form:

$$S^{tan} = S_{YX} = -\sigma_{YX}\cdot(b\phi^{3/2}c_X^{-1}) = \sigma_{YX}\cdot S_{YX}^{el}, \quad (39)$$

where $S_{YX}^{el}\ [= -b\phi^{3/2}c_X^{-1}]$ is the slope of the plot for the corresponding elementary FN-type equation. For notational simplicity, we no longer explicitly show the dependence on X^{-1}. Obviously, a tangent to this theoretical FN plot, taken at abscissa-value X^{-1}, also has slope S^{tan} as given by Eq. (39).

It can be shown [14] that this tangent intersects the L-axis at the value $\ln\{I^{tan}(X^{-1})\}$ given via:

$$I^{\tan}(X^{-1}) = \rho_{YX}(X^{-1}) \cdot C_{YX}(X^{-1}), \qquad (40)$$

where the *intercept correction function* $\rho_{YX}(X^{-1})$ is given by:

$$\left.\begin{aligned}
\ln\{\rho_{YX}\} &= [\sigma_{YX} - \nu_F] \cdot [b\phi^{3/2}/c_X X] \\
&= [\sigma_{YX} - \nu_F] \cdot G_F^{ET}
\end{aligned}\right\}, \qquad (41)$$

where $G_F^{ET} \equiv b\phi^{3/2}/F_C$. Apart from the universal constant b, all parameters in this formula are or can be functions of X^{-1}, but this is not shown explicitly.

Note that, in this paper, all correction functions ρ are the new type of intercept correction function introduced in Ref. [14], rather than the older type of intercept correction function used in pre-2012 papers. The subscripts *YX* are included as a reminder that, in principle, the forms of the correction functions may depend on which specific variables are represented by *X* and *Y*.

Obviously, experimental data can also be plotted on an FN plot. Often, but not always, an experimental FN plot is either a nearly straight line, or basically breaks into two nearly straight segments. A nearly straight FN plot or segment is usually analyzed by fitting to it a straight line with (usually negative) slope S_X^{fit}, intercept I_{YX}^{fit} and equation:

$$Y = \ln\{I_{YX}^{fit}\} + S_X^{fit}/X. \qquad (42)$$

Normally, the task is to extract estimates of c_X (and sometimes C_{YX} and/or c_Y) from the measured values S_X^{fit} and I_{YX}^{fit}. For non-metals, this can be far more complicated than has been generally realized. The abstract principles involved (set out below) are becoming clear, but our detailed understanding of how to do this reliably in real emission situations is still very much under development.

3.2 The Tangent Method

Although other methods of FN plot analysis exist, the most flexible method is the *tangent method*. In this method, it is assumed that the straight line fitted to the experimental data can be modelled by a tangent to the theoretical plot, taken at some specific value X_t^{-1} called the *fitting value*. Functions evaluated at the fitting value are subscripted "t", and the name "factor" (rather than "function") is used to indicate the value thus obtained. Thus, the tangent to the theoretical plot, taken at the abscissa value X_t^{-1}, can be written as the straight line:

$$\left.\begin{aligned}
Y &= \ln\{I^{\tan}\} + S^{\tan}/X \\
&= \ln\{\rho_{YX,t}C_{YX,t}\} - \sigma_{YX,t}b\phi^{3/2}/c_{X,t}X
\end{aligned}\right\}, \qquad (43)$$

where $\sigma_{YX,t}$, $\rho_{YX,t}$, $C_{YX,t}$ and $c_{X,t}$ are values taken at the fitting value X_t.

This assumption that the fitted line can be modelled by a tangent is not exactly true, because the fitted line is in principle a chord to the theoretical FN plot. In principle, a *chord correction* [24] could be made, but this is difficult to do exactly, and there is no evidence that making a chord correction significantly affects final extracted values. (Other uncertainties are nearly always much greater than the uncertainty associated with neglecting the chord correction.)

In principle, if no chord correction is made, the data-analysis procedure is then to identify Eq. (42) with Eq. (43) and extract values of $c_{X,t}$, $C_{YX,t}$ and $c_{Y,t}$ using the formulae:

$$c_{X,t}^{extr} = -\sigma_{YX,t}b\phi^{3/2}/S_X^{fit}, \qquad (44)$$

$$C_{YX,t}^{extr} = I_{YX}^{fit}/\rho_{YX,t}, \qquad (45)$$

$$\left.\begin{aligned}
c_{Y,t}^{extr} &= C_{YX,t}^{extr}/\{a\phi^{-1}(c_{X,t}^{extr})^2\} \\
&= \{I_{YX}^{fit}(S_X^{fit})^2\}/[(ab^2\phi^2)(\rho_{YX,t}\sigma_{YX,t}^2)]
\end{aligned}\right\}. \qquad (46)$$

If a chord correction is made, then I_{YX}^{fit} in formulae (45) and (46) is replaced [24] by I^{corr}, where

$$I^{corr} = \rho^{chord}I_{YX}^{fit}, \qquad (47)$$

where ρ^{chord} is a *chord correction factor*. As indicated above, expected values for ρ^{chord} are not reliably known; however, an approximate estimate can be obtained from the work of Spindt et al. [25], who fitted a chord to a plot of $v(y)$ vs y (see their Fig. 5). It has been shown [24] that their result is equivalent to taking $\rho^{chord} \approx 1.2$.

The correction factors $\sigma_{YX,t}$ and $\rho_{YX,t}$ cannot be measured, but have to be estimated theoretically, using specific (physically plausible) mathematical assumptions about the forms of ν_F and C_{YX} and an estimate of the value of X_t^{-1}. Herein lie two of the main difficulties of FN plot analysis.

In the universal FN-type Eq. (16), all of ν_F^{GB}, ϕ, c_X, c_Y and C_{YX} can in principle be functions of X^{-1}. Hence, the detailed forms of Eq. (37), and hence Eqs. (38) and (41), can in principle be very complicated, involving many individual terms, many of which have never been carefully investigated. No general approach seems practicable. These formulae can be applied successfully in the so-called orthodox emission situation (see below), where ϕ, c_X, c_Y and C_{YX} are assumed constant and the mathematical forms of σ_{YX} and ρ_{YX} are well known, but other situations are problematic. To progress scientifically, it looks necessary to proceed in a series of focused investigations, each of which involves specific mathematical approximations that allow some specific physical effect or effects to be explored. One initial line of investigation has been into the effects of barrier form, as discussed below.

One also has to determine the fitting value, X_t^{-1}. The first estimate is always the mid-point of the range of X^{-1}-values covered by the experimental data being analyzed. However, when the curvature of an FN plot is non-uniform (which is usually the case), then the mid-range value is probably not the best choice, and the error in the extracted result is in principle slightly increased (especially for A_f and α_f). For example, in the orthodox emission situation, a theoretical plot based on a Schottky-Nordheim barrier has greater curvature on the left-hand side (low X^{-1}-value side), and the best choice of X_t^{-1} is somewhat to the left of the mid-range value, as demonstrated in Ref. [26]. The issue of the best choices of X_t^{-1} for FN plots related to non-orthodox situations has not yet been systematically investigated.

In cases where the correction functions are slowly varying functions of X^{-1}, the exact choice of fitting value is not important. Thus, in orthodox and "nearly orthodox" emission situations, the slope correction factor can usually be adequately approximated as $s_t \equiv s(f_t) \approx 0.95$, where s is the well known slope correction function for the SN barrier (e.g., [11, 16]). However, in cases where FN plots are obviously curved, and hence σ_{YX} must be varying relatively rapidly, the choice of X_t^{-1} is expected to be important. More research is needed on this issue.

3.3 Analysis of $i_m(V_m)$-Form FN Plots

As indicated above, an FN plot of the form $[\ln\{i_m/V_m^2\}$ vs $\{1/V_m\}]$ is called here an $i_m(V_m)$-form FN plot. For convenience, the subscript "m" or "mm" (rather than the variables themselves) will be used to label parameters belonging to an $i_m(V_m)$-form FN plot. For such a plot, c_X becomes $c_m = \Theta\zeta_C^{-1}$; thus, from Eq. (44), an extracted value ζ_C^{extr} of the true local conversion length ζ_C can in principle be derived from the FN-plot slope using:

$$
\left.
\begin{aligned}
(\zeta_C^{extr})^{-1} &= -(\sigma_{mm,t}/\Theta_t)\cdot(b\phi^{3/2})/S_{mm}^{fit} \\
&\equiv -\sigma_{SR}b\phi^{3/2}/S_{mm}^{fit}
\end{aligned}
\right\}, \quad (48)
$$

where Θ_t is the voltage ratio at the V_m-value where the tangent is taken, and σ_{SR} is the *effective slope correction factor for the series resistance (SR) situation*. This parameter σ_{SR} is defined by Eq. (48) and given in terms of $\sigma_{mm,t}$ by:

$$\sigma_{SR} = \sigma_{mm,t}/\Theta_t. \quad (49)$$

For analogy with what is done in some existing literature, we also introduce an $i_m(V_m)$-form slope characterization parameter ζ_C^{app} (or "apparent LCL") defined via:

$$(\zeta_C^{app})^{-1} \equiv -b\phi^{3/2}/S_{mm}^{fit}. \quad (50)$$

The correct extracted value ζ_C^{extr} of the true LCL ζ_C is related to this via:

$$(\zeta_C^{\text{extr}})^{-1} = \sigma_{\text{SR}} \cdot (\zeta_C^{\text{app}})^{-1}, \qquad (51)$$

and, using Eq. (22), the corresponding extracted value γ_C^{extr} of the true FEF γ_C is related to ζ^{app} via:

$$\gamma_C^{\text{extr}} = \sigma_{\text{SR}} \cdot [\zeta_M / \zeta_C^{\text{app}}]. \qquad (52)$$

The reciprocals of ζ_C and ζ_C^{app} are used above, rather than the parameters themselves, in order to make the relevant formulae look similar to FEF-related formulae existing in the literature and discussed below.

A common (but unfortunate) literature approach is to pre-convert the experimental data, in effect by using the formulae $F_A = V_m / \zeta_M$, $J_M = i_m / A_M$, and make a $J_M(F_A)$-form FN plot. Let this have fitted slope $S_{\text{MA}}^{\text{fit}}$. In the elementary data-analysis approach nearly always used, a *slope characterization parameter* (or *apparent FEF*, or *pseudo-FEF*), denoted here by β^{app}, is then derived from the formula:

$$\beta^{\text{app}} = -b\phi^{3/2} / S_{\text{MA}}^{\text{fit}}. \qquad (53)$$

Since $S_{\text{MA}}^{\text{fit}} / S_{\text{mm}}^{\text{fit}} = \zeta_M$, if follows from Eqs. (50) and (53) that:

$$(\zeta_C^{\text{app}})^{-1} = \beta^{\text{app}} / \zeta_M, \qquad (54)$$

and hence, from Eq. (52), the correct extracted value γ_C^{extr} of the true electrostatic FEF is obtained from:

$$\gamma_C^{\text{extr}} = \sigma_{\text{SR}} \cdot \beta^{\text{app}}. \qquad (55)$$

A serious weakness of much modern LAFE literature is that it uses the same symbol "β" for both of the quantities denoted here by γ_C and β^{app}. This hides the existence of σ_{SR} and is equivalent to taking $\sigma_{\text{SR}} = 1$. This can be a very poor approximation when series resistance or "saturation" is present, as it is known [13] that in these circumstances σ_{SR} can be significantly less than unity. Consequently, many FEF-values reported in the literature are in fact spuriously large [13].

We make the trivial point that, although formula (55) looks marginally simpler than

formula (52), this is deceptive. In order to construct a $J_M(F_A)$-form FN plot, it is necessary to divide every measured voltage (V_m) value by ζ_M (in practice usually by d_{sep}). It is less work to directly use the V_m-values in the FN plot and multiply the fitted slope value, or the corresponding slope characterization parameter value, by ζ_M (in practice usually by d_{sep}).

Physically, ζ_C should often be a relatively well-defined quantity, with a relatively well-defined value. Extraction of a reliable value is straightforward in "orthodox" emission situations, as defined below, in which (by definition) no series resistance or other complications are present (so $\Theta = 1$), and $\sigma_{\text{mm,t}}$ and σ_{SR} become given by $s_t \approx 0.95$.

However, the situation is different when significant series resistance is present. Extraction of a reliable value for ζ_C, using Eq. (47) or Eq. (50), then needs good estimates of the values of both the voltage ratio Θ_t and the slope correction factor $\sigma_{\text{mm,t}}$ (which in this case may include terms derived by differentiation with respect to Θ). A further difficulty is that the series resistance R_s may be current-dependent, with the nature of this dependence depending on the detailed physical nature of the conducting path between the voltage generator and the tip emitting region. At present, there is very little systematic practical knowledge about the likely behaviour and value of R_s for conducting paths that are not exclusively metallic; consequently, very little empirical knowledge exists about likely values of Θ_t or $\sigma_{\text{mm,t}}$. These difficulties mean that, when significant series-resistance effects occur, it is currently impossible to extract reliable ζ_C-values or reliable γ_C-values from an $i_m(V_m)$-form plot (or reliable γ_C values directly from an $J_M(F_A)$-form plot). Discussion of this is continued in Section 4.

3.4   The   Barrier-Effects-Only Approximations

Even if one makes the assumption that no series resistance is present (hence $\Theta = 1$ and

$\mathrm{d}\Theta/\mathrm{d}V_m=0$), there remain several effects (for example, field dependent changes in emission-system geometry, when a carbon nanotube is pulled upwards by Maxwell stress) that can in principle create V_e-dependence in B_X and/or C_{YX}, and some of these have never been investigated in detail. What is now needed is systematic investigation of the various possibilities, where this is practicable.

With Eqs. (38) and (41), the *barrier-effects-only approximation* (previously called the "basic approximation" [14]) is to take into account only those terms that relate to the direct dependence on X^{-1} and the dependence of v_F on X^{-1}. This approximation disregards all terms in the first square bracket in Eq. (37). In the barrier-effects-only approximation, the various independent theoretical and emission variables are linearly related, and the general correction functions σ_{YX} and ρ_{YX} become given by *slope and intercept correction functions* σ^B and ρ^B defined by formulae [14] as:

$$\left.\begin{aligned}\sigma^B &\equiv v_F - X_C \mathrm{d}v_F/\mathrm{d}X_C \\ &= v_F - F_C \mathrm{d}v_F/\mathrm{d}F_C\end{aligned}\right\}, \qquad (56)$$

$$\left.\begin{aligned}\ln\{\rho^B\} &\equiv [\sigma^B - v_F]\cdot(b\phi^{3/2}/F_C) \\ &= [\sigma^B - v_F]\cdot G_F^{ET}\end{aligned}\right\}, \qquad (57)$$

where X here is one of the theoretical or emission variables.

Eqs. (56) and (57) apply to a barrier of any mathematical form. As indicated above, the so-called *orthodox approximation* involves, *in addition*, the assumption that the barrier is a Schottky-Nordheim barrier. In this case, v_F becomes v_F^{SN} and is given by the relevant particular value $v(f)$ of the principal SN-barrier function $v(l')$ [11, 15]. σ^B becomes given by the SN-barrier function s [11], ρ^B becomes given by the SN-barrier function r_{2012} discussed in Ref. [14], and the defining equations reduce to [11]:

$$s = v - f\mathrm{d}v/\mathrm{d}f, \qquad (58)$$

$$\left.\begin{aligned}\ln\{r_{2012}\} &= [s - v]\cdot G_F^{ET} \\ &= -(f\mathrm{d}v/\mathrm{d}f)G_F^{ET} = \eta u\end{aligned}\right\}. \qquad (59)$$

where all relevant parameters denote characteristic values, but this is not shown explicitly. Here, u is the SN-barrier function defined by $u = -\mathrm{d}v/\mathrm{d}f$ [11] (see Appendix C).

The so-called *elementary approximation* (much used in modern LAFE literature) involves, *in addition to* the assumptions made at the start of this section, the assumption that the barrier is exactly triangular. In this case, $\sigma^B = 1$ and $\rho^B = 1$.

3.5 The Orthodox Data-Analysis Approach

The *orthodox approach* to FN-plot analysis is based on making a set of physical and mathematical assumptions, about the physical measurement situation and about the theory of emission. This *orthodox emission situation* is defined formally in Appendix B. In such a situation, FN-plot analysis is straightforward. No real emission situation is "exactly orthodox", but many real situations are "very nearly orthodox", and the various assumptions made are adequately valid.

This "orthodox approach" is a development of earlier methods, in particular those used by Charbonnier and Martin [27] and Spindt et al. [25]; these were based on the Murphy-Good FN-type equation [12], which assumes emission through an SN barrier, but approximates λ_L^{SN} as equal to a mathematical pre-factor sometimes denoted by t_F^{-2} (see [11]). Exact analytical forms and numerical values have long been known for the SN-barrier functions (see [11]), but the existence of simple approximations for v and s has been key to their application in CFE data analysis. Many such approximations have been proposed; some of these are listed in [24]. In recent years, significant steps forward have been: (a) the realization that the natural physical variable for the argument of v is the scaled barrier field f, rather than the Nordheim parameter y [$=f^{1/2}$] previously used; and (b) the discovery of a

good, simple, accurate algebraic approximation for $v(f)$; namely Eq. (12) above. It has been shown [24] that, on average over the range $0 \leq f \leq 1$, Eq. (12) is more accurate than any other approximation of equivalent complexity. Related approximate expressions can be given [11] for relevant SN-barrier functions, including $u(f)$, $s(f)$ and $r_{2012}(f)$, which also have good accuracy. These expressions are given in Appendix C.

By using simulated input data for electron escape through an SN barrier and these simple expressions for $s(f)$ and $r_{2012}(f)$, it has been demonstrated that (in an orthodox emission situation) application of the tangent method leads to accurate extraction of emission characterization parameters, in particular the field enhancement factor and formal emission area [14].

3.6 Correction Factors for Other Barrier Shapes

Many earlier calculations of local emission current density have included calculations of the barrier form correction factor v_F, for a variety of emitter shapes and related barrier forms. However, there have been few calculations of slope and intercept correction factors. Recent explorations [28, 29] have generated the following conclusions.

(1) For planar emitters, the precise form of the model used for the exchange-and-correlation (XC) contribution has relatively little effect on predicted values of σ^B and $\ln\rho^B$ [28].

(2) For a spherical emitter, the barrier (if XC effects are disregarded) is the so-called *Coulomb barrier*, well known in nuclear physics. This barrier has an analytical solution for v_F from which estimates can be derived for σ^B and $\ln\rho^B$. Theoretically predicted FN plots for the Coulomb barrier can be significantly curved, particularly for low-radius emitters [29].

(3) For a spherical emitter, as with a planar emitter, the inclusion of an XC term has a significant effect of the values of v_F, σ^B and $\ln\{\rho^B\}$. However, provided that the sphere radius is "not too small", there is relatively little difference between the results of using Schottky's planar image-PE approximation to model XC effects and the results of using the spherical image-PE approximation [29].

(4) For a spherical emitter of small radius, the electrostatic term ceases to be a valid approximation for electrostatic effects associated with a real single-tip-geometry emitter, because the influence of the emitter shank increases as the tip radius decreases. For a real small-apex-radius emitter, the sphere-on-orthogonal-cone (SOC) model [19] represents the electrostatics better. Preliminary investigations [29], illustrated in Fig. 2, show that, as expected, the results for the two models diverge as apex radius decreases.
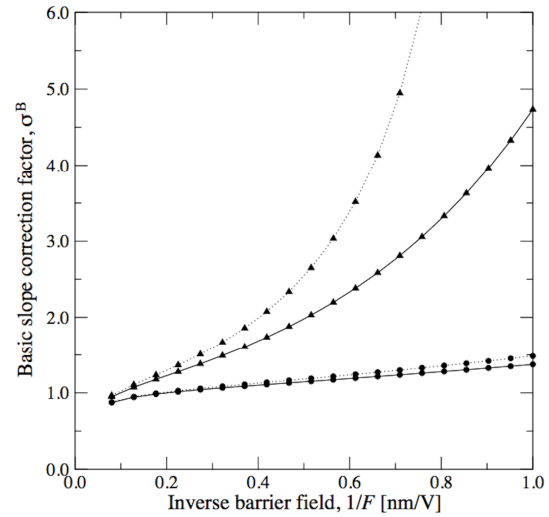
FIG. 2. Plots illustrating how the slope correction function σ^B varies as a function of inverse barrier field $1/F$. Dotted lines are for a spherical emitter; continuous lines are for an emitter modelled using the sphere-on-orthogonal-cone (SOC) model [19]. Circles are for apex radius $r_a = 20$ nm; triangles are for $r_a = 5$ nm. SOC-model parameters used were: $\phi = 4.50$ eV, $n=0.1$, r_a as indicated, $a = r_a/4$.

140

Unfortunately, evidence has recently come to light [30] that the quasi-classical quantum-mechanics used in existing analyses of CFE from non-planar emitters is likely to be valid only when the Schrödinger equation separates in Cartesian coordinates, which, obviously, is not the case for non-planar emitters. Hence, most or all existing treatments of field electron emission from non-planar emitters may need adjustment. This is an active topic of research, but it is not yet clear what detailed form the theoretical adjustment should take. Consequently, we do not give further examples of previous (unadjusted) results here.

This leaves us with the situation that (with the exception of a few special cases) the only emitters where we can be sure that the results of FN plot analysis are strictly valid are those that comply adequately with the conditions for orthodox emission. A test for identifying emitters that do *not* comply now exists [13] and is described next.

3.7. A Test for Lack of Orthodoxy

For most of the past 50 years, FN-plot analysis has used either the orthodox approach (using either the tangent method or a simplified version of it), or an *elementary approach* based on the elementary approximation defined above.

However, the assumptions of the orthodox emission situation exclude many complications that can occur in real situations. The excluded complications include significant effects resulting from: series resistance; leakage currents; patch fields; field emitted vacuum space-charge; current-induced changes in emitter temperature; field penetration and band-bending; quantum confinement; and field-related changes in emitter geometry, emission area and/or local work-function. These complications can affect measured current-voltage characteristics.

The test for "lack of orthodoxy" (i.e., whether the measured characteristics are incompatible with the orthodox emission

hypothesis) involves extracting *f*-values from an experimental FN plot, using the formula

$$f^{\text{extr}} = -s_{\text{t}}\eta / [S^{\text{fit}} \cdot (X^{-1})^{\text{expt}}], \qquad (60)$$

with $s_{\text{t}} \approx 0.95$. For simplicity, we no longer show either universal variable X, Y as a subscript. The test, however, applies to any form of FN plot. By using Eq. (60), *f*-values can be extracted that correspond to the range of X values measured.

For any given ϕ-value, a set of four indicative boundary *f*-values $\{f_{\text{lb}}, f_{\text{low}}, f_{\text{up}}, f_{\text{ub}}\}$ can be defined as discussed in Ref. [13]. For $\phi = 4.50$ eV, these values are $\{0.10, 0.15, 0.45$ and $0.70\}$; for other ϕ-values, boundary *f*-values can be derived from table 2 in Ref. [13]. The range of extracted *f*-values is then compared with these boundary values. One of the following three situations then applies. (1) If the extracted range is totally inside the range $\{f_{\text{low}} < f^{\text{extr}} < f_{\text{up}}\}$ of "apparently reasonable" *f*-values, then the orthodoxy test is passed. (2) If any part of the extracted range is "clearly unreasonable" because $f^{\text{extr}} < f_{\text{lb}}$ or $f^{\text{extr}} > f_{\text{ub}}$, then the orthodoxy test is "clearly failed". (3) If some part of the extracted range is outside the "clearly reasonable" range, but not in either of the "clearly unreasonable" ranges, then "further investigation is needed".

If case (1) applies, then characterization data extracted from the FN plot (in particular, the apparent FEF-value) can be treated as reliable. If case (2) applies, then extracted characterization data are almost certainly spurious. If case (3) applies, then extracted characterization data are unreliable and are likely to be spurious.

4. Analysis of Measured Current-Voltage Data When Significant Series Resistance Exists

Although series resistance in the conducting path from the high-voltage generator to the emitting region at the tip apex is not the only possible cause of orthodoxy-test failure, it is currently thought to be the commonest cause. As just

indicated, when the orthodoxy test is failed, then the usual "orthodox" and "elementary" methods of extracting characterization parameters from FN plots will generate spurious results. In Ref. [13], the orthodoxy test described above was applied to a small sample of 19 published FN plots, taken from emitters fabricated from various non-metals. Approximately 40% of these failed the test, indicating that the associated published FEF-values are spuriously large. If this sample is representative of the literature as a whole (which may or may not be the case), then one might expect that there are many hundreds of published field emission papers that report FEF-values that are in fact spuriously large.

Consequently, it was argued in Ref. [13] that (certainly until such time as we better understand any systematic trends involved) the orthodoxy test should always be applied to FN plots taken from non-metallic emitters, and the results of the test should be published alongside any published FN plot.

Obviously, better methods of data analysis for non-orthodox emission situations are also needed. This section describes progress with explorations into several methods of extracting more reliable characterization data when the presence of series resistance is thought (or hypothesized) to be the only significant problem.

4.1 Analysis via a Slope Correction Factor, for the Schottky-Nordheim Barrier

We first report an investigation [31] that originally aimed to estimate the effective slope correction factor σ_{SR} [$=\sigma_{mm,t}/\Theta$], assuming constant series resistance and emission through an SN barrier. This scenario has analytical solutions, since all relevant quantities can be expressed as functions of chosen constant-values and a single variable; namely the (true) scaled barrier field f. This makes the scenario particularly suitable for analysis by computer algebra packages, in particular the

MAPLE™ package used by one of us [JHBD].

The emission voltage V_e, emission current i_e and emission resistance R_e are given by:

$$V_e = \zeta_C F_R f, \tag{61}$$

$$i_e = A_f \theta f^2 \exp[-v(f) \cdot \eta / f], \tag{62}$$

$$R_e = V_e / i_e. \tag{63}$$

The measured current i_m can be taken as equal to i_e, and the measured voltage V_m is given by

$$V_m = V_e + i_e R_s. \tag{64}$$

Expressions for dV_m in terms of df and for di_m in terms of df can be obtained via Eqs. (64) and (62), respectively, and the slope S_{mm} of the $i_m(V_m)$-form FN plot can be evaluated from:

$$S_{mm} = V_m \left[2 - i_m^{-1} V_m (di_m / dV_m) \right]. \tag{65}$$

From this, predicted values of the effective slope correction function in the series-resistance situation (σ_{SR}) can be obtained from:

$$\sigma_{SR} = S_{mm} / (b \phi^{3/2} \zeta_C). \tag{66}$$

Fig. 3a shows the predicted $i_m(V_m)$-form FN plots, for the parameter values $\phi = 4.50$ eV (hence $F_R = 14.06$ V/nm) and $\zeta_C = 100$ nm, and for various values of the product ($A_f R_s$). Fig. 3b shows a plot of σ_{SR} vs $1/V_m$ for the value $A_f R_s = 10^{-1}$ Ω m^2. Note that the predicted FN plots "turn over" at the left-hand side.

These predicted FN plots do not well resemble experimental FN plots found in the literature for materials that are thought to fail the orthodoxy test because of series resistance. Further, the parameter σ_{SR} varies significantly with $1/V_m$, which makes choice of a fitting value difficult. At present, the precise reasons for this non-agreement of predicted and measured FN plot shapes are not clear. In many cases, the most plausible reason might be current-dependence in R_s, but other possibilities need thinking about. These might include field-dependent

changes in emitter geometry or some anomalous effect associated with the fact that (with LAFEs) the current is drawn from

many individual emitting tips rather than from a single tip.

a

b
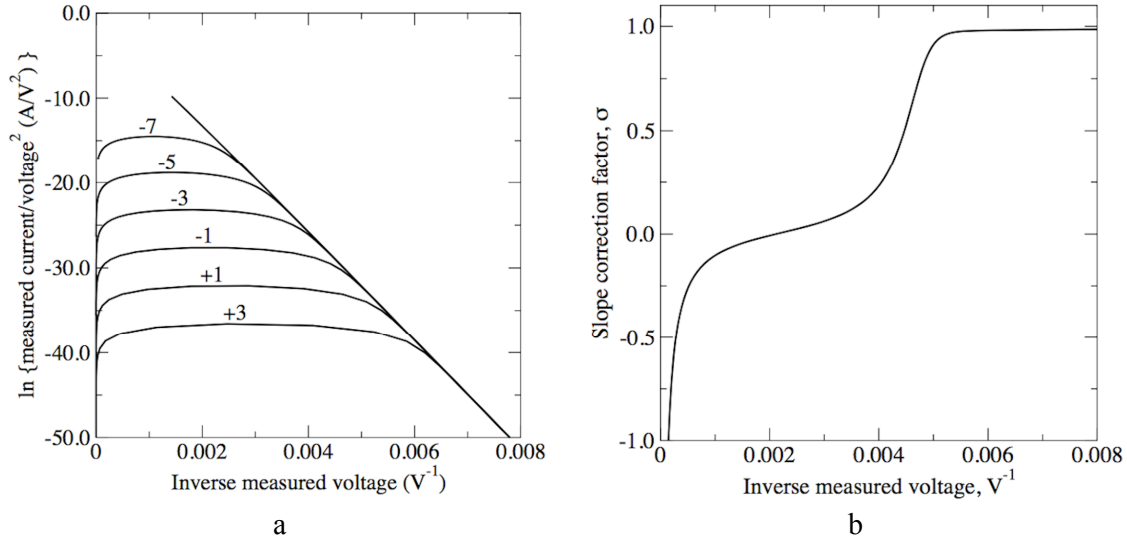
FIG. 3. To illustrate the results of simulating circuit performance when a high resistance R_s is placed in series with a field electron emitter (with formal emission area A_f) operating in accordance with the new-standard FN-type equation. (a) $i_m(V_m)$-form FN-plots, for various values of the product A_fR_s. A curve marked "N" corresponds to an A_fR_s-value of 10^N Ω m². (b) Plot showing the effective slope correction factor σ_{SR} as a function of inverse measured voltage V_m^{-1}, for $A_fR_s = 10^{-1}$ Ω m².

Provisional conclusions are that future theoretical research needs to explore the consequences, for predicted FN plots, of current-dependence in the series resistance, but that other methods of dealing with series resistance need further exploration and could be more effective in the short term.

4.2 Analysis via Simulation of Constant Series-Resistance Effects

The most obvious alternative method involves the assumptions that the series resistance is, in fact, constant, and that an $i_e(V_e)$-form FN plot ought to be a nearly straight line. This method has had longest use in the context of electronic random-access memory (e.g., [32]), but related thinking has also been used in the context of LAFEs (see [33-35]). Some criterion (which may be statistical or empirical) is needed for assessing the straightness of the FN plot. The method then works as follows. A value is assumed for R_s. For each of a range of values of i_m (=i_e), a value V_e is obtained from Eq. (19), and an $i_e(V_e)$-form FN plot is drawn. This procedure is carried out for a range of

values of R_s, and the straightest resulting plot is selected as the definitive plot. Emitter characterization parameters are then derived from this "definitive" $i_e(V_e)$-form plot, by a conventional orthodox or elementary method.

This procedure, as applied in the context of electronic random access memory, is well described by Miranda [32]. There is scope for further theoretical investigation of how best to apply it in the context of LAFEs, but it should be remembered that the assumption of constant series resistance may be more plausible for electronic random access memory devices than for LAFEs.

4.3 Phenomenological Adjustment

A further alternative method is *phenomenological adjustment* of the extracted slope characterization parameter, which we denote here by c_X^{app}. In practice, c_X^{app} would normally be one of the parameters $(\zeta_C^{app})^{-1}$ or β^{app} discussed earlier.

The method of "phenomenological adjustment" [31] assumes that emission in

143

fact takes place through an SN barrier, and takes place over the same range of *f*-values as does orthodox emission. A value $(1/f^{\text{orth}})_{\text{mid}}$ is assumed for the typical mid-range value of $1/f$ for practical orthodox field emitters; a value around 4 seems appropriate. This value is then compared with the "experimental" value $(1/f^{\text{extr}})_{\text{mid}}$ extracted, via Eq. (60), for the X^{-1}-value that corresponds to the mid-point of the range of experimental X^{-1} values used in the experiments, and an *adjustment factor* ω_{adjust} is obtained from:

$$\omega_{\text{adjust}} = (1/f^{\text{extr}})_{\text{mid}} / (1/f^{\text{orth}})_{\text{mid}}. \qquad (67)$$

Non-orthodox emitters often fail the orthodoxy test, because their extracted *f*-values are too high ($1/f$ too low); in this case the value of ω_{adjust} will be less than unity.

The method assumes that a phenomenological estimate c_X^{est} of the true value of the auxiliary parameter c_X can be obtained from the extracted slope characterization parameter c_X^{app}, by using ω_{adjust} as a "phenomenological estimate" of the slope correction factor σ_{SR} and hence that:

$$c_X^{\text{est}} \sim \omega_{\text{adjust}} \cdot c_X^{\text{app}}. \qquad (68)$$

The method will work for FEFs, VCFs and (the reciprocals of) LCLs. In the case of FEFs, Eq. (68) becomes:

$$\gamma_C^{\text{est}} \sim \omega_{\text{adjust}} \cdot \beta^{\text{app}}, \qquad (69)$$

where β^{app} is the slope characterization parameter (apparent FEF) as defined by Eq. (53). (In the literature, β^{app} is usually denoted simply by β, and is usually simply called an FEF.) γ_C^{est} is the estimated ("Ansatz-adjusted") value of the true characteristic FEF for the emitter concerned, as obtained by phenomenological adjustment.

As a specific (worst-case) example, consider data-entry 20 in table 4 in Ref. [13]. This entry relates to the high-field part of an FN plot for what is described as a "flexible SnO$_2$ nanoshuttle", and a FEF-value of around 130 000 is reported. The *f*-value range derived as part of the orthodoxy test is 5.6 to 33.2. This corresponds to a mid-$(1/f)$-range value of $(1/f^{\text{extr}})_{\text{mid}} = 0.104$, and (if we take $(1/f^{\text{orth}})_{\text{mid}}$ as 4, as suggested above), to an adjustment-factor ω_{adjust} of 0.026. Thus, the adjusted FEF-value γ_C^{est} is around 3400.

The estimates derived via the above procedure should not be taken as scientifically valid numerical estimates of c_X-values, but they should have sufficient qualitative validity to be useful in technological contexts. In particular, this adjustment has the effect of reducing published FEF-values for materials that fail the orthodoxy test, and this may be of use in literature searches for materials with especially high values of true (electrostatic) macroscopic FEF. However, it is emphasized that this method currently has only the limited scientific basis set out here. A need exists for its degree of validity to be investigated by appropriate simulations, but currently this is difficult, because in many or most cases we do not currently know how to correctly model the effect that is presumed to be responsible for the problem in the first place.

5. Discussion

Hopefully, this paper demonstrates that useful progress is being made, both in giving a systematic scientific description of Fowler-Nordheim theory, and in establishing how to correctly analyze FN plots taken from materials that are not good conductors. Particular recent advances, discussed above, have been the incorporation of the voltage ratio Θ into equations, and the idea of phenomenological adjustment. However, much more remains to be done. The following seem immediately useful tasks.

(1) The orthodoxy test should be applied to a wider range of published FN plots, in order to establish the presence of any systematic trends.

(2) For emitters that have tested as "effectively orthodox", improved

methods need to be developed for extracting information about formal area efficiency α_f, so that we can obtain better understanding of the range of values that this parameter might take.

(3) The effect of series resistance on measured CFE current-voltage characteristics needs to be explored *experimentally* in well-controlled situations (for example, a known resistance value in series with a STFE of moderate-to-large apex radius, whose characteristics are known) and compared with simulations.

(4) The procedure of "phenomenological adjustment" needs to be applied to a range of published FN plots found to be non-orthodox.

(5) The consequences of using semiconductor-like band-structures, rather than metal-like band-structures, in theoretical discussions of FN plot interpretation need to be explored.

More generally, this work confirms our view that FN-plot analysis is best done by using the raw experimental data and $i_m(V_m)$-form plots (or alternatively $J_M(V_m)$-form plots), with FEF-values deduced from extracted LCL values (where reliable values are available).

Acknowledgement

Appendix A: Estimation of the Uncertainty Limits for λ_L

For the new-standard FN-type equation, where tunnelling takes place through an SN barrier, estimates can be made of the range within which the pre-exponential correction factor λ_L lies. As shown in Table 4, λ_L is the product of components, most of which have a range of variability or uncertainty associated with them. Values for the first three rows derive from calculations by Mayer [36]; a formula for temperature effects was first given by Murphy and Good [12]; the uncertainty related to row 5 comes from information provided by Modinos [37, 38]. This table is an improved version of one presented some years ago [39]. The values here can also be taken as "first estimates" applying to the value of λ_L in the general FN-type equation. There is some reason to think that, in comparison with more general "phase-integral" [40] methods for evaluating transmission probabilities, the methods normally used in FE theory (described earlier) are first-order approximations; consequently, Table 4 may in fact underestimate the true range of uncertainty.

TABLE 4. Estimated values for λ_L and its components (for "orthodox" FN-type equation based on SN barrier) (estimates made in September 2014).

Row No.	Physical origin of correction-factor component	Symbol for component	Value of correction-factor component	Source
1	Tunnelling pre-factor	P_F	~ (0.4 to 1.1)	[36]
2	Correct summation over states	λ_D	~ (0.9 to 1.3)	[36]
3	Combination of above effects[a]	$\lambda_D P_F$	~ (0.5 to 1.0)	[36]
4	Temperature effects at 300 K	λ_T (300 K)	~ 1.1	[12]
5	Electronic effects [atomic wave-functions & band-structure effects]	λ_E	~ (0.01 to 10)	[37,38]
6	All effects together	λ_L	~ (0.005 to 11)	

[a]Note that high values of λ_D tend to be associated with low values of P_F.

Appendix B: Definition of the Orthodox Field Electron Emission Measurement Situation

A field electron emission measurement situation is termed "orthodox" if the following conditions are adequately satisfied.

(1) The "emission voltage" (i.e., the voltage between the emitting surface region and the counter-electrode) can be treated as uniform across the emitting surface and equal to the measured voltage.

(2) The emission current can be treated as equal to the measured current, with this measured current being controlled solely by the emission at the emitter surface.

(3) Emission can be treated as if it involves deep tunnelling through a Schottky-Nordheim barrier, with the emission current described by a related FN-type equation in which the independent variable is, or is exactly proportional to, the measured voltage, and the only equation parameter depending on the measured voltage is the barrier-form correction factor.

(4) The emitter local work function is constant across the emitting region, is constant in time, is current independent and is equal to its assumed value.

These conditions are equivalent to assuming that, in the universal FN-type equation, the parameters ϕ, c_X, c_Y and C_{YX} may be treated mathematically as constants, ϕ has the correct value, and v_F^{GB} may be set equal to the SN-barrier-function value v_F.

Appendix C: Definitions and Approximations for Subsidiary SN-Barrier Functions

All the SN-barrier functions can be obtained from the principal SN-barrier function $v(f)$, discussed in Ref. [15]. The definitions and approximated expressions [based on Eq. (12)] given here are adapted from Ref. [11]. For Eq. (B4), values of η need to be derived from Eq. (13).

$$v(f) \approx 1 - f + (f/6)\ln f. \tag{C1}$$

$$u(f) = -\mathrm{d}v/\mathrm{d}f \approx (5 - \ln f)/6. \tag{C2}$$

$$s(f) = v - f\mathrm{d}v/\mathrm{d}f = v + uf \approx 1 - f/6. \tag{C3}$$

$$\left.\begin{array}{l} r_{2012}(f) = \exp[\eta u] \\ \qquad \approx \exp[(\eta/6)(5 - \ln f)] \end{array}\right\}. \tag{C4}$$

References

[1] Sommerfeld, A. and Bethe, H., "Handbuch der Physik", vol. 24, Part 2 ed. Geiger, H. and Scheel, K. (Berlin: Springer, 1933), p. 333.

[2] Forbes, R.G., Ultramicroscopy, 79 (1999) 25.

[3] Landau, L.D. and Lifshitz, E.M., "Quantum Mechanics" (First English Edition) (Oxford: Pergamon, 1958), §50. In this edition only, see Eq. (50.12).

[4] Forbes, R.G., J. Appl. Phys., 103 (2008) 114911.

[5] Fowler, R.H. and Nordheim, L., Proc. R. Soc. Lond. A 119 (1928) 173.

[6] Forbes, R.G. and Deane, J.H.B., Proc. R. Soc. Lond. A 467 (2011) 2927. See electronic supplementary material for information concerning relevant universal constants.

[7] Schottky, W., Phys. Z. 15 (1914) 772.

[8] Forbes, R.G., J. Vac. Sci. Technol. B 17 (1999) 526.

[9] Fowler, R.H., "Statistical Mechanics" (2nd edition) (Cambridge: CUP, 1936). See p. 357.

[10] Dyke, W.P. and Dolan, W.W., Adv. Electronics Electron Phys. 8 (1956) 89.

[11] Forbes, R.G. and Deane, J.H.B., Proc. R. Soc. Lond. A. 463 (2007) 2907.

[12] Murphy, E.L. and Good, R.H., Phys. Rev. 102 (1956) 1464.

[13] Forbes, R.G., Proc. R. Soc. Lond. A 469 (2013) 20130271.

[14] Forbes, R.G., Fischer, A. and Mousa, M.S., J. Vac. Sci. Technol. B 31 (2013) 02B103.

[15] Deane, J.H.B. and Forbes, R.G., J. Phys. A: Math. Theor. 41 (2008) 395301.

[16] Burgess, R.F., Kroemer, H. and Houston, J.M., Phys. Rev. 90 (1953) 515.

[17] Stern, T.E., Gossling, B.S. and Fowler, R.H., Proc. R. Soc. Lond. A 124 (1929) 699.

[18] Gomer, R., "Field Emission and Field Ionization" (Oxford: OUP, 1961).

[19] Dyke, W.P., Trolan, J.K., Dolan, W.W. and Barnes, G., J. Appl. Phys. 24 (1953) 570.

[20] Forbes, R.G., Edgcombe, C.J. and Valdrè, U., Ultramicroscopy 95 (2003) 57.

[21] Gomer, R., J. Chem. Phys. 20 (1952) 1772.

[22] Edgcombe, C.J. and Valdrè, U., Solid-State Electron. 45 (2001) 857.

[23] Forbes, R.G., J. Vac. Sci. Technol. B 27 (2009) 1200.

[24] Forbes, R.G. and Deane, J.H.B., J. Vac. Sci. Technol. B 28 (2010) C2A33.

[25] Spindt, C.A., Brodie, I., Humphrey, L. and Westerberg, E.R., J. Appl. Phys. 47 (1976) 5248.

[26] Forbes, R.G., Deane, J.H.B., Hamid, N. and Sim, H.S., J. Vac. Sci. Technol. B 22 (2004) 1222.

[27] Charbonnier, F.M. and Martin, E.E., J. Appl. Phys. 33 (1962) 1897.

[28] Fischer, A., Mousa, M.S. and Forbes, R.G., J. Vac. Sci. Technol. B 31 (2013) 032201.

[29] Fischer, A., Mousa, M.S., Deane, J.H.B. and Forbes, R.G., 26th International Vacuum Nanoelectronics Conf., Roanoke, July 2013.

[30] Forbes, R.G., ArXiv:1412.1821v4.

[31] Forbes, R.G. and Deane, J.H.B., 26th International Vacuum Nanoelectronics Conf., Roanoke, July 2013.

[32] Miranda, E., Electronics Lett. 40 (2004) 1153.

[33] Cha, S.I., Kim, K.T., Arshad, S.N., Mo, C.B., Lee, K.H. and Hong, S.H., Adv. Mater. 18 (2006) 553.

[34] Chen, L.-F., Ji, Z.-G., Mi, Y.-H., Ni, H.-L. and Zhao, H.-F., Phys. Scr. 82 (2010) 035602.

[35] Wisitsora-at, A., Hsu, S.-H., Kang, W.P., Davidson, J.L. and Tuantranont, A., J. Vac. Sci. Technol. B 30 (2012) 022204.

[36] Mayer, A., Deane, J.H.B. and Forbes, R.G., 23rd International Vacuum Nanoelectronics Conference, Palo Alto, July 2010.

[37] Modinos, A., Solid-State Electron. 435 (2001) 809.

[38] Modinos, A., Private communication to RGF.

[39] Forbes, R.G., J. Vac. Sci. Technol. B 26 (2008) 788.

[40] Fröman, N. and Fröman, P.O., "Physical Problems Solved by the Phase-Integral Method" (Cambridge: CUP, 2002).

Jordan Journal of Physics

ARTICLE

On the Distribution of Massive White Dwarfs and Its Implication for Accretion-Induced Collapse

Ali Taani

Physics Department, Faculty of Science, Al-Balqa' Applied University, P.O. Box 1199, 77110 Salt, Jordan.
Physics department, University of Sharjah, P. O. Box 27272 Sharjah, United Arab Emirates.

Abstract: A White Dwarf (WD) star and a main-sequence companion may interact through their different stellar evolution stages. This sort of binary population has historically helped us improve our understanding of binary formation and evolution scenarios. The data set used for the analysis consists of 115 well-measured WD masses obtained by the Sloan Digital Sky Survey (SDSS). A substantial fraction of these systems could potentially evolve and reach the Chandrasekhar limit, and then undergo an Accretion-Induced Collapse (AIC) to produce millisecond pulsars (MSPs). I focus my attention mainly on the massive WDs ($M_{WD} \geq 1 M_{\odot}$), that are able to grow further by mass-transfer phase in stellar binary systems to reach the Chandrasekhar mass. A mean value of $M \sim 1.15 \pm 0.2 M_{\odot}$ is being derived. In the framework of the AIC process, such systems are considered to be good candidates for the production of MSPs. The implications of the results presented here to our understanding of binary MSPs evolution are discussed. As a by-product of my work, I present an updated distribution of all known pulsars in Galactic coordinates pattern.
Keywords: Stars; Neutron stars; White dwarfs; X-ray binaries; Fundamental parameters.

Introduction

Standard stellar evolution models predict that all main-sequence stars in our galaxy with a mass lower than $10 M_{\odot}$ will end their lives as white dwarfs (WD), which represent more than 97% of all stars in the galaxy. Because their structural and evolutionary properties are relatively well understood, the characteristics and the physical parameters of WD populations can be used to constrain the evolutionary models and assess the amount of mass, which was lost by their progenitor stars due to the stellar evolution process [1-2]. We only know of a few confirmed examples of very massive WDs (> 1.2 $M_{\odot}$). Those binary systems are of particular interest because a small amount of accreted mass could drive them above the Chandrasekhar limit, beyond which they become gravitationally unstable [3]. Sloan Digital Sky Survey1 (SDSS)

has provided us with a very large sample of WD/main-sequence (WDMS) binaries [4]. This survey allowed us to make a meaningful contribution in terms of the pulsar production. One needs to implement the accretion-induced collapse (AIC) of a WD, which may lead to the formation of a proto neutron star [5 – 8]. This process represents a path alternative to thermonuclear disruption of accreting WDs in Type Ia supernovae (SNe). The scenario for O-Ne-Mg WD begins once the nuclear reaction starts at the center, the burning propagates throughout the entire star and the ignition occurs in the interior. The burning that propagates outward makes central temperatures and pressures high enough to lead instead to a collapse of the WD and induce the contraction of the star. This continues until it reaches the

Corresponding Author: Ali Taani   **Email**: ali82taani@gmail.com , ali.taani@bau.edu.jo

Chandrasekhar limit, and finally the star collapses homogeneously leading to the formation of a neutron star. Consequently, the AIC can be a significant contribution to the total number and evolution of low mass X-ray binaries [9]. In the AIC scenario, the explosion energy is expected to be small (10^{49} erg s^{-1}) and the resulting dim and short-lived, making it hard to detect by electromagnetic means [10] and neutrino means alone [11]. Gravitational-wave observations may provide crucial information necessary to reveal a potential AIC. On the other hand, the coalescence of double CO WDs of which the total mass exceeds the Chandrasekhar limit is also likely to end in a collapse induced by electron capture to form a rapidly rotating neutron star, rather than an SNe Ia [12]. However, the nature of the Type Ia progenitors, as well as their precise explosion mechanism, remain a subject of active investigation, both observationally as well as theoretically [13 – 14]. In either AIC or a WD-WD merger, the WD will be rapidly rotating prior to collapse and must eject a sizable fraction of its mass (~0.1 - 0.2 $M_\odot$) into a disk during the collapse in order to conserve angular momentum [15, 7].

The Observed Population of WDs

Our present study of SDSS has the following aspects. First, the large and more homogeneous sample of SDSS 2, now available, allows us to test for possible dependencies of the formation and evolution of WD on the stellar masses at the onset of common envelope evolution. Second, I select the sample of massive WDs in binary systems in the range of M $\geq$ 1$M_\odot$ (which is considered a relatively small number) causing a higher accretion rate onto the WD, which can reach the Chandrasekhar limit. Finally, the star collapses homogeneously, leading to the formation of a rapidly rotating pulsar. Potential biases affecting the SDSS sample have been analyzed with respect to the WD mass distribution [16]. The sample of WDs analyzed here consists of 115 sources (see Table 1). Fig. 1 shows the Gaussian distribution with mean at M_{WD} ~ 1.15$M_\odot$, where the median mass of these sources is M_{WD} = 1.181 ± 0.16$M_\odot$. Furthermore, the knowledge of this distribution is therefore fundamental to understanding the mechanisms involved in the final stages of stellar evolution. I fit the Gauss function to the mass distributions. The Gauss function I chose reads:

$$y = y0 + \frac{A}{w0\sqrt{\frac{\pi}{2}}}\exp\left(-2\left(\frac{x-x0}{w0}\right)^2\right) \quad (1)$$

where y_0, x_0, w_0 and A are offset of y-axis, center of x-axis, width and area represented by the curve, respectively. The value of R (correlation coefficient) expresses the quality of the fitted result. The fitting results are listed in Table 2. It is noteworthy to mention here that the AIC process leads to millisecond pulsar (MSP) with mass less than Chandrasekhar limit [17] and the binding energy also increases; this effect is significant in the estimation of the amount of mass accretion [15]. If matter is accreted at a rate of $M_\odot$ ~ 10^{16}gs^{-1} [18] and the total mass accreted exceeds a critical value ΔM_{crit} ~ 0.1 - 0.2$M_\odot$ within 10^9 yrs, then the massive WD will be recycled to become an MSP after the mass reaches the Chandrasekhar limit. One can consider an estimate of the amount of gravitational binding energy (mass loss), due to the conversion from O-Ne-Mg WD matter to MSP. Let us begin with the magnitude of the gravitational potential energy in NS [19]:

$$E = \frac{GM^2}{R} \quad (2)$$

where G is the gravitational constant, M the mass of the companion, R the NS radius.

$$E = \left(\frac{2GM}{c^2}\right)\frac{Mc^2}{2R} \rightarrow \frac{R_S Mc^2}{2R} \quad (3)$$

where R_S is Schwartzchild radius ($R_S = 2GM/c^2$ ~ 3 km for (M = 1$M_\odot$)).

$$E = \eta Mc^2 \quad (4)$$

where η = R_S/ 2R, thus:

$$E \sim 0.1 Mc^2. \quad (5)$$

As a result, around 10% of mass will go as binding energy and reduce the mass of the amount 1.4$M_\odot$ by about 0.14$M_\odot$, where the total energy is:

$$Mc^2(1-\eta). \quad (6)$$

This effect is significant in the estimation of the amount of accreted mass. However, unfortunately, most of the studies argued that the binding energy of the NS is not commonly considered [15]. More modeling is required to support such a conclusion.

TABLE 1. Parameters of binary systems of WDs with compact companions. Data were taken from SDSS catalogue.

IAU Name	$M_{wd}(M_\odot)$	Errors $M_{wd}(M_\odot)$	$M_{seccandary}(M_\odot)$	$E_{rros}M_{sec}(M_\odot)$	$R_{wd}(R_\odot)$
SDSSJ001247.18+001048.7	1.23	0.442	0.38	0.072	0.00538
SDSSJ001855.19+002134.5	1.24	0.391	0.38	0.072	0.00526
SDSSJ002157.90-110331.6	1.08	0.051	0.319	0.09	0.0071
SDSSJ002959.94+001132.7	1.15	0.386	0.431	0.1	0.00637
SDSSJ003301.53+005716.9	1.19	0.286	0.38	0.072	0.00588
SDSSJ003643.33+252754.9	1	0.113	0.118	0.004	0.00807
SDSSJ003731.07+010947.0	0.98	0.629	0.319	0.09	0.00826
SDSSJ004511.95+250330.9	1.13	0.037	0	0	0.00654
SDSSJ004604.14+011037.4	1.16	0.386	0.464	0.088	0.00618
SDSSJ005245.11-005337.2	1.26	0.365	0.319	0.09	0.00502
SDSSJ011634.11+002956.5	0.93	0.348	0.319	0.09	0.00898
SDSSJ013504.31-085919.0	1.23	0.222	0.319	0.09	0.00538
SDSSJ015434.31-010611.1	0.98	0.688	0.255	0.124	0.00818
SDSSJ015657.37-003341.6	0.91	0.357	0.464	0.088	0.0093
SDSSJ020925.74+064213.9	1.15	0.15	0.319	0.09	0.00644
SDSSJ021309.19-005025.4	1.02	0.423	0.38	0.072	0.00779
SDSSJ024642.55+004137.2	0.95	0.099	0.38	0.072	0.00873
SDSSJ024645.89-010624.1	1.31	0.355	0.38	0.072	0.0044
SDSSJ030351.97+003548.4	1.307	0.281	0.431	0.1	0.00448
SDSSJ030904.82-010100.8	0.977	0.406	0.355	0.072	0.00846
SDSSJ031206.82-002145.4	1.13	0.651	0.319	0.09	0.00654
SDSSJ032656.44+002232.1	1.105	0.447	0.431	0.1	0.00694
SDSSJ033804.40+002740.3	1.37	0.091	0	0	0.0038
SDSSJ035912.46-044630.2	1.24	1.058	0.38	0.072	0.00525
SDSSJ052624.54+621344.2	1.07	0.037	0.38	0.072	0.00723
SDSSJ073250.34+393633.9	0.905	0.074	0	0	0.00917
SDSSJ074207.89+275845.1	1.385	0.054	0.319	0.09	0.00355
SDSSJ075325.93+164132.7	1.19	0.411	0.464	0.088	0.00581
SDSSJ080304.61+121810.3	1.04	0.274	0.431	0.1	0.00768
SDSSJ080653.95+160729.8	0.91	0.269	0.38	0.072	0.0091
SDSSJ081312.09+324758.6	0.9	0.204	0.255	0.124	0.00917
SDSSJ081811.70+173224.5	1.04	0.173	0.38	0.072	0.00768
SDSSJ081831.07-010923.1	1.14	0.311	0.38	0.072	0.00648
SDSSJ083722.44+265417.3	0.94	0.065	0.319	0.09	0.00877
SDSSJ083827.09+415015.5	1.07	0.365	0.464	0.088	0.00723
SDSSJ083920.48+125959.5	1.12	0.154	0.118	0.004	0.0066
SDSSJ084009.24+281201.9	1.07	0.262	0.38	0.072	0.00756
SDSSJ084056.91+275513.7	1.07	0.203	0.38	0.072	0.0073
SDSSJ084307.27+122610.1	0.95	0.129	0.196	0.085	0.0086
SDSSJ084400.82+052305.7	0.94	0.284	0.319	0.09	0.00893
SDSSJ085847.47+371115.5	1.03	0.366	0.464	0.088	0.00849
SDSSJ091143.09+222748.8	1.46	0.051	0.38	0.072	0.0027
SDSSJ091309.70+223346.7	0.98	0.167	0.431	0.1	0.00828
SDSSJ092200.71+181714.1	1.02	0.187	0.38	0.072	0.0078
SDSSJ092313.99+205119.9	1.16	0.18	0.38	0.072	0.00623
SDSSJ092433.98+204020.0	1.04	0.113	0.319	0.09	0.00754
SDSSJ093236.83+053026.6	1.02	0.16	0.464	0.088	0.0078
SDSSJ093426.60+053753.6	0.93	0.277	0.319	0.09	0.00912
SDSSJ093427.91+204658.6	1.03	0.418	0.196	0.085	0.00759
SDSSJ093526.43+245423.4	1.02	0.224	0.431	0.1	0.00785
SDSSJ093632.33+341932.6	1.03	0.114	0.319	0.09	0.00767

IAU Name	$M_{wd}(M_\odot)$	Errors $M_{wd}(M_\odot)$	$M_{seccandary}(M_\odot)$	$E_{rros}M_{sec}(M_\odot)$	$R_{wd}(R_\odot)$
SDSSJ094002.40+534202.9	0.95	0.159	0.255	0.124	0.00868
SDSSJ094542.61+173859.9	1.01	0.185	0.472	0.062	0.00821
SDSSJ094720.94+111734.7	1.12	0.193	0.464	0.088	0.0074
SDSSJ094821.30+365935.3	1.26	0.135	0.38	0.072	0.00501
SDSSJ094952.73+012603.4	1.14	0.248	0.319	0.09	0.00648
SDSSJ100015.18+304330.5	0.93	0.214	0.255	0.124	0.00898
SDSSJ100609.18+004417.0	0.93	0.083	0.118	0.004	0.00879
SDSSJ101006.92+301211.3	1.2	0.158	0.255	0.124	0.00568
SDSSJ101116.29+182749.5	0.92	0.229	0	0	0.00992
SDSSJ101124.31+644655.5	1.15	0.166	0.118	0.004	0.00636
SDSSJ101614.69+490930.3	1.01	0.168	0.319	0.09	0.00801
SDSSJ102213.46+294119.9	1.275	0.315	0.319	0.09	0.00483
SDSSJ104459.32+360554.7	1.24	0.052	0.255	0.124	0.00519
SDSSJ105038.62+413834.5	0.95	0.085	0.196	0.085	0.00861
SDSSJ110736.88+612232.8	1	0.043	0.464	0.088	0.00815
SDSSJ114720.00+112813.3	0.91	0.296	0.464	0.088	0.00909
SDSSJ114913.52-014728.6	0.9	0.057	0.319	0.09	0.00917
SDSSJ120222.10+411810.8	0.97	0.414	0.38	0.072	0.0087
SDSSJ121928.05+161158.7	0.98	0.124	0.196	0.085	0.00818
SDSSJ122634.97+322020.8	1.36	0.108	0.319	0.09	0.00379
SDSSJ122850.46-022509.4	1.18	0.379	0	0	0.00599
SDSSJ122930.65+263050.4	1.04	0.077	0.38	0.072	0.0077
SDSSJ125207.48+444827.8	0.9	0.231	0	0	0.00938
SDSSJ125919.51+321935.4	0.9	0.116	0.38	0.072	0.00915
SDSSJ131156.69+544455.8	1.19	0.036	0.431	0.1	0.0058
SDSSJ132652.62+000855.3	0.97	0.446	0.464	0.088	0.00863
SDSSJ134557.68+330050.6	0.97	0.097	0.464	0.088	0.00839
SDSSJ134714.30+412909.6	1.25	0.142	0.431	0.1	0.00513
SDSSJ135502.75+574058.3	1.46	0.049	0	0	0.0027
SDSSJ142241.90+513537.9	1.23	0.043	0	0	0.00537
SDSSJ143519.16+362952.0	1.02	0.121	0.319	0.09	0.00773
SDSSJ145514.56-022822.2	0.94	0.381	0.149	0.075	0.00866
SDSSJ151714.96+423924.7	1.25	0.02	0.38	0.072	0.00507
SDSSJ151817.97+455334.1	0.97	0.245	0.464	0.088	0.00833
SDSSJ154609.98+200320.6	1.12	0.208	0.464	0.088	0.00674
SDSSJ154928.56+385419.3	0.93	0.222	0.431	0.1	0.00882
SDSSJ155332.86+045735.1	0.91	0.174	0.38	0.072	0.0091
SDSSJ155933.42+340502.5	0.96	0.254	0	0	0.00838
SDSSJ160821.47+085149.9	0.98	0.083	0.196	0.085	0.00826
SDSSJ160824.57+285524.9	1.06	0.286	0.319	0.09	0.00742
SDSSJ161715.27+081849.0	1.02	0.295	0.464	0.088	0.0079
SDSSJ161726.96+385557.5	1.02	0.282	0.319	0.09	0.00807
SDSSJ162324.05+343647.7	0.97	0.071	0.118	0.004	0.00832
SDSSJ170127.36+253302.6	1.01	0.08	0.38	0.072	0.00793
SDSSJ170843.52+215829.0	1.27	0.224	0.464	0.088	0.00502
SDSSJ171145.42+555444.4	0.94	0.04	0.319	0.09	0.01017
SDSSJ171411.14+294508.2	0.91	0.231	0.319	0.09	0.00933
SDSSJ172008.58+565211.8	1.29	0.276	0.464	0.088	0.00471
SDSSJ205059.37-000254.3	0.95	0.099	0.319	0.09	0.00862
SDSSJ205316.52-010616.5	0.9	0.112	0.38	0.072	0.00915
SDSSJ210624.12+004030.2	1.03	0.105	0.464	0.088	0.00774
SDSSJ210751.44+005854.4	1.01	0.268	0	0	0.00811
SDSSJ211132.76+011522.2	0.96	0.124	0.431	0.1	0.00847

IAU Name	$M_{wd}(M_\odot)$	Errors $M_{wd}(M_\odot)$	$M_{seccandary}(M_\odot)$	$E_{rros}M_{sec}(M_\odot)$	$R_{wd}(R_\odot)$
SDSSJ211205.31+101427.9	1.06	0.051	0.196	0.085	0.00744
SDSSJ214447.51+004201.5	1.01	0.446	0.149	0.075	0.00785
SDSSJ215744.77-004015.1	1.2	0.345	0.319	0.09	0.00575
SDSSJ220848.99+122144.7	1.24	0.134	0	0	0.00568
SDSSJ224522.42-000109.5	1.11	0.222	0.38	0.072	0.00686
SDSSJ224932.02+000645.7	1.08	0.217	0.196	0.085	0.00709
SDSSJ231014.62+001439.9	1.07	0.32	0.38	0.072	0.00722
SDSSJ232527.81-005416.7	0.93	0.194	0.255	0.124	0.00898
SDSSJ232624.72-011327.2	1.46	0.372	0.38	0.072	0.00269
SDSSJ232816.06+010036.0	1.31	0.931	0.38	0.072	0.00447
SDSSJ234749.84+431424.6	0.99	0.079	0.255	0.124	0.0082
SDSSJ235324.74+351623.2	1.08	0.211	0.255	0.124	0.00709
SDSSJ011355.84-093938.0	1.24	0.156	0.319	0.09	0.00519
SDSSJ041518.90+165238.2	1.28	0.066	0	0	0.00483
SDSSJ042437.67+063408.2	0.92	0.169	0.464	0.088	0.0099
SDSSJ044542.27+120246.7	1.15	0.168	0.255	0.124	0.00635
SDSSJ064411.89+285301.1	0.96	0.122	0	0	0.00936
SDSSJ064715.54+275948.3	1	0.13	0	0	0.00799
SDSSJ085224.02+111520.8	0.93	0.407	0.319	0.09	0.00898
SDSSJ093349.93+151718.5	1	0.125	0.431	0.1	0.00825
SDSSJ100811.87+162450.4	1.23	0.07	0.464	0.088	0.00575
SDSSJ113223.69+225313.1	0.98	0.053	0.464	0.088	0.00845
SDSSJ113511.13+000923.9	0.935	0.157	0.319	0.09	0.00875
SDSSJ125645.47+252241.6	1.01	0.06	0.255	0.124	0.00818
SDSSJ140516.05+232246.9	0.94	0.069	0	0	0.00883
SDSSJ141451.60+193638.9	1.07	0.13	0.196	0.085	0.00716
SDSSJ173430.11+335407.5	1.19	0.133	0.319	0.09	0.00586
SDSSJ213225.96+001430.5	0.92	0.125	0.319	0.09	0.00904
SDSSJ011123.90+000935.2	0.93	0.202	0.431	0.1	0.00899
SDSSJ014232.59-083528.4	1.07	0.05	0.38	0.072	0.00722
SDSSJ025347.51+335221.0	1.02	0.121	0.431	0.1	0.00808
SDSSJ044831.02+214909.8	1.01	0.11	0.38	0.072	0.00793
SDSSJ072130.60+374228.3	0.96	0.102	0.319	0.09	0.00854
SDSSJ072434.72+321609.4	0.98	0.051	0.319	0.09	0.00835
SDSSJ085223.75+071326.0	0.92	0.231	0.319	0.09	0.00896
SDSSJ102102.25+174439.9	1.06	0.087	0.319	0.09	0.00768
SDSSJ112308.40-115559.3	1.26	0.07	0.255	0.124	0.00501
SDSSJ112651.03-081640.1	1.26	0.125	0.431	0.1	0.00501
SDSSJ120953.67+185815.7	0.96	0.126	0.464	0.088	0.00883
SDSSJ130012.49+190857.4	1.09	0.103	0.319	0.09	0.0069
SDSSJ135207.77+185033.8	1.1	0.122	0.38	0.072	0.00684
SDSSJ141052.79+375435.6	1.03	0.074	0.464	0.088	0.00767
SDSSJ142503.62+073846.4	0.97	0.13	0.38	0.072	0.0087
SDSSJ142631.93+091621.1	1.4	0.075	0.38	0.072	0.00343
SDSSJ142951.19+575949.0	1.07	0.131	0.38	0.072	0.0073
SDSSJ143143.83+565728.2	1	0.285	0.255	0.124	0.00799
SDSSJ145305.77+001048.2	0.95	0.054	0.319	0.09	0.00861
SDSSJ153009.49+384439.8	0.92	0.282	0.431	0.1	0.00895
SDSSJ155808.49+264225.7	1.06	0.309	0.319	0.09	0.00736
SDSSJ162354.45+630640.4	1	0.089	0.319	0.09	0.00799
SDSSJ173849.76+635042.0	0.93	0.123	0.38	0.072	0.00898
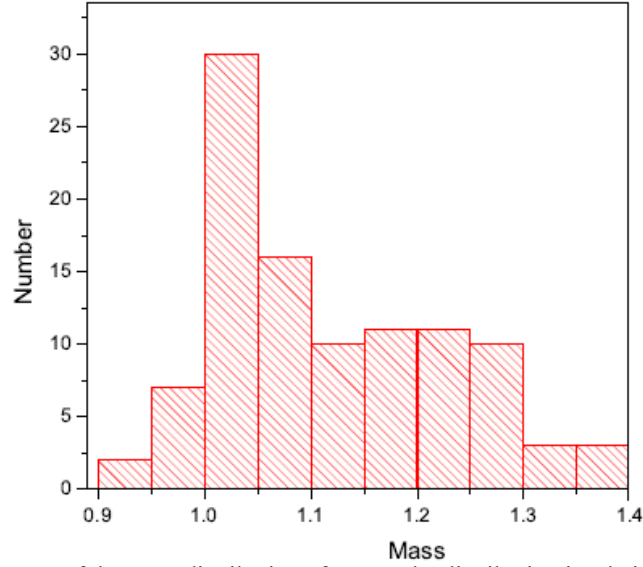
FIG. 1. Histograms of the mass distribution of WDs. The distribution is relatively Gaussian.

TABLE 2. The fitting results of the distribution for mass of WDs.

Quantity	y_0	x_0	w	A	σ	χ^2/Dof	R^2
$M_{W\,Ds}$	0.53 ± 0.64	0.79 ± 0.012	0.40 ± 0.03	12.30 ± 0.92	0.20	3.311	0.955
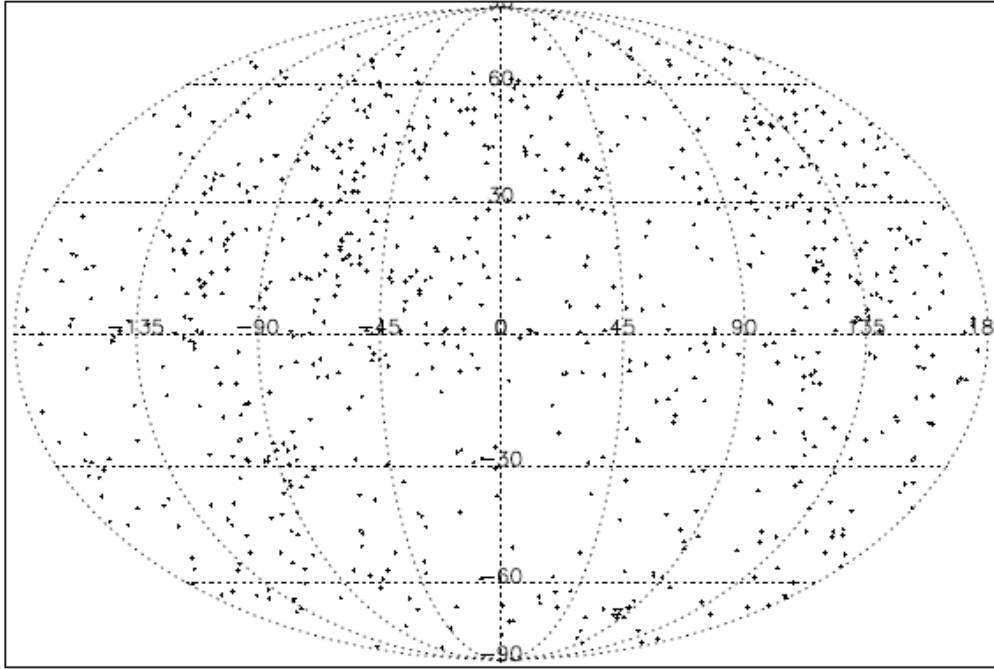
FIG. 2. The full-sky distribution of all known WDs, shown in Galactic coordinates in which the plane of the Galaxy is at the equator and the Galactic center is at the origin. The data are taken from [23].

Fig. 2 shows the spatial density distribution of the current sample of all known WD systems throughout the Galaxy. The scale-height of the WDs is somewhat completed and uniformly distributed.

Summary and Conclusions

Interacting binaries can play an important role in terms of studying the mass transfer and orbital motion of the companions as well as the effects of binary evolution on the final fate of the compact objects and SNe.

In the frame of this process, the AIC scenario to produce binary MSPs must be invoked, since it is expected to turn into normal magnetized rotating neutron stars, which in binaries can evolve into MSPs through the recycling process. In addition, it could provide us with a better match to the period distributions of some types of binary MSPs. One example is the double relativistic pulsar PSR J0737–3039 [20 − 21], and it seems to be an interesting issue requiring further studies for the analysis of the formation of neutron stars in Galactic disk as well as globular clusters. Since the evolution of accreting WDs seriously affects the pulsar production via mass and angular momentum accretion during the AIC scenario, substantial adjustments to the current picture on MSP progenitor population are requires. I will add this clarification and point out possibilities for future research.

Finally, it is worth mentioning here that the most highly magnetized WDs are massive as well as isolated. This depends on the strength of the WD magnetic field. The matter flowing through the inner Lagrangian point (L1) can form either a full or a partial accretion disk [22] or else follow the magnetic field lines down to the surface at the magnetic poles. Thus, it is important to monitor long orbital period of WD systems in order to gain insight into the dynamics and binary evolution of those systems that are most likely to undergo the AIC process.

References

[1] Warner, B. and Woudt, P.A., ASP Conf. Seri., 261 (2002) 406, arXiv: astro-ph/0109397.

[2] Zorotovic, M., Schreiber, M.R., Gänsicke, B.T. and Nebot Gómez-Morán, A., A&A, 520 (2010) 86.

[3] Mereghetti, S., Tiengo, A., Esposito, P., La Palombara, N., Israel, G.L. and Stella, L., Science, 325 (2009) 1222.

[4] Abazajian, K.N., Adelman-McCarthy, J.K., Agüeros, M.A., Allam, S. S. et al., ApJS, 182 (2009) 543.

[5] Nomoto, K., Astrophys. J., 322 (1987) 206.

[6] Taani, A., Zhang, C.M., Al-Wardat, M. and Zhao, Y.H., AN, 333 (2012a) 53.

[7] Taani, A., Zhang, C.M., Al-Wardat, M. and Zhao Y.H., Ap&SS, 340 (2012b) 147.

[8] Tauris, T.M., Sanyal, D., Yoon, S.-C. and Langer, N., A&A, 558A (2013) 39.

[9] van den Heuvel, E.P.J., Science, 303 (2004) 1143.

[10] Darbha, S., Metzger, B.D., Quataert, E., Kasen, D., Nugent, P. and Thomas, R., MNRAS, 409 (2010) 846.

[11] Metzger, B.D., Piro, A.L. and Quataert, E., MNRAS, 396 (2009) 304.

[12] Podsiadlowski, Ph., Langer, N., Poelarends, A.J.T., Rappaport, S., Heger, A. and Pfahl, E., ApJ, 612 (2004) 1044.

[13] Han, Z., ApJ, 677 (2008) L109.

[14] Wang, B. and Han, Z., Ap&SS, 329 (2010) 293.

[15] Bagchi, M., arXiv:1004.2730v2 (2011).

[16] Rebassa-Mansergas, A., Nebot Gómez-Morán, A., Schreiber, M. R., Girven, J. and Gänsicke, B.T., MNRAS, 413 (2011) 1121.

[17] Zhang, C.M., Wang, J., Zhao, Y.H. et al., A&A, 527 (2011) A83.

[18] Zhang, C.M. and Kojima, Y., MNRAS, 366 (2006) 137Z.

[19] Shapiro, S.L. and Teukolsky, S.A., "Black Holes, White Dwarfs and Neutron Stars", 8th Ed. (Wiley, New York, 1983) chapter 14.

[20] Burgay, M., D'Amico, N., Possenti, A., Manchester, R.N., Lyne, A.G., Joshi, B.C., McLaughlin, M.A. et al., Nature, 426 (2003) 531.

[21] Lyne, A.G., Burgay, M., Kramer, M., Possenti, A., Manchester, R.N., Camilo, F., McLaughlin, M.A. et al., Science, 303 (2004) 1153.

[22] Zhang, C.M., Wickramasinghe, D.T. and Ferrario, L., MNRAS, 397 (2009) 2208Z.

[23] Ritter, H. and Kolb, U., A&A, 404 (2003) 301 (update RKcat7.21, 2014) http://www.mpa-garching.mpg.de/RKcat/

Jordan Journal of Physics

ARTICLE

Non-Destructive SR-XRF Analysis of Ancient Mamluk-Ayyubid Glazed Pottery Fragments from Karak Castle, Jordan

A. Aldrabee[a], **A. Wriekat**[a], **K. AbuSaleem**[a,b] and **M. Radtke**[c]

[a] *Jordan Atomic Energy Commission(JAEC), Shafa Bdran 11934, Amman, Jordan.*
[b] *The University of Jordan, Amman 11942, Jordan.*
[c] *BAM Federal Institute for Materials Research and Testing, Richard-Willstätter-Str. 11, 12489 Berlin, Germany.*

Abstract: Sixteen Ayyubid-Mamluk glazed pottery sherds were analyzed in order to identify and characterize the elemental composition to determine their provenance. The tested sherds were collected from the historical site of Karak Castle, southern Jordan. Chemical analysis for the sixteen samples has been carried out using Synchrotron Radiation X-ray Fluorescence Spectrometry (SR-XRF) Technique. Furthermore, the semi-quantitative analysis of the elements Fe – Cu – Zn – Br – Rb – Sr – Y – Zr – Nb – Mo – Pd – Ag – Cd and Pb has been performed for the samples based on Principal Component Analysis (PCA) and hierarchical Cluster Analysis with Bray-Curtis in order to define grouping of different glazed pottery by obtaining information on their similarity and clustering. The results of chemical analysis provided persuasive evidence that the Karak Castle pottery sherds have at least three different sources of provenance.

Keywords: SR-XRF; Semi-quantitative; Karak Castle; Ayyubid-Mamluk pottery; Non-destructive, Multivariate statistical.

Introduction

During the past years, several studies have been carried out concerning the analysis of archaeological ceramics employing different techniques. Many studies dealt with the determination of chemical composition [1]. One of the most important questions asked by archaeologists is pertinent to the provenance of the excavated object. Provenance studies provide a more objective assessment of the movement of pottery as each vessel carries a chemical 'fingerprint' derived from the clay of which it was made. Thus, it becomes a simple matter to establish chemical compositional groups, using a suitable multivariate statistical procedure, in order to detect outliers or overlapping samples which could indicate imports or exports [2].

According to their analyzing ability, the Synchrotron Radiation X-ray Fluorescence Spectrometry (SR-XRF) has gained an increasing interest in the field of elemental analysis [3]. Several works showing the advent of technique based on XRF can be found in the literature during the past decade. This technique can be claimed as an instrumental key that has revolutionized the analytical scene in archaeometry, as in other fields [4-8].

Semi-quantitative procedures [9] are very well suited for the analysis of samples with various unknown chemical compositions and matrices. It should be noted that the term 'semi-quantitative' is contradictory and is not used in a uniform way. In certain cases, this may lead to misunderstandings and therefore the word 'semi-quantitative' is set in quotation marks [10]. As for glass and ceramic samples, the problem of quantitative XRF analysis does not arise

---

normally from the irregular shape, but because of the difficulty of evaluating the auto absorption correction due to matrix low Z elements which in most cases cannot be detected by standard solid-state portable detectors [11].

Semi-quantitative analytical procedures are increasingly becoming popular among scientists. It is worth mentioning here that the accuracy of an analytical procedure depends to a great extent on the spectral resolution, counting statistics, matrix correction and analytical procedure which are especially optimized to provide fast analysis of metals and alloy composition [10]. The energy and intensity of the XRF spectral lines are not only in accordance with the corresponding element, but also with its abundance in the sample [12].

This study presents the characterization of a group of ancient pottery. The characterization focuses on the statistical methods of chemical composition based on semi-quantitative measurements in order to define grouping of different pottery sherds. The extracted information will help know more about the provenance sources of Ayyubid-Mamluk ceramic in the site, which will strengthen the

information drawn from the elaboration of compositional data and shed new light on the importance of the region as an agricultural center and a trade link between the Mamluk centers in Egypt and Syria during the Ayyubid-Mamluk period.

Archaeological Site Settings and Sampling

Karak Castle is one of the largest crusader castles in the levant (Fig. 1). It is located in Karak town which is now the administrative center of Liwa Al-Karak. It is situated on a hilltop about 1000 meters above sea level and is surrounded at three sides by deep valleys. The town is located 130 km south of Amman the capital of Jordan. It is located on the King's Highway, east of the Dead Sea in the biblical land of Moab. The Castle, perched on an elevated escarpment, was laid out on a roughly trapezoidal plan which followed the contours of the ridge on the western and eastern sides (240m and 220m, respectively), while on the northern and southern fronts (130m and 85m, respectively) the castle was protected by deep dry moats [13].
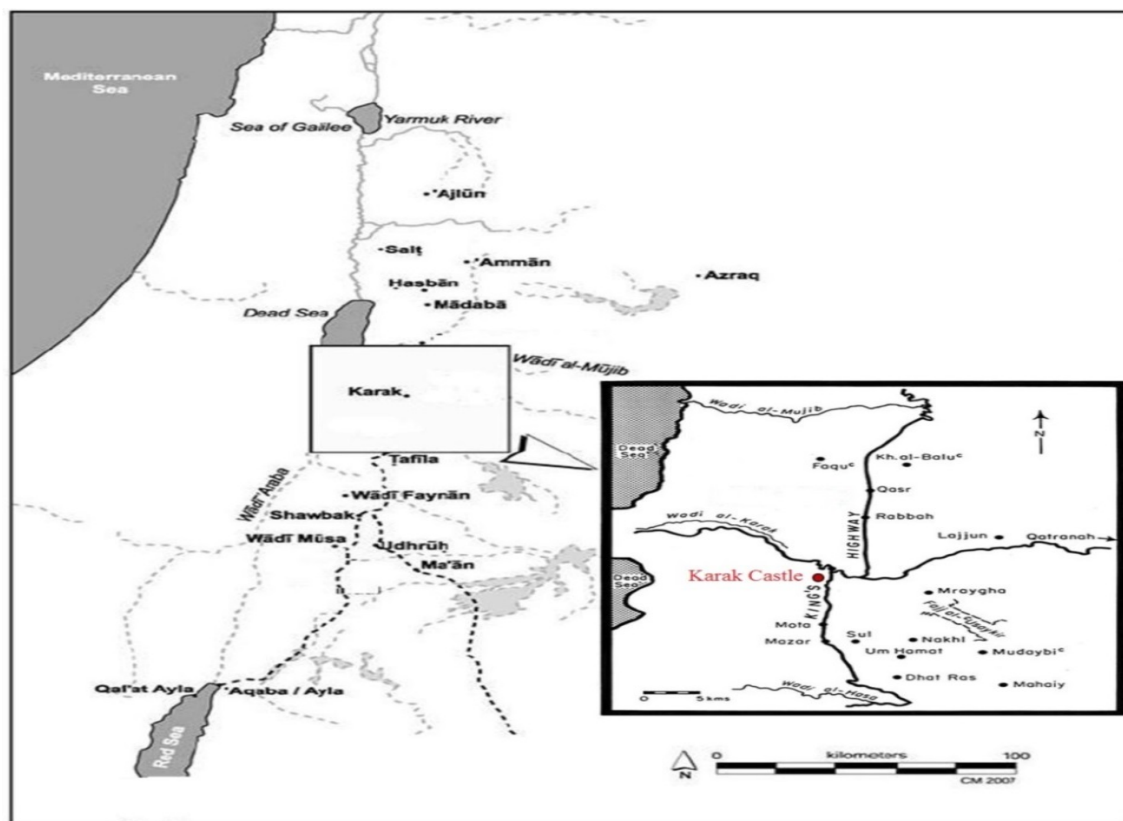
FIG. 1. Map of Jordan showing Karak Castle site and the Karak plateau.

FIG. 2. The ancient glazed ceramic sherds from Karak Castle.

Measurements and Analysis

To perform the analysis of the samples using SR-XRF, the inner part (core) of the samples was exposed to synchrotron X-ray Beam. All measurements were carried out in BAMLine at BESSY II Synchrotron light source in Berlin-Germany using 40 keV incident energy X-ray beam, focused to a (0.8x0.8) mm^2 spot size. From each tested sample, data have been acquired using an Si(Li) detector from two selected points on the core to be representative of the sample. The measurement time was 60 seconds for each sample. All measurements have been performed at room temperature. The spectra were processed by the AXIL-PC computer software program [14] based on IAEA standard program package QXAS. In order to be able to perform a semi-quantitative analysis, the elemental composition of the samples has to be identified. This task can be achieved by calculating the area under the XRF peaks. The used software in this analysis has the capability to perform the task. Semi-quantitative estimation can be a useful tool for determination of elemental concentrations, because the latter are proportional to the weight concentrations that can be measured using this technique.

The intensity of emission from each element can classify the elements. The area under the peak (counts) for a certain element in an XRF spectrum is used to calculate the abundance of the element in the sample, since the peak intensities are proportional to the concentration of the element present in the sample.

Statistical Methods

In the archaeological studies, Cluster Analysis together with Principal Component Analysis (PCA) are the most common methods used to classify items in subgroups. The PCA is a mathematical technique that allows n-dimensional identification of sample groups and is a very powerful method of exploratory multivariate statistical analysis. Also, it is often used in the interpretation of XRF artifact characterization for helping archaeologists to identify discrete compositional groups within a data set. This information may then be applied to formulate and test hypotheses on trade and exchange routes and socio-economic relationships. Cluster Analysis is a method which provides evidence for grouping the objects within the data set. The results are commonly presented as dendrograms showing

159

the order and levels of clustering as well as the distances between individual samples [15-17].

In this work, the Bray-Curtis coefficient [18] was used to calculate similarity matrices for analysis. The Bray-Curtis coefficient is widely used in provenance determination of cultural heritage artifacts. The dendrograms were constructed using a group-average linkage hierarchical Cluster Analysis [19]. All data have been maintained and processed by the computer software package Unscrambler X Ver.10.1 (Camo ASA software, Oslo, Norway).

Results and Discussion

The SR-XRF results of Karak Castle samples are presented in Table1. The analysis results are represented by the net peak area data (in counts) for selected elements of the XRF spectra which reflect the abundance of these elements in the samples in order to perform a semi-quantitative analysis. Only 14 elements were analyzed: Fe, Cu, Zn, Br, Rb, Sr, Y, Zr, Nb, Mo, Pd, Ag, Cd and Pb. The final data set consists of 16 samples with 14 elements for ceramic pottery sherds from Karak Castle site with a total of 224 data entries. PCA and Cluster Analysis were performed. The multivariate statistical analyses have been carried out to verify the similarity between the samplings.

PCA and Cluster Analysis are routinely applied to analytical data for the purpose of group identifying of chemically similar sherds. Chemically similar sherds can be interpreted as representing, as they are made of the same raw materials or mixtures of raw materials. But this is not necessarily at the same time. Fig. 3 and Fig. 4 illustrate the Principal Component Analysis (PCA) and Cluster Analysis (CA) for the data presented in Table (1).

The data have been applied to the raw data matrix of dimensions 16×14 (samples × chemical parameters). Fig. 3 represents the scatter score plot of PC1 and PC2. The corresponding score plot suggests two large groups, while three samples; namely: CSL10, CSL12 and CSL16 do not belong to any of these two groups. Each of the two groups contains the samples that belong to the same pottery provenance source.

The two groups are characterized as follows:

(1) Group A (CSL1, CSL2, CSL3, CSL4, CSL5, CSL6 and CSL11). This group is characterized by high concentration of Iron and Strontium and low concentration of Lead as compared to samples of group B.

(2) Group B (CSL7, CSL8, CSL9, CSL13, CSL14 and CSL15). The samples belonging to this group are characterized by very high concentrations of Lead and medium concentrations of Zirconium compared to samples of group A. The samples CSL10, CSL12 and CSL16 do not belong to any of these groups as demonstrated by their different elemental composition. CSL10 shows average concentrations of Lead and Iron, while CSL12 contains high content of Lead. Sample CSL 16 contains high content of Iron and very little content of Lead. This differentiates them from groups A & B.

The hierarchical Cluster Analysis is based on Median linking and Bray-Curtis distances. The resulting dendrograms for 16 ceramic sherd samples (from Karak Castle site) were normalized as the area under the peak data as presented in (Fig. 4). The graph shows that the data set has two large distinguished groups: the 1st group consists of (CSL1, CSL2, CSL3, CSL4, CSL5, CSL6 and CSL11), and the 2nd group contains (CSL7, CSL8, CSL9, CSL13, CSL14 and CSL15). This result conforms with the PCA result. It is worth noticing that samples CSL10, CSL12 and CSL16 do not belong to any of these two groups. (CSL12 and CSL16 could to a lesser extent belong to Group B and Group A, respectively, but the verification of this result needs deeper interpretation).

Non-Destructive SR-XRF Analysis of Ancient Mamluk-Ayyubid Glazed Pottery Fragments from Karak Castle, Jordan

TABLE 1. Net peak area (in counts) for selected elements of SR-XRF results for Karak Castle site samples.

	^{26}Fe	^{28}Cu	^{30}Zn	^{35}Br	^{37}Rb	^{38}Sr	^{39}Y	^{40}Zr	^{41}Nb	^{42}Mo	^{46}Pd	^{48}Cd	^{47}Ag	^{82}Pb
CSL 1	3005.2	59.2	113.3	90.1	217.6	4211.7	BDL	2069.0	98.0	BDL	BDL	BDL	BDL	201.3
CSL 2	4608.1	4109.8	122.0	109.0	BDL	2957.6	252.3	800.5	78.1	BDL	BDL	BDL	204.4	4778.2
CSL 3	4240.8	2842.5	131.7	BDL	BDL	3331.9	265.0	5675.8	95.5	BDL	BDL	BDL	BDL	388.5
CSL 4	3650.9	49.1	179.2	45.3	143.7	3483.8	189.0	1608.7	96.4	78.1	BDL	BDL	BDL	81.9
CSL 5	3649.0	6039.7	277.5	100.7	BDL	3871.3	274.6	2020.4	172.1	110.3	BDL	BDL	BDL	384.3
CSL 6	7452.9	85.3	143.9	BDL	381.2	3574.7	BDL	1603.4	165.2	74.0	BDL	BDL	80.3	6778.0
CSL 7	3262.1	1066.3	68.5	370.6	BDL	2039.4	BDL	3171.6	226.6	BDL	130.4	218.3	394.8	63574.6
CSL 8	3331.9	261.0	87.9	409.3	BDL	2309.8	BDL	2602.6	204.9	BDL	132.7	75.3	528.2	72693.6
CSL 9	4622.6	2736.5	92.5	519.5	BDL	2021.3	BDL	7606.1	321.3	BDL	172.4	BDL	616.2	87328.9
CSL 10	6057.9	BDL	BDL	87.5	BDL	2661.9	BDL	7908.00	540.6	BDL	BDL	119.4	BDL	33463.7
CSL 11	3767.5	41.7	81.1	BDL	193.8	2691.8	BDL	3479.1	241.6	161.4	BDL	BDL	BDL	3093.7
CSL 12	5337.9	1165.6	80.0	BDL	BDL	1400.2	BDL	3371.9	320.3	BDL	472.5	241.4	1548.9	137267.0
CSL 13	3393.1	832.9	BDL	BDL	BDL	2334.8	BDL	9379.1	577.3	BDL	122.9	108.2	411.5	38787.0
CSL 14	3345.6	1107.2	58.0	340.4	BDL	1159.0	BDL	2208.8	BDL	BDL	BDL	66.2	1304.7	60970.8
CSL 15	4687.7	1166.7	153.4	BDL	BDL	2601.1	BDL	7947.4	447.8	BDL	143.6	97.3	485.1	44800.5
CSL 16	13853.6	BDL	87.2	80.4	310.9	1442.5	BDL	15229.3	1155.1	BDL	BDL	75.4	BDL	432.2

* BDL.: Below Detection Limit.
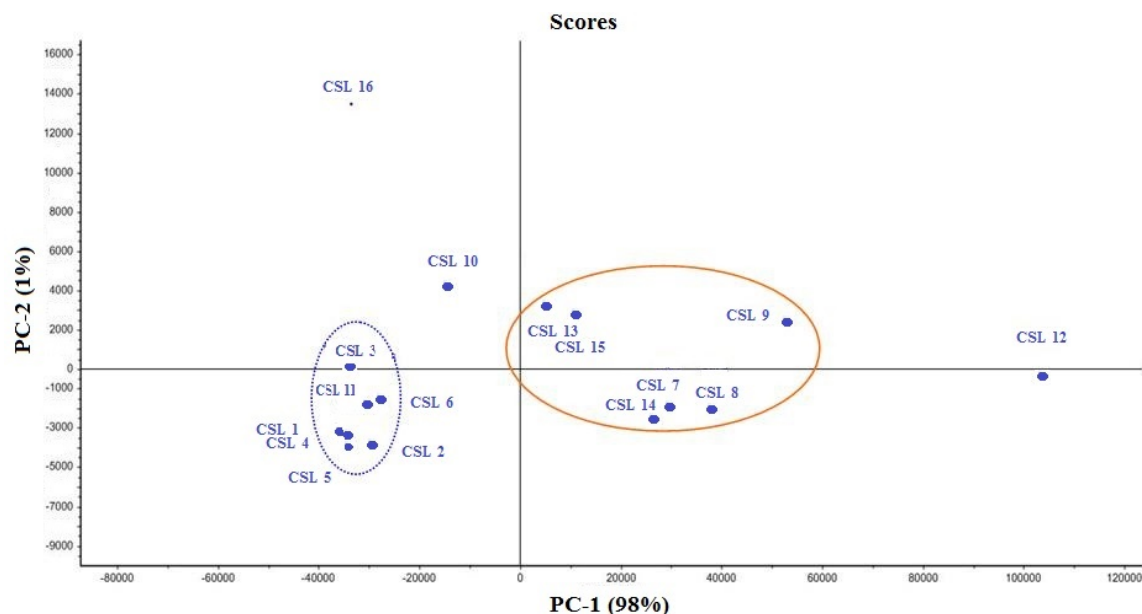
FIG. 3. Score plot of PCA of the area under the peaks of SR-XRF results for Karak Castle samples. PC1 vs. PC2 data matrix of dimensions 16x14 (16= number of samples from the site; 14= number of elements).
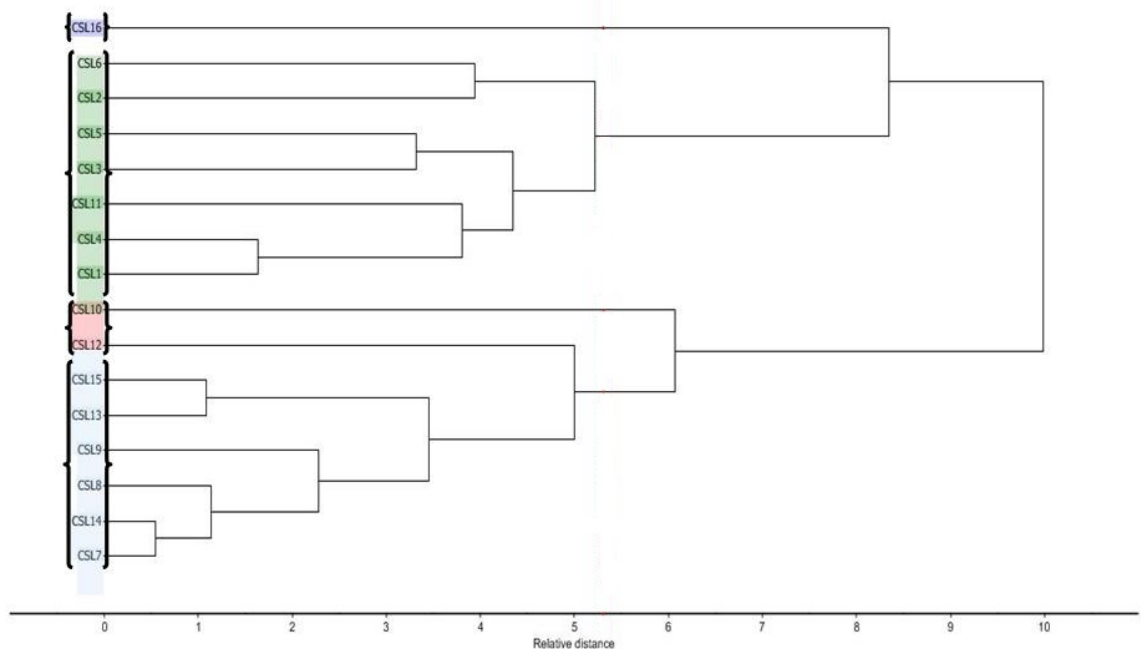
FIG. 4. Hierarchical clustering dendrograms by Median linking and Bray-Curtis distance for 16 ceramic sherd samples from Karak Castle site (area under the peaks of SR-XRF results).

Conclusions

This study demonstrates the growing importance of interdisciplinary research, particularly the importance of using SR-XRF in archaeological investigations. The increasing importance of non-destructive techniques manifests itself in archaeometry. This work investigates the chemical characterization of

sixteen glazed pottery sherds dated to Ayyubid-Mamluk period from Karak Castle site in southern Jordan, in order to extract information about their original provenance. Multivariate statistical analysis gives good results concerning the fabric characterization of clay (matrix and colour) conforming to results coming from archaeologists. It is possible to confirm the use of chemical characterization of pottery sherds

and statistical techniques of data handling to complete and integrate the work of archaeologists in provenance studies.

The ceramic sherd samples showed two large groups representing two different provenance regions. Also, it is evident that some samples do not belong to any of the two identified groups.

Unfortunately, the few studies available from Karak Castle site did not discuss or mention the ceramic, which were excavated from the site. Therefore, the significance of the present investigation stems from the fact that it will help archaeologists explain the cultural contacts and behaviors during the Islamic period and contribute to an understanding of human behaviors, especially when results are integrated

with those of typological and technological studies, among others.

Acknowledgments

References

[1] Franco, C., Paola, F. and Gilardoni, S., Annali di Chimica, 93 (2003).

[2] Punyadeera, C., Pillay, A.E., Jacobson, L. and Whitelaw, G., X-Ray Spectrometry, 26 (1997).

[3] El-Hasan, T., Szczerba, W., Radtke, M., Riesemeier, H., Buzanich, G. and Kersten, M., Environmental Science & Technology. 45(22) (2011) 9799.

[4] Mahnke, H.E., Denker, A. and Salomon, J., C. R. Physique, 10 (2009).

[5] Sciau, Ph., Salles, Ph., Roucau, C., Mehta, A. and Benassayag, G., Micron, 40 (2009).

[6] Dooryhe, E., Martinettoa, P., Walterb, Ph. and Annea, M., Radiation Physics and Chemistry, 71 (2004).

[7] Strub, E., Plarre, R., Radtke, M., Reinholz, U., Riesemeier, H., Schoknecht, U., Urban, K. and Jungel, P., Nuclear Instruments & Methods in Physics Research Section B-Beam Interactions with Materials and Atoms, 266(10) (2008) 2405.

[8] Görner, W., Eichelbaum, M., Matschat, R., Rademann, K., Radtke, M., Reinholz, U. and Riesemeier, H., Insight, 48(9) (2006) 540.

[9] Ferrero, J.L., Roldan, C., Ardid, M. and Navarro, E., Nuclear Instruments and Methods in Physics Research A, 422 (1999).

[10] Zwicky, C.N. and Lienemann, P., X-Ray Spectrometry, 33 (2004).

[11] Milazzo, M., Nuclear Instruments and Methods in Physics Research B, 21 (2004).

[12] Nuevo, M.J. and Martín Sánchez, A., Appl. Radiat. Isot., 69(3) (2011).

[13] Milwright, M., "The Fortress of the Raven Karak in the Middle Islamic Period (1100–1650)", 1st edition, (Leiden, Netherlands, 2008).

[14] Van Espen, P., Janssens, K. and Nobels, J. Chemometrics and Intelligent Laboratory Systems, 1 (1986).

[15] Ravisankar, R., Chandrasekaran, A., Kiruba, S., Raghu, Y., Prasad, M.V.R, Satpathy, K.K. and Maheswaran, C., Archives of Applied Science Research, 3(1) (2011).

[16] Forster, N., Grave, P., Vickery, N. and Kealhofer, L., X-Ray Spectrum, 40(5) (2011).

[17] Bakraji, E.H., X-Ray Spectrum, 35 (2006).

[18] Bray, J.R. and Curtis, J.T., Ecological Monographs, 27 (1957).

[19] Clifford, H.T. and Stephenson, W. "An Introduction to Numerical Classification", (Academic Press, London, 1975).

Jordan Journal of Physics

ARTICLE

Impact of Superficial Building Materials on Indoor Radon Level

J. M. Sharaf[a], **M. S. Hamideen**[b] and **H. H. Saleh**[c]

[a] *Department of Physics, The University of Jordan, Amman, Jordan.*
[b] *Department of Applied Sciences, Faculty of Engineering Technology, Al-Balqa' Applied University, Amman, Jordan.*
[c] *Physics Department, Al-Hussein Bin Talal University, Ma'an, Jordan.*

Abstract: This study is undertaken to determine the activity concentration of ^{226}Ra, ^{232}Th, ^{40}K and radon emanation coefficient of some superficial materials commonly used in dwelling for interior decoration. Eighty samples of four different materials were collected from local suppliers and analyzed, employing high resolution gamma-ray spectroscopy. Mean activity concentrations for ^{226}Ra ranged from 18.5 Bq/kg in marble, 60 Bq/kg in granite, 67 Bq/kg in ceramic up to 164 Bq/kg in porcelain, while for ^{232}Th it ranged from 12 Bq/kg in marble, 53 Bq/kg in ceramic, 54.5 Bq/kg in granite up to 64 Bq/kg observed in porcelain samples and for ^{40}K mean activity concentrations ranged from the lowest value of 137 Bq/kg in marble samples up to the highest value of 1042 Bq/kg in granite samples. The mean activity concentrations of ^{40}K obtained for ceramic and porcelain samples were 499 and 525 Bq/kg, respectively. Radium equivalent activity values for the materials examined were lower than the international recommended maximum value of 370 Bq/kg, except for two granite samples where the values were found to be 433 and 565 Bq/kg. The annual indoor effective doses received by an individual from the examined samples did not exceed the exemption dose criterion of 0.3 mSv. The results also show that all the examined materials, apart from granite, appear to have low radon emanation coefficients.

Keywords: Natural radioactivity; Radon emanation coefficient; Annual effective dose.

Introduction

Natural radionuclides in building materials are sources of external and internal exposure in dwellings, workplaces and industrial buildings. External radiation exposure is caused by the gamma emitting radionuclides. Internal radiation exposure, mainly affecting the respiratory tract, is due to the short-lived decay products of radon, which are exhaled from building materials into the room air. Therefore, radiation exposure of the population may be increased appreciably by the use of building materials containing above-normal levels of natural radionuclides to levels comparable or even greater than the exposure from medical radiation [1-3].

In most cases, the natural radioactivity content of building materials is determined by gamma-ray spectrometry. The external radiation exposure is estimated either by direct exposure measurements or by mathematical calculations. More complicated is the evaluation of the internal radiation exposure. Radon emanation from a material depends not only on the radium content of the material, but also on many other factors, including for example grain size, permeability, material density and ventilation rate. Several methods for the measurement of radon emanation and exhalation were developed and reported in the literature [4-5].

In recent years, there has been a significant increase in the use of granite, marble and glazed tiles as covering or decorative building materials for home interiors instead of conventional or mosaic tiles. Because of their appearance, availability, attractive colors, polished surface and durability against external conditions and high scratch resistance, granite and marble tiles are commonly used as wall and floor covering, facing materials for buildings, kitchen countertop, vanity tops and inner and outer decorative materials. Ceramic and porcelain tiles are also used in bathrooms, toilets and kitchens. Radionuclides' concentrations and radon emanation or exhalation coefficients of various covering materials used in different countries have been reported in the literature. These include granite [1, 3, 6-7], marble [8-10], ceramic and porcelain [11-15].

However, covering or decorative building materials derived from rock and soil include primordial radionuclides such as ^{226}Ra, ^{232}Th, and ^{40}K varying from one country to another and from one location to another in the same country [35]. While many reports on activity concentration and radon emanation coefficients of these materials have been published, their large variability has made the existing data insufficient to conclude which types of tiles, for example, have a higher activity level than others.

The purpose of this study is to determine: radioactivity present in these materials, their radon emanation and exhalation coefficients and their possible contribution to the indoor radon concentration. The results obtained are also used to assess any possible radiological hazard to occupants of the dwellings using such materials. In addition, the results are compared with the corresponding results available in the literature.

Materials and Methods

In the present work, samples of covering and decorative building materials were collected from local tile manufacturing companies and agencies supplying raw construction materials. The materials collected were granite, marble ceramic and porcelain tiles. The samples were crushed, ground, homogenized, sieved through 0.15 mm mesh, sealed in cylindrical plastic containers of 5.0 cm diameter and 4.0 cm height, dry-weighed and marked according to the name and producer company. The samples were then stored for almost a month in order to achieve secular equilibrium between the series parents and the subsequent daughters following radon in the decay sequence.

A total of 80 samples including granite, marble, ceramic and porcelain were involved in the measurements. Details concerning the petrographic features, mineral chemistry, geochemistry and physico-mechanical properties of the investigated samples are available in the literature for marble and granite rocks [5, 3, 17 and 18] and for ceramic and porcelain tiles [19-20, 11].

Measurements were performed using a High Purity Germanium (HPGe) detector supplied by EG&G Ortec. The detector is an n-type gamma-x ray (GMX) detector, operated at 3500 V, with a useful energy range of 3 keV to 10 MeV, a standard energy resolution of 2.02 keV and a relative efficiency of 56.9% at 1.33 MeV of ^{60}Co. The absolute efficiency calibration of the detector was performed using the radionuclide specific efficiency method, in which the uncertainty in gamma-ray intensities, the influence of coincidence summation and self-absorption effects of the emitting gamma photons are avoided. The IAEA certified reference materials RG-set (RGU-1, RGTh-1, RGK-1), each sealed in a cylindrical plastic container identical to those of samples, were used in the calibration process. Spectra were collected for 12 hours. Areas under the energy peaks of interest were used for drawing the peak efficiency curve between log of efficiency versus log of peak energy. A polynomial was fitted to the curve and the result was stored for further use.

The gamma-ray transition lines 295.20 keV (19.2%) and 351.90 keV (37.1%) from (^{214}Pb) and 609.30 keV (46.1%) and 1764 keV (16%) from (^{214}Bi) were used as the signature of ^{226}Ra. The gamma-ray transition lines 238.6 keV (43.6%) from (^{212}Pb), 583.14 keV (86.0%) from (^{208}Tl) and 911.07 keV (29.0%) from (^{228}Ac) were used as the signature of ^{232}Th. The activity concentration of ^{40}K was measured directly from its only 1460 keV (10.7%) transition line.

Prior to the sample measurements, an empty container, identical to those of samples and reference materials, was put into the shielded detector and measured for 12 hours to determine the laboratory background which was later subtracted from the measured gamma-ray spectrum of each sample. Measured background

and counting time were then used to determine the minimum detectable activity (MDA) for each peak of interest according to the Currie method [21]. The values obtained are given in Table 1.

TABLE 1. Background counting rates and minimum detectable activities (MDA) obtained with the standard sources.

Nuclide	Energy (keV)	Background count/h	MDA (Bq/kg)
^{214}Pb	295.2	48.8	0.19
^{214}Pb	351.9	85.6	0.25
^{214}Bi	609.3	68.8	0.23
^{214}Bi	1764.1	66.5	0.22
^{228}Ac	911.1	10.2	0.09
^{208}Tl	583.2	10.4	0.09
^{212}Pb	238.6	23.6	0.13
^{40}K	1460.8	798211.8	24.5

Calculation and Analysis

Investigation of the radiation contents of the samples was carried out by placing sample containers sequentially on the top of the detector cap and counting for at least 12 h for each sample. The specific activity A_i (Bq/kg) of a radionuclide i of peak energy E_i was calculated using the formula [5,12]:

$$A_i = \frac{C_i}{\varepsilon(E_i).I.t.M},\qquad(1)$$

where C_i is the net peak area of gamma-ray at energy E_i, $\varepsilon(E_i)$ is the absolute efficiency for gamma rays at a particular energy, I is the absolute transition probability of gamma decay, t is the counting live-time and M is the dried sample mass.

Radium equivalent activity Ra $_{eq}$ is an index that was introduced to account for the radiation hazard from a radionuclide mixture within a material [22-23]. Assuming that 370 Bq/kg of ^{226}Ra, 259 Bq/kg of ^{232}Th and 4810 Bq/kg of ^{40}K produce the same gamma-ray dose rate, Ra $_{eq}$ was calculated using the following relation[16]:

$$Ra_{eq} = A_{Ra} + 1.43A_{Th} + 0.077A_K\qquad(2)$$

where A_{Ra}, A_{Th}, and A_K are the specific activities in Bq/kg of ^{226}Ra, ^{232}Th and ^{40}K, respectively.

A radium equivalent activity of 370 Bq/kg in building materials will produce an external gamma radiation dose rate of 1.5 mSv/year; i.e., to keep the external gamma-ray dose below that

value, a building material is considered to be permissible if the condition Ra$_{eq}$ < 370 is satisfied.

However, the indoor-absorbed dose rate D (nGy/h) due to the external gamma radiation from marble, ceramic, porcelain and granite tiles utilized as building materials, may be calculated from the activity concentrations of ^{226}Ra, ^{232}Th and ^{40}K present in those materials, using the following relation [24]:

$$D = 0.12 \times A_{Ra} + 0.14 \times A_{Th} + 0.0096 \times A_k\qquad(3)$$

The indoor annual effective dose E$_{eff}$ (mSv/y) was estimated from the value of D by adopting a conversion factor of 0.7 Sv/Gy and an annual exposure time of 7000 h/y, considering that people on average spend 80% of their time indoors, using the following formula [25-26,23]:

$$E_{eff} = 0.7\ (SvGy^{-1}) \times 7000(h\ y^{-1}) \times D\ (Gy/h)\qquad(4)$$

For superficial and other building materials with restricted fractional mass usage, similar to those examined in this study, the exemption dose criterion is 0.3 mSv/y. Effective doses exceeding the dose criterion of 1 mSv/y should be taken into account in terms of radiation protection.

The radon emanation coefficient of samples, defined as radon escape to production ratio, was calculated based on two gamma spectroscopic measurements [4, 27-28]. The first measurement was carried out directly after sealing the samples, while the second measurement was carried out after attaining to secular equilibrium between radon and its progeny. Assuming that radon activities are always equal to those of its progenies, gamma rays emitted from ^{214}Pb and ^{214}Bi were counted in both measurements. Based on the theoretical ^{222}Rn ingrowth curve, Fig. 1, and assuming that all radon atoms at the time of sample container sealing (t = 0) exist in the solid phase, the net count rate of gamma ray C(t) at time t (day) can be given as:

$$C(t) = C_{eq}(1 - e^{\lambda t}) + C_0 e^{\lambda t}\qquad(5)$$

where λ is the decay constant of radon, C_{eq} and C_o are the net count rates at t >30 days and t = 0, respectively[4]. As counting rate is proportional to radon activity through a calibration constant, which cancels out when activity ratio is calculated, the radon emanation coefficient F (%) was calculated using direct counting rate ratios instead of measured activities as [23]:

$$F = \frac{C_{eq} - C_o}{C_{eq}} \times 100$$

(6)

The detection limit of F is related to the obtained total number of counts within the measurement time or to ^{214}Pb and ^{214}Bi activities of the samples.

Assuming that A_{Ra} (Bq kg^{-1}) is the concentration of ^{226}Ra, then the radon mass exhalation rate E_m (Bq kg^{-1} h^{-1}) is calculated as [22, 27, 5 and 12]:

$$E_m = F A_{Ra} \lambda \quad .$$

(7)
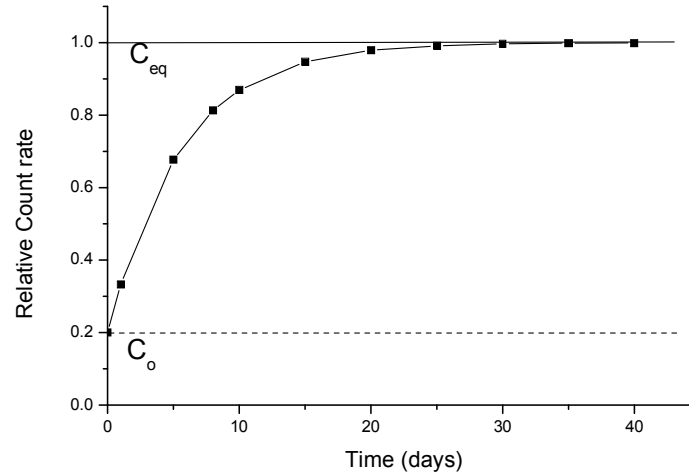
FIG. 1. Radon ingrowth curve.

Results and Discussion

Activity Concentration

Tables 2-5 list the activity concentration (in Bq/kg) of ^{226}Ra, ^{232}Th, ^{40}K, the radon emanation coefficient F (%), the radon mass exhalation rate E_m (Bq kg^{-1} h^{-1}), the radium equivalent activity Ra_{eq} (Bq/kg), the total absorbed dose rate D (nGy/h) and the annual effective dose E_{eff} (mSv) for all the examined samples. For comparison purposes, summaries of the above data are presented in Table 6. As it can be seen in the tables, substantial variability was observed both between and within the examined materials. The ^{226}Ra, ^{232}Th and ^{40}K activity concentrations were different in different types of granite, marble, ceramic and porcelain samples available in the local market. This is due to the different composition of these materials and uneven distribution of the radionuclides within the samples. The variation observed in similar materials is also a function of the local geology as building materials are extracted from different regions of earth crust and are used directly in building construction [29].

Mean concentration values of ^{226}Ra, ^{232}Th and ^{40}K measured in marble samples are significantly lower than those found in other material samples, as shown in Fig. 2. Mean activity concentrations of ^{226}Ra ranged from 18.5 Bq/kg in marble, 60 Bq/kg in granite, 67 Bq/kg in ceramic up to 164 Bq/kg in porcelain. The minimum measured value of ^{226}Ra activity concentration was 1.0±0.1 Bq/kg in the marble sample (M8), whereas the maximum value was 228±5 Bq/kg in the porcelain sample (P8). Granite and ceramic were also highly populated with ^{226}Ra, but still their activities are less than that observed in porcelain tiles, characterized by the presence of zircon mineral that has a relatively high uranium activity concentration [13].

The mean activity concentration of ^{232}Th ranged from 12 Bq/kg in marble, 53 Bq/kg in ceramic, 54.5 Bq/kg in granite up to 64 Bq/kg observed in porcelain samples. The minimum observed ^{232}Th activity concentration was 1.6±0.2 Bq/kg in the marble sample (M5) and the maximum was 228±3 Bq/kg in the granite sample (G19). It is also observed from the results that ^{232}Th has relatively the least concentration value in comparison to those of ^{226}Ra and ^{40}K in the samples examined.

TABLE 2. Activity concentration (Bq/kg) of ^{226}Ra, ^{232}Th, ^{40}K, radon emanation coefficient F (%), radon mass exhalation rate E_m (Bq kg^{-1} h^{-1}), radium equivalent activity Ra_{eq} (Bq/kg), total absorbed dose rate D (nGy/h) and annual effective dose E_{eff} (mSv) for granite samples.

Sample Code	Country of origin	Activity concentration (Bq/kg)			F (%)	E_m (Bq/kg.h)	Ra_{eq} (Bq/kg)	D (nGy/h)	E_{eff} (mSv)
		^{226}Ra	^{232}Th	^{40}K					
G1	Jordan	38±2	46±1	989±39	5.2	0.015	179	20.5	0.10
G2	S. Africa	22±1	33±1	324±12	23	0.038	94	10.4	0.05
G3	S. Africa	18±1	14±1	63±4	19	0.026	43	4.7	0.02
G4	China	89±3	112±6	1253±52	5.9	0.040	346	38.4	0.19
G5	S. Arabia	38±2	46±1	1076±48	16.3	0.047	187	21.3	0.10
G6	S. Arabia	32±1	76±3	1662±59	18.1	0.044	269	30.4	0.15
G7	S. Arabia	43±2	35±2	284±28	32	0.104	115	12.8	0.06
G8	S. Arabia	28±1	18±1	1282±54	38	0.081	153	18.2	0.09
G9	Italy	42±1	65±2	1133±46	22	0.070	222	25.0	0.12
G10	Italy	57±2	84±3	1152±45	11.4	0.049	266	29.7	0.15
G11	Italy	67±2	35±2	1071±56	1.8	0.009	200	23.2	0.11
G12	Italy	53±2	37±2	1250±47	18.8	0.075	202	23.5	0.12
G13	Italy	106±3	157±5	1331±55	2.1	0.017	433	47.5	0.23
G14	India	14±1	87±2	926±24	7.4	0.034	210	22.7	0.11
G15	India	61±2	48±1	1322±35	5.9	0.027	231	26.7	0.13
G16	Spain	71±1	43±1	1358±36	16	0.086	237	27.6	0.14
G17	Spain	116±2	76±2	1334±34	11	0.097	327	37.4	0.18
G18	Spain	59±1	121±2	1438±38	8	0.036	343	37.8	0.19
G19	Finland	152±1	228±3	1123±31	16	0.184	565	60.9	0.30
G20	Finland	62±1	54±1	1368±33	4	0.019	245	28.1	0.14
G21	Finland	45±1	39±1	942±26	18	0.061	173	19.9	0.10
G22	Egypt	81±3	55±2	663±21	14	0.086	211	23.8	0.12
G23	Egypt	32±5	63±2	1375±42	4.8	0.012	228	25.9	0.13
G24	Egypt	118±4	59±2	288±12	22	0.196	225	25.2	0.12
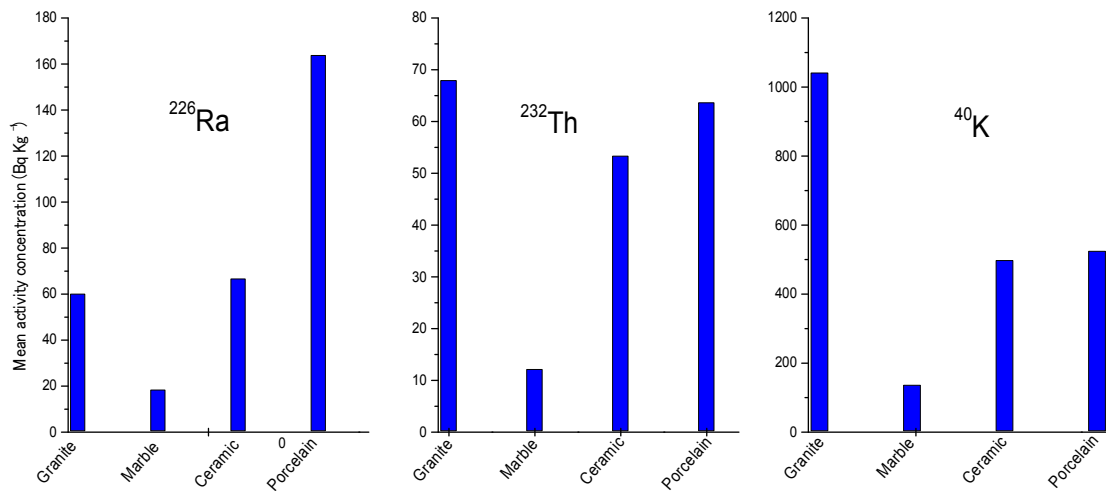
FIG. 2. Mean activity concentration of ^{226}Ra, ^{232}Th and ^{40}K in granite, marble, ceramic and porcelain samples.

TABLE 3. Activity concentration (Bq/kg) of ^{226}Ra, ^{232}Th, ^{40}K, radon emanation coefficient F (%), radon mass exhalation rate E_m (Bq kg^{-1} h^{-1}), radium equivalent activity Ra_{eq} (Bq/kg), total absorbed dose rate D (nGy/h) and annual effective dose E_{eff} (mSv) for marble samples.

Sample Code	Country of origin	Activity concentration (Bq/kg)			F (%)	E_m (Bq/kg.h)	Ra_{eq} (Bq/kg)	D (nGy/h)	E_{eff} (mSv)
		^{226}Ra	^{232}Th	^{40}K					
M1	Jordan	19±1	14±1	93±2	9.7	0.014	46	5.1	0.03
M2	Jordan	16±2	7.5±1.2	28±7	1.7	0.002	29	3.2	0.02
M3	Jordan	20.4±0.8	13±1	85±2	11.7	0.018	46	5.1	0.02
M4	Jordan	28±2	8.2±0.4	42±2	8.5	0.018	43	4.9	0.02
M5	Jordan	19±2	1.6±0.2	29±6	13.9	0.020	24	2.8	0.01
M6	Italy	5.1±0.2	2.2±0.1	28±2	5.2	0.002	9	1.0	0.01
M7	Italy	14±1	18±1	116±18	2.8	0.003	49	5.3	0.03
M8	Italy	1.0±0.1	3.9±0.7	28±3	ND	ND	8	1.1	0.01
M9	Italy	37±3	19±1	31±2	7.4	0.021	67	7.4	0.04
M10	Italy	16±2	2.4±0.4	33±3	14.9	0.018	22	2.6	0.01
M11	Spain	13.6±0.1	12.2±0.1	36±3	33	0.032	34	3.7	0.02
M12	Spain	12±1	4.6±1.2	94±4	19.8	0.018	26	3.0	0.01
M13	Malaysia	17±2	16±2	247±6	28	0.036	59	6.7	0.03
M14	S. Arabia	31±2	29±2	31±4	17.1	0.040	74	8.0	0.04
M15	S. Arabia	28±3	13±1	47±3	0.9	0.002	50	5.6	0.03
M16	S. Arabia	19±1	35±4	56±4	2.7	0.016	73	7.7	0.04
M17	Greece	11±1	2.3±0.6	108±7	31	0.026	21	2.7	0.01
M18	Greece	53±4	32±2	774±21	5.8	0.023	158	18.3	0.09
M19	Greece	25±2	42±2	988±31	1.1	0.002	161	18.4	0.09
M20	China	13±1	2.2±0.1	162±11	25.4	0.025	29	3.4	0.02
M21	Turkey	29.4±1.6	2.4±0.2	34.4±3.1	1.8	0.004	35	4.2	0.02
M22	Turkey	2.3±0.2	4.4±0.3	26±2	ND	ND	9	1.1	0.01
M23	Turkey	15.2±0.6	12.6±0.7	377±26	16.7	0.019	62	7.2	0.04
M24	Egypt	11.8±1.2	4.8±0.6	28±2	8.7	0.008	21	2.4	0.01
M25	Egypt	5.5±0.4	3.2±0.1	45±4	9.2	0.004	14	1.5	0.01

TABLE 4. Activity concentration (Bq/kg) of ^{226}Ra, ^{232}Th, ^{40}K, radon emanation coefficient F (%), radon mass exhalation rate E_m (Bq kg^{-1} h^{-1}), radium equivalent activity Ra_{eq} (Bq/kg), total absorbed dose rate D (nGy/h) and annual effective dose E_{eff} (mSv) for ceramic samples.

Sample Code	Country of origin	Activity concentration (Bq/kg)			F (%)	E_m (Bq/kg.h)	Ra_{eq} (Bq/kg)	D (nGy/h)	E_{eff} (mSv)
		^{226}Ra	^{232}Th	^{40}K					
C1	Jordan	33±3	36±3	420±28	4.8	0.012	117	13.0	0.06
C2	Jordan	70±5	52±5	537±40	2.8	0.015	154	20.8	0.10
C3	Turkey	78±7	61±4	486±54	3	0.018	203	22.6	0.11
C4	Turkey	53±11	44±4	414±24	5.5	0.022	148	16.5	0.08
C5	Spain	92±6	42±4	726±23	5	0.035	208	23.9	0.12
C6	Spain	72±5	56±5	464±22	2	0.011	188	16.5.	0.08
C7	Egypt	106±8	63±4	348±21	12	0.096	223	24.9	0.12
C8	Egypt	81±5	55±4	364±14	14	0.086	188	20.9	0.10
C9	Italy	79±3	66±3	692±38	2.8	0.017	227	25.4	0.12
C10	Italy	48±4	42±2	462±40	0.5	0.002	144	16.1	0.08
C11	Italy	56±5	44±4	441±40	0.4	0.002	153	17.1	0.08
C12	Syria	53±8	56±5	522±42	0.5	0.002	173	19.2	0.09

Sample Code	Country of origin	Activity concentration (Bq/kg)			F (%)	E_m (Bq/kg.h)	Ra_{eq} (Bq/kg)	D (nGy/h)	E_{eff} (mSv)
		^{226}Ra	^{232}Th	^{40}K					
C13	Syria	75±6	64±6	590±46	ND	ND	212	23.6	0.12
C14	Syria	65±6	54±5	664±54	0.8	0.004	193	21.7	0.11
C15	China	61±4	53±5	386±44	3.2	0.015	167	18.4	0.09
C16	China	72±6	58±6	568±38	3.1	0.017	199	22.2	0.11
C17	UAE	103±8	62±3	669±42	6.3	0.050	243	27.5	0.13
C18	India	45±4	42±3	347±18	8.2	0.028	132	18.0	0.09
C19	India	28±2	64±5	374±20	17	0.036	148	15.9	0.08

TABLE 5. Activity concentration (Bq/kg) of ^{226}Ra, ^{232}Th, ^{40}K, radon emanation coefficient F (%), radon mass exhalation rate E_m (Bq kg^{-1} h^{-1}), radium equivalent activity Ra_{eq} (Bq/kg), total absorbed dose rate D (nGy/h) and annual effective dose E_{eff} (mSv) for porcelain samples.

Sample Code	Country of origin	Activity concentration (Bq/kg)			F (%)	E_m (Bq/kg.h)	Ra_{eq} (Bq/kg)	D (nGy/h)	E_{eff} (mSv)
		^{226}Ra	^{232}Th	^{40}K					
P1	Spain	117±7	62±3	584±33	0.2	0.002	251	28.3	0.14
P2	Spain	96±8	53±4	442±25	ND	ND	206	23.2	0.11
P3	Spain	192±8	68±4	395±29	0.4	0.006	320	36.4	0.18
P4	Spain	182±7	58±2	612±44	ND	ND	312	35.5	0.17
P5	Spain	78±4	72±5	504±52	ND	ND	220	24.3	0.12
P6	Italy	89±4	44±3	283±28	0.5	0.003	174	19.6	0.10
P7	Italy	146±6	98±3	557±35	0.4	0.004	329	36.6	0.18
P8	Italy	228±5	58±4	696±24	ND	ND	365	42.2	0.21
P9	Italy	214±8	76±6	484±24	ND	ND	360	41.0	0.20
P10	China	186±6	64±4	528±36	ND	ND	318	36.3	0.18
P11	China	212±6	65±4	655±51	0.4	0.006	355	40.8	0.20
P12	China	227±8	46±3	564±47	0.2	0.003	336	39.1	0.19

TABLE 6. Mean, median, minimum, maximum and standard deviation values of the measured data for granite, marble, ceramic and porcelain samples.

Material	Statistics	Activity concentration (Bq/kg)			F (%)	E_m (Bq/kg.h)	Ra_{eq} (Bq/kg)	D (nGy/h)	E_{eff} (mSv)
		^{226}Ra	^{232}Th	^{40}K					
Granite									
	Mean	60	68	1042	14	0.061	238	27	0.13
	Median	55	54.5	1142.5	15	0.044	224	25	0.12
	Min.	14	14	63	1.8	0.012	43	4.7	0.02
	Max.	152	228	1662	38	0.196	565	60.9	0.30
	S.D.	35	47.6	420.5	9	0.048	109	11.7	0.06
Marble									
	Mean	18.5	12	137	12	0.016	47	5.3	0.03
	Median	16	8	42	9	0.018	35	4.2	0.02
	Min.	1	1.6	26	ND	0.0	8	1	0.01
	Max.	53	35	988	33	0.04	161	18.4	0.09
	S.D.	11.5	11.4	241	9.8	0.011	39	4.5	0.02

Material	Statistics	Activity concentration (Bq/kg)			F (%)	E_m (Bq/kg.h)	Ra_{eq} (Bq/kg)	D (nGy/h)	E_{eff} (mSv)
		^{226}Ra	^{232}Th	^{40}K					
Ceramic									
	Mean	67	53	499	5	0.025	180	20	0.10
	Median	70	55	464	3	0.012	188	20.8	0.10
	Min.	28	36	347	ND	0.0	117	13	0.08
	Max.	106	66	726	17	0.096	243	27.5	0.13
	S.D.	21	9	123	4.8	0.027	35	3.9	0.02
Porcelain									
	Mean	164	64	525	0.18	0.0020	296	33.6	0.17
	Median	184	63	543	0.1	0.0035	319	36.4	0.18
	Min.	78	44	283	ND	0.0	174	19.6	0.10
	Max.	228	98	696	0.5	0.0060	365	42.2	0.21
	S.D.	56	14.5	115	0.2	0.0024	65.5	7.7	0.04

The mean activity concentration of ^{40}K, in the studied samples, ranged from the lowest value of 137 Bq/kg for marble samples up to the highest value of 1042 Bq/kg for granite samples. The mean activity concentrations obtained for ceramic and porcelain samples were 499 and 525 Bq/kg, respectively. The lowest observed ^{40}K activity concentration was 26±2 Bq/kg in the marble sample (M22) and the highest was 1662±59 Bq/kg in the granite sample (G6).

It can be seen from the results that the mean activity concentrations measured in the marble samples were significantly lower than the typical world average values of 50, 50 and 500 Bq/kg for ^{226}Ra, ^{232}Th and ^{40}K, respectively [30]. In addition, the mean activity concentrations of ^{226}Ra and ^{232}Th measured in granite, ceramic and porcelain samples were slightly higher than the quoted values, while the mean value of ^{40}K was found to be higher than the world average for granite samples only. However, the natural radioactivity levels measured in all samples are comparable to those measured in other countries and the average worldwide ranges [31].

Radiological Hazard Indices

The radium equivalent activity (Ra_{eq}) of the examined samples was calculated according to Eq. (2) to evaluate the relative radiological hazard due to external irradiation. The lowest mean value found was for marble (47 Bq/kg), while the highest was for porcelain (296 Bq/kg). The other mean values obtained were 180 and 238 Bq/kg for ceramic and granite, respectively. It is clear that all the estimated mean values of Ra_{eq} (Fig. 3) were lower than the recommended maximum value of 370 Bq/kg. However, the

exceptions are two granite samples, where Ra_{eq} was found to be 433 and 565 Bq/kg for the samples (G13) and (G19), respectively.

The indoor absorbed gamma dose rate (D) in air was calculated, using the measured activity concentration data, according to Eq. (3). The values obtained are listed in Tables 2-5. The obtained mean values were 27, 5.3, 20 and 33.6 nGy/h for granite, marble, ceramic and porcelain samples, respectively. The lowest observed D value was 1 nGy/h for the marble sample (M6) and the highest value was 60.9 nGy/h for the granite sample (G19). All the estimated D values for the samples examined were lower than the world average indoor gamma absorbed dose rate of 84 nGy/h [25]. However, the correlation of D values to those of Ra_{eq} is shown in Fig. 4, for granite samples. The significant correlation between the two indices (R = 0.99) is expected due to the common specific activity concentrations of ^{226}Ra, ^{232}Th and ^{40}K, utilized in their evaluation (Eqs. 2 and 3) although weighting or conversion factors as well as units were different.

Finally, the annual effective dose E_{eff} was calculated from the sample D values according to Eq. (4). The estimated E_{eff} mean values were 0.13, 0.03, 0.10 and 0.17 mSv for granite, marble, ceramic and porcelain samples, respectively. The minimum observed E_{eff} value was 0.01 mSv for many marble samples and the maximum value was 0.3 mSv for the granite sample (G19). It can be seen from Tables 2-5 that all the estimated E_{eff} values did not exceed the exemption dose criterion of 0.3 mSv [25].
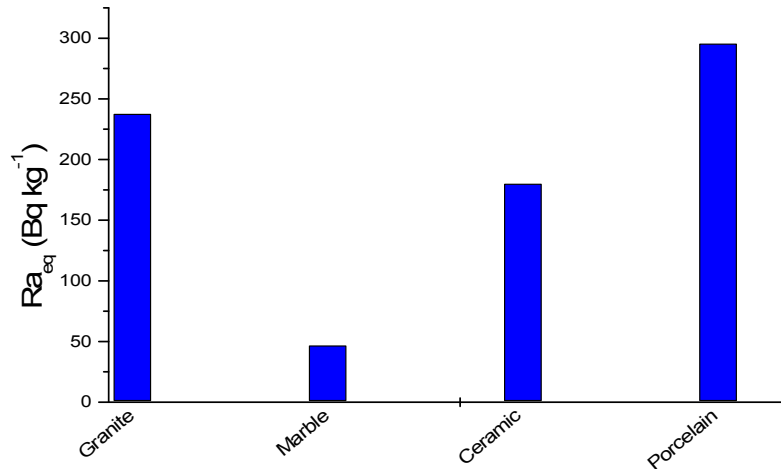
FIG. 3. Mean values of radium equivalent activity (Ra_{eq}) for granite, marble, ceramic and porcelain samples. (All the measured values are less than the recommended maximum value of 370 Bq kg^{-1}).
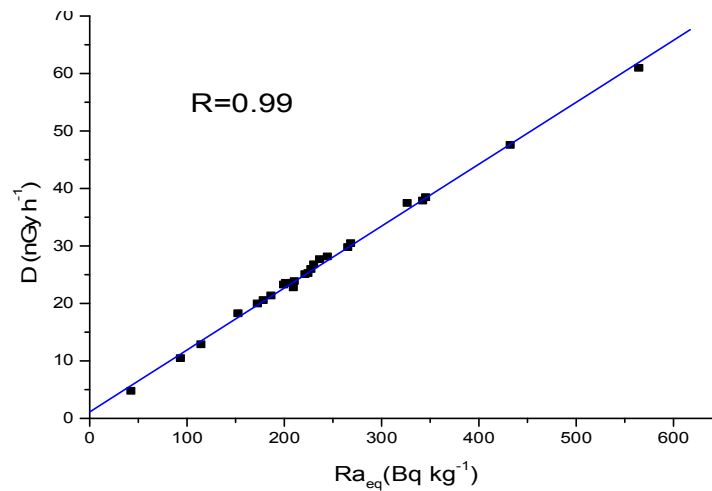
FIG. 4. The correlation of the absorbed dose rate (D) values to those of radium equivalent activity (Ra_{eq}), for granite samples.

Radon Emanation Coefficient and Exhalation Rate

The radon emanation coefficient F (%) and radon mass exhalation rate E_m (Bq kg^{-1} h^{-1}) of the examined samples are listed in Tables 2-5. The emanation coefficient varied from a non-detectable (ND) value in some marble, ceramic and porcelain samples to a maximum value of 38 % in the granite sample (G8). Although the values of F in granite samples have shown a wide dispersion (range: 1.8-38% and standard deviation of 35), it is agreed that granite has higher radon emanation coefficients than other examined marble, ceramic and porcelain samples. The mean radon emanation coefficient estimated for the examined materials (Fig. 5) were 0.18, 5, 12 and 14% in porcelain, ceramic, marble and granite, respectively. The values observed here are in good agreement with the

corresponding values reported in the literature [12, 32] as shown in the figure.

However, the radon exhalation rates ranged from a non-detectable (ND) value to a maximum value of 0.196 Bq/kg.h observed in the granite sample (G24). Many marble and ceramic samples and half of the porcelain samples did not show any detectable radon exhalation, while higher values occurred among granite samples. The mean radon exhalation rate for granite was 0.061 Bq/kg.h, while much lower mean values were observed as 0.016, 0.025 and 0.002 Bq/kg.h for marble, ceramic and porcelain, respectively. This evidence confirms the theory about the difficulties facing radon to escape from condensed solid matrices such as ceramic and porcelain mainly due to reduction of the grain micro-porosity during the manufacturing process that blocks radon emanation. Although high

radium activity concentrations are potentially associated with both ceramic and porcelain, it is highly likely that radon produced through the decay of such radium remains locked up in glass-like matrices [33]. Generally, the natural stones of magmatic origin such as granites are considered as significant sources of radon emanation [3]. The results also confirm that no correlation is present between radon exhalation rate and material radium content and that the emanation rate is not constant within a given type of material or from one type to another with approximately the same radium content.
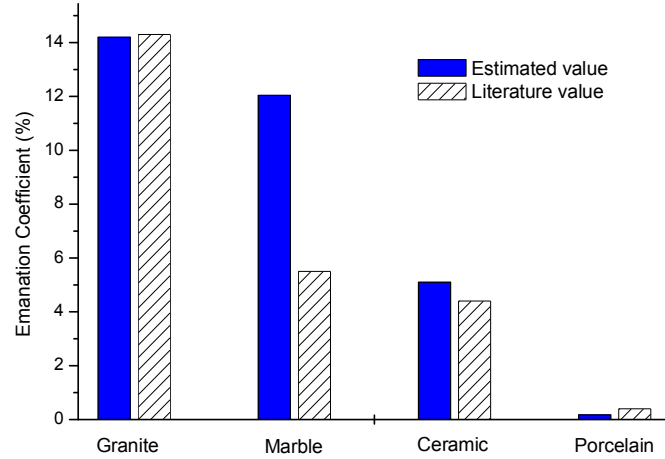
FIG. 5. Mean radon emanation coefficient estimated for the examined materials.

To assess the contribution of superficial materials to indoor radon concentration, a $5\times4\times3$ m^3 sealed room with its entire floor tiled with one of the studied materials, is assumed. The radon concentration C_{Rn} (Bq/m^3) due to radon exhalation from the floor can be obtained by [36]:

$$C_{Rn} = \frac{E_x.A}{(\lambda_{Rn} + \lambda_v)V} \qquad (8)$$

where A is the floor area (m^2), V is the room volume (m^3), λ_{Rn} is the radon decay constant (h^{-1}), λ_v is the air ventilation rate (h^{-1}) and E_x is the radon exhalation rate (Bq.m^{-2}.h^{-1}) which is given by [18]:

$$E_x = \frac{1}{2}A_{Ra}.\lambda_{Rn}.\rho.F.d \qquad (9)$$

where ρ is the material density (kg.m^{-3}) and d is the material or tile thickness (m).

Based on the measured values of A_{Ra}, ρ and F, the values of E_x were calculated for two samples of each material examined: one with the highest radium activity concentration and the second with the highest radon emanation coefficient. Assuming that outdoor air has a negligible radon concentration, the calculated E_x values were used to estimate the indoor radon concentration released by 20 m^2 floor tiles into a 60 m^3 room for various air change rates (ACH) as shown in Table 7. It can be seen from the table that the data obtained ranged from a minimum value of 1.3 Bq/m^3 for porcelain tiles up to a maximum value of 326 Bq/m^3 for granite tiles.

TABLE 7. Radon concentration (Bq. m^{-3}) due to radon exhalation from selected floor tile samples, for different air changes per hour (ACH).

Sample Code	Density (kg.m^{-3})	Thickness (m)	E_x (Bq.m^{-2}.h^{-1})	Radon concentration (Bq.m^{-3})		
				ACH = 0	ACH = 0.5	ACH = 1
G19	2684	0.03	7.41	326.42	4.87	2.45
G8	2560	0.03	3.10	136.56	2.04	1.00
M18	2545	0.03	0.89	39.21	0.60	0.30
M11	2502	0.03	1.27	55.94	0.83	0.42
C7	2311	0.01	1.11	48.90	0.73	0.37
C19	2284	0.01	0.41	18.10	0.27	0.14
P12	2412	0.008	0.03	1.3	0.02	0.01
P6	2368	0.008	0.03	1.3	0.02	0.01

Conclusions

This study presented data concerning the activity concentration of the natural radionuclides and radon emanation coefficients for different types of covering and decorative building materials. The mean activity concentration values of ^{226}Ra, ^{232}Th and ^{40}K measured in marble samples were significantly lower than the typical world average values, while those measured in granite, ceramic and porcelain samples were higher than the quoted values, but comparable with values measured in other countries [31]. The isotopic gamma analysis and radiological assessment of the examined materials indicated that some granite samples have the potential to significantly influence indoor external gamma dose level. Radium equivalent activity values for all of the examined materials were lower than the international recommended maximum value of 370 Bq/kg, except for two granite samples, where Ra$_{eq}$ was found to be 433 and 565 Bq/kg. The annual indoor effective doses received by an individual from the examined samples did not exceed the exemption dose criterion of 0.3 mSv.

The results also show that all the examined materials, apart from granite, appear to have low radon emanation coefficients. Although most of the ceramic and porcelain samples have shown high activity concentrations of radium, their emanation coefficients are generally law. Their contribution to indoor radon concentrations is expected to be negligible, similar to that of marble, but still have the potential to significantly influence indoor external gamma dose rate. In general, for houses with adequate ventilation, all covering and decorative materials make no significant contribution to indoor radon and gamma radiation constitutes their major contribution to the indoor dose. Although the values obtained for radon concentration were calculated under the worst case scenario with key parameters (^{226}Ra content and F) having their highest values, it is safe to anticipate that the contribution to indoor radon concentrations is not likely to be a health concern in most cases, especially when compared with the international action limit of 200 Bq/m^3 [35].

References

[1] Tzortzis, M., Tsertos, H., Christofides, S. and Christodoulides, G., J. Env. Rad., 70 (2003) 223.

[2] Lee, E.M., Menezes, G. and Finch, E.C., Health Phys., 86 (2004) 378.

[3] Pavlidou, S., Koroneos, A., Papastefanou, C., Christofides, G., Stoulos, S. and Vavelides, M., J. Envi. Rad., 89 (2006) 48.

[4] White, G.J. and Rood, A.S., J. Env. Rad., 54 (2001) 401.

[5] Al-Jarallah, M.I., Fazal-ur-Rehman, Musazay, M.S. and Aksoy, A., Rad. Meas., 40 (2005) 625.

[6] El-Arabi, A.M., Rad. Meas., 42 (2007) 94.

[7] Turhan, S., Ann. Nuc. En., 44 (2012) 34.

[8] Khatibeh, A., Ahmad, N. and Matiullah Kenawy, M.A., Radiat. Meas., 28 (1997) 345.

[9] Krstić, D., Nikezić, D., Stevanović, N. and Vučić, D., Rad. Meas., 42 (2007) 1731.

[10] Turhan, S. and Varinlioglu, A., Rad. Prot. Dos., 151 (2012) 546.

[11] Bruzzi, L., Baroni, M., Mazzotti, G., Mele, R. and Righi, S., J. Environ. Radioact., 47 (2000) 171.

[12] Righi, S. and Bruzzi, L., J. Env. Rad., 88 (2006) 158.

[13] Ballesteros, L., Zarza, I., Ortiz, J. and Serradell, V., J. Environ. Radioact., 99 (2008) 1525.

[14] Righi, S., Guerra, R., Jeyapandian, M., Verita, S. and Albertazzi, A., Radioprot., 4 (2009) 413.

[15] Amin, S.A. and Naji, M., Rad. Phy. Chem., 86 (2013) 37.

[16] UNSCEAR, United Nation Scientific Committee on the Effect of Atomic Radiation (1988).

[17] Aslam, M., Orfi, S.D., Khan, K. and Jabbar, A., Radioanal. Nucl. Chem., 253 (2002) 483.

[18] Rizzo, S., Brai, M., Basile, S., Bellia, S. and Hauser, S., App. Rad. Isot., 55 (2001) 259.

[19] Márquez, J. M., Rincon, J. M. and Romero, M., Ceramics Internacional, 34 (2008) 1867.

[20] Turhan, S., Arikan, I. and Demirel, H., Rad. Phys. Chem., 80 (2011) 620.

[21] Curri, L., Anal. Chem., 40 (1968) 586.

[22] Beretaka, J. and Mathew, P.J., Health Phys., 48 (1985) 87.

[23] Veiga, R., Sanches, N., Anjos, R.M., Macario, K., Bastos, J., Iguatemy, M., Aguiar, J.G., Santos, A.M.A., Mosquera, B., Carvalho, C., Baptist Filho, M. and Umisedo, N.K., Radiat. Meas., 41 (2006) 189.

[24] EC, Radiation Prot. (1999).

[25] UNSCEAR, United Nations Scientific Committee on the Effects of Atomic Radiation (2000).

[26] Otoo, F., Adukpo, O., Darko, E., Emi-Reynolds, G., Awudu, A., Ahiamadjie, H., Tandoh, J., Hasford, F., Adu, S. and Gyampo, O., J. Envi. Eart. Sci., 3 (2011), 261.

[27] El Afifi, E.M. and Awwad, N.S., J. Env. Rad., 82 (2005) 7.

[28] Sakoda, A., Nishiyama, Y., Hanamoto, K., Ishimori, Y., Yamamoto, Y., Kataoka, T., Kawabe, A. and Yamaoka, K., App. Rad. Isot., 68 (2010) 1180.

[29] Sharaf, J.M. and Hamideen, M.S., Appl. Rad. Isot., 80 (2013) 61.

[30] NEA-OECD, Reported by NEA group of experts, OECD, Paris (1979).

[31] Trevisi, R., Risica, S., D'Alessandro, M., Paradiso, D. and Nuccetelli, C., J. Env. Rad., 105 (2012) 11.

[32] Moharram, B.M., Suliman, M.N., Zahra, N.F., Shennawy, S.E. and El Sayed, A.R., Ann. Nucl. En., 45 (2012) 138.

[33] Verita, S., Righi, S., Guerra, R. and Jeyapandian, M., Radioprot., 44 (2009) 445.

[34] ICRP, Ann. ICRP Publication, 65 (1993) 23.

[35] UNSCEAR, United Nations Scientific Committee on the Effects of Atomic Radiation (2008).

[36] Chen, J., Rahman, N.M. and Abu Atiya, I., J. Envi. Rad., 101 (2010) 317.

Jordan Journal of Physics

ARTICLE

On the Optimization of the Microstructure and Mechanical Properties of Al-Co-Cr-Cu-Fe-Ni-Ti –Based High Entropy Alloys

A.M. Manzoni[a], **S. Singh**[a,b], **H.M. Daoud**[c], **R. Völkl**[c], **U. Glatzel**[c] and **N. Wanderka**[a]

[a] *Helmholtz-Zentrum Berlin für Materialien und Energie GmbH, Hahn-Meitner-Platz 1, D-14109 Berlin, Germany.*
[b] *Department of Physics and Nanotechnology, SRM University, Kattankulathur, Kancheepuram Dt 603 203, India.*
[c] *Metals and Alloys, University Bayreuth, Ludwig-Thoma-Str. 36b, D - 95447 Bayreuth, Germany.*

Abstract: Widely investigated AlCoCrCuFeNi high entropy alloy has been chosen for optimization of the microstructural and mechanical properties. Different paths have been chosen for optimization; namely the decrease of segregating element Cu, the increase of oxidation protective elements Al and Cr and the approach towards a γ-γ' microstructure as in Ni-based superalloys. Microscopical observation has been made for each optimization step and compared with results obtained by Vickers microhardness measurements. Out of five derivate alloys: $AlCoCrFeNi$, $Al_{23}Co_{15}Cr_{23}Cu_8Fe_{15}Ni_{16}$, $Al_8Co_{17}Cr_{17}Cu_8Fe_{17}Ni_{33}$, $Al_8Co_{17}Cr_{14}Cu_8Fe_{17}Ni_{33}Mo_1Ti_1W_1$ and $Al_{10}Co_{25}Cr_8Fe_{15}Ni_{36}Ti_6$, the most promising one has been chosen for further investigation.

Keywords: High entropy alloys; Microstructure; Transmission electron microscopy.

Introduction

For centuries, the concept of alloy creation has been based on the idea of having one base element and optimizing it with additional elements or at the most use binary alloys. This concept has already been broken by the discovery of metallic glasses, which consist of several elements none of which can be considered more important than the others. However, this notion has been restricted to amorphous materials, until the introduction of high entropy alloys or compositionally complex alloys at the beginning of the 21st century [1-2]. Since then, this new class of materials, consisting of five or more principal elements with close atomic radii, has been subject to intensive investigation all over the world. The family of elements that has been most observed

is Al-Co-Cr-Cu-Fe-Ni-Ti in various compositions [3-6].

The most outstanding property of high entropy alloys is their potential of forming single solid solutions. However, this has only been obtained in a very limited number of high entropy alloys [7-10] and is furthermore not the best option for good mechanical properties. Over time, it has been found that a two phase microstructure can lead to achieve better results. Several compositions and morphologies have been tried until an "optimum" morphology consisting of a disordered fcc matrix and ordered fcc precipitates has been chosen for future investigation.

This work focuses on the microstructural evolution from the "classic" equiatomic AlCoCrCuFeNi [11-14] alloy over AlCoCrFeNi

---

[15-16], $Al_{23}Co_{15}Cr_{23}Cu_8Fe_{15}Ni_{16}$ [17], $Al_8Co_{17}Cr_{17}Cu_8Fe_{17}Ni_{33}$ [17-18] and $Al_8Co_{17}Cr_{14}Cu_8Fe_{17}Ni_{33}Mo_1Ti_1W_1$ [19] to the optimized $Al_{10}Co_{25}Cr_8Fe_{15}Ni_{36}Ti_6$ alloy. The as-cast alloys have been investigated by optical microscopy, transmission electron microscopy (TEM) and three dimensional atom probe (3D-AP).

Experimental

The equiatomic alloys AlCoCrCuFeNi and AlCoCuFeNi have been melted in a vacuum levitation induction furnace. The elements were of 99.999% purity. The $Al_{23}Co_{15}Cr_{23}Cu_8Fe_{15}Ni_{16}$, $Al_8Co_{17}Cr_{17}Cu_8Fe_{17}Ni_{33}$, $Al_8Co_{17}Cr_{14}Cu_8Fe_{17}Ni_{33}Mo_1Ti_1W_1$ and $Al_{10}Co_{25}Cr_8Fe_{15}Ni_{36}Ti_6$ alloys were cast in a vacuum induction furnace out of elements of 99.99% purity. All alloys were remelted several times in order to ensure homogeneity. The ingots were then cooled inside the furnace. Their mass was about 20 g.

Specimens for investigation with optical microscopy and hardness measurements were ground with different grinding papers and polished in three steps (3 μm and 1 μm diamond suspension) with a final polishing step consisting of 50 nm sized silica grains in a colloidal OP-U suspension. Some alloys were etched with an etching solution consisting of HCl, HNO_3 and H_2MoO_4.

Discs of 3 mm diameter and 140 μm thickness were punched in order to prepare specimens for transmission electron microscopy (TEM) investigations. They were mechanically ground down to a thickness of about 110 μm and then electrochemically polished with a polishing solution of 83 % ethanol, 10 % perchloric acid and 7 % glycerine at -20°C and a voltage of 30 V. TEM investigations were made in a Philips CM30 with an acceleration voltage of 300 kV, equipped with an energy dispersive X-ray (EDX) detector by EDAX which is used to analyze the chemical composition of the phases.

Three-dimensional atom probe (3D-AP) measurements have been performed on two alloys; $Al_8Co_{17}Cr_{17}Cu_8Fe_{17}Ni_{33}$ and $Al_8Co_{17}Cr_{14}Cu_8Fe_{17}Ni_{33}Mo_1Ti_1W_1$. Specimens for 3D-AP investigations were first cut into rods of 0.2 ×0.2 ×10 mm³ and then thinned down to a tip diameter of about 50 nm by using a final polishing solution of 98% butoxyethanol and 2% perchloric acid and a final voltage of 3 V. For more detailed information, see Ref. [15, 17]. The three-dimensional atom probe used in this study is a TAP, CAMECA instrument. The 3D-AP analyses were performed at a temperature of about 70 K with a pulse voltage fraction of 20% to the standing DC voltage and with a pulse repetition rate of 1000 Hz. Investigations are performed in a vacuum lower than 10^{-7} Pa.

Vickers microhardness measurements were carried out in Reichert-Jung MHT-10 microhardness tester with a load of ~0.5 N.

Results and Discussion

FIG. 1 shows a pseudo-ternary phase diagram (Al-Ti)-(Ni-Co)-Fe. It is a schematic view that aims at visualizing the fact that commercially used alloys are situated at the corner positions; i.e., having one (or sometimes two) base element, in this case, Al- or Ti-based, Fe-based or Ni- or Co-based. As Al and Ti shift the alloys' properties in the same direction and Ni and Co are also known to have similar behaviors, they have been grouped together. These elements have been chosen at the corners of the phase diagram, because most commercially used alloys are Al- or Ti- (blue circles), Co- or Ni- (green circles) or Fe-based (red circles). Some have a Fe-Ni binary basis (brown circles), but rare are the commercial alloys with three or more elements and a composition close to the equiatomic. The corresponding regions lie inside the orange circle and this is where the high entropy alloys (orange discs) of the present study are situated.
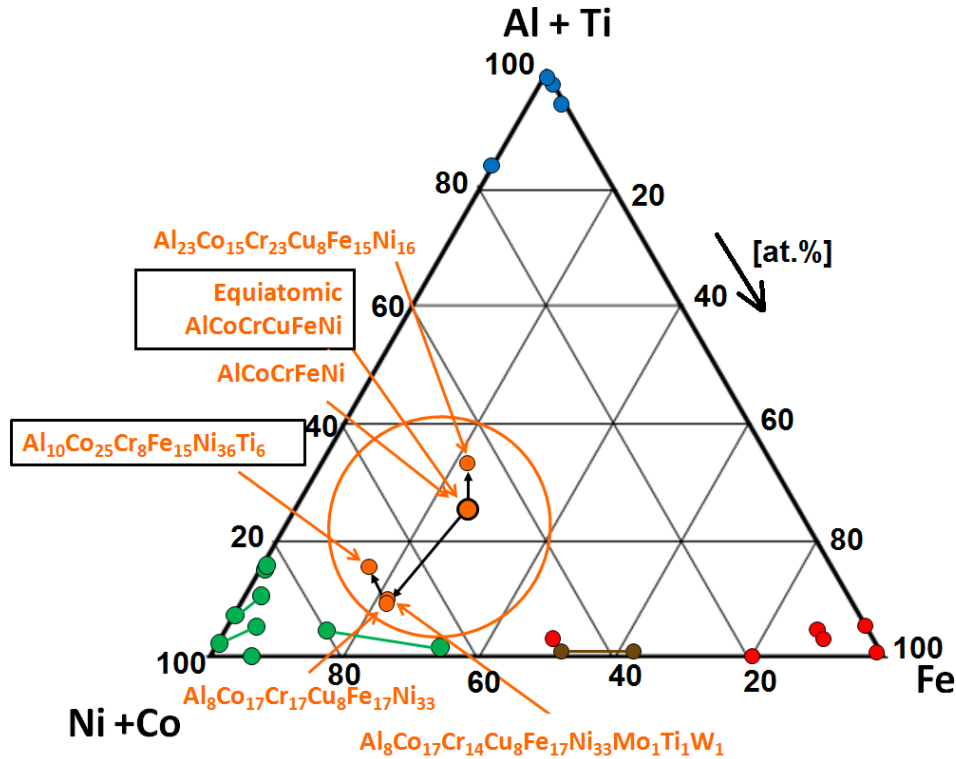
FIG. 1. A pseudo-ternary phase diagram (Al-Ti)-(Ni-Co)-Fe. Blue dots represent commercially used Al- or Ti-based alloys (e.g. the Al 4XXX series, the Al 8XXX series, Ti-B11007 or Ti-1Al-8V-5Fe), red dots commercially used Fe-based alloys (e.g. PH-13-8, X10 CrAlSi 24, the TRIP steels, 1RK91, X6 CrNi 22-13 or X10 NiCrAlTi 32-20), green dots commercially used Ni-based alloys (e.g. CMSX-4, CMSX-10, Waspaloy, Inconel 617, Stellite or Inconel 718) and brown dots Fe-Ni binary alloys (e.g. the Alloy 800). The investigated high entropy alloys are represented in orange. The black arrows point to the way of the alloy evolution.

The optimization path for AlCoCrCuFeNi has taken three ways, based on several well-known facts:

- Reduction of segregated phases. Cu-based phases segregate easily and can thus create disturbances inside the grains as well as at the grain boundaries → the Cu amount will be decreased ($Al_{23}Co_{15}Cr_{23}Cu_8Fe_{15}Ni_{16}$, $Al_8Co_{17}Cr_{17}Cu_8Fe_{17}Ni_{33}$, $Al_8Co_{17}Cr_{14}Cu_8Fe_{17}Ni_{33}Mo_1Ti_1W_1$) or removed completely (AlCoCrFeNi and $Al_{10}Co_{25}Cr_8Fe_{15}Ni_{36}Ti_6$).

- Optimize the oxidation properties of the alloy → the content of Al and Cr will be increased ($Al_{23}Co_{15}Cr_{23}Cu_8Fe_{15}Ni_{16}$).

- Preferential formation of a two-phase microstructure in the alloy. The microstructure of AlCoCrCuFeNi shows two main phases (except for the Cu-rich phases) with a tendency towards the well-known cubic microstructure in Ni-based alloys →

this features will be increased by increasing the amount of Ni and then fine-tuning by adjusting or adding other elements ($Al_8Co_{17}Cr_{17}Cu_8Fe_{17}Ni_{33}$, $Al_8Co_{17}Cr_{14}Cu_8Fe_{17}Ni_{33}Mo_1Ti_1W_1$ and $Al_{10}Co_{25}Cr_8Fe_{15}Ni_{36}Ti_6$).

FIG. 2 shows the optical micrographs of all six investigated alloys: AlCoCrCuFeNi, AlCoCrFeNi, $Al_{23}Co_{15}Cr_{23}Cu_8Fe_{15}Ni_{16}$, $Al_8Co_{17}Cr_{17}Cu_8Fe_{17}Ni_{33}$, $Al_8Co_{17}Cr_{14}Cu_8Fe_{17}Ni_{33}Mo_1Ti_1W_1$ and $Al_{10}Co_{25}Cr_8Fe_{15}Ni_{36}Ti_6$. All alloys show a dendritic morphology. In the case of $Al_{10}Co_{25}Cr_8Fe_{15}Ni_{36}Ti_6$ (FIG. 2f), the dendrites have the largest dimensions (up to 400 μm). In all cases (except for AlCoCrCuFeNi, FIG. 2a), a disturbingly large segregation of Cu could be avoided by the reduction of the Cu content or can be unmade by adequate heat treatments (e.g. 1250°C/1h in the case of $Al_8Co_{17}Cr_{17}Cu_8Fe_{17}Ni_{33}$ and $Al_8Co_{17}Cr_{14}Cu_8Fe_{17}Ni_{33}Mo_1Ti_1W_1$ [19]).
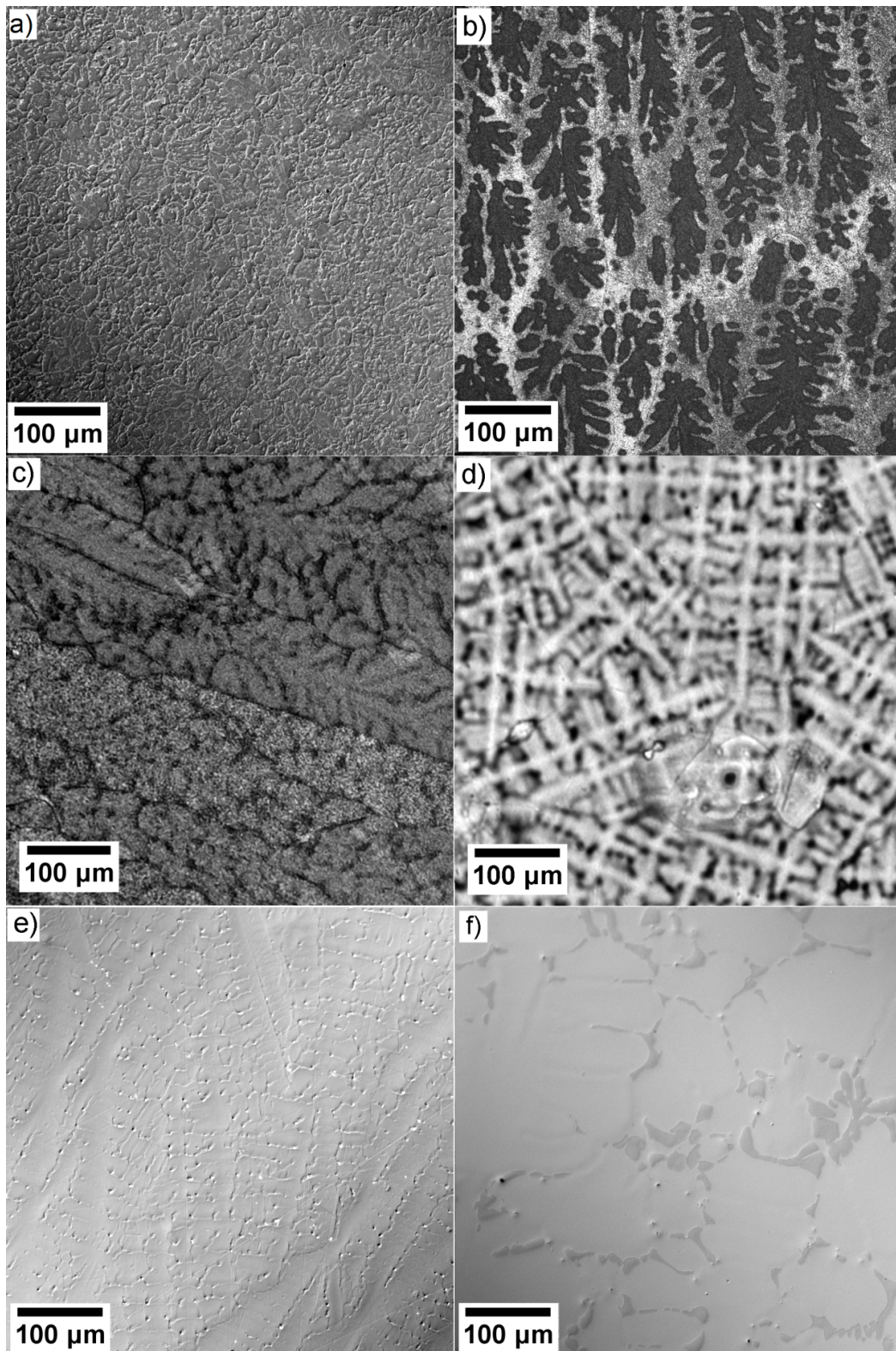
FIG. 2. Optical micrographs of a) AlCoCrCuFeNi (polished), b) AlCoCrFeNi (etched), c) $Al_{23}Co_{15}Cr_{23}Cu_8Fe_{15}Ni_{16}$ (etched), d) $Al_8Co_{17}Cr_{17}Cu_8Fe_{17}Ni_{33}$ (etched), e) $Al_8Co_{17}Cr_{14}Cu_8Fe_{17}Ni_{33}Mo_1Ti_1W_1$ (etched) and f) $Al_{10}Co_{25}Cr_8Fe_{15}Ni_{36}Ti_6$ (polished).
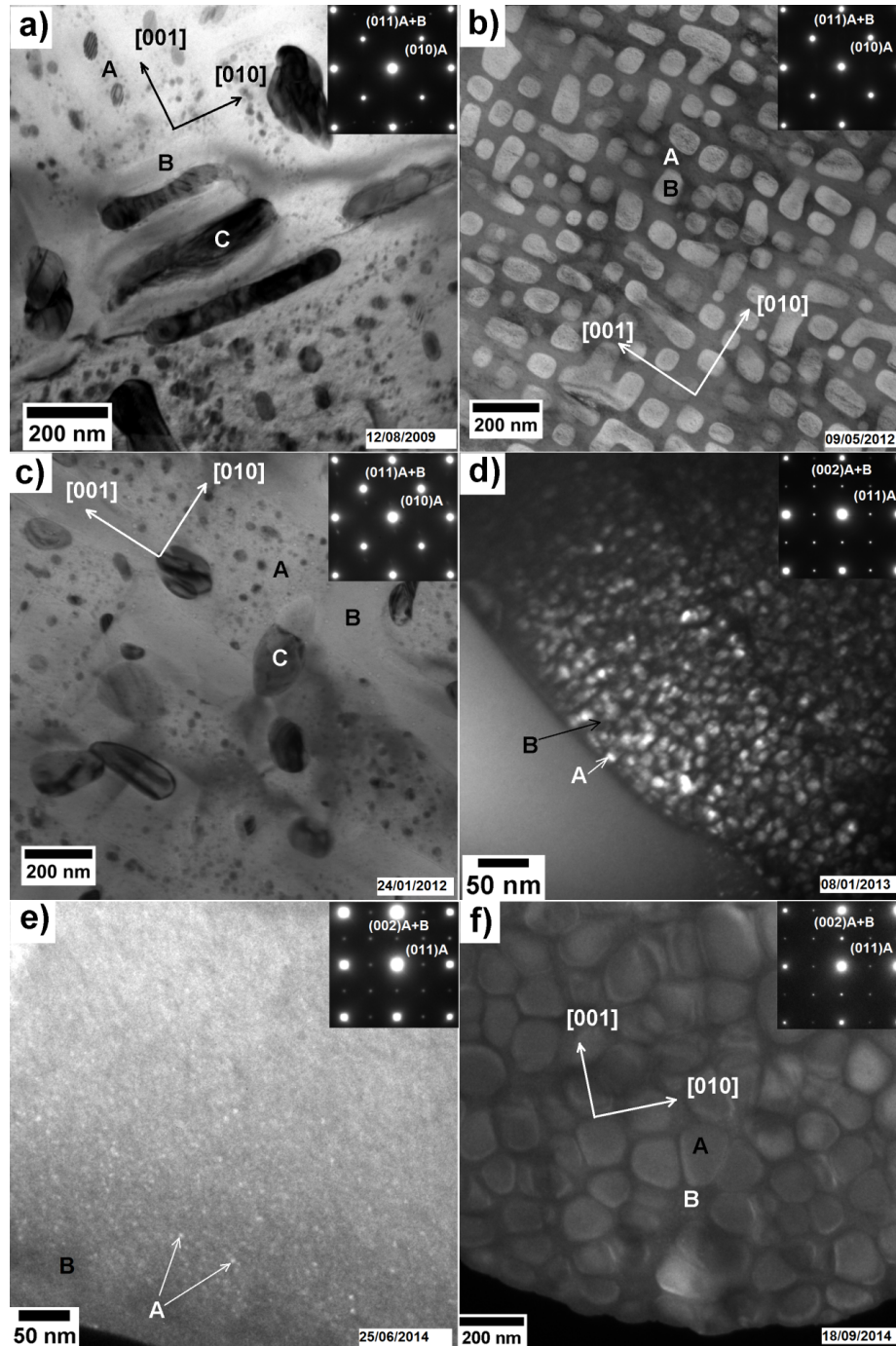
FIG. 3. TEM images of the dendritic regions of all investigated alloys: a) BF image of AlCoCrCuFeNi, at a random orientation, and a SAD taken along the [100] zone axis of the Al-Ni rich matrix and the Cr-Fe rich precipitate; b) BF of AlCoCrFeNi and the corresponding SAD taken along the [100] zone axis; c) BF of $Al_{23}Co_{15}Cr_{23}Cu_8Fe_{15}Ni_{16}$, at a random orientation, and a SAD taken along the [100] zone axis of the Al-Ni rich matrix and the Cr-Fe rich precipitate; d) DF of $Al_8Co_{17}Cr_{17}Cu_8Fe_{17}Ni_{33}$ and the corresponding SAD taken along the [100] zone axis; e) DF of $Al_8Co_{17}Cr_{14}Cu_8Fe_{17}Ni_{33}Mo_1Ti_1W_1$ and the corresponding SAD taken along the [100] zone axis; and f) DF of $Al_{10}Co_{25}Cr_8Fe_{15}Ni_{36}Ti_6$ and the corresponding SAD taken along the [100] zone axis. A stands for the Al-Ni rich phase, B for the Cr-Fe rich phase and C for the Cu-rich phase. In all SADs, two diffraction spots have been highlighted. One of them has a high intensity and belongs to both the ordered matrix and the disordered platelet. The other spot is a so-called superlattice spot which has a weaker intensity and thus belongs to only the Al-Ni rich matrix of ordered B2 structure. [010] and [001] directions have been indicated in the images in a), b), c) and f).

In order to gain information on a smaller scale, the alloys have been investigated by TEM. FIG. 3 shows bright or dark field images of the dendritic regions of the six alloys and selected area diffraction patterns (SADs) taken along the [100] zone axes of the matrix and the main precipitate. The bright field (BF) image of the original alloy AlCoCrCuFeNi (FIG. 3a) shows an Al-Ni rich matrix of B2 structure (called A), with 10 – 50 nm small Cu rich precipitates. Bright imaged Cr-Fe rich platelets of a disordered bcc phase (called B) as well as dark imaged Cu rich platelets of B2 structure (called C) can be distinguished [11]. This image has been taken along a direction which puts the Cu platelets in diffracting conditions. The SAD in the upper right corner has been taken along the [100] zone axis of the A-Ni rich matrix and the Cr-Fe rich platelets. The two highlighted diffraction spots belong to both the ordered matrix and the disordered platelet (in the case of the (011) spot) or only the Al-Ni rich matrix of ordered B2 structure (in the case of the (010) spot). The (010) superlattice spot can only be obtained from an ordered structure. FIG. 3b shows a BF image of AlCoCrFeNi, in which the bright imaged Cr-Fe rich precipitates of disordered bcc structure (B) can be distinguished inside a dark imaged matrix Al-Ni rich of B2 structure (A) [15]. The corresponding SAD has been taken in the same direction. FIG. 3c shows a BF image of $Al_{23}Co_{15}Cr_{23}Cu_8Fe_{15}Ni_{16}$. This microstructure is close to the one in AlCoCrCuFeNi: an Al-Ni rich matrix of B2 structure (A) with 10 – 200 nm Cu rich precipitates (C) and bright imaged Cr-Fe rich platelets of a disordered bcc structure (B) can be observed [17]. This image has been taken along a direction which puts the Cu platelets in diffracting conditions. The SAD in the upper right corner has been taken along the [100] zone axis of the A-Ni rich matrix and the Cr-Fe rich platelets. These three alloys are characterized by a global bcc structure.

FIG. 3d shows the DF image of $Al_8Co_{17}Cr_{17}Cu_8Fe_{17}Ni_{33}$. Note the different scale, at which a dark imaged matrix of almost nominal composition and disordered fcc structure (B) can be seen. The ~20 nm sized bright imaged precipitates are Al-Cu-Ni rich and present an $L1_2$ structure (A) [17]. The corresponding SAD has been taken in the same direction. In order to shift the melting point of the alloy to higher temperature and to increase the existing area of

the phase with the $L1_2$ structure, Mo, Ti and W were added to the alloy. However, Mo, Ti and W alter the microstructure of $Al_8Co_{17}Cr_{14}Cu_8Fe_{17}Ni_{33}Mo_1Ti_1W_1$ only slightly: FIG. 3e shows the DF image of $Al_8Co_{17}Cr_{14}Cu_8Fe_{17}Ni_{33}Mo_1Ti_1W_1$. The expected effect of the added elements was negligible. The precipitates are smaller than the ones observed in the $Al_8Co_{17}Cr_{17}Cu_8Fe_{17}Ni_{33}$ alloy: a dark imaged matrix of almost nominal composition and disordered fcc structure (B) with ~10 nm sized bright imaged Al-Cu-Ni rich precipitates with an $L1_2$ structure (A) [19]. The corresponding SAD has been taken in the same direction. The final alloy, $Al_{10}Co_{25}Cr_8Fe_{15}Ni_{36}Ti_6$, has a two-phase microstructure which is characterized by a matrix of a disordered fcc structure (B). The precipitates are Al-Ni-Ti rich and of $L1_2$ structure (A), but much bigger than in the two preceding alloys; namely up to 200 nm [20]. The corresponding SAD has been taken in the same direction. The last three alloys have a global fcc structure and show a γ-γ' morphology known from Ni-based alloys.

The microchemical compositions of the most important phases of the dendritic regions are summarized in Table 1. The main phases; namely the matrix and the most prominent precipitates, as well as the additional phases and some comments on the alloys' behaviors are summarized in Table 2.

In addition to the microstructural investigations, the alloys have been investigated for their microhardness. FIG. 4 shows the Vickers microhardnesses for the six alloys. The first three alloys of global bcc structure are much harder (> 400 HV) than the last three alloys of global fcc structure (< 350 HV). A high hardness is favorable, but unfortunately all three bcc alloys are too brittle for mechanical application. The complete removal of Cu as well as the addition of more Al and Cr do not seem to be a good path to follow for the optimization of AlCoCrCuFeNi.

The hardnesses of $Al_8Co_{17}Cr_{17}Cu_8Fe_{17}Ni_{33}$ and $Al_8Co_{17}Cr_{14}Cu_8Fe_{17}Ni_{33}Mo_1Ti_1W_1$ are too low, compared to Ni-based alloys (e.g. ~ 420 HV for CMSX4). However, the last alloy, $Al_{10}Co_{25}Cr_8Fe_{15}Ni_{36}Ti_6$ shows a medium hardness and the handling of the alloy during cutting and casting shows a promising ductility. This alloy will thus be kept for further optimization.

On the Optimization of the Microstructure and Mechanical Properties of Al-Co-Cr-Cu-Fe-Ni-Ti –Based High Entropy Alloys

TABLE 1. Chemical composition of the main phases in the dendrites of the six investigated alloys AlCoCrCuFeNi, AlCoCrFeNi, $Al_{23}Co_{15}Cr_{23}Cu_8Fe_{15}Ni_{16}$, $Al_8Co_{17}Cr_{17}Cu_8Fe_{17}Ni_{33}$, $Al_8Co_{17}Cr_{14}Cu_8Fe_{17}Ni_{33}Mo_1Ti_1W_1$ and $Al_{10}Co_{25}Cr_8Fe_{15}Ni_{36}Ti_6$. Data have been taken from the references given in the Ref. column. The error bar is given by the standard deviation 2 σ.

Phase	Concentration [at.%]									Measuring method	Ref
	Al	Co	Cr	Cu	Fe	Ni	W	Mo	Ti		
AlCoCrCuFeNi											
Al-Ni rich matrix	**25.8 ± 3**	17.9 ± 3	3.0 ± 3	10.4 ± 3	12.1 ± 3	**30.8 ± 3**				TEM/EDX	[11]
Cr-Fe rich platelets	2.2 ± 3	20 ± 3	**43.2 ± 3**	0.3 ± 3	**29 ± 3**	5.3 ± 3				TEM/EDX	[11]
Cu rich platelet	4.9 ± 3	1.8 ± 3	1.1 ± 3	**85 ± 3**	2.0 ± 3	5.2 ± 3				TEM/EDX	[11]
AlCoCrFeNi											
Al-Ni rich matrix	**32.0±3.4**	22.6±2.0	4.9±1.4		13.0±1.1	**27.5±2.6**				TEM/EDX	[15]
Cr-Fe rich precipitates	4.9±3.6	22.3±0.6	**35.7±5.1**		**29.9±2.1**	7.7±3.4				TEM/EDX	[15]
$Al_{23}Co_{15}Cr_{23}Cu_8Fe_{15}Ni_{16}$											
Al-Ni rich matrix	28.9±1.5	21.2±1.1	10.3±3.1	6.1±0.4	12.6±1.1	20.8±1.3				TEM/EDX	[17]
Cr-Fe rich platelets	3.8±0.3	13.3±1.1	50.1±3.0	2.3±0.9	26.0±0.9	4.6±1.6				TEM/EDX	[17]
Cu rich phase	9.4±0.5	2.9±0.5	3.8±2.6	76.1±4.5	2.8±1.3	5.2±0.6				TEM/EDX	[17]
$Al_8Co_{17}Cr_{17}Cu_8Fe_{17}Ni_{33}$											
Al-Ni rich precipitate	11.5±1.0	14.0±2.9	8.6±1.6	6.1±1.7	12.6±1.4	47.1±5.0				3D-AP	[17]
Matrix	7.1±0.7	19.0±1.1	19.5±1.1	3.1±0.5	19.4±1.1	31.8±1.3				3D-AP	[17]
$Al_8Co_{17}Cr_{14}Cu_8Fe_{17}Ni_{33}Mo_1Ti_1W_1$											
Al-Ni rich precipitate	**20.4±0.6**	13.4±0.7	7.8 ± 0.4	5.1 ± 0.2	11.3±1.1	**39.4±1.2**	0.1± 0.1	0.9±0.4	1.6 ± 0.2	3D-AP	[19]
Matrix	8.0 ± 0.1	18.9±0.1	14.2±0.3	3.3 ± 0.1	18.3±0.2	35.8±0.4	0.2± 0.1	0.7 ± 0.1	0.7 ± 0.0	3D-AP	[19]
$Al_{10}Co_{25}Cr_8Fe_{15}Ni_{36}Ti_6$											
Al-Ni rich matrix	12.1±1.4	22.3±0.9	3.1 ± 1.1	7.7 ± 1.7	45.5±2.9				9.3 ± 1.2	TEM/EDX	This work
Cr-Fe rich platelets	8.8 ± 2.2	29.5±1.8	7.7 ± 1.2	20.0±4.2	30.7±4.3				3.2 ± 1.7	TEM/EDX	This work

TABLE 2. Summary of the main phases and the additional phases as well as some comments on the six investigated alloys AlCoCrCuFeNi, AlCoCrFeNi, $Al_{23}Co_{15}Cr_{23}Cu_8Fe_{15}Ni_{16}$, $Al_8Co_{17}Cr_{17}Cu_8Fe_{17}Ni_{33}$, $Al_8Co_{17}Cr_{14}Cu_8Fe_{17}Ni_{33}Mo_1Ti_1W_1$ and $Al_{10}Co_{25}Cr_8Fe_{15}Ni_{36}Ti_6$.

As-cast alloy	Matrix (dendrite)	Main precipitating phase (dendrite)	Additional phases (dendrite)	Comments	Ref.
AlCoCrCuFeNi	Al-Ni rich, B2 structure	Cr-Fe rich, disordered bcc/	Cu rich phases of different shapes and structures	Too brittle for mechanical application	[11]
AlCoCrFeNi	Al-Ni rich, B2 structure	Cr-Fe rich, disordered bcc	-	Too brittle for mechanical application	[15]
$Al_{23}Co_{15}Cr_{23}Cu_8Fe_{15}Ni_{16}$	Al-Ni rich, B2 structure	Cr-Fe rich, disordered bcc	Cu rich platelets	Too brittle for mechanical application	[17]
$Al_8Co_{17}Cr_{17}Cu_8Fe_{17}Ni_{33}$	Cr-Co-Fe rich, disordered fcc	Al-Cu-Ni rich, L1$_2$ structure	-	Too soft for mechanical application	[17-18]
$Al_8Co_{17}Cr_{14}Cu_8Fe_{17}Ni_{33}Mo_1Ti_1W_1$	Cr-Co-Fe rich, disordered fcc	Al-Cu-Ni rich, L1$_2$ structure	-	Too soft for mechanical application	[19]
$Al_{10}Co_{25}Cr_8Fe_{15}Ni_{36}Ti_6$	Cr-Co-Fe rich, disordered fcc	Al-Ni-Ti rich, L1$_2$ structure	-	To be investigated	This work
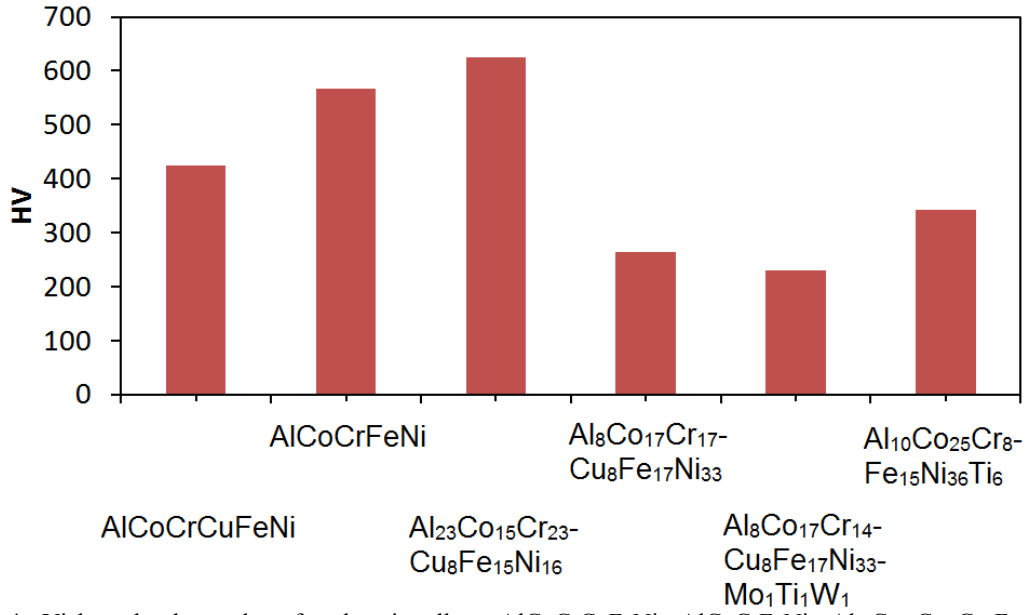
FIG. 4. Vickers hardness data for the six alloys AlCoCrCuFeNi, AlCoCrFeNi, $Al_{23}Co_{15}Cr_{23}Cu_8Fe_{15}Ni_{16}$, $Al_8Co_{17}Cr_{17}Cu_8Fe_{17}Ni_{33}$, $Al_8Co_{17}Cr_{14}Cu_8Fe_{17}Ni_{33}Mo_1Ti_{1-}W_1$ and $Al_{10}Co_{25}Cr_8Fe_{15}Ni_{36}Ti_6$.

Summary

The initial high entropy alloy AlCoCrCuFeNi with equiatomic composition is characterized by a high number of phases and has insufficient mechanical properties, which inhibit the use of this alloy in the present state. Therefore, an optimization of this alloy has been achieved by the following steps:

- Reduction of segregated phases → the Cu content was reduced or removed completely.

- Optimization of the oxidation properties → the content of Al and Cr was increased.

- Preferential formation of a two-phase microstructure in the alloy → addition of Ti or variation of the composition of the other alloying elements. The microstructure shows the well-known γ-γ' microstructure.

The following high entropy alloys have been developed during the pathway of the optimization:

AlCoCrCuFeNi, AlCoCrFeNi, $Al_{23}Co_{15}Cr_{23}Cu_8Fe_{15}Ni_{16}$, $Al_8Co_{17}Cr_{17}Cu_8Fe_{17}Ni_{33}$, $Al_8Co_{17}Cr_{14}Cu_8Fe_{17}Ni_{33}Mo_1Ti_1W_1$ and $Al_{10}Co_{25}Cr_8Fe_{15}Ni_{36}Ti_6$. They have been investigated by optical, scanning electron microscopy and transmission electron microscopy as well as Vickers hardness measurements. The most promising alloy finally was found $Al_{10}Co_{25}Cr_8Fe_{15}Ni_{36}Ti_6$. However, further optimization of this alloy is necessary in order to increase its microhardness.

References

[1] Yeh, J.W., Knowl. Bridge, 40 (2003) 1.

[2] Ranganathan, S., Curr. Sci., 85 (2003) 1404.

[3] Tong, C.J., Chen, M.R., Chen, S.K., Yeh, J.W., Shun, T.T., Lin, S.J. and Chang, S.Y., Metall. Mater. Trans. A, 36A (2005) 1263.

[4] Jiang, L., Lu, Y.P., Dong, Y., Wang, T.M., Cao, Z.Q. and Li, T.J., Intermetallics, 44 (2014) 37.

[5] Ng, C., Guo, S., Luan, J., Shi, S. and Liu, C.T., Intermetallics, 31 (2012) 165.

[6] Chen, M.R., Lin, S.J., Yeh, J.W., Chen, S.K., Huang, Y.S. and Tu, C.P., Materials Transactions, 47 (2006) 1395.

[7] Cantor, B., Chang, I.T.H., Knight, P. and Vincent, A.J.B., Mater. Sci. Eng., A, 375 (2004) 213.

[8] Senkov, O.N., Wilks, G.B., Miracle, D.B., Chuang, C.P. and Liaw, P.K., Intermetallics, 18 (2010) 1758.

[9] Shun, T.T., Hung, C.H. and Lee, C.F., J. Alloys Compd., 493 (2010) 105.

[10] Zhang, Y., Zhou, Y.J., Lin, J.P., Chen, G.L. and Liaw, P.K., Adv. Eng. Mater., 10 (2008) 534.

[11] Singh, S., Wanderka, N., Murty, B.S., Glatzel, U. and Banhart, J., Acta. Mater., 59 (2011) 182.

[12] Chen, H.Y., Tsai, C.W., Tung, C.C., Yeh, J.W., Shun, T.T., Yang, C.C. and Chen, S.K., Annales De Chimie-Science Des Materiaux, 31 (2006) 685.

[13] Zhang, K.B., Fu, Z.Y., Zhang, J.Y., Shi, J., Wang, W.M., Wang, H., Wang, Y.C. and Zhang, Q.J., J. Alloys Compd., 502 (2010) 295.

[14] Tung,. C.C., Yeh, J.W., Shun, T.T., Chen, S.K., Huang, Y.S. and Chen, H.C., Mater. Lett., 61 (2007) 1.

[15] Manzoni, A., Daoud, H., Völkl, R., Glatzel, U. and Wanderka, N., Ultramicroscopy, 132 (2013) 212.

[16] Zhang, Y., Ma, S.G. and Qiao, J.W., Metallurgical and Materials Transactions a-Physical Metallurgy and Materials Science, 43A (2012) 2625.

[17] Manzoni, A., Daoud, H., Mondal, S., van Smaalen, S., Völkl, R., Glatzel, U. and Wanderka, N., J. Alloys Compd., 552 (2013) 430.

[18] Daoud, H.M., Manzoni, A., Völkl, R., Wanderka, N. and Glatzel, U., JOM, 65 (2013) 1805.

[19] Manzoni, A., Daoud, H., Völkl, R., Glatzel, U. and Wanderka, N., Submitted to Ultramicroscopy, (2015).

[20] Daoud, H.M., Manzoni, A.M., Wanderka, N. and Glatzel, U., Submitted to JOM, (2015).

Authors Index

Subject Index

المراجع: يجب طباعة المراجع بأسطر مزدوجة ومرقمة حسب تسلسلها في النص. وتكتب المراجع في النص بين قوسين مربعين. ويتم اعتماد اختصارات الدوريات حسب نظام Wordlist of Scientific Reviewers.

الجداول: تعطى الجداول أرقاما متسلسلة يشار إليها في النص. ويجب طباعة كل جدول على صفحة منفصلة مع عنوان فوق الجدول. أما الحواشي التفسيرية، التي يشار إليها بحرف فوقي، فتكتب أسفل الجدول.

الرسوم التوضيحية: يتم ترقيم الأشكال والرسومات والرسومات البيانية (المخططات) والصور، بصورة متسلسلة كما وردت في النص.

تقبل الرسوم التوضيحية المستخرجة من الحاسوب والصور الرقمية ذات النوعية الجيدة بالأبيض والأسود، على ان تكون أصيلة وليست نسخة عنها، وكل منها على ورقة منفصلة ومعرفة برقمها بالمقابل. ويجب تزويد المجلة بالرسومات بحجمها الأصلي بحيث لا تحتاج إلى معالجة لاحقة، وألا تقل الحروف عن الحجم 8 من نوع Times New Roman، وألا تقل سماكة الخطوط عن 0.5 وبكثافة متجانسة. ويجب إزالة جميع الألوان من الرسومات ما عدا تلك التي ستنشر ملونة. وفي حالة إرسال الرسومات بصورة رقمية، يجب أن تتوافق مع متطلبات الحد الأدنى من التمايز (1200 dpi Resolution) لرسومات الأبيض والأسود الخطية، و 600 dpi للرسومات باللون الرمادي، و 300 dpi للرسومات الملونة. ويجب تخزين جميع ملفات الرسومات على شكل (jpg)، وأن ترسل الرسوم التوضيحية بالحجم الفعلي الذي سيظهر في المجلة. وسواء أرسل المخطوط بالبريد أو عن طريق الشبكة (Online)، يجب أرسال نسخة ورقية أصلية ذات نوعية جيدة للرسومات التوضيحية.

مواد إضافية: تشجع المجلة الباحثين على إرفاق جميع المواد الإضافية التي يمكن أن تسهل عملية التحكيم. وتشمل المواد الإضافية أي اشتقاقات رياضية مفصلة لا تظهر في المخطوط.

المخطوط المنقح (المعدَل) والأقراص المدمجة: بعد قبول البحث للنشر وإجراء جميع التعديلات المطلوبة، فعلى الباحثين تقديم نسخة أصلية ونسخة أخرى مطابقة للأصلية مطبوعة بأسطر مزدوجة، وكذلك تقديم نسخة إلكترونية تحتوي على المخطوط كاملا مكتوبا على Microsoft Word for Windows 2000 أو ما هو استجد منه. ويجب إرفاق الأشكال الأصلية مع المخطوط النهائي المعدل حتى لو تم تقديم الأشكال إلكترونيا. وتخزن جميع ملفات الرسومات على شكل (jpg)، وتقدم جميع الرسومات التوضيحية بالحجم الحقيقي الذي ستظهر به في المجلة. ويجب إرفاق قائمة ببرامج الحاسوب التي استعملت في كتابة النص، وأسماء الملفات على قرص مدمج، حيث يعلَم القرص بالاسم الأخير للباحث، وبالرقم المرجعي للمخطوط للمراسلة، وعنوان المقالة، والتاريخ. ويحفظ في مغلف واقٍ.

الفهرسة: تقوم المجلة الأردنية للفيزياء بالإجراءات اللازمة لفهرستها وتلخيصها في جميع الخدمات الدولية المعنية.

حقوق الطبع

يُشَكِّل تقديم مخطوط البحث للمجلة اعترافاً صريحاً من الباحثين بأنَ مخطوط البحث لـم يُنْشَر ولـم يُقَدَّم للنشر لدى أي جهَة أخرى كانت وبأي صيغة ورقية أو إلكترونية أو غيرها. ويُشترط على الباحثين ملء أنموذج يَنَصُ على نقْل حقوق الطبع لتُصبح ملكاً لجامعة اليرموك قبل الموافقة على نشر المخطوط. ويقوم رئيس التحرير بتزويد الباحثين بإنموذج نقل حقوق الطبع مع النسخة المُرْسَلَة للتنقيح. كما ويُمنع إعادة إنتاج أيَ جزء من الأعمال المنشورة في المجلّة من دون إذن خطّيٍ مُسْبَق من رئيس التحرير.

إخلاء المسؤولية

إن ما ورد في هذه المجلة يعبر عن آراء المؤلفين، ولا يعكس بالضرورة آراء هيئة التحرير أو الجامعة أو سياسة اللجنة العليا للبحث العلمي أو وزارة التعليم العالي والبحث العلمي. ولا يتحمل ناشر المجلة أي تبعات مادية أو معنوية أو مسؤوليات عن استعمال المعلومات المنشورة في المجلة أو سوء استعمالها.

معلومات عامة

المجلة الأردنية للفيزياء هي مجلة بحوث علميّة عالمية متخصصة مُحكمة تصدر بدعم من صندوق دعم البحث العلمي، وزارة التعليم العالي والبحث العلمي، عمان، الأردن. وتقوم بنشر المجلة عمادة البحث العلمي والدراسات العليا في جامعة اليرموك، إربد، الأردن. وتنشر البحوث العلمية الأصيلة، إضافة إلى المراسلات القصيرة Short Communications، والملاحظات الفنية Technical Notes، والمقالات الخاصّة Feature Articles، ومقالات المراجعة Review Articles، في مجالات الفيزياء النظرية والتجريبية، باللغتين العربية والإنجليزية.

تقديم مخطوط البحث

تقدم البحوث عن طريق إرسالها إلى البريد الإلكتروني : jjp@yu.edu.jo

تقديم المخطوطات إلكترونيًا: اتبع التعليمات في موقع المجلة على الشبكة العنكبوتية.

ويجري تحكيمُ البحوثِ الأصيلة والمراسلات القصيرة والملاحظات الفنية من جانب مُحكّمين اثنين في الأقل من ذوي الاختصاص والخبرة. وتُشَجّع المجلة الباحثين على اقتراح أسماء المحكمين. أما نشر المقالات الخاصّة في المجالات الفيزيائية النَشِطَة، فيتم بدعوة من هيئة التحرير، ويُشار إليها كذلك عند النشر. ويُطلَب من كاتب المقال الخاص تقديم تقرير واضح يتسم بالدقة والإيجاز عن مجال البحث تمهيداً للمقال. وتنشر المجلةُ أيضاً مقالات المراجعة في الحقول الفيزيائية النشطة سريعة التغيُر، وتشجَع كاتبي مقالات المراجعة أو مُستَكتبيها على إرسال مقترحٍ من صفحتين إلى رئيس التحرير. ويُرفَق مع البحث المكتوب باللغة العربية ملخص (Abstract) وكلمات دالة (Keywords) باللغة الإنجليزية.

ترتيب مخطوط البحث

يجب أن تتم طباعة مخطوط البحث ببنط 12 نوعه Times New Roman، وبسطر مزدوج، على وجه واحد من ورق A4 (21.6 × 27.9 سم) مع حواشي 3.71 سم ، باستخدام معالج كلمات ميكروسوفت وورد 2000 أو ما اسْتَجَد منه. ويجري تنظيم أجزاء المخطوط وفق الترتيب التالي: صفحة العنوان، الملخص، رموز التصنيف (PACS)، المقدّمة، طرق البحث، النتائج، المناقشة، الخلاصة، الشكر والعرفان، المراجع، الجداول، قائمة بدليل الأشكال والصور والإيضاحات، ثَمّ الأشكال والصور والإيضاحات. وتُكتَب العناوين الرئيسة بخطٍ **غامق**، بينما تُكتَب العناوين الفرعية بخطٍ *مائل.*

صفحة العنوان: وتشمل عنوان المقالة، أسماء الباحثين الكاملة وعناوين العمل كاملة. ويكتب الباحث المسؤول عن المراسلات اسمه مشارا إليه بنجمة، والبريد الإلكتروني الخاص به. ويجب أن يكون عنوان المقالة موجزا وواضحا ومعبرا عن فحوى (محتوى) المخطوط، وذلك لأهمية هذا العنوان لأغراض استرجاع المعلومات.

الملخص: المطلوب كتابة فقرة واحدة لا تزيد على مائتي كلمة، موضحة هدف البحث، والمنهج المتبع فيه والنتائج وأهم ما توصل إليه الباحثون.

الكلمات الدالة: يجب أن يلي الملخص قائمة من 4-6 كلمات دالة تعبر عن المحتوى الدقيق للمخطوط لأغراض الفهرسة.

PACS: يجب إرفاق الرموز التصنيفية، وهي متوافرة في الموقع http://www.aip.org/pacs/pacs06/pacs06-toc.html.

المقدمة: يجب أن توضّح الهدف من الدراسة وعلاقتها بالأعمال السابقة في المجال، لا أن تكون مراجعة مكثفة لما نشر (لا تزيد المقدمة عن صفحة ونصف الصفحة مطبوعة).

طرائق البحث (التجريبية / النظرية): يجب أن تكون هذه الطرائق موضحة بتفصيل كاف لإتاحة إعادة إجرائها بكفاءة، ولكن باختصار مناسب، حتى لا تكون تكرارا للطرائق المنشورة سابقا.

النتائج: يستحسن عرض النتائج على صورة جداول وأشكال حيثما أمكن، مع شرح قليل في النص ومن دون مناقشة تفصيلية.

المناقشة: يجب أن تكون موجزة وتركز على تفسير النتائج.

الاستنتاج: يجب أن يكون وصفا موجزا لأهم ما توصلت إليه الدراسة ولا يزيد عن صفحة مطبوعة واحدة.

الشكر والعرفان: الشكر والإشارة إلى مصدر المنح والدعم المالي يكتبان في فقرة واحدة تسبق المراجع مباشرة.

Name: .... :الأسم

Specialty:..:التخصص

Address: ....:العنوان

P.O. Box:.. : صندوق البريد

City & Postal Code: ....:المدينة/الرمز البريدي

Country: ....:الدولة

Phone: ....:رقم الهاتف

Fax No:..:رقم الفاكس

E-mail:...البريد الإلكتروني:

No. of Subscription: ....:عدد الإشتراكات

Method of Payment: ....:طريقة الدفع

Amount Enclosed:...:المبلغ المرفق

Signature: ....:التوقيع

Cheques should be paid to Deanship of Research and Graduate Studies - Yarmouk University.

I would like to subscribe to the Journal
For

      ❑ One Year

      ❑ Two Years

      ❑ Three Years

One Year Subscription Rates		
	Inside Jordan	Outside Jordan
Individuals	JD 8	€ 40
Students	JD 4	€ 20
Institutions	JD 12	€ 60

Correspondence

المملكة الأردنية الهاشمية

جامعة اليرموك

المجلة الأردنية

للفيزياء

مجلة بحوث علمية عالمية متخصصة محكّمة

تصدر بدعم من صندوق دعم البحث العلمي

العدد الخاص